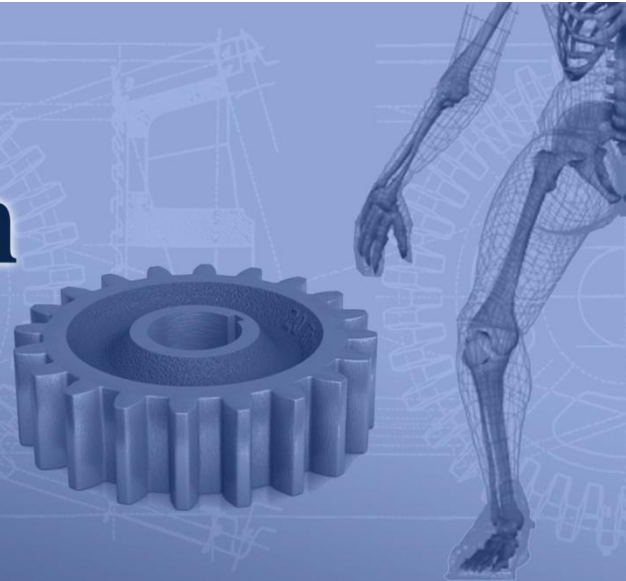




# **Sustainable Construction & Design**

**Volume 2, 2011**



**Metal Structures Centre – 2011**

---

---





# **Sustainable Construction & Design**

**Volume 2, 2011  
Issue 1**

Published by  
Laboratory Soete – Ghent University  
Sint-Pietersnieuwstraat 41  
9000 Gent – Belgium  
<http://www.tribology-fatigue.ugent.be/>

Edited by: Jeroen Van Wittenberghe  
ISSN: 2032-7471

## Editor

Jeroen Van Wittenberghe

## Co-editing organization



MSC - Metal Structures Centre

## Editorial Board

Serge Claessens  
Patrick De Baets  
Wim De Waele  
Sergei Glavatskikh  
Stijn Hertelé  
Sven Vandeputte  
Walter Vermeirsch

## International Scientific Advisory Committee

Magd Abdel Wahab  
Rudi Denys  
Ney Francisco Ferreira  
Gabor Kalacska  
Eli Saul Puchi Cabrera  
Dik Schipper  
Mariana Staia  
Laszlo Zsidai

## Sustainable Construction & Design, volume 2, issue 1, 2011

ISSN 2032-7471

Published by:  
Laboratory Soete – Ghent University  
Sint-Pietersnieuwstraat 41  
9000 Gent – Belgium  
<http://www.tribology-fatigue.ugent.be/>

*Cover design by Jeroen Van Wittenberghe*

*The texts of the papers in this volume were set individually by the authors or under their supervision.  
Only minor corrections to the text may have been carried out by the publisher.*

No responsibility is assumed by the publisher, editor and authors for any injury or damage to persons or property as a matter of products liability, negligence or otherwise, or from any use or operation of any methods, products, instructions or ideas contained in the material herein.

© Laboratory Soete 2011

The rights of this publication are held by the Laboratory Soete according to the Creative Commons, Attribution 2.0. This means users are allowed to share and remix the work, but with attribution to the authors. All with the understanding that other rights on the works are not affected by this license. The full license text can be found on <http://creativecommons.org/licenses/by/2.0/be/>

## Editorial

This first issue of the 2011 volume is dedicated to contact mechanics of materials and components. In the different papers a focus is given on new developments in the fields of tribology, contact fatigue, wear and damage behaviour of materials. Experimental test results as well as new analysis techniques are presented.

From this issue the SCAD journal will be co-edited by the Metal Structures Centre (MSC). The MSC is a recently established partnership between the Laboratory Soete of Ghent University, OCAS and the Belgian Welding Institute and consolidates the research on metal structures in Flanders. The year 2011 will be important for the MSC partners, since in the coming months they all will move to a central campus. This way a new research cluster is created. The new research centre will coordinate and further develop the knowledge and competencies on the design, the use and the evaluation of the behaviour of steel structures.

Finally, I can also look back at a successful edition of last SCAD conference, that took place on 16 and 17 February in Ghent. With over 180 participants this year's conference further exceeded the success of the 2010 edition. I would like to take the opportunity to express my gratitude to all who participated or contributed to this year's conference.



*SCAD 2011 conference, past 16 and 17 February in Ghent, Belgium.*

Jeroen Van Wittenberghe

SCAD journal editor



# Contents

---

## 2011, Volume 2, Issue 1: Contact mechanics of materials and components

Experimental and numerical investigation into effect of elevated temperature on fretting fatigue behavior .....	2
<i>Hojjati Talemi R., Soori M., Abdel Wahab M., De Baets P.</i>	
Dry sliding friction and wear response of WC-Co hardmetal pairs in linearly reciprocating and rotating contact.....	12
<i>Perez Delgado Y., Bonny K., De Baets P., Neis P.D., Rodriguez Fereira V., Malek O., Vleugels J., Lauwers B.</i>	
Characterization and modeling of friction and wear: an overview.....	19
<i>Al-Bender F., De Moerlooze K.</i>	
Tribological behavior of composite-steel on rolling/sliding contacts for various loads .....	29
<i>Ando M., Sukumaran J.</i>	
Height-independent topographic parameters of worn surfaces.....	35
<i>Barányi I., Czifra Á., Kalácska G.</i>	
Review and classification of fretting fatigue test rigs .....	41
<i>De Pauw J., De Baets P., De Waele W.</i>	
Degradation of carbon reinforced epoxy composites under sliding in ambient air.....	53
<i>Dhieb H., Buijnsters J.G., Celis J.P.</i>	
Turning specialities of ZrO <sub>2</sub> ceramics.....	59
<i>Fledrich G., Pálincás I., Keresztes R., Zsidai L., Petróczki K.</i>	
Improved handling characteristics of off-road vehicles by applying active control of steering wheel torque .....	66
<i>Kis J., Jánosi L.</i>	
Development environment for haptic feedback device on mobile agricultural equipment.....	75
<i>Jánosi L., Kis J.</i>	
Abrasive wear of different hot-dip galvanized multilayers.....	82
<i>Szabadi L., Kalácska G., Pék L., Pálincás I.</i>	
Investigation of friction hysteresis using a laboratory-scale tribometer .....	92
<i>Neis P.D., De Baets P., Perez Delgado Y., Ferreira N.F.</i>	
Developing small-aircraft service and re-construction of landing-gear leg support.....	99
<i>Lefánti R., Kalácska G., Oldal I., Petróczki K.</i>	

Machinability of engineering polymers .....	106
<i>Keresztes R., Kalácska G., Zsidai L., Dobrocsi Z.</i>	
Roughness measurement problems in tribological testing.....	115
<i>Rodriguez Fereira V., Sukumaran J., Ando M., De Baets P.</i>	
Effect of velocity on roll/slip for low and high load conditions in polymer composite.....	122
<i>Sukumaran J., Ando M., Rodriguez Fereira V., De Baets P.</i>	
The symmetrical behaviour of carbon nanotubes junctions .....	128
<i>Pataki T.I., Szakál Z.</i>	
Comparing strength properties of natural and synthetic rubber mixtures.....	134
<i>Renner T., Pék L.</i>	
Novel cylinder positioning system realised by using solenoid valves .....	142
<i>Földi L., Béres Z., Sárközi E.</i>	
Symmetry and similarity properties of 2D figures .....	152
<i>Szakál Z., Zsoldos I.</i>	

**2011, Volume 2, Issue 1**

**Contact mechanics of materials and components**

# EXPERIMENTAL AND NUMERICAL INVESTIGATION INTO EFFECT OF ELEVATED TEMPERATURE ON FRETTING FATIGUE BEHAVIOR

R. Hojjati Talemi<sup>1</sup>, M. Soori<sup>2</sup>, M. Abdel Wahab<sup>1</sup> and P. De Baets<sup>1</sup>

<sup>1</sup> Department of mechanical construction and production, Faculty of Engineering, Gent University, Belgium

<sup>2</sup> Department of mechanical engineering, Islamic Azad University, Takestan Branch, Takestan, Iran

**Abstract** Fretting fatigue damage occurs in contacting parts when they are subjected to fluctuating loadings and sliding movements at the same time. This phenomenon may occur in many applications such as bearings/ shafts, bolted and riveted connections, steel cables, and steam and gas turbines. In this paper, the effect of elevated temperature on fretting fatigue life of Al7075-T6 is investigated using a new device for fretting fatigue tests with variable crank shaft mechanism. Also a finite element modeling method was used to estimate crack propagation lifetime in aluminum alloy, Al7075-T6 specimens at elevated temperature under fretting condition. In this method, shear and normal stresses that are caused by contact load are updated at each crack growth increment. Finally, a comparison between the experimental and numerical results is done in order to evaluate the FE simulation.

The experimental results show that: (i) fretting fatigue life of the material increases with temperature up to 350°C by 180% for low stresses and decreases by 40% for high stresses, (ii) this fashion of variation of fretting fatigue life versus temperature is believed to be due to degradation of material properties which occurs by overaging and wear resistance increase due to oxidation of aluminum alloy. While overaging gives rise to degradation of mechanical strength of material and hence the reduction of its fretting fatigue life, surface oxidation of the specimens brings some improvement of fatigue behavior of the material. Metallurgical examination of the specimens reveals that temperature results in precipitation of impurities of Al-7075-T6. The size of precipitated impurities and their distances gets bigger as temperature increases. This could be a reason for material degradation of specimens which are exposed to heating for longer time duration.

**Keywords** Al7075-T6, Fretting Fatigue, Crack propagation, Overaging, Finite element

## 1 INTRODUCTION

Fretting is a wear phenomenon that occurs between two contacting surfaces having small amplitude oscillatory motion [1]. The formation of debris and their entrapment between the contacting surfaces are thought to be one of the origins of crack initiation and premature failure of the engineering components under fretting fatigue conditions. Fretting fatigue mechanism is complex and despite the fact that many attempts have so far been devoted to the study of this process, still there are numerous issues associated with this phenomenon which have remained to be clarified. This phenomenon is schematically shown in Figure 1. Fretting fatigue may occur in mechanical components such as fasteners, turbine blades, bearings/ shafts, steel cables, steam and gas turbines [1]. The aviation industry is another area in which fretting fatigue failures are commonly observed.

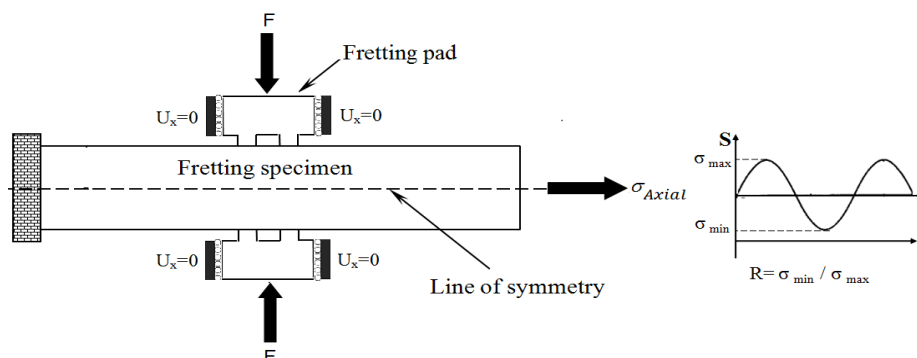


Figure 1. Schematic illustration of fretting fatigue.

Fretting fatigue in turbine dovetails is shown in Figure 2 [2]. Fretting fatigue may reduce the endurance limit of a component by half or more, in comparison to the normal fatigue conditions. Wear and fretting cracks are two direct consequences of fretting fatigue. Figure 3 shows deep pitting in the contact zone of two specimens under fretting fatigue conditions.

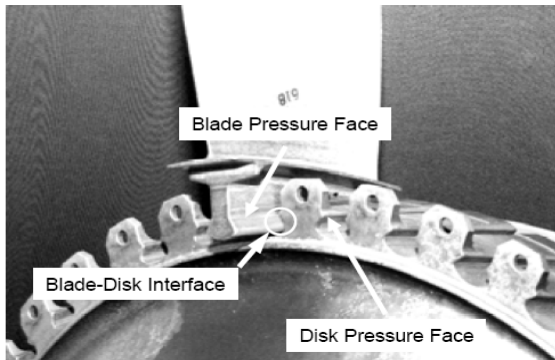


Figure 2. Fretting fatigue in turbine dovetails [2].

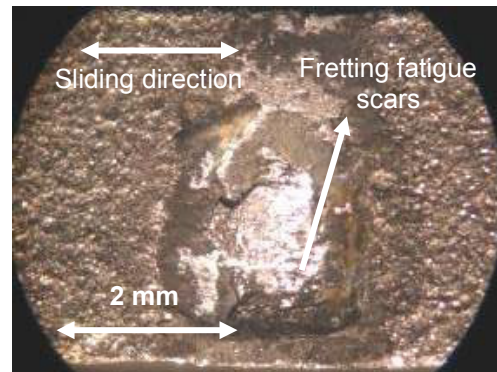


Figure 3. Deep pitting in the contact zone of two specimens under fretting fatigue conditions [3].

Figure 4 shows a fracture surface of a specimen after failure by fretting fatigue [3]. The figure clearly indicates that the fracture surface consists of three different regions; a fretting fatigue zone created by crack propagation, a crack growth zone and a tensile region which gives rise to fracture of specimen when it is sufficiently weakened by the crack zone development. It is generally thought that crack initiation is governed primarily by the local contact stresses and slips amplitude, whereas propagation is more related to the far-field or bulk stresses [1]. A micrograph of fretting crack propagation in a stainless steel alloy is depicted in Figure 5. The crack trajectory can be explained by stress intensity factors  $K_I$  and  $K_{II}$ . Cracks initially grow oblique to the direction of normal force [4] (see figure 5). At this stage, which corresponds to a gross slip conditions between contacting surfaces, the effect of friction force prevails and  $K_{II}$  is the dominant mode of fracture. After the initial oblique propagation, the angle of crack gradually reduces and finally crack coincides with normal force direction. This stage corresponds to a state of partial slip in which a combination of the effects of modes  $K_I$  and  $K_{II}$  takes place. In the third stage, crack grows perpendicular to the normal load direction, due to tensile stress, only by mode  $K_I$ .

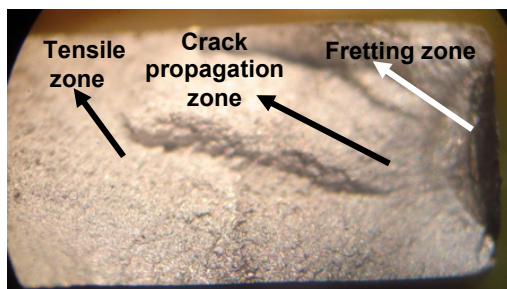


Figure 4. Fracture surface of a specimen after failure by fretting fatigue [3].

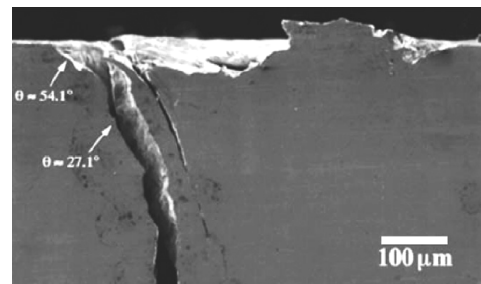


Figure 5. A micrograph of a fretting crack propagation in a stainless steel alloy [4]

Fretting fatigue life can be affected by many parameters such as contact pressure,  $F$ , axial stress,  $\sigma$ , friction between the pads and the specimen, pad geometry, sliding amplitude and temperature. The effect of heating on fretting fatigue has sufficiently been studied by different researchers [5, 6]. Fretting fatigue behavior of materials at elevated temperatures while being influenced by temperature is not the same for all materials. Hamdy and Waterhouse [7] have shown that mechanical strength of Ti-6Al-4V at temperatures up to 600°C diminishes as temperature increases. Hamdy and Waterhouse [5] reported that fretting fatigue life of aged Inconel 718 at elevated temperatures up to 600°C was the same as that for normal fatigue at room temperature. Fretting fatigue life of materials has been examined by different authors such as Mutoh and Satoh [6] and Jina et al [8].

In this work, the effect of elevated temperature on fretting fatigue life of Al7075-T6 is investigated. Also it is known that the study of the influence of various parameters on fretting fatigue behavior of materials is costly and time consuming, numerical simulation is a cheap and easy to use tool by means of which fretting

fatigue phenomenon can be characterized. Thus, the effect of temperature is studied using numerical codes such as ABAQUS [9] and FRANC2D/L [10]. Finally, the numerical results are validated by fretting fatigue tests.

## 2 EXPERIMENTS

### 2.1 Material and specimen

The specimen is machined from aluminum 7075-T6 forged plates by wire electrical discharge method. The longitudinal tensile properties (along the loading axis) were determined, i.e., the elastic modulus was 70 GPa and yield strength was 502 MPa. The specimen shown in Figure 6 had a width of 14.5 mm, a thickness of 4.5 mm and a gauge length of 70 mm. The pads are made of stainless steel 410 with yield and ultimate strength of 420 and 700 MPa, respectively. Each pad has two bases (contacting surfaces) through which the load is exerted on the specimen. The bases have a thickness of 3.1 mm and a length of 12 mm (figure 7).

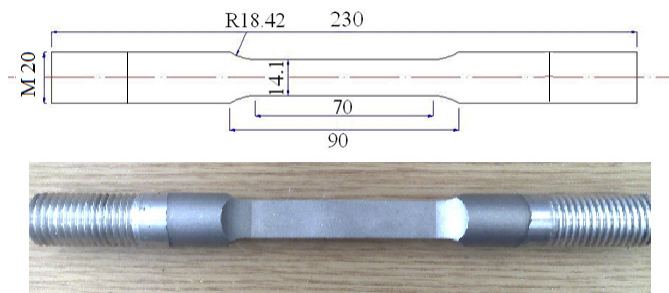


Figure 6. Flat specimens used for fretting fatigue tests.

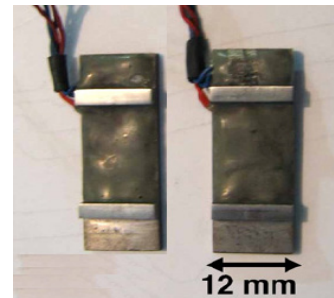


Figure 7. Pad used in the experiments.

### 2.2 Test setup and procedure

The fretting fatigue testing device used in this work has been developed by Majzoobi and Hojjati *et al.* [11]. A general view of the device and its diagrammatic representation are illustrated in Figure 8. The axial fluctuating load is applied to the specimen by a variable crank mechanism. The mechanism consists mainly of a stepped eccentric shaft and two suspension plates [11]. The contact loading system, shown in Figure 9, is completely embedded in the lower cross head which is supported by the two main columns of the device and can be moved vertically. The contact loading system consists of two pads, two adjusting screws and two load cells.

The contact load is induced by two adjusting screws and is measured using two load cells. The load cell readings can ensure that the contact loads produced by tightening screws in two opposite directions are equal. The contact is of the type of flat on flat. The pads are constrained to move vertically as this may affect the sliding oscillations between specimen and pads.

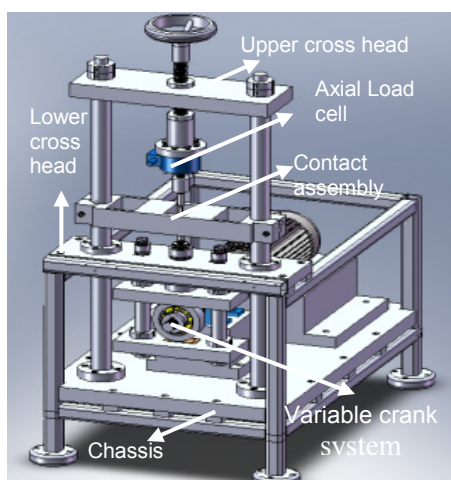


Figure 8. A general view of the testing device [11].

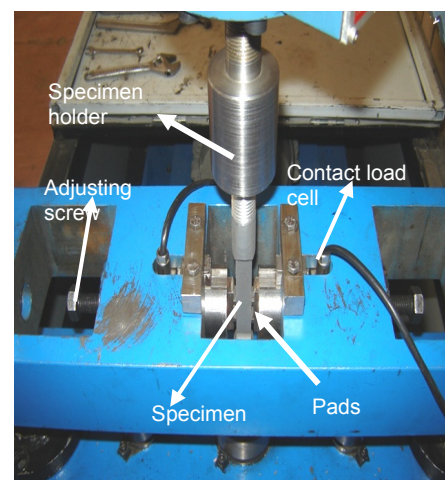


Figure 9. Contact loading system of the testing device [11].

Two load cells are mounted between the adjusting screws and the pads (see figure 9) monitor the contact load on separate digital displays. The frequency of the device can vary using an inverter up to a maximum of 25 Hz. Two heating blowers on each side of the specimen were used to achieve the test temperature (Figure 10). The test temperature was measured and controlled using K-type thermocouples attached on the pad surface and monitored with digital display (Figure 11). Since the temperatures at the contact area and pads might be different, each test was conducted after measuring temperatures on the specimen and pads using a temperature calibration specimen. Before each test, the specimen was kept at 260°C for about an hour to have a uniform temperature distribution over the gauge area of encompassing the contact area. Further details about test setup can be found in reference [11]. The experiments are conducted for stress ratio,  $R=0.1$ , frequency of 25 HZ at a constant force of  $F=1200\text{ N}$ , and working stresses of 110, 150, 200, and 280 MPa. Furthermore, in order to validate the fretting fatigue tests results a number of tensile tests were conducted on specimens at different temperatures and the ultimate strength of material was measured. For each temperature, the specimens were heated up in a furnace for different time durations. This is because the duration of fatigue tests depends on stress level and for low stresses; the specimens are exposed to heating for longer time. Also fractography of fractured surfaces and metallography are performed using optical microscopy.



Figure 10. Heating blower



Figure 11. Temperature display

### 2.3 Test results

The results of fretting fatigue tests on heated specimens and variation of fretting fatigue life versus maximum stress in each temperature is illustrated in Figures 12 and 13. It can be clearly observed that fretting fatigue life increases with temperature for low stresses and decreases for high stresses. This fluctuation in fretting fatigue life versus temperature is thought to be basically due to degradation of material properties which occurs by overaging and wear resistance increase due to oxidation of aluminum alloy. This can be explained more by the fact that aluminum comes in heat-treatable and non-heat treatable alloys. Heat treatable aluminum alloys get their strength from a process called ageing. While the workability index in the 7075 alloy is improved approximately 50% by over-aging, significant decrease in tensile strength can occur when aluminum is subjected to over-aging.

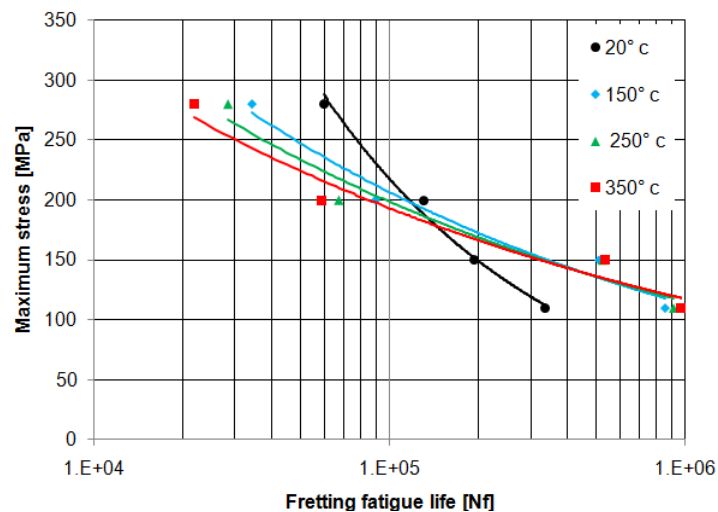


Figure 12. Maximum stress versus fretting fatigue life for different temperatures

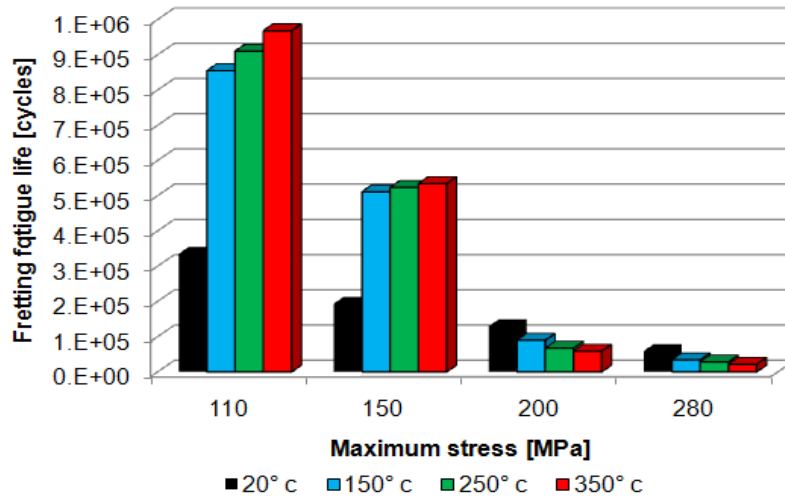


Figure 12. Maximum stress versus fretting fatigue life for different temperatures

After process of heating the material is ductile, since no precipitation has occurred. After a time the solute material precipitates and hardening develops. As the composition reaches its saturated normal state, the material reaches its maximum hardness. The precipitate, however, continues to grow. The fine precipitates disappear. They have grown larger, and as a result the tensile strength of the material decreases. This is called overaging. The tensile strength variation during aging and overaging are shown in Figure 14. While overaging gives rise to degradation of mechanical strength of material and hence the reduction of its fretting fatigue life, surface oxidation of the specimens brings about improvement of fatigue behavior of the material. From the tensile tests the variation of the ultimate strength shows that strength of material decreases as temperature rises (Figure 15).

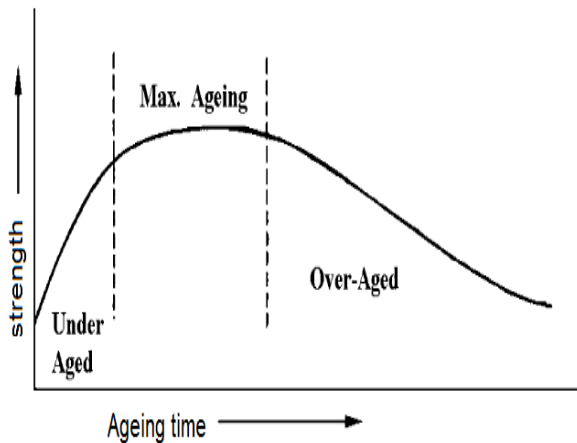


Figure 14. The effect of ageing on strength of aluminum

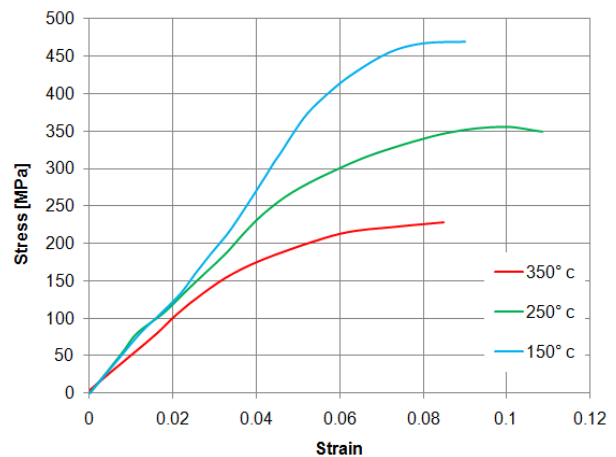


Figure 15. Stress versus strain curve for different temperatures

Optical examination of the specimens in Figure 16 reveals that temperature results in precipitation of impurities of Al-7075-T6. The size of precipitated impurities and their distances gets bigger as temperature increases. This could be a reason for material degradation of specimens which are exposed to heating for longer time duration. However, to the best of authors' belief, the ageing phenomenon can be recognized as the most effective parameter and responsible for the reduction of fretting fatigue life of specimens at high stresses and at low stresses oxidation of aluminum alloy at contact surface of specimen and pad plays as a lubricant role that causes a significant rise in fretting fatigue life.

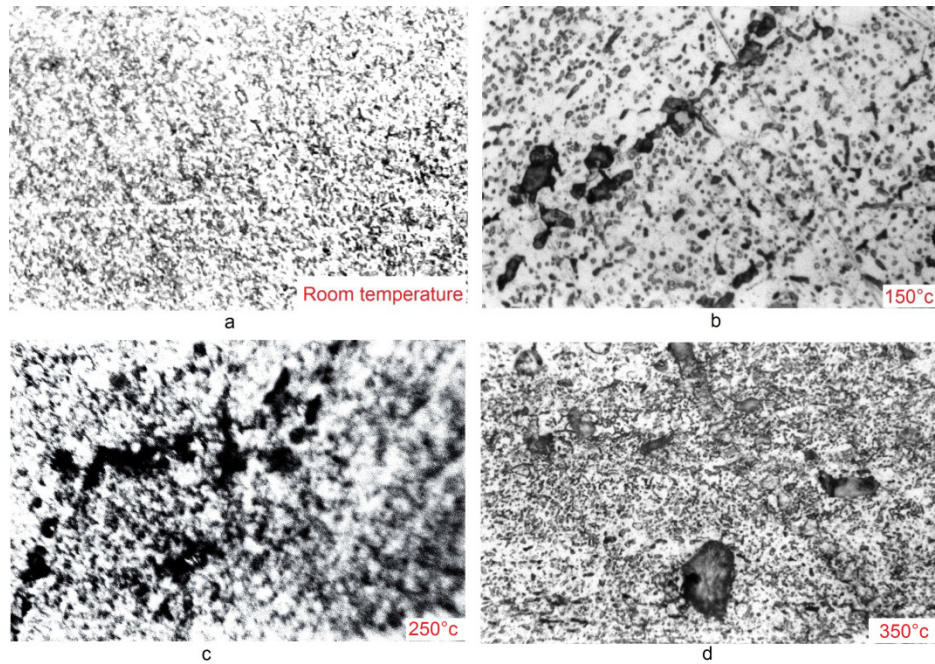


Figure 16. The microstructure of the material (a) at 20°C, (b) at 150°C, (c) at 250°C and (d) at 350°C for 12 hours (magnification x 1000)

Fractured surfaces of tested specimens were examined using optical microscopy. Some typical results are illustrated in Figures 17 and 18 for different temperatures at different stresses. As the figures suggest, the fracture surfaces typically consist of two different regions; a fatigue zone created by crack propagation and a tensile region which gives rise to fracture of specimen when it is sufficiently weakened by the crack zone development.



Figure 17. Fracture surface of specimen at stress of 110 MPa and 350°C

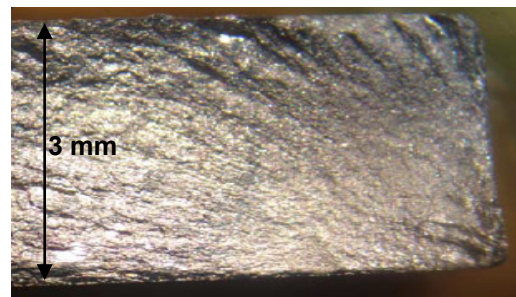


Figure 18. . Fracture surface of specimen at stress of 280 MPa and 250°C

### 3 NUMERICAL SIMULATIONS

#### 3.1 Finite element analysis

A commercial finite element code, ABAQUS [9], was used to analyse the specimen without crack under a given loading condition as a first step. This analysis was done in order to predicate location of initial crack for crack propagation analyse, since previous studies suggests that the location of fretting fatigue crack initiation corresponds with a maximum value of  $\sigma_{xx}$  [1, 12]. The finite element model for flat pad is shown in Figure 19. Note that only one-quarter of the test configuration is considered due to double symmetry with respect to the X and Y axes. Along with the “master-slave” interfacial algorithm developed for contact modelling in the finite element code, ABAQUS, the four-node plane strain elements were utilized. The Lagrange multiplier of friction was used. First, specimens were analyzed using the contact force,  $F/2$  and the axial stress,  $\sigma_{axil}$ . These were applied to the finite element model in the three steps. In the first step, the contact force,  $F/2$  was applied to establish contact between pad and specimen. In the second and third steps, either the maximum bulk stress,  $\sigma_{Max}$  or the minimum bulk stress,  $\sigma_{Min}$ , were applied, respectively. In order to have more accurate results, the finite element mesh was refined in the contact region. An acceptable element size was determined to be at least  $9 \mu\text{m} \times 9 \mu\text{m}$  in the refined contact zone from the

convergence study [13]. The fretting fatigue crack propagation was thereafter conducted using the finite element code, FRANC2D/L [10]. For this purpose, the same geometry and boundary conditions as used in ABAQUS code including the contact interface was modeled. The contact was defined with a gap element using a new material at interface of pad and specimen, with coefficient of friction equal to 0.5. This means that in each step for crack propagation the effect of contact pad was considered and the stress intensity factors were updated after each crack increment. This proposed technique would solve most problems in previous studies where sub-modeling was used for crack propagation [13]. Then, the temperature distribution also was generated on material-by-material basis which has capability to assign different coefficient of thermal expansion and one temperature for the entire model [10]. Finally, an edge crack was inserted in the model considering the contact to perform the crack growth analysis by FRANC2D/L code, which has capability for incremental crack growth using fracture mechanics principles as elaborated later.

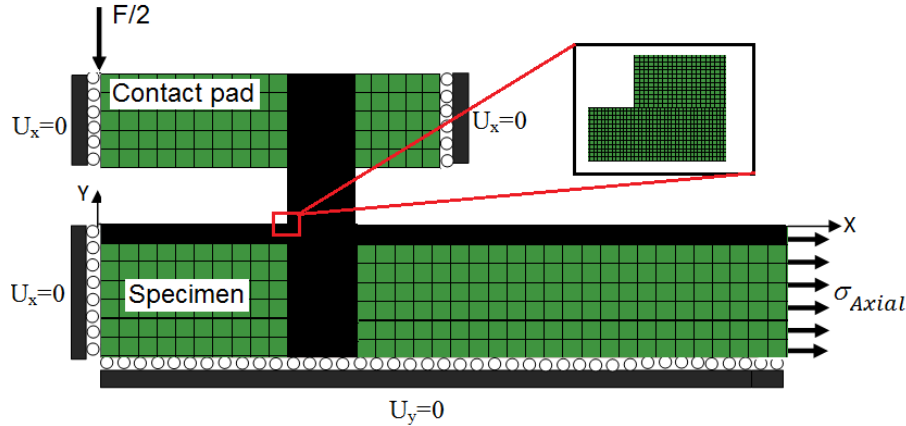


Figure 19. The schematic illustration of finite element model of fretting Fatigue assembly.

### 3.2 Crack propagation analysis

The crack propagation needs the location, length and orientation of the initial crack. As mentioned above the location of initial crack extract from the FE model using ABAQUS code where the maximum value of  $\sigma_{xx}$  takes place, the length and the orientation of the crack propagation path was represented by a curvilinear path consisting of, S, straight segments, as shown in Figure 20. In the first step, an initial crack of length, ( $l_0 = 0.01$  mm), with an orientation, ( $\theta_1 = 45^\circ$ ) from the y-axis was introduced on the contact surface which is observed from previous experimental studies results [14]. The analysis was then performed with a crack length increment of  $\Delta l$ . The incremented crack kinked at the tip of the initial crack at  $(x_2, y_2)$  to produce a new crack at a slope of  $\theta_2$  in the second step of the analysis, and this process was continued.

In FRANC2D/L, the mesh is modified in each incremental step using the Suhara-Fukuda algorithm [15]; the algorithm generates a mesh of triangular elements as shown in Figure 21, and the new crack geometry is represented at each incremental step to reflect the current crack configuration. Along with other theories, the code uses the maximum tangential stress theory, proposed by Erdogan and Sih [16], to determine the crack growth direction. The crack angle,  $\theta_i$  at the  $i$ th step was computed by

$$\theta_i = \theta_{i-1} + 2 \tan^{-1} \left[ \frac{K_{I\text{Max}} - \sqrt{K_{I\text{Max}}^2 + 8K_{II\text{Max}}^2}}{4K_{II\text{Max}}} \right] \quad (1)$$

Where  $K_{I\text{Max}}$  and  $K_{II\text{Max}}$  are the maximum stress intensity factors at the  $i$ th step corresponding to the two crack propagation modes, Mode I and Mode II, at the maximum load. In this way crack trajectory was developed incrementally for a given loading condition using maximum tensile stress criterion. Further, the crack growth rate was assumed to be governed by the Mode I stress intensity factors,  $K_{I\text{Max}}$  and  $K_{I\text{min}}$  [17]. The modified crack closure integral technique of Rybicki and Kanninen [18] was used to calculate these stress intensity factors. These values were then used with the sigmoidal crack growth model to determine the crack propagation life.  $\Delta l$  was considered 0.1 mm for crack propagation. Final failure occurs when the value of stress intensity factor,  $K_I$  tends to its critical value,  $K_{IC}$ .

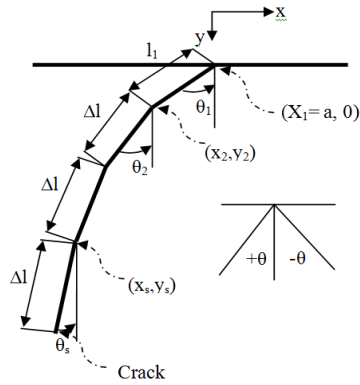


Figure 20. Trajectory of crack growth

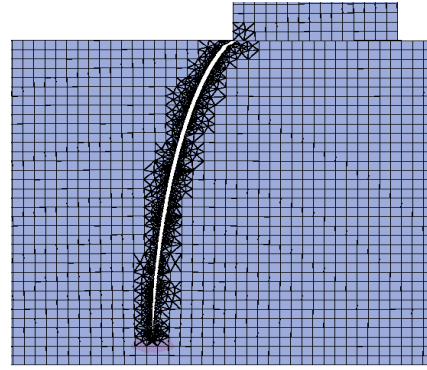


Figure 21. An initial crack in FRANC2D/L and triangular elements around the crack.

FRANC2D/L CRACK GROWTH (N40\_F2DL\_CG) code was used in order to predict the crack growth life time curve. This program, realized by Domenico [19], calculates crack growth life in generic 2D layered structures. The core of the program is Franc2D/L (based on Franc2D, Copyright (C) Paul 'Wash' Wawrzynek and Tony Ingraffea) [10], which is used to extract stress intensity factors (SIF) history files for generic geometries and sets of loads. N40\_F2DL\_CG imports SIF history files and integrates the material  $da/dN$  equation (NASGRO model) for calculating crack growth for variable amplitude spectrum of loads. FRANC2D/L CRACK GROWTH code is able to show the amount of  $K_I$ ,  $K_{II}$  and  $K_{III}$  in every increment of crack propagation and it is designed to deal with Forman NASGRO material models (equation 2). The elements of the NASGRO crack growth rate equation were developed by Forman and Newman at NASA, and it has been implemented in FRANC2D/L CRACK GROWTH as follows [20]:

$$\frac{da}{dN} = C \left[ \frac{(1-f)}{(1-R)} \Delta K \right]^n \frac{\left( 1 - \frac{\Delta K_{th}}{\Delta K} \right)^p}{\left( 1 - \frac{K_{max}}{K_{crit}} \right)^p} \quad (2)$$

Where  $C$ ,  $n$ ,  $p$  and  $q$  are empirical constants, which are obtained by curve fitting the test data and  $f$  is the ratio of crack opening SIF to maximum SIF. The value of  $f$  is related to stress (load) ratio, flow stress and the plane stress/strain constraint factor. These values are provided by the FRANC2D/L CRACK GROWTH material database for each material. It is worth mentioning that  $\Delta K_{th}$  is not a simple threshold stress intensity range for long crack, but it includes the effect of short crack by involving 'intrinsic crack length', and the parameter  $f$ . Also  $C=6 \times 10^{-10}$  and  $n=2.51$  was used as fatigue ductility exponent [21], hence number of the cycles ( $dN$ ) for a crack grow ( $da$ ) in each increment, can be computed. Finally, the specimen fracture life was obtained.

### 3.3 Finite element results and the effect of temperature on crack propagation

Figure 22 reveals the stress contours for Von-Mises stress. It is interesting to note that the maximum von-Mises stress occurs near the sharp edge contact between the pad and the specimen. The simulations were validated by making a comparison between the number of cycles as predicted by numerical simulations in this work and the experimental measurements using replica. The results are shown in Figure 23 for different stress at temperature 150°C. As the results suggest a maximum of 22% difference is observed that is quite normal in fatigue context.

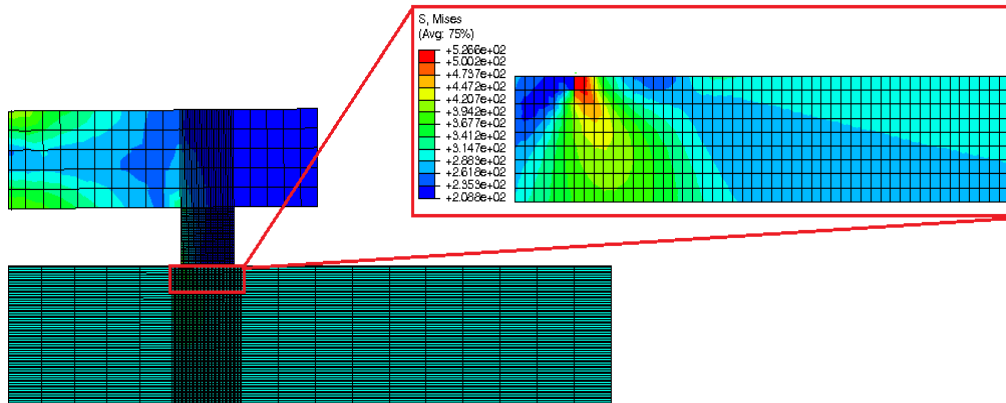


Figure 22. von-Mises equivalent stress distribution of fretting pairs ( $\sigma_{axial}=280$  Mpa and  $F= 1200$ )

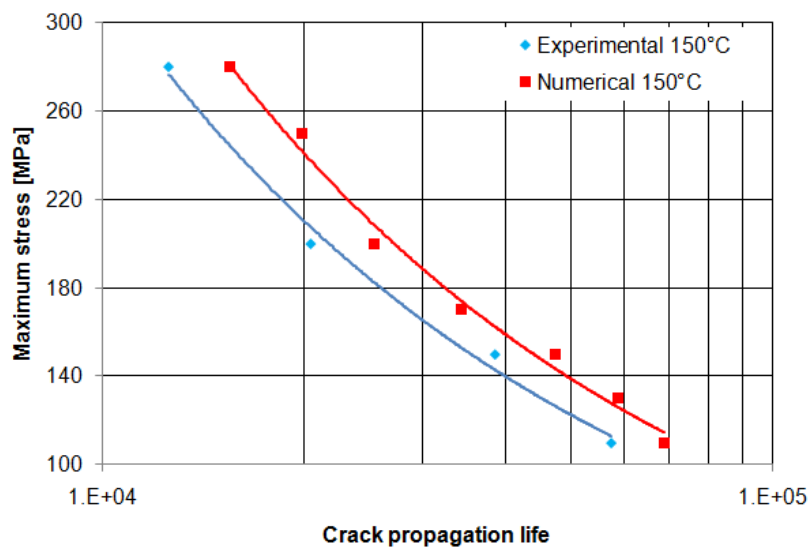


Figure 23. A comparison between experimental and numerical crack growth

#### 4. CONCLUSIONS

The experimental results reveal that fretting fatigue life of the material increases with temperature by 180% for low stresses and decreases by 40% for high stresses. This fashion of variation of fretting fatigue life versus temperature is believed to be due to degradation of material properties which occurs by overaging and wear resistance increase due to oxidation of aluminum alloy. While overaging gives rise to degradation of mechanical strength of material and hence the reduction of its fretting fatigue life, surface oxidation of the specimens brings about improvement of fatigue behavior of the material. The variation of the ultimate strength versus temperature that is obtained from the tensile tests reveals the same trend as observed for fretting fatigue life versus temperature at different stress levels. Metallurgical examination of the specimens reveals the size of precipitated impurities and their distances gets bigger as temperature increases. This could be a reason for material degradation of specimens which are exposed to heating for longer time duration.

Numerical simulation of fretting fatigue was performed using Abaqus and FRANC2D/L codes. The former predicts the normal and tangential contact stress distributions and the latter calculates the number of cycles required for a known crack propagation rate at elevated temperature. The calculation of cycles is based on Forman NASGRO equation when  $\Delta K$  is computed by FRANC2D/L then it is possible to predict the cycles for a specific value of crack growth. The results indicate that the numerical simulations are capable of predicting the crack growth cycles and orientation at different stresses and temperatures. The computed crack propagation lives were compared to the results of experimental study where total fatigue life was measured.

## 5. ACKNOWLEDGEMENTS

The authors wish to thank the Ghent University for the financial support received by the Special Funding of Ghent University (Bijzonder Onderzoeksfonds), in the framework of BOF project (BOF 01N02410).

## 6. REFERENCES

- [1] Hills DA, Nowell D. Mechanics of fretting fatigue. Kluwer Academic Publisher, 1994.
- [2] Shin. Ki S. Prediction of fretting fatigue behavior under elastic-plastic conditions. Mechanical Science and Technology 2009;23:2714-2721.
- [3] Majzoobi GH, Ahmadkhani AR. The effects of multiple re-shot peening on fretting fatigue behavior of Al7075-T6. Surface & Coatings Technology 2010;205(1):102-109.
- [4] Stachowiak GW, Batchelor AW. Engineering Tribology. Butterworth Heinemann publisher, 2001.
- [5] Hamdy MM, Waterhouse RB. The fretting wear of ti-6al-4v and aged inconel 718 at elevated-temperatures. Wear 1981;71(2):237-248.
- [6] Mutoh Y, Satoh T. High temperature fretting fatigue. Mechanical Engineering Publication, 1994.
- [7] Hamdy MM, Waterhouse RB. The fretting fatigue behaviour of Ti-6Al-4V at temperatures up to 600 °C. Wear 1979;56:1-8.
- [8] Jina, O., Mallb S, Sahanb O. Fretting fatigue behavior of Ti-6Al-4V at elevated temperature. Int J Fatigue 2005;27:395-401.
- [9] ABAQUS v 6.10, Standard User Manual, 2010.
- [10] FRANC2D/L. A crack propagation simulator for plane layered structures. Engineering SoCaE, editor. Ithaca, New York Cornell University, 1998.
- [11] Majzoobi GH, Hojjati R, Nematian M, Zalnejad E, Ahmadkhani AR. A new device for fretting fatigue testing. Transactions of The Indian Institute of Metals 2010;63(2-3):5.
- [12] Ruiz C, Boddington PHB, Chen KC. AN INVESTIGATION OF FATIGUE AND FRETTING IN A DOVETAIL JOINT. Experimental Mechanics 1984;24(3):208-217.
- [13] Fadag HA, Mall S, Jain VK. A finite element analysis of fretting fatigue crack growth behavior in Ti-6Al-4V. Eng Fract Mech 2008;75(6):1384-1399.
- [14] Lykins CD, Mall S, Jain V. A shear stress-based parameter for fretting fatigue crack initiation. Fatigue Fract Eng Mater Struct 2001;24(7):461-473.
- [15] Shaw RD, Pitchen RG. MODIFICATIONS TO SUHARA-FUKUDA METHOD OF NETWORK GENERATION. International Journal for Numerical Methods in Engineering 1978;12(1):93-99.
- [16] Erdogan F, Sih G. On the crack extension in plates under plane loading and transverse shear. Journal of Basic Engineering Trans ASME 1963;85(4):519-527.
- [17] Shkarayev S, Mall S. Computational modelling of shot-peening effects on crack propagation under fretting fatigue. The Journal of Strain Analysis for Engineering Design 2003;38(6):495-506.
- [18] Rybicki EF, Kanninen MF. A finite element calculation of stress intensity factors by a modified crack closure integral. Eng Fract Mech 1977;9(4):931-938.
- [19] Quaranta D. FRANC2D/L CRACK GROWTH: A crack propagation simulator for plane layered structures (based on Franc2D, Copyright (C) Paul 'Wash' Wawrzynek and Tony Ingraffea). Ltd PA, editor. Switzerland.
- [20] Forman RG, Mettu SR. Behavior of Surface and Corner Cracks Subjected to Tensile and Bending Loads in Ti-6Al-4V Alloy. Fracture Mechanics 22nd Symposium, Vol. 1 Philadelphia: ASTM STP 1131, H.A. Ernst, A. Saxena and D.L. McDowell, eds., American Society for Testing and Materials, 1992.
- [21] Wang QY, Pidaparti RM. Static characteristics and fatigue behavior of composite-repaired aluminum plates. Composite Structures 2002;56(2):151-155.

# DRY SLIDING FRICTION AND WEAR RESPONSE OF WC-CO HARDMETAL PAIRS IN LINEARLY RECIPROCATING AND ROTATING CONTACT

Y. Perez Delgado<sup>1</sup>, K. Bonny<sup>1</sup>, P. De Baets<sup>1</sup>, P.D. Neis<sup>1</sup>, V. Rodriguez Ferreira<sup>1</sup>, O. Malek<sup>2,3</sup>, J. Vleugels<sup>2</sup>, B. Lauwers<sup>3</sup>

<sup>1</sup>Ghent University, Laboratory Soete, Belgium

<sup>2</sup>Catholic University of Leuven, Metallurgy and Materials Engineering Department, Belgium

<sup>3</sup>Catholic University of Leuven, Mechanical Engineering Department, Belgium

**Abstract** This paper presents an experimental evaluation of friction and wear properties of WC-Co cemented carbides. A comparison is made between unlubricated rotating and linearly reciprocating pin-on-plate sliding pairs. The plate specimens were WC-10wt%Co grades surface finished by polishing or sequential wire-EDM steps, whereas WC-6wt%Co pins were used as counter body. The tests were carried out at room temperature using a sliding speed of 0.30m/s and mean Hertzian contact pressures of 1.76 and 2.08 GPa, i.e., normal contact loads of 15N and 25N, respectively. The worn surfaces on plate samples were quantified in terms of 2-D wear profiles obtained by means of surface topography scanning equipment. Wear mechanisms such as polishing and abrasion were identified using optical microscopy. Inferior tribological characteristics for wire-EDM surface finish compared to polishing were found. Higher friction coefficient and wear levels were measured in unidirectional rotating sliding experiments compared to linearly reciprocating test conditions.

**Keywords** friction and wear, wire-EDM, wear particles, reciprocating and rotating sliding contact.

## 1 INTRODUCTION

Inspired by economical and especially ecological motives, engineers have developed new or improved materials able to operate in harsh environments, e.g., high temperature, unlubricated contact, abrasive or erosive circumstances, corrosive surroundings, etc. to which machine elements (gears, brakes, bearings, etc.) and tools ( punches, dies, cutting tools, etc.) are often exposed. Currently, hardmetals are widely used for those applications due to their excellent mechanical properties having unique combination of high hardness, strength, resistance to compressive deformation, wear and corrosion resistance at high temperatures [1]. Cobalt (Co) is the most preferred binder in WC-based hardmetals due to its outstanding wetting and adhesion characteristics in combination with tungsten carbide (WC), leading to unique properties [2]. Nevertheless, some disadvantages such as high hardness make it intrinsically difficult to shape by means of traditional machining techniques such as grinding with boron nitride and/or diamond. Electrical Discharge Machining (EDM) allows the production of complex shapes. However, this machining process could degrade the surface quality in consequence of mechanical and thermal impact. Some research has already been performed on the effects of wire-EDM on friction and wear behaviour of WC-Co cemented carbides in reciprocating sliding contact [3-5]. A problem, however, is the lack of knowledge of tribological behaviour of WC-10wt%Co cemented carbide on continuous unidirectional rotating sliding contact.

This paper aims to evaluate and compare the friction and wear response of cemented carbides in reciprocating and rotating sliding contact, and examines how the tribological characteristics are affected by the geometry of the sliding motion (linearly reciprocating or unidirectionally rotating), interaction of wear particles, contact loading and surface finish.

## 2 EXPERIMENTAL PROCEDURE

The WC-10wt%Co cemented carbide was produced by liquid phase sintering. The physical and mechanical properties of WC-10wt%Co are listed in Table 1 as a function of chemical and microstructural features. The Vickers hardness was measured with indentation weights of 10 kg (Model FV-700, Future-Tech Corp., Tokyo, Japan). The grain size distribution was acquired using computer analysis software by the linear intercept method. The fracture toughness,  $K_{IC}$ , 10kg, was obtained by Vickers indentation using the formula of Shetty [6]. The Young's modulus,  $E$ , was obtained by the resonance frequency method (ASTM C 1259-94) on a Grindo-sonic (J.W. Lemmens, Elektronika N.V., Leuven, Belgium). The electrical resistivity was obtained by the 4-point contact method using a Resistomat Mikroohmmeter (Type 2302, Gernsbach, Germany).

Table 1. Chemical, microstructural, mechanical and physical properties of WC-10wt%Co cemented carbide.

Chemical properties	Microstructure			Mechanical properties			Physical properties	
Binder amount	$d_{av}$	$d_{50}$	$d_{90}$	HV <sub>10</sub>	$K_{IC(10kg)}$	$E$ -modulus	Density	Electrical resistivity
	[ $\mu$ m]	[ $\mu$ m]	[ $\mu$ m]	[kg/mm <sup>2</sup> ]	[Mpa mm <sup>0.5</sup> ]	[GPa]	[g/mm <sup>3</sup> ]	[10 <sup>-6</sup> $\Omega$ m]
10 wt% Co	2.2	1.8	4.2	1149 $\pm$ 10	>14.9 $\pm$ 0.1	578 $\pm$ 6	14.33	1.3

The WC-10wt%Co samples were machined and surface finished by wire-EDM or polishing. The polished surface variant was obtained by initially performing a grinding process using JF415DS grinding equipment (Jung, Göppingen, Germany) by means of a diamond abrasive wheel (type MD4075B55, Wendt Boart, Brussels, Belgium). The subsequent polishing operation was carried out with micrometer sized diamond paste up to optical finish. On the other hand, the wire-EDM surface finishing procedure was performed on a ROBOFIL 2000 (Charmilles Technologies, Switzerland) in de-ionized water (dielectric conductivity 11  $\mu$ S/cm), using brass (CuZn37) wire electrode with diameter 0.25 mm and tensile strength 500 MPa. In this paper, the rough and finest EDM surface finishes E2 and E24, respectively, were selected for sliding wear experiments. The corresponding wire-EDM settings are listed in Table 2. Additional information on the wire-EDM operation of the composites is given in [7,8].

Table 2. Device setting and parameters for rough and finer cutting regimes

Wire-EDM regime	E2	E24
Cut	Rough	Fine
Open voltage [V]	-80	120
Pulse duration, $t_e$ [ms]	2.1	0.4
Pulse interval, $t_o$ [ms]	10	0.6
Reference servo voltage $A_j$ [v]	46	0
Pulse ignition height IAL [A]	10	6
Flushing pressure [bar]	15	0
Wire tension [N]	1	1
Wire winding speed [m/min]	9.6	8

The surface roughness of the WC-Co cemented carbide with wire-EDM and polished surface finish was measured according to the ISO 4288 standard. The resulting  $R_a$  roughness values are summarized in Table. 3. Amongst the wire-EDM'ed composites, the highest roughness level is encountered with E2, whereas polished specimens are discerned to display the smoothest surface.

Table 3. Surface roughness of polished, rough and fine wire-EDM'ed cemented carbide

Surface finish	Polishing	E2	E24
$R_a$ ( $\mu\text{m}$ )	$\leq 0.02$	2.08	0.15

Sliding wear testing was conducted using two different configurations: (i) a Plint TE77 machine with linear reciprocating pin-on-plate contact according to the ASTM G133 standard, and (ii) a CSM tribometer with rotating pin-on-disk contact in accordance with the ASTM G99-95a standard, respectively. Each wear experiment was performed in unlubricated conditions and in ambient air, i.e.,  $23 \pm 1$  and  $60 \pm 1$  % relative humidity. Schematic illustrations of the applied linearly reciprocating pin-on-flat and rotating pin-on-disk sliding wear system are outlined in Figure 1.

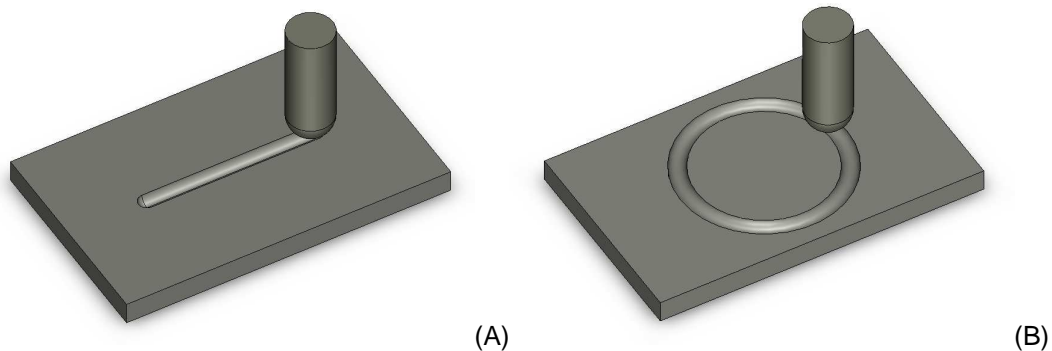


Figure 1. Geometric configuration of A) reciprocating and B) rotating sliding test.

The pin material was a WC-6wt%Co cemented carbide (CERATIZIT grade MG12). The radius of the hemisphere was 4.04 mm, with an  $R_a$  and  $R_t$  surface roughness of  $0.35 \mu\text{m}$  and  $2.68 \mu\text{m}$ , respectively. The pin material displays an E-modulus of 609 GPa, a Vickers hardness HV10 of  $1913 \text{ kg/mm}^2$ , a compressive strength of 7.2 GPa and fracture toughness  $K_{IC, 10\text{kg}}$  of  $8.4 \text{ MPa m}^{1/2}$ . The counter plate samples were made of WC-10wt%Co cemented carbide and displayed dimensions of  $58 \text{ mm} \times 38 \text{ mm} \times 4 \text{ mm}$ . The test duration was associated with a sliding distance of 10km. Normal contact pressures of 1.76 and 2.08 GPa were imposed, i.e., contact loads of 15N and 25N, respectively, at a constant sliding velocity of 0.3 m/s.

### 3 RESULTS AND DISCUSSION

#### 3.1 Effect of wear particles on friction and wear response

The influence of surface finishing operations and the imposed normal contact pressure on the tribological behavior of WC-10wt%Co is examined in Fig. 2, which compares polished and wire-EDM'ed test samples in reciprocating and rotating sliding contact with respect to their dynamic coefficient of friction resulting from a 10 km sliding wear path, using WC-6wt%Co pins at a speed of 0.3 m/s together with normal pressures of 1.76 and 2.08 GPa. Each value is an average of at least three sliding experiments with identical test parameters. The standard deviation in friction coefficient between different samples of the same material was determined to be less than 5 %. The dynamic friction coefficient was discerned to vary within 0.45 – 0.58. The differences in friction level between the distinctive surface finishing operations are quite pronounced. The dynamic friction coefficient is higher for wire-EDM surfaces compared to equivalent polished surface finish variant. Moreover, the highest friction levels are encountered with the roughest wire-EDM surface finish variant, i.e., E2. For instance, reciprocating pin-on-plate sliding with a contact load of 15 N yielded a dynamic friction coefficient of 0.52 for surface finish variant E2, whereas dynamic friction coefficients of 0.47 and 0.45 were obtained for the finer wire-EDM step E24 and polishing, respectively. Amongst the various surface finishes and imposed normal contact pressures the WC-10wt%Co specimens are found to yield higher friction coefficient on rotating sliding compared to the reciprocating sliding motion. Within the range of imposed contact pressures, the dynamic coefficient of friction is noticed to vary significantly. Indeed, raising the contact load is discerned to decrease the friction level.

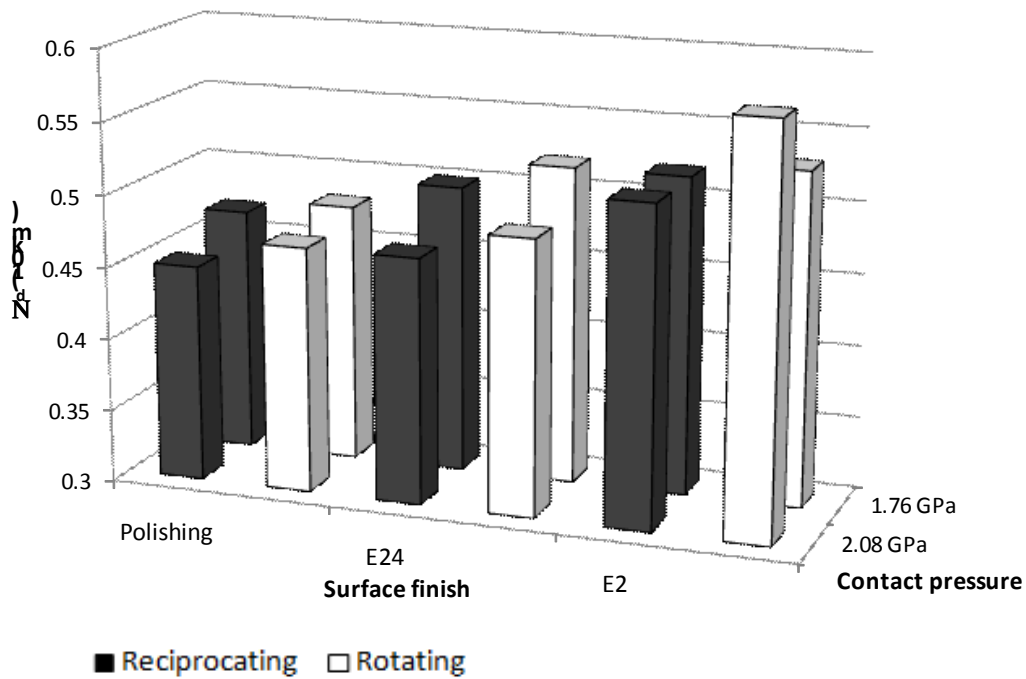
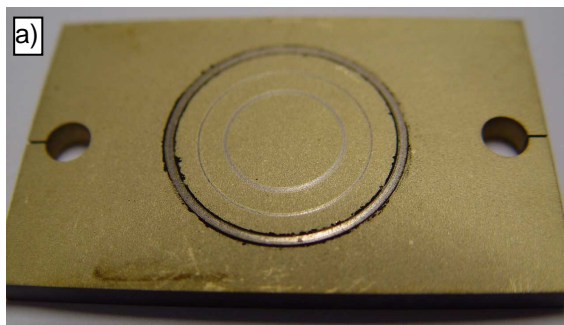


Figure 2. Dynamic friction coefficient as a function of surface finishing operation for WC-10wt%Co slid at 0.3 m/s with 15 and 25N contact load against WC-6wt%Co pins for 10 km

The observed friction curves during the sliding wear tests increase rapidly throughout the first meters of sliding, subsequently decline and increase towards an equilibrium situation (after running-in), in which fluctuation in friction are considerably smaller in reciprocating sliding motion. However, higher fluctuations in friction coefficient are observed in continuous rotating sliding tests. These instabilities can be explained in terms of continuous breaking and regenerating of micro-junctions at the contact surface. Additionally, it is apparent that the increase in friction coefficient can be attributed to the presence of wear particles at the sliding contact. In fact, there is a built-up of debris particles at the edge of the wear track that subsequently are pushed and clustering into the contact area, which are certainly related to small centrifugal force action on the particles as consequence of the rotating motion. This finding is in full agreement with the literature in the influence of wear particles, and the effect of reciprocating and rotating motion [9-13]. A visual inspection of worn surfaces after wear testing revealed the presence of wear debris accumulated at the edge of the wear tracks, but occasionally also within, along and adjacent to the wear tracks; see Figure 3.



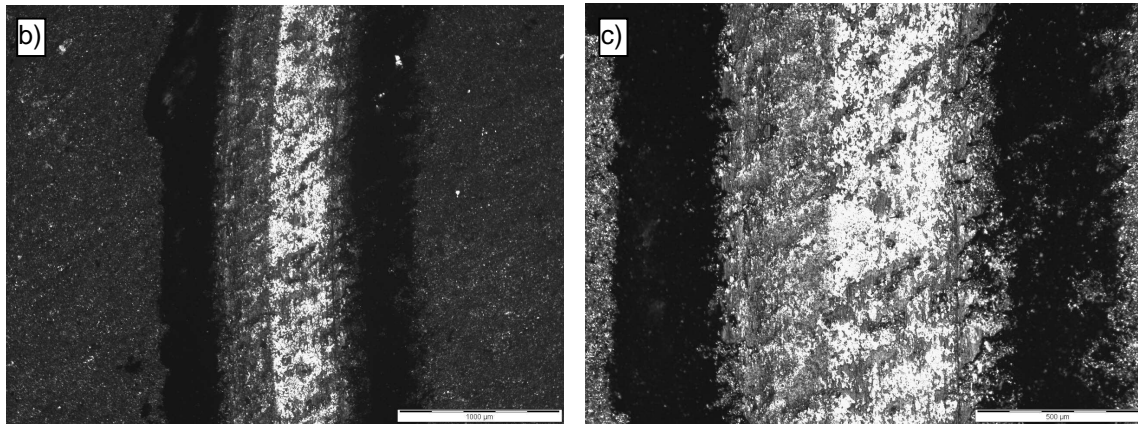


Figure 3. Surface view digital photograph (a) and micrographs with magnifications 50x (b) or 100x (c) on wear tracks of WC-10wt%Co with surface finish E2 rotated against WC-6wt.%Co for 10 km at a 0.3 m/s sliding speed with mean Hertzian contact pressure 2.08GPa

Both reciprocating and rotating sliding wear experiments were continued up to a total sliding distance of 10 km ensuring that the wear processes had reached a 'steady state' condition. Wear volumes could be extracted from the generated wear tracks by means of profilometric surface scanning measurement. The wear volumes of WC-10wt%Co cemented carbide as a function of surface finishing variant are compared in Figure 4. The wire-EDM'ed grades are characterized by higher wear volumes compared to their polished equivalents. The test samples evaluated in rotating sliding contact show higher wear damage compared to identical samples tested in reciprocating motion. A possible explanation for this finding could be that wear debris particles tend to break up more easily when the direction or the motion of the applied stress is reversed [11].

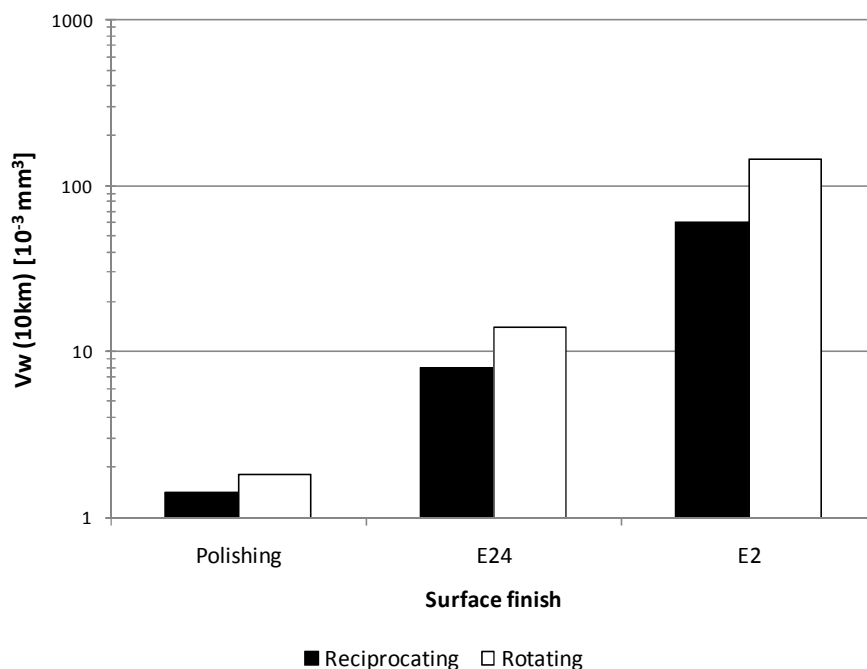


Figure 4. Wear volume as a function of surface finishing operation for WC-10wt%Co slid at 0.3 m/s with a mean Hertzian contact pressure of 1.76GPa against WC-6wt%Co pins for 10 km.

Whatever the underlying cause of the wear particle generation may be, the frictional characteristics of a sliding system are directly affected by the presence of such wear particles. However, the precise nature of the wear particle behaviour at the interface of a sliding contact needs to be further investigated by means of scanning electron microscopy (SEM) and energy dispersive X-ray (EDX) spectroscopy, for instance.

#### 4 CONCLUSIONS

Reciprocating and rotating wear testing of WC-10wt%Co cemented carbide surface finished by sequential wire-EDM or polishing in dry sliding contact with WC-6wt%Co counter body revealed significant increase of friction coefficient and wear level by wire-EDM. However, substantial improvements were obtained with finer-executed EDM finishing steps. Differences in tribological behaviour can be attributed to the wire-EDM induced recast layer, exhibiting lower wear resistance compared to the polished surface. Higher friction coefficient and wear volume was encountered in rotating sliding contact compared to linearly reciprocating conditions, which are believed to involve stronger interaction between wear debris at the sliding contact interface. The nature of the compound layer in the wear track and wear particles must be further elucidated by thorough investigation of cross-sectioned wear tracks.

#### 5 NOMENCLATURE

$\mu_d$	Dynamic coefficient of friction	-
$V_w$	Wear volume	mm <sup>3</sup>
$R_a$	average roughness profile variation	μm
E2	rough wire-EDM step	-
E24	fine wire-EDM step	-

#### 6 ACKNOWLEDGEMENTS

The authors would like to acknowledge the support of the Fund for Scientific Research Flanders (FWO, Grant No. G.0539.08) and the Flemish Institute for the promotion of Innovation by Science and Technology in industry (IWT, Grant No. GBOU-IWT-010071-SPARK). The authors gratefully recognize all the support, scientific contributions and stimulating collaboration from partners from Laboratory Soete, Ghent University (UGent) and Catholic University of Leuven (K.U.Leuven). Authors are also thankful to CERATIZIT for supplying the pins and hardmetals.

#### 7 REFERENCES

- [1] Q. Yang, T. Senda, N. Kotani, and A. Hirose, Sliding wear behavior and tribofilm formation of ceramics at high temperatures. *Surface and Coatings Technology*, 2004. 184(2-3): p. 270-277.
- [2] Zhengui, Y., Stiglich, J.J., Sudarshan, T.S.: WC-Co enjoys proud history and bright future. *Metal Powder Report* 53(2), 32–36 (1998)
- [3] K. Bonny, P. De Baets, Y. Perez et al, Friction and wear characteristics of WC–Co cemented carbides in dry reciprocating sliding contact, *Wear* 268 (2010) 1504–1517.
- [4] Y. Perez, K. Bonny, O. Malek P. De Baets et al, Tribological behavior of wire-EDM'ed ZrO<sub>2</sub>-composites and cemented carbides, *Sustainable Construction and Design* (2010).
- [5] Bonny, K., et al., Influence of electrical discharge machining on the reciprocating sliding wear response of WC-Co cemented carbides. *Wear*, 2009. 266(1-2): p. 84-95.
- [6] Shetty, D. K., Wright, I. G., Mincer, P. N. and Clauer, A. H. (1985), Indentation Fracture of WC-Co Cermets, *Journal of Materials Science* 20, 5, pp 1873-1882.
- [7] Bonny K, De Baets P, Vleugels J, Van der Biest O, Lauwers B, et al. EDM machinability and dry sliding friction of WC-Co cemented carbides. *International Journal of Manufacturing Research* 2009;4(4):375-394.
- [8] K. Bonny, P. De Baets, J. Vleugels, A. Salehi, O. Van der Biest, B. Lauwers, and W. Liu, EDM machinability and frictional behavior of ZrO<sub>2</sub>-WC composites. *International Journal of Advanced Manufacturing Technology*, 2009. 41(11-12): p. 1085-1093.
- [9] Peter J. Blau, Matthew Walukas. Sliding friction and wear of magnesium alloy AZ91D produced by two different methods. *Tribology International* 33 (2000) 573–579.

- [10] Etsuo Marui, Hiroki Endo. Effect of reciprocating and unidirectional sliding motion on the friction and wear of copper on steel. *Wear* 249 (2001) 582–591.
- [11] D.H. Hwang, D.E. Kim, S.J. Lee. Influence of wear particle interaction in the sliding interface on friction of metals. *Wear* 225-229 (1999) 427-439.
- [12] D. Odabas, S. Su. A comparison of the reciprocating and continuous two-body abrasive wear behavior of solution-treated and age-hardened 2014 Al alloy. *Wear* 208 (1997) 25–35.
- [13] Marcia M. Maru and Deniol K. Tanaka. Influence of Loading, Contamination and Additive on the Wear of a Metallic Pair under Rotating and Reciprocating Lubricated Sliding. *J. of the Braz. Soc. of Mech. Sci. & Eng.* July-September 2006, Vol. XXVIII, No. 3. 278 - 285.

# CHARACTERIZATION AND MODELING OF FRICTION AND WEAR: AN OVERVIEW

F. Al-Bender<sup>1</sup>, K. De Moerlooze<sup>1,2</sup>

<sup>1</sup> Katholieke Universiteit Leuven, Dept. Mech. Eng., Div. PMA, Celestijnenlaan 300B, B-3001 Leuven  
<sup>2</sup> with Leuven Air Bearings N.V. since Sept. 2010

**Abstract** In this age of virtual design, high-performance machines, and precise motion control, the ability to characterize friction and wear processes and then to model and simulate them, becomes a pertinent issue. This communication gives a condensed overview of the generic characteristics of friction, thereafter, generic models, developed at KULeuven, PMA, are presented and discussed.

In regard to friction, both sliding and rolling are considered. The characterization concerns (i) the relationship between the friction (traction) force and the state of sliding of the system (displacement, velocity,...), at a given normal load; (ii) the relationship between the coefficient of friction and the normal load.

As regards frictional behaviour in function of sliding (rolling) state, the main features are: (i) pre-sliding (pre-rolling) hysteresis and (ii) gross-sliding (rolling) dynamics. Models are presented that capture those features and relate them to the contact characteristics. Comparison with experimental results is also presented for the main features. Secondly, the dependence of the coefficient of friction on the normal load is identified and modelled.

Finally, regarding wear simulation, the generic friction model is extended to cater for an asperity population that changes during the lifetime of sliding. Based on fatigue considerations, asperities get broken after a certain number of contact cycles, and are replaced by smaller ones. With the aid of this model, we try to correlate energy dissipation with wear evolution, and support that by experimental observation.

**Keywords** : Friction, traction, wear, normal load, friction coefficient, theoretical models, experimental results, Stribeck curve, friction lag, hysteresis, rolling.

## 1 INTRODUCTION

Friction modelling has been steadily gaining in interest over the last few decades. However, owing to the complexity of the friction and wear phenomenon, no comprehensive, practicable friction model that shows all of the experimentally observed aspects of friction force dynamics in one formulation is available. Most available friction and wear models are, in essence, empirical, that is, based on limited observations and interpretations. In this sense, the resulting models are valid only for the specific scope of test conditions, such as the level and type of excitation, used to obtain the data. On the other hand, development of simulation models and, where possible, predictive theories, at scales from atomic, through continuum, to useful engineering models, can fill empty gaps in the toolboxes available to designers and analysts.

Besides the field of tribology, where the origin of friction is one of the main topics, modelling and compensation of friction dynamics are treated in several other domains. In the machining and assembly industry, demand for high-accuracy positioning systems and tracking systems is increasing. Research on controlled mechanical systems with friction is motivated by the increasing demand for these systems. Friction can severely deteriorate control system performance in the form of higher tracking errors, larger settling times, hunting, and stick-slip phenomena. In short, friction is one of the main players in a wide variety of mechanical systems.

This communication presents an overview of friction model-building, which starts from the generic mechanisms behind friction to construct models that simulate observed macroscopic friction behaviour. First, basic friction properties are presented. Then, the generic friction model is outlined. Hereafter, the relationship between friction coefficient and normal load is considered from theoretical and experimental point view. A theory for tarctive rolling is then presented with experimental validation. Finally, the gereric friction model is extended to deal with wear in sliding contacts.

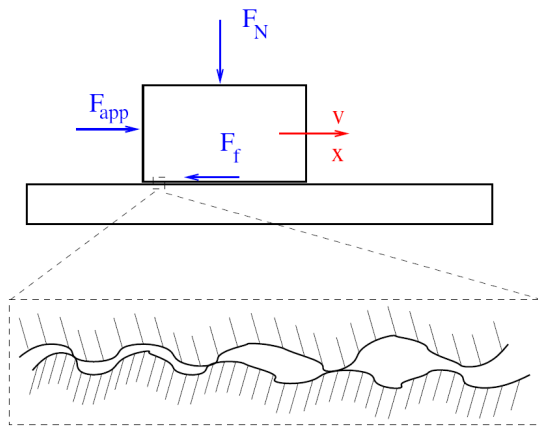


Figure 1. Basic friction configuration.

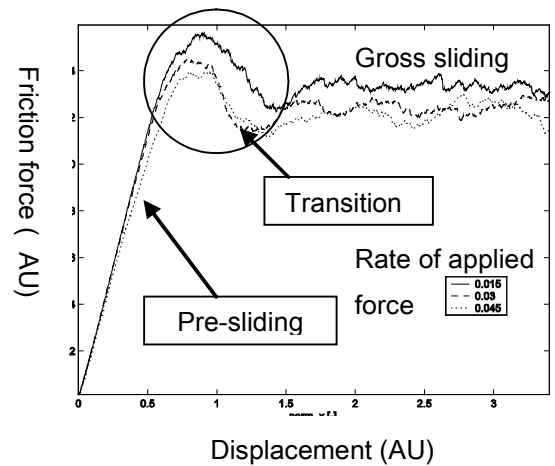


Figure 2. The two friction regimes and the transition between them.

## 2 BASIC FRICTION BEHAVIOR

Considering friction as a mechanical system, (see Fig.1), a close examination of the sliding process reveals two friction regimes, namely, the pre-sliding regime and the gross sliding regime, (see Fig.2). In the pre-sliding regime the adhesive forces, owing to asperity contacts, are dominant, and thus the friction force is primarily a function of displacement rather than velocity. The reason for this behaviour is that the asperity junctions deform elasto-plastically, thus behaving as nonlinear hysteretic springs.

As the displacement increases, more and more junctions break and have less time to reform, resulting eventually in gross sliding.

The sliding regime is, thus, characterized by a continuous process of asperity junction formation and breaking such that the friction force becomes predominantly a function of the velocity [1]. The transition from pre-sliding to gross sliding is a *criticality* that depends on many factors such as the relative velocity (to be envisaged as the displacement rate) and acceleration of the sliding objects, see [2].

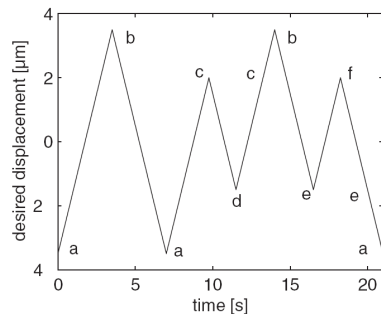


Figure 3. Example of desired motion in the pre-sliding regime.

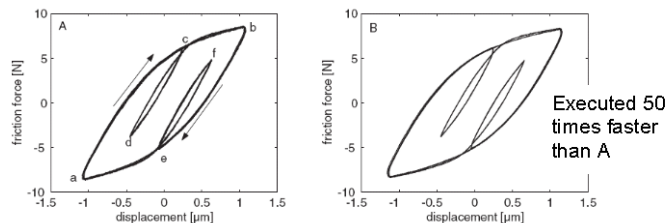


Figure 4. Hysteresis behavior as a result of the trajectory of Fig. 3.

### 2.1 Pre-sliding behavior

At very small displacements, that is, in the pre-sliding regime, experiments reveal a hysteretic displacement-dependent friction force [3,4]. When a pre-sliding displacement command, such as that shown in Fig. 3, is applied to the block, the force-displacement behavior of Fig.4 results. The position signal is chosen such that there is an inner loop within the outer hysteresis loop. The resulting friction-position curve is rate independent (compare the right and left panels of Fig.4). In other words, the friction-position curve is independent of the speed of the applied position signal. When an inner loop is closed, (c-d-c), the curve of the outer loop (a-c-b) is followed again, proving the nonlocal memory characteristic of the hysteresis. The shape of the hysteresis function is determined by the distribution of the asperity heights, the tangential stiffness, and the normal stiffness of the contact.

This hysteresis behaviour arises primarily from micro-slip, that is, the breaking of adhesive contacts, just as in the Maxwell-Slip model discussed further below. The contribution of deformation losses, which are hysteresis losses in the bulk materials, depends on the relative value of this part as compared to the

adhesive part, as well as on the tangential stiffness of the asperities, which governs the extent of deformation before slip.

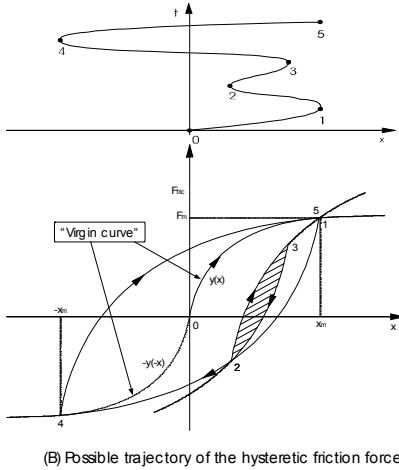


Figure 5. Characteristics of hysteresis with nonlocal memory.

$$F_{\text{virgin}} = f(x)$$

$$\text{with } f(x) = \begin{cases} y(x) & ; x \geq 0 \\ -y(-x) & ; x \leq 0 \end{cases}$$

Upon reversal at any point  $x_m$ , a doubly dilated version of the virgin curve is followed:

$$F_{\text{fric}} = F_m + 2f\left(\frac{x - x_m}{2}\right)$$

(B) Possible trajectory of the hysteretic friction force

Masing's rules for describing hysteresis

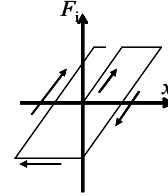
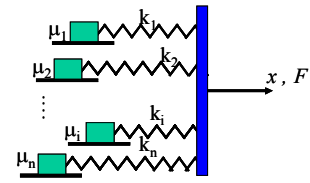


Figure 6. Modeling of hysteresis using Maxwell-Slip elements.

Figure 5 explains the constitution of hysteresis according to Masing's rules, shown to the right thereof. This behaviour can also be modeled discretely by a parallel connection of Maxwell-Slip elements [5], as shown in Fig. 6.

## 2.2 Gross sliding

When the asperity junctions are continually being created and broken, the frictional interface is in the gross sliding regime. Two main characteristics are of interest here. The first is the steady-state friction force behavior with increasing steady-state sliding velocities, generally known as the Stribeck curve, Fig. 7. The second is the change of the friction force with the velocity variation, known as the *friction lag* or *friction memory* phenomenon, Fig. 8.

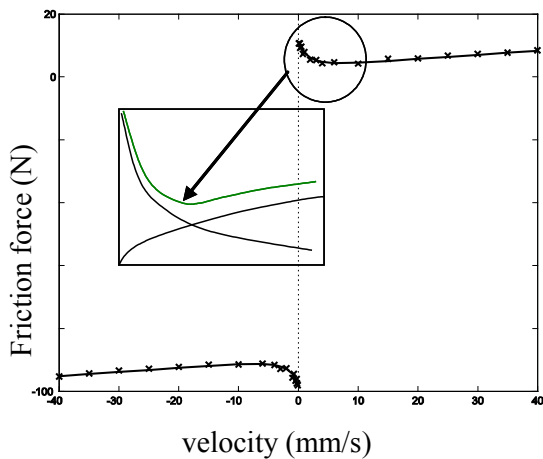
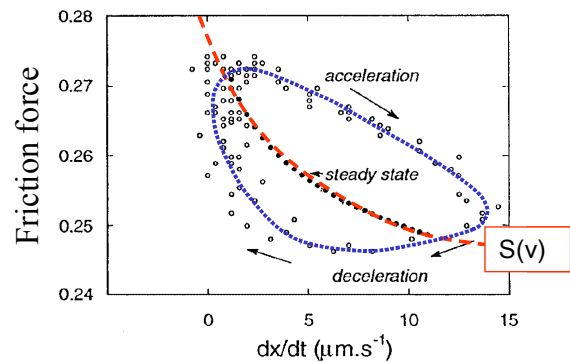


Figure 7. The Stribeck curve consists of velocity weakening,  $s(v)$ , and velocity strengthening.



Model:

$$\frac{dF}{dt} = f(1 - F/s(v)), \quad f(0) = 0.$$

Figure 8. Friction lag and its constitutive equation.  $s(v)$  is the velocity weakening curve also called the "Stribeck effect".

## 2.3 The Stribeck curve

When the friction force is measured at constant velocity values (Fig. 7), the resulting functional relationship has a characteristic form. For increasing velocities, the friction force initially decreases to a minimum (*velocity weakening*) and then increases again (*velocity strengthening*). In lubricated sliding, this

characteristic is known as the Stribeck curve, where the velocity weakening arises from the initial buildup of hydrodynamic pressure, while the velocity strengthening is attributed to the viscous shear of the lubricating film.

The same behaviour seems to hold true for dry friction, which justifies using the same name, that is, the Stribeck curve, to describe it. The actual form of the friction-velocity curve is determined by various process parameters, namely, the normal creep or, equivalently, the time evolution of adhesion, the surface topography, and the asperity parameters, primarily the tangential stiffness and inertia [2,6,8].

## 2.4 Friction lag

Friction lag, also called hysteresis in the velocity, or frictional memory, is manifested by a lag in the friction force relative to the sliding velocity. The origin of friction lag in lubricated friction relates to the time required to modify the lubricant film thickness, which is known as the *squeeze effect*. Friction lag is also observed in dry friction experiments (Fig. 8), where lubrication is not used. The mechanism causing friction lag in dry sliding is similar to that for lubricated friction, namely, that the local adhesion coefficient increases with the time of contact of two opposing asperities, owing to normal creep. In other words, time is required before the friction force changes with changing sliding velocity. Since the normal creep is caused by the sinking of the surfaces into each other, this mechanism is akin to the squeeze effect in lubricated friction. Thus, the friction force is higher for acceleration than for deceleration, so that the dynamic friction force curve circles around the steady-state curve. The Stribeck curve  $s(v)$  acts as the attractor.

## 3 A GENERIC FRICTION MODEL

In order to reconstruct the friction behavior outlined above, in the framework of a mechanical theory, a generic model was developed [6,8].

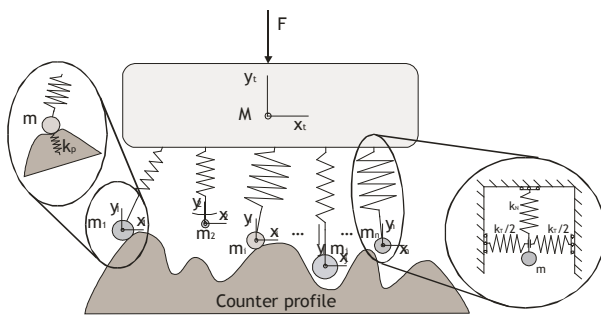


Figure 9(a). A generic representation of the sliding contact of rough bodies [8].

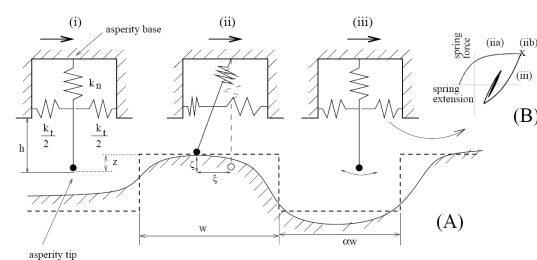


Figure 9(b). A simplified consideration of the contact cycle of a single asperity [6].

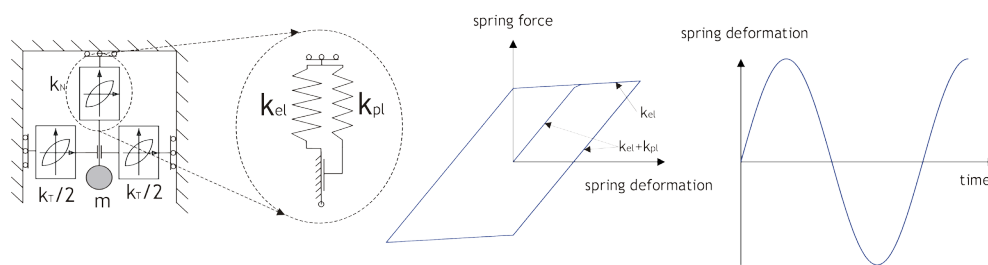


Figure 9(c). Modelling of elasto-plastic behaviour of asperity deformation.

The model comprises an upper body containing point-mass asperities supported on hysteresis springs (Fig. 9), which slides against a rigid, profiled lower surface, subject to adhesion and deformation. The latter is modelled by elasto-plastic springs (Fig. 9(c)). The life cycle of an average asperity contact is depicted in Fig. 9(b). (A) An asperity is initially moving freely (i) until it touches the lower rigid surface (ii). After sticking and slipping, it breaks completely loose from the lower profile (iii). (B) depicts the hysteretic force-deformation diagram during a contact cycle of the asperity, where upon breaking loose, the asperity is assumed to dissipate its elastic energy through internal hysteresis losses, until it comes again in contact with a counter asperity. Adhesion may be treated either as a normal force between the asperities or as a tangential (local friction) force, yielding essentially similar results in terms of behaviour [8].

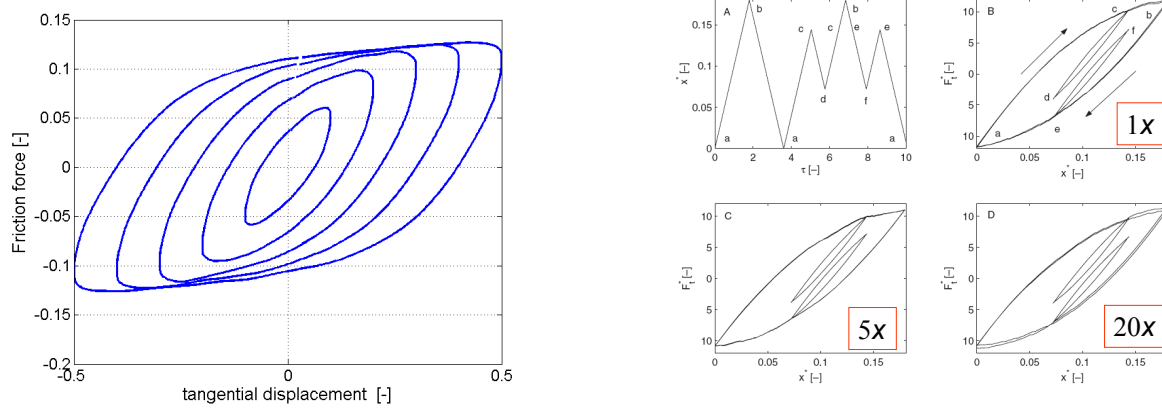


Figure 10. Simulation results of pre-sliding hysteresis using the generic model. Cf. Fig. 3.

### 3.1 Typical results of the generic model

The generic model yields results that are reviewed in the self-explanatory Figs. 10 through 13. The parameters used for the simulation have been chosen *ad hoc* only to illustrate typical behaviour, although they can also be identified from experimental results.

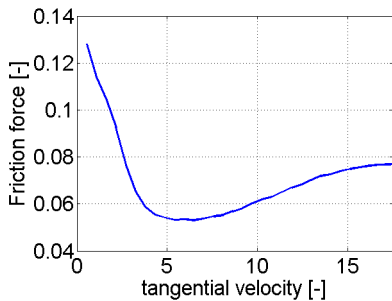


Figure 11. The Stribeck curve obtained from the generic model of [8], using arbitrary model parameters.

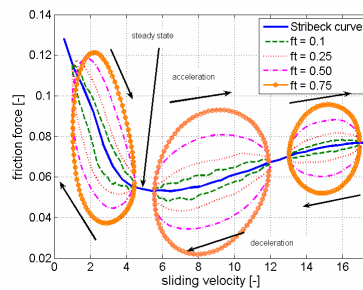


Figure 12. Friction lag using the generic model. The higher the acceleration, the more the loops depart from the Stribeck curve.

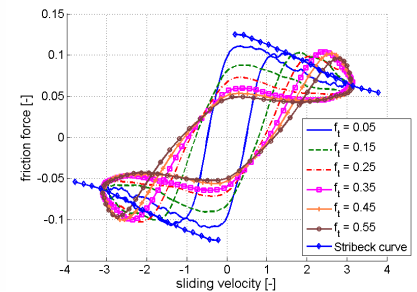


Figure 13. Periodic friction-velocity curves using the generic model.

## 4 THE DEPENDENCY OF THE COEFFICIENT OF FRICTION ON THE NORMAL LOAD

For a given sliding pair, the coefficient of friction is not constant, but appears to depend appreciably on the normal load, as shown in [10]. In that study, three material pairs (metals and plastic) were examined from pre-sliding up to gross sliding, with more than one order-of-magnitude variation of the normal load. Typical results are shown in Fig. 14.

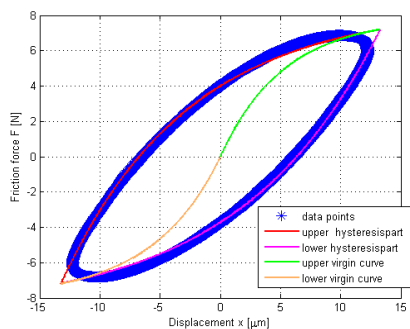


Figure 14.(a) For each normal load, the pre-sliding hysteresis curve is measured and the virgin-curve is identified.

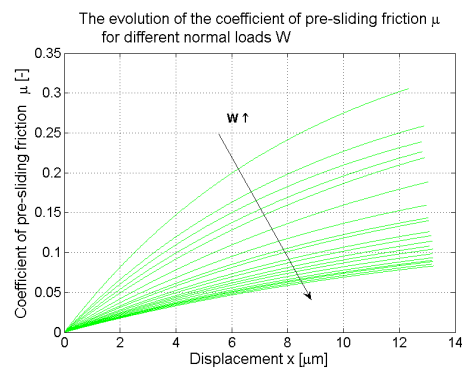
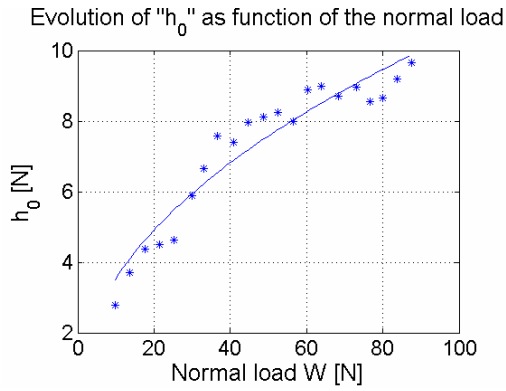
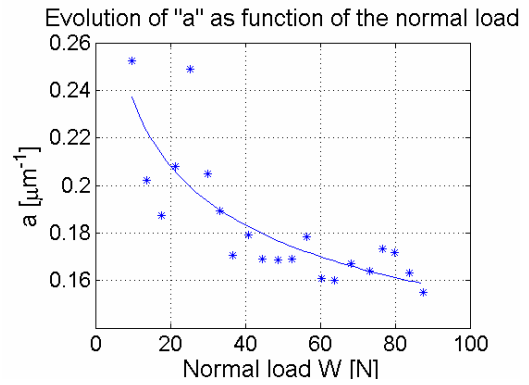


Figure 14.(b) The evolution of the normalised virgin-curves, or the coefficient of friction for increasing normal load.

Figure 15.(a) Evolution of  $h_0$ , for PET on PET.Figure 15.(b) Evolution of  $a$ , for PET on PET.

To analyze these results, each virgin curve was fitted by means of a three-parameter function:

$$F(x) = h_0 \left( 1 - e^{-a(x-x_0)} \right) \quad (1)$$

where,  $h_0$  scales the friction force and  $a$  the pre-sliding distance, ( $x_0$  is the position of the origin point).

Typical behaviour of these two parameters is shown in Fig. 15, where one can clearly notice that (i)  $h_0$  increases less than linearly with the load, which means that the coefficient of friction decreases with increasing normal load, and (ii)  $a$  decreases with the normal load, meaning that the pre-sliding distance increases with load. The range of variation of these two parameters depends on the material combination.

This behaviour has been modelled theoretically, making use of (i) the Maxwell-slip structure for modelling the contact in pre-sliding (Fig. 16) and (ii) the Greenwood and Williamson theory for modelling the local friction force at each asperity. The results of this latter model show that a decreasing coefficient of friction in the normal load always results. The trend is most pronounced for low values of the Plasticity Index and of the normal load, as shown in Fig. 17.

Thus the contact parameters influencing hysteresis behaviour and variation of the friction coefficient with normal load are: elasticity, hardness, surface topography and adhesion.

When this analysis is applied to the whole of the pre-sliding region, the behaviour shown in Fig. 18 is obtained [9]. Let us note that this behaviour can also be predicted by the generic model described in ref. [8].

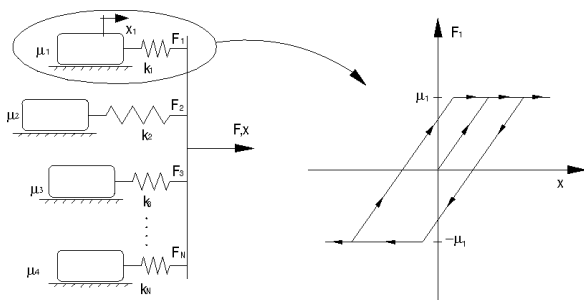


Figure 16. The Maxwell-slip model for pre-sliding.

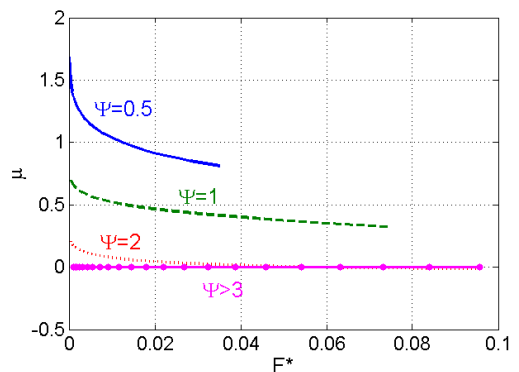


Figure 17. The static friction coefficient as function of the normal load for different values of the Plasticity Index.

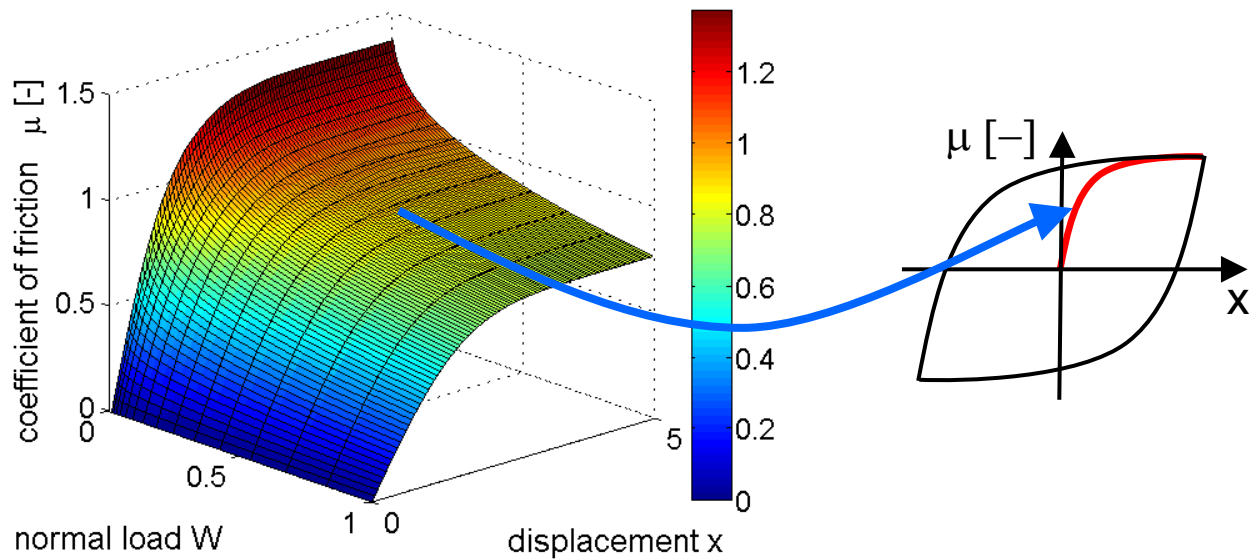


Figure 18. The variation of the coefficient of friction with the displacement and the normal load during pre-sliding.

## 5 MODELLING OF TRACTIVE ROLLING FRICTION

Tractive rolling is caused by the so-called creepage (or 'rigid slip') between the rolling surfaces. This creepage causes the points, which enter the contact patch mated with each other, to progressively stretch and finally slip when reaching the trailing edge and exiting the contact patch. This situation is adequately illustrated by Figures 19-20, ref. [11].

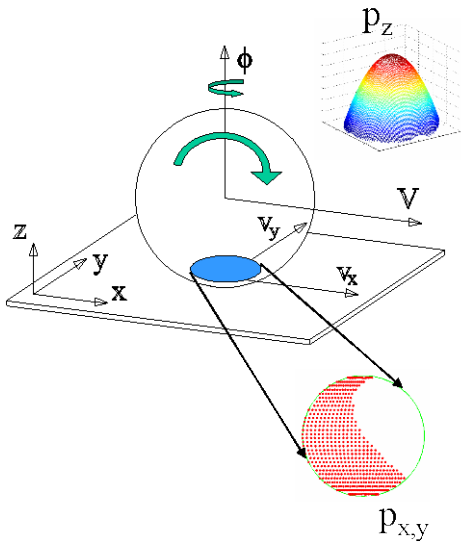
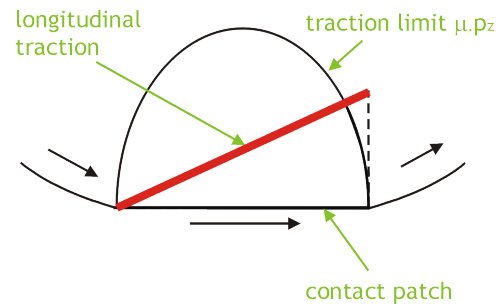


Figure 19. Configuration of tractive rolling. The pressure distribution in the contact patch is Hertzian. Creepages (longitudinal, transverse and spin) are caused by differences in rigid motions between the ball and the flat.



$$\mathbf{S} = \mathbf{C} - \frac{\partial \mathbf{u}}{\partial x} + \frac{\partial \mathbf{u}}{\partial q}$$

$$\mathbf{u} = f(\mathbf{C}, x, y, q)$$

Figure 20. Build up of traction through the contact patch, ending by the traction (slip) limit. The constitutive slip equation states that the slip  $\mathbf{S}$  is equal to the creepage  $\mathbf{C}$  less the total derivative of the surface displacement.

Considering, for example, the presence of only spin creepage, as is the case of a ball between V-grooves, the traction field and the associated hysteresis behaviour are depicted in Fig. 21. The hysteresis properties, namely, rate independence and nonlocal memory, resemble those identified in sliding contacts. Thus, we see that sliding and rolling have similar friction (dynamics) properties during pre-rolling. During gross rolling, the Stribeck effect and the friction-lag are much less pronounced. This is so because during rolling, the

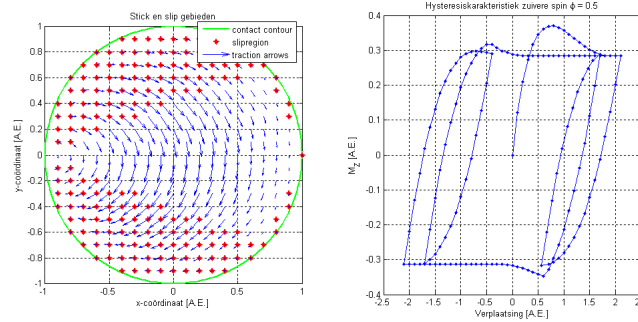


Figure 21. Left: steady-state rolling traction field. Right: the hysteresis curve of the traction moment in function of the rolling displacement.

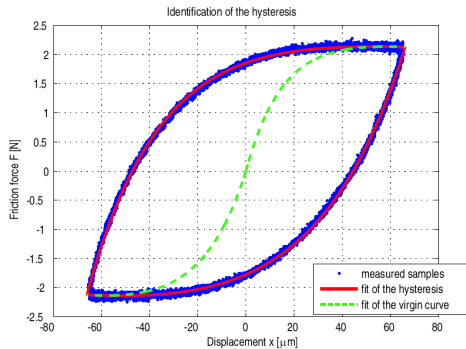
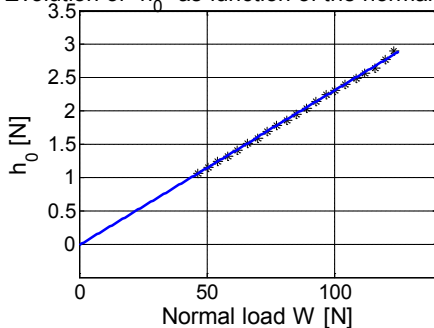


FIGURE 22. Experimentally measured pre-rolling hysteresis curve, with theoretical fit, of a ball rolling between two V-grooves.

relative speeds between slipping points on the surfaces remains very low (unless the contact as a whole is slipping, in which case rolling ceases to exist). This point is best illustrated by Figures 22 and 23. However, since creepage is generally dependent on the dynamics of the rolling system, i.e. that it changes during dynamic rolling, this situation can lead to very complex dynamics as presented in ref [13].

Evolution of " $h_0$ " as function of the normal load



Evolution of " $a$ " as function of the normal load

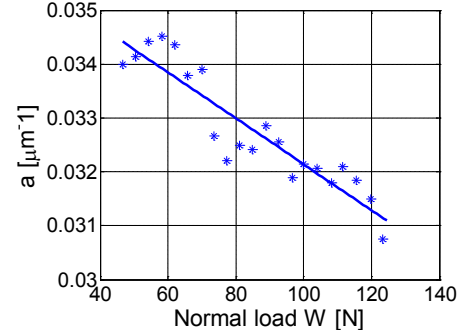
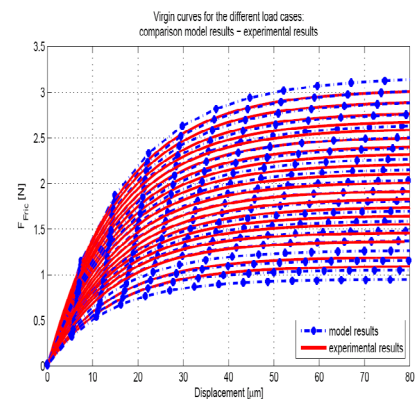


Figure 23. Evolution of  $h_0$  (left) and  $a$  (right), of Eq. (1), in the normal load, for rolling contact. We note that  $h_0$  is almost linear in the load and  $a$  varies relatively only slightly.

Finally, the theoretical model has been validated by comparison with experiment. The results are shown in Fig. 24 where very good agreement is observed (maximum error of 16 %).

Figure 24. Comparison between experimental measurement and theoretical predictions of the virgin curve during pre-rolling.



## 6 THEORETICAL MODELLING AND EXPERIMENTAL CHARACTERISATION OF WEAR

Theoretical modelling of wear is a valuable aid for designing and optimizing tribological systems, in particular those involving unlubricated contacts. However, most of the existing models are empirical in nature, which limits their applicability and predictive power. This motivates us to extend the generic friction model, outlined in section 3, by elaborating it with energy-based, asperity-degradation/modification mechanisms, in the form of a local fatigue law: when the energy accumulation in an asperity, owing to repeated elastic-plastic deformation exceeds a certain threshold, the asperity breaks off. Simulation results, using a set of arbitrary model parameters, in unidirectional as well bidirectional sliding, show qualitative agreement with experimental observations (see further). Apart from the running-in phase, which the simulations show clearly, a linear trend between the wear volume and the energy dissipation is observed, as shown in Fig. 25, (ref. [14]).

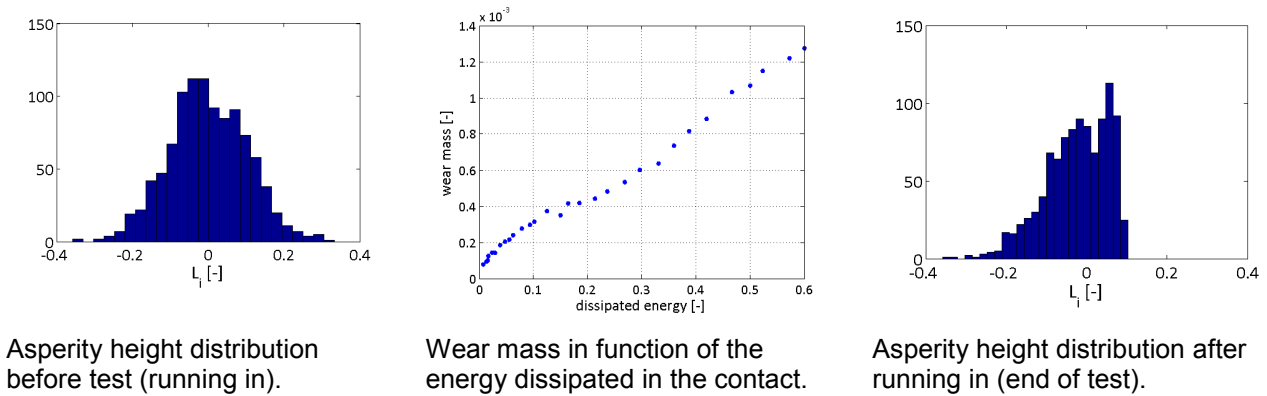


Figure 25. Typical results of the generic wear model simulations.

With the objective of experimentally correlating several wear-process parameters, accurately and continuously over the duration of a sliding test, we developed a novel rotational test rig with axes supported on aerostatic bearings [15]. It enables online, simultaneous measurement of normal load, friction force, angular position and normal displacement with high accuracy, see Fig. 26.

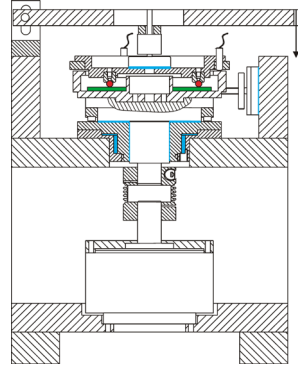
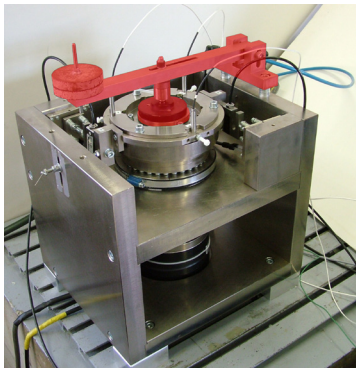


Figure 26. Test rig for accurate wear measurement.

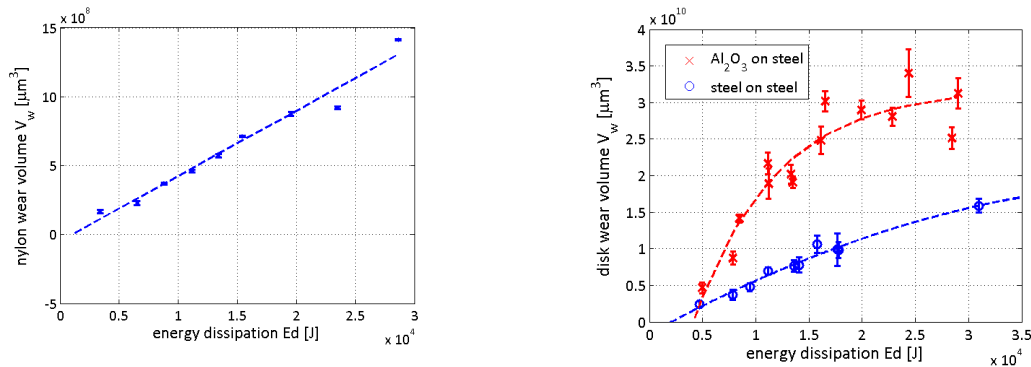


Figure 27. Wear volume in function of the energy dissipated in the contact for nylon on steel (left) and steel, respectively Alumina on steel (right) .

A set of ball-on-disc experiments was then performed, with ball materials being nylon, steel and ceramic, on hard steel disc material. The performed experiments correlate three process variables and parameters: normal load, wear volume and dissipated energy. The basic trends observed show that the relationship between those three variables are quasi linear, but generally with nonzero intercepts (see Fig. 27), corresponding to energy thresholds; except that of wear of alumina on steel (right Figure) [15].

## 7 CONCLUSIONS

Friction is a complex, nonlinear phenomenon that depends not only on the contacting surfaces and their physical and topographical properties but also on the dynamics of the system comprising friction. Evolution of wear in the contact adds further to the complexity of friction systems. Modelling of friction is important in many fields of science and engineering. We have presented an overview of our research into the modelling and experimental validation of friction, traction and wear. It became hopefully clear from the presentation that modelling of the friction phenomenon, based on the generic contact mechanisms, can lead to results that are qualitatively in agreement with experimentally observed behaviour. In the case of rolling, even very good quantitative agreement is achieved. In order to develop those models further towards predictive models, which will be a very powerful engineering tool, questions regarding the determination and assignment of model parameters have to be dealt with. This is the subject of future work.

## 8 ACKNOWLEDGEMENTS

This research was partially supported by the Fund for Scientific Research - Flanders (F.W.O.) under Grant FWO4283. The scientific responsibility is assumed by its authors.

## 9 REFERENCES

- [1] ArmstrongHélouvry B. Control of Machines with Friction. Norwell, MA: Kluwer, 1991.
- [2] Al-Bender F, Lampaert V, Swevers J. Modelling of dry sliding friction dynamics: from heuristic models to physically motivated models and back. CHAOS, An Interdisciplinary Journal of Nonlinear Science. 2004, 14(2): 446-460.
- [3] Swevers J., Al-Bender F, Ganseman C, Prajogo T. An integrated friction model structure with improved presliding behaviour for accurate friction compensation. IEEE Transactions on Automatic Control. 2000, 45(4): 675-686.
- [4] Lampaert V, Al-Bender F, Swevers J. Experimental characterisation of dry friction at low velocities on a developed tribometer setup for macroscopic. Tribology Letters, 2004, 16(1): 95-105.
- [5] Al-Bender F, Symens W, Swevers J, Van Brussel H. Theoretical analysis of the dynamic behavior of hysteresis elements in mechanical systems. International Journal of Non-linear Mechanics. 2004, 39: 1721-1735.
- [6] Al-Bender F, Lampaert V, Swevers J. A novel generic model at asperity level for dry friction force dynamics. Tribology Letters. 2004, 16(1): 81-93.
- [7] Al-Bender F, Lampaert V, Swevers J. The Generalized Maxwell-slip model: a novel model for friction simulation and compensation. IEEE Transactions on Automatic Control. 2005, 50(11): 1883-1887.
- [8] De Moerlooze K, Al-Bender F, Van Brussel H, A Generalised Asperity-Based Friction Model Source: TRIBOLOGY LETTERS 40(1), 113-130, 2010.
- [9] Al-Bender F, De Moerlooze K, On the relationship between normal load and friction force in pre-sliding frictional contacts, Part 1: Theoretical analysis, WEAR, 269(3-4), 174-182, 2010.
- [10] De Moerlooze K, Al-Bender F, On the relationship between normal load and friction force in pre-sliding frictional contacts, Part 2: Experimental investigation, WEAR 269(3-4), 183-189, 2010.
- [11] Al-Bender, F.; De Moerlooze, A Model of the Transient Behavior of Tractive Rolling Contacts, Advances in Tribology, 214894 (17 pp.), 2008.
- [12] De Moerlooze, K.; Al-Bender, F., Experimental Investigation into the Tractive Prerolling Behavior of Balls in V-Grooved Tracks, Advances in Tribology, 561280 (10 pp.), 2008.
- [13] De Moerlooze, F. Al-Bender, H. Van Brussel, Modeling of the dynamic behavior of systems with rolling elements, International Journal of Non-Linear Mechanics, Volume 46, Issue 1, January 2011, 222-233.
- [14] Kris De Moerlooze, Farid Al-Bender, Hendrik Van Brussel, A novel energy-based generic wear model at the asperity level, paper submitted to Wear, 2010.
- [15] Kris De Moerlooze, Farid Al-Bender, Hendrik Van Brussel, An experimental study of ball-on-flat wear on a newly developed rotational tribometer, paper submitted to Wear, 2010.

# TRIBOLOGICAL BEHAVIOR OF COMPOSITE-STEEL ON ROLLING/SLIDING CONTACTS FOR VARIOUS LOADS

M. Ando<sup>1</sup>, J. Sukumaran<sup>2</sup>

<sup>1</sup>Szent István University, GÉTI, Páter Károly utca 1. 2100 Gödöllő, Hungary

<sup>2</sup>University of Gent, Department of Mechanical Construction and Production, Sint-Pietersnieuwstraat, 41, 9000 Gent, Belgium

**Abstract** Composites have replaced metals in the bearing industry for the exclusive performances from its properties were it can accommodate resins, fabrics and additives. Roll-slip is common behaviors in application were non-conformal contact exhibits like bearings, rollers and cams. Two elements control the tribological behavior of the material which is the rolling and the sliding element. Composite-steel contacts were tested using a twin-disc setup with open tribo-system to study the influence of load on the frictional behavior of the polymer composites. The contacts were tested with four different loads under 20% slip ratio for a regular interval of time. The curves from the friction force with respect to different loads follows a tendency of linear increase in friction force were the rolling resistance is the dominating mechanism. For the given condition the macro level investigations shows the absence of transfer layer on the steel counterparts. The tendency of the friction curve and the micrograph explicitly deliberates the involvement of abrasion and adhesion in the harder polymer from metal counterpart. The temperature variable is isolated in case of the above research. The examination of the contact surface reveals the formation of craters on the junction of polymer and textile.

**Keywords** Effect of the load, rolling/sliding, composites-steel non conformal contact

## 1 INTRODUCTION

Composite-steel pairs are normally used in dry running condition where high strength and internal lubrication are necessary. Generally, composites used in tribological applications were examined from the perspective of fillers and fibers [1, 2]. Considering the tribological properties, Fibers aid to the friction behaviour of the composites. Studies with respect to the fiber orientation resulted in instabilities on the coefficient of friction [3].

As the requirements are achieved by the combination of fibers, resins and filler materials at various proportions [3]. Most of the researches studying the tribological behaviour of composites are focused on sliding. Various standards like pin-on disc, pin on ring and block on drum are used to evaluate the sliding phenomenon. Previous results from pin-on-disc on polyester composites has produced a rapid increase during the initial period of sliding due to factors like plastic deformation, contact area, and the intrinsic property of the composite material [4]. In these kind of testing the tendency of the curve changes with respect to the mechanism involved where either plastic deformation or adhesion determines the friction behaviour [3]. However, the use of composites in rollers, gears and bearings has rolling component together with sliding to have the roll-slip phenomenon which is never studied. In such a case simultaneous occurrence of both the mechanism (adhesion, plastic deformation) creates difficulties to segregate the influence of individual components (rolling/sliding) over friction behaviour. Moreover, the presence two mechanisms simultaneously produces different topographies of contact surface. Thus the contact condition changes with respect to the used model producing incomparable results. A close standard to test the roll-slip of composite-steel pair is the twin-disc model where only limited researches has been done for polymer – metal [5-8].

In most of the tribological investigations the parameters is varied to place the material in the suitable application range where velocity and load are the most common parameters [4, 9, 10]. From the fundamentals it is well known that load has a significant effect on the friction behaviour of the material. Liu et al on using different materials to investigate the influence of load on the tribological characteristics has proved that the friction force increases linearly with increasing load on using similar materials [11]. The difference between the material exists in the rate of increase of friction force to the normal force proves that most of the material has similar tendency as the effect of load.

In the current research an open tribo system is used to study the friction behaviour of composite-steel pairs under rolling/sliding conditions. Influencing factors like surface roughness or the composite pair, frictional heating and transfer film are suppressed by a specially developed program. Images from the contact surface are used to identify the dominating mechanisms involved in the friction process.

## 2 MATERIALS AND METHODS

On testing the composite-steel pair for roll-slip commercially available polyester composites (Orkot) is tested against 40CrMn tool steel. Orkot is used as a bearing material in marine applications, the composite itself is impregnated with polyester resin and PTFE. Tests performed on Orkot against steel at 15 MPa has proven results having co-efficient of friction 0.13 (from datasheet). Material properties for both the materials are given in Table 1.

Table 1. Materials properties

Properties	40CrMn	Orkot
Yield strength [MPa]	415	55
Young's modulus [GPa]	205	3.3
Impact Strength (Charpy) [kJ/m <sup>2</sup> ]	590	122
Hardness	220 HB	100 Rockwell M
Maximum allowable service temp. [°C]	-	130

To modelling the roll/slip phenomenon the twin-disc setup is the appropriate test device. On testing roll-slip a slip ratio will be involved which is the rolling to sliding ratio achieved by having different speeds for two disc. But, in the current setup both the shaft rotates at same speed and hence the required slip ratio is achieved by changing the diameter of the test material and the counterface material. In the used parameter the diameter of the polymer wheel was 120% compared to the steel wheel (100% = 74.93 mm), which means the slip ratio is 20%. Image of the twin disc set-up is shown in Figure 1. Under the measurement was used online data acquisition system (Lab View). The friction torque was measure online using a torque meter (4 – Lorenz Messtechnik DR-20-type) attached to the shaft of the counterface material. The temperature with infra red sensor (3) 180° away from the instant of contact point on the polymer wheel. Dead weights are used (5) to achieve constant normal force along the measurement. The speed of the two shaft controlled online.

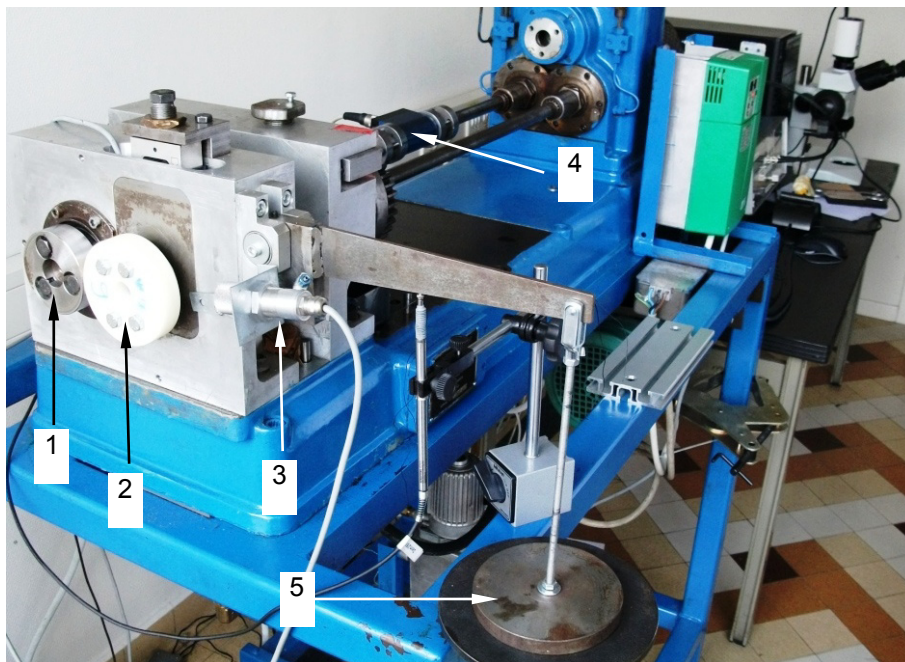


Figure 1. Twin-disc set-up to modelling rolling/sliding

Four different dead weights are used to study the effect of the load on the friction behaviour of the composite-steel pair. The applied normal load and the corresponding contact mean and maximum contact pressure for a contact zone is given in Table 2.

Table 2. Show the normal force, Hertzian pressure and contact zone for composite-steel pair

Applied normal force [N]	Maximum pressure [MPa]	Mean pressure [MPa]	Contact area [mm×mm]
61	77.23	60.66	0.126×8
111	104.18	81.83	0.170×8
161	125.47	98.55	0.204×8
210	143.30	112.55	0.233×8

A running in of 5 minutes is used prior to data collection, a test duration of 2 minutes is used at low and high speed condition. Every parameter was measured five times to check for the repeatability. Two different speeds 10 rpm (low) and 700 rpm (high) are used along with the different loads. All the tests are conducted at dry running condition (because of the internal lubrications e.g. PTFE). Image of the contact surface is acquired before and after the measurement using Olympus SFX microscope and QiCAM video camera.

### 3 RESULT AND DISCUSSION

The current research was focused on studying the tribological behaviour of composite metal pair on dry running condition. The aim of the experiments is to identify the boundary for friction behaviour under ideal condition without the influence of frictional heating and the transfer layer. The Figure 2. shows the results using the same parameters for five time (10 rpm). It is clear from the plotted curve that the repeatability of the test are good where the curves follow the same pattern and line close to each other.

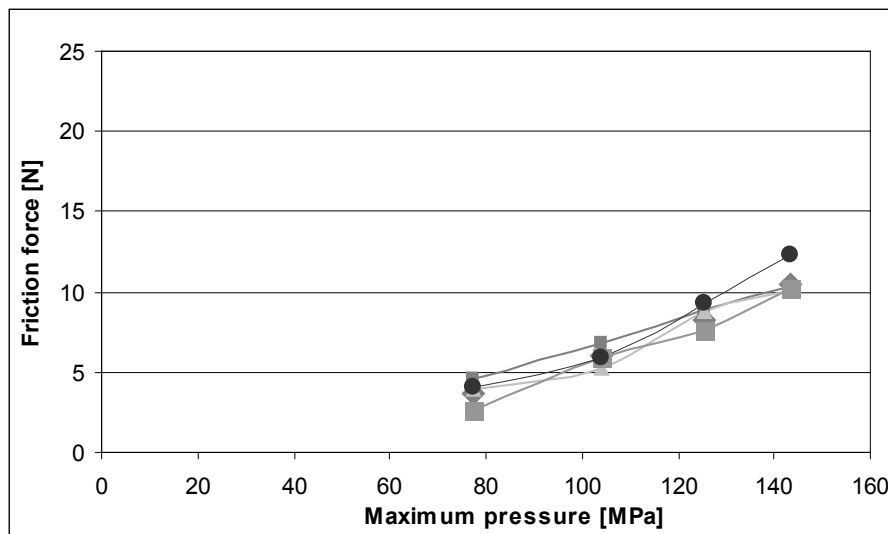


Figure 2. Friction force at low velocity

Curves were also plotted for two different speeds with friction force as a function of maximum pressure. Figure 3. illustrates the friction force with the fitted linear curve also having an error of  $\pm 2\sigma$ . From the plot a linear cure is the best fit to describe the tendency of the curve. But one should keep in mind that this function is valid from 75 MPa. The lower limit of contact pressure for the operating condition is important, because if the material is tested with low loads for e.g. 20 MPa maximum pressure it causes less than zero friction force (from this trend lines). Negative friction force cannot be achieved since there is always a friction force involved due to sliding and also a rolling resistance as well. The normal force has huge influence to the rolling resistance which is due to the intrinsic property of the material. In case of Orkot composite a relatively large young modulus (because the fibers) reduces the rolling resistance on comparing with a common engineer polymer. The Table 3. contains the equation from the curve fitting of the measured points.

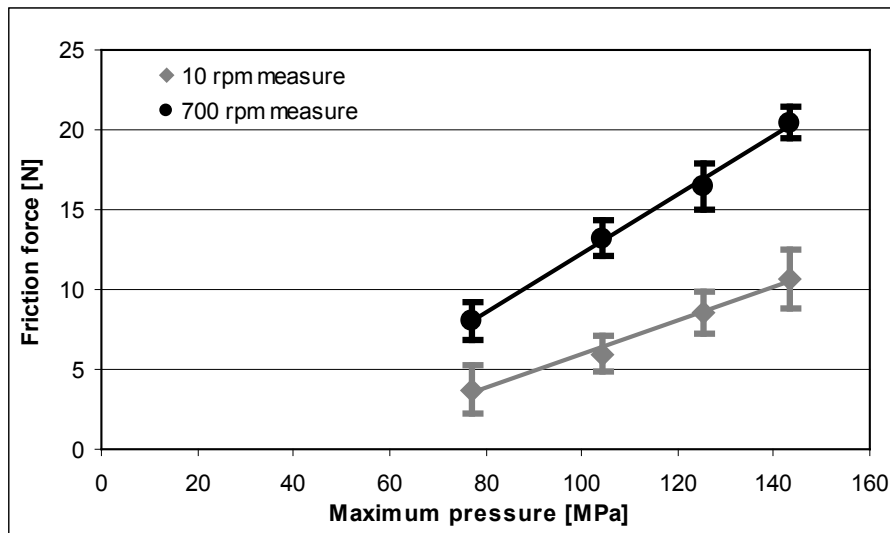


Figure 3. Effect of the pressure to the friction force

Table 3. Equations of the fitted curves and their  $R^2$  values

Speed	Equation	$R^2$ value
10 rpm	$F = 0.106 \cdot p - 4.690$	0.9323
700 rpm	$F = 0.184 \cdot p - 6.134$	0.9831

In case of high speed the inclination of the curve is almost two times bigger than the low speed. Where it is better to reduce the contact pressure (used bigger dimensions) on high speeds which leads to energy saving by having reduced friction force. But in case of low speed the larger geometry doesn't cause considerable saving.

Figure 4. shows the friction force as a function normal force for low and high speed condition. The tendency of the friction curve for the corresponding normal forces follows a linear pattern which is same as that of the plot used in the friction force against the Hertzian pressure. Here, there are difference of the slope too. Important change that if choose smaller normal force (e.g. 10 N), the friction force will positive values (based on the fitted curves). Because of this, the fitted curves are possible to describe the phenomenon in lower (e.g. 30 N) and higher (e.g. 230N) interval also.

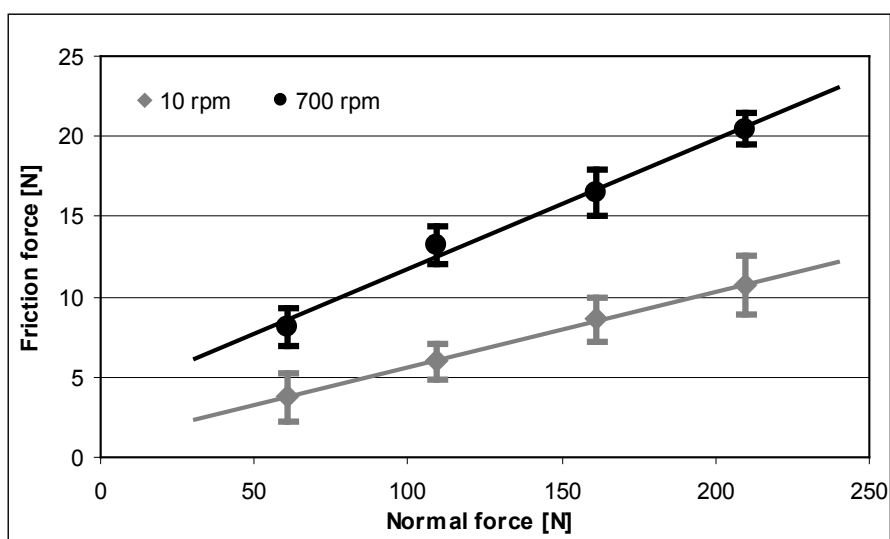


Figure 4. Effect of the normal load to the friction force

Because the linear effect there it is possible that the friction and the rolling coefficient are constant. Usually in case of high loads the adhesion properties are considered to be very important. But from the obtained

result didn't show considerable change (no blending in the results), which mean there is no vital effect of the adhesion. May be the presence of PTFE could have possibly reduced the adhesion effect. To clearly study the rolling and the sliding coefficient values further experiments needed.

Tribological tests on evaluating the friction characteristics uses temperature to explain the tendency as a outcome of frictional heating. In the current research the influence of frictional heating is made negligible by allowing enough cooling time between two measurements and by using the cleaning agents which removes the induced heat in the test cycle. On measuring the temperature of the contact surface from the composite disc temperature of  $24\pm 2^{\circ}\text{C}$  was observed which is close to the room temperature. Even with online monitoring system the measured surface temperature fluctuates a little. The temperature of the contact surface has reached a maximum value of  $26^{\circ}\text{C}$  which is very low considering the earlier researches on rolling/sliding contacts of polymers, where the increase in temperature was up till  $80^{\circ}$ . Investigation on the image of the contact surface also briefs that there is no deposit of polymer on the counterface material.

#### 4 MICROGRAPH

Pictures of the contact surface were made using Olympus SRZ microscope. Images were captured before and after every test cycle for all loads. Figure 5(a) show the initial surface before testing where the fibers are not really visible to make potential change in the friction characteristics. But on the consecutive testing the matrix tends to be removed and scale like surface morphology is seen showing the fibers leaving the matrix. The machine mark from the tool steel is also visible on Figure 5.

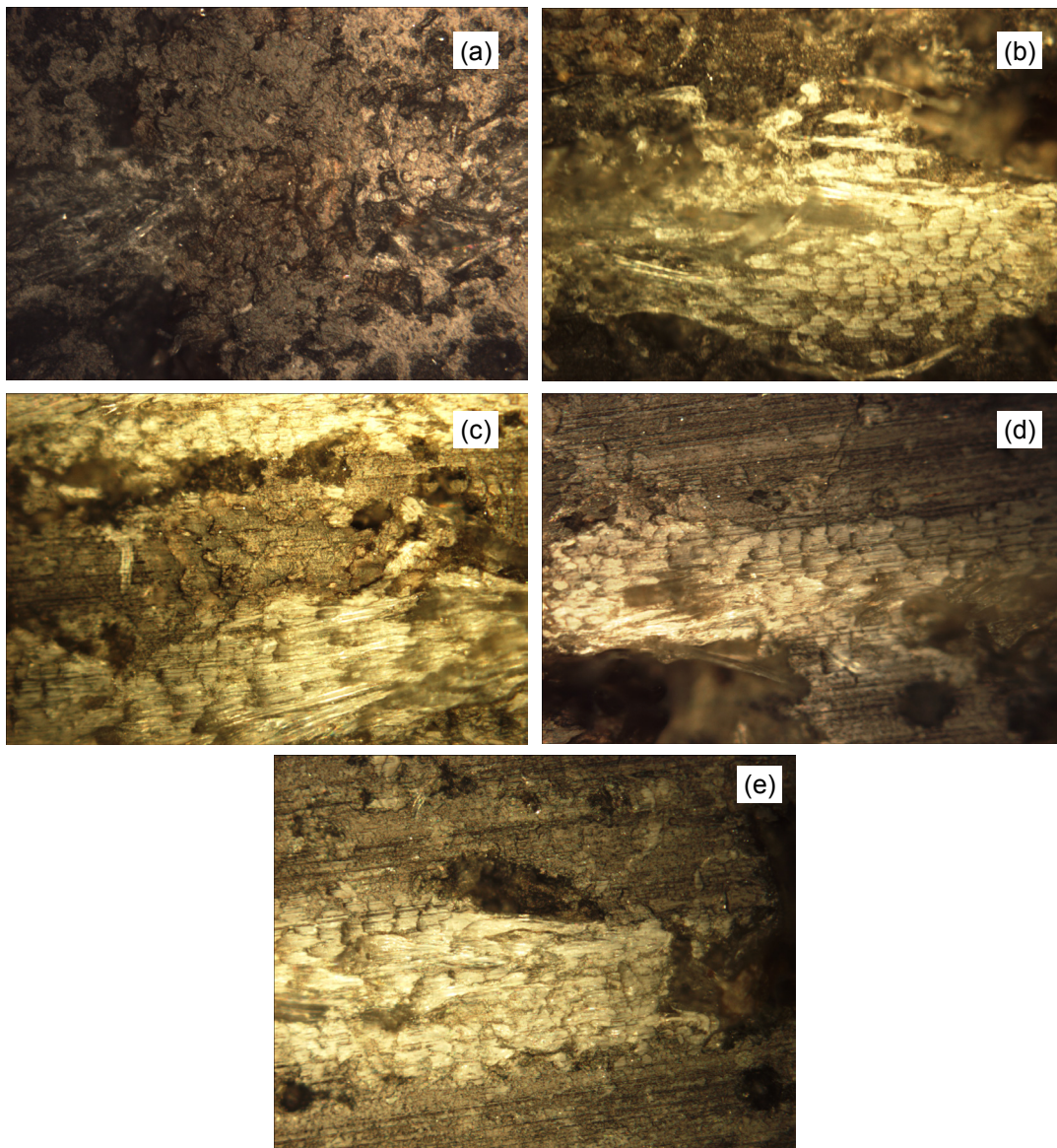


Figure 5. Contact surface before test (a), after test in case of 61 N (b), 111 N (c), 161 N (d) and 210 N (e)

The limited experiment time cause limited wear also. From 61 N to 210 N (Figure 5. b-e) the surface topography is almost the same. The rolling leads to periodical deformation, which is actually little displacement close to the surface. This displacement breaks the joints between the polyester matrix and the textile. For this effect the matrix can easy remove that fields where the textile is close to the surface. This is the reason, that after the experiments the textile structure becomes visible over the polymer surface. Effect of the load just the dept of the craters on the border between the textile and the matrix. Because the high normal load (and the high maximum contact pressure) larger displacement exhibits, which destroy the structure beneath the layers also.

## 5 CONCLUSION

Polymer composite which is widely used in the bearing industry is tested for the influence of load on the friction behaviour under low and high speed condition. On both high and low speeds the friction force showed same tendency having a linear increase in friction force for increasing load. The rate of increase in friction force is much sensitive on high speed. The linear curves are well fitted, because in this system there is no effect of the temperature and the other conditions were also steady. Based on the results the PTFE content helps the composite to avoid the adhesion effect also. If the applications has high contact speed, it is worth to use larger dimensions to reduce the contact pressure. The new geometry leads to energy saving applications, but in case of low loads this saving relatively less. From low load (61 N) the periodical stress lead cracks, craters and visible textile of the surface. High load only increases the depth of the cracks and craters.

## 6 REFERENCES

- [1] Srivastava V.K., Pathak J.P., Friction and wear properties of bushing bearing of graphite filled short glass fibre composites in dry sliding, *Wear* 197(1-2), 145–150, 1996.
- [2] Kishore, Sampathkumaran P., Seetharamu S., Thomas P., Janardhana M., A study on the effect of the type and content of filler in epoxy–glass composite system on the friction and slide wear characteristics, *Wear*, 259(1-6), 634–641, 2005.
- [3] Quintelier J., Online wear monitoring of polymer matrix composites with advanced measurement techniques, Ph.D Thesis, Gent University, 2007.
- [4] Myshkin N.K., Petrokovets M.I., Kovalev A.V., Tribology of polymers: Adhesion, friction, wear, and mass-transfer, *Tribology International*, 38(11-12), 910–921, 2005.
- [5] Hooke C.J., Kukureka S.N., Liao P., Rao M., Chen Y.K., The friction and wear of polymers in non-conformal contacts, *Wear*, 200(1-2), 83–94, 1996.
- [6] Kukureka S.N., Chen Y.K., Hooke C.J., Liao P., The wear mechanisms of acetal in unlubricated rolling – sliding contact, *Wear*, 185(1-2), 1–8, 1995.
- [7] Gordona D.H., Kukureka S.N., The wear and friction of polyamide 46 and polyamide 46/aramid-fibre, composites in sliding–rolling contact, *Wear*, 267(1-4), 669–678, 2009.
- [8] Chena Y.K., Modib O.P., Mhaya A.S., Chrysanthou A., O'Sullivan J.M., The effect of different metallic counterface materials and different surface treatments on the wear and friction of polyamide 66 and its composite in rolling–sliding contact, *Wear*, 255(1-6), 714–721, 2003.
- [9] Su F., Zhang Z.Z., Guo F., Men X.H., Liu W.M., Friction and wear properties of fabric/phenolic composites with plasma treated-hybrid glass/PTFE fabric, *Composites Science and Technology*, 67(6), 981–988, 2007.
- [10] Gopal P., Dharani L. R., Blum F. D., Load, speed and temperature sensitivities of a carbon-fiber reinforced phenolic friction material, *Wear*, 181-183(Part 2 March), 913–921, 1995.
- [11] Liu Y., Schaefer J.A., The sliding friction of thermoplastic polymer composites tested at low speeds, *Wear*, 261(5-6), 568–577, 2006.

# HEIGHT-INDEPENDENT TOPOGRAPHIC PARAMETERS OF WORN SURFACES

I. Barányi<sup>1,2</sup>, Á. Czifra<sup>1</sup>, G. Kalácska<sup>2</sup>

<sup>1</sup> Óbuda University, Donát Bánki Faculty of Mechanical Engineering and Security Technology

<sup>2</sup> Institute for Mechanical Engineering Technology, Faculty of Mechanical Engineering, Szent István University, Gödöllő,

**Abstract:** Surface microtopography plays a dual role in the course of friction and wear processes. It affects the contact and temperature conditions, and it undergoes significant changes in accordance with the wear mechanism. Fractal dimension (Df), root mean square gradient (Sdq), surface area ratio (Sdr) and surface kurtosis (Sku) parameters of microtopographies provides opportunities for understanding more deeply the wear processes independently from the amplitude of the roughness. Wear experiments and surface roughness measurements before and after wear were performed. Investigations extended to wear in the course of the non-lubricated ferrodo-steel material pairs, and lubricated camshaft-bushing pairs.

**Keywords:** wear, microtopography, power spectral density, fractal dimension, 3D parameters

## 1 INTRODUCTION

Efficient research in the course of the past decades has provided experts involved in surface microtopography research with a number of tools and methods to design an operationally optimized surface. At the same time, this knowledge is utilized only to a small degree in the analysis and control of tribological processes. Characteristically, designers continue to content themselves by requiring few – first of all height-dependent – roughness parameters [1].

In the first half of the 90s, computers of adequate speed of operation and processing softwares became increasingly available, make it possible to realize 3D surface characterisation. In the literature different directives can be found none of them has become widely used. Beside the extension of 2D parameter based technique to 3D many other new parameters and methods have been developed. One is the power spectral density (PSD) technique when “global” surface characterisation is carried out using complex mathematical tools. PSD provides full length scale analysis which takes into consideration not only the dominant topographic elements but also the submicro features, in contrast with traditionally surface characterisation methods. The fractal dimension derived from PSD topography seems to be an efficient tool for characterization. Some topographic parameters such as Sdr connected exclusively to 3D topographic analysis, but some others have 2D pairs (for instance Sdq or Sku).

In the course of friction and wear processes, surface topography plays a dual role. On the one hand, it affects the contact and temperature conditions occurring between the contacting surfaces which determine the tribological process together with a third body; on the other hand, it undergoes significant changes in accordance with the wear mechanism operating between the surfaces.

In the present study topographical measurements and special 3D parameter-based characterizations were performed to study the changes of microtopographies in wear. Laboratory wear tests of ferrodo-steel sliding pair were carried out and also industrial worn machine elements were investigated. Fractal dimension (Df), root mean square (RMS) gradient (Sdq), surface area ratio (Sdr) and surface kurtosis (Sku) of topographies before and after wear were analysed and compared.

## 2 INVESTIGATED TOPOGRAPHIES

The first part of investigation was the wear test of ferrodo-steel sliding pair. Steel (55Si7) sliding tracks were used for the tests, on which 18 mm ferrodo specimens were slid. The steel had ground surfaces. Two different grinding wheels were used for producing ‘fine’ (sign: F) and ‘rough’ (sign: R) surfaces. Two machining directions were used: one of them was perpendicular to (sign: N) while the other was parallel (sign: P) with the sliding direction. The stroke of the sliding was 180 mm and the load was 1000 N. The sliding speed was 50 mm/s. No lubrication was applied. First test series were slide for 2 hours while the second test series were slide for 6 hours. Steel track microtopography was recorded at two different places using a Mahr Perthen Concept 3D type stylus instrument. The size of the surface measured was 1x1 mm and the sampling distance was 2 µm in both directions. Measurements were performed on identical surface

sections before and after the wear process, therefore the changes of a given surface section can be traced accurately, not only statistically, in the course of the wear process.

The second part of investigations was the topographic measurements of camshaft-bushing pair. Original and worn one was measured from both of them. The worn camshaft and thrust bushing was operated 115000 km in a car. Measurement topography size and also the sampling distance were similar than in case of steel sliding track. Table 1 summarise the wear tests parameters and set-up of topographic measurements.

Sliding pair	Specimen	Wear time	Machining vs. Sliding direction	Average roughness of original topography	Repetitions of topography measurements	Sign
Ferodo-steel	Steel	2 h	Paralell (P)	Fine (F) $Sa \approx 0.2 \mu m$	2	2hPF_A
						2hPF_B
				Rough (R) $Sa \approx 1.6 \mu m$	2	2hPR_C
						2hPR_D
			Perpendicular (N)	(F) $Sa \approx 0.2 \mu m$	2	2hNF_E..F
				(R) $Sa \approx 1.6 \mu m$	2	2hNR_G..H
		6h	Perpendicular (N)	(F) $Sa \approx 0.1 \mu m$	6	6hNF_I..N
Cam-shaft - Bushing	Cam	115000 km	Paralell (P)	(F) $Sa \approx 0.3 \mu m$	1	Ch115PF_O
	Bushing		Paralell (P)	Very fine (VF) $Sa \approx 0.04 \mu m$	1	Bu115PWF_P

Table 1. Wear test and measuring conditions

Figure 1.-3. show some topographies. The original microtopography of 2hNF\_E surface disappeared and new surface texture was formed in accordance with the direction of relative movement. The scratches formed seem "fine" and uniform. In case of Figure 2. the original surface texture has not disappeared, but the peak zone of microtopography changed: scratches were formed in the sliding direction. Figures 3. show chamshaft and bushing surfaces formed by abrasive wear similar than steel surface in Figure 1. and 2. Scratches are laying long on the surfaces, and they are not too deep, so abrasive mild wear can be supposed in all cases.

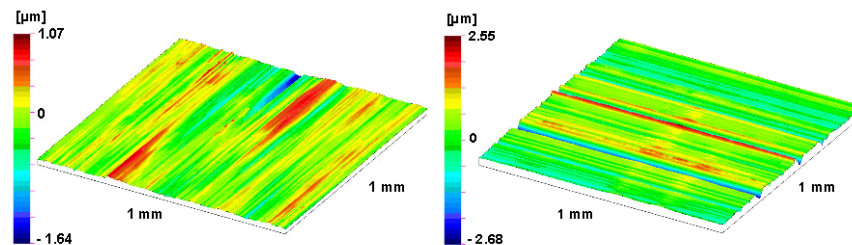


Figure 1. 2hNF\_E surface before wear and after 2 hour sliding

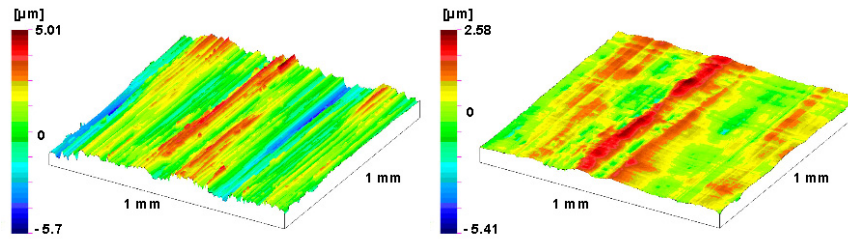


Figure 2. 2hNR\_H surface before wear and after 2 hour sliding

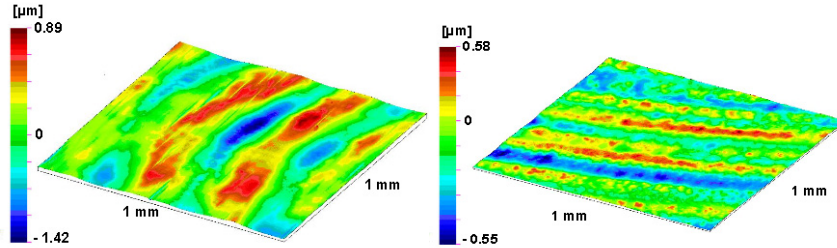


Figure 3. Worn surface of chamshaft (Ch115PF\_O) and thrust bushing (Bu115PWF\_P)

### 3 CHARACTERISATION TECHNIQUE

To characterize the measured topographies an algorithm was developed in cooperation with Department of Machine and Industrial Product Design, Budapest University of Technology and Economics and interpreted as a parametric-based 3D surface and PSD analysis software. Theoretical base of 3D parameters and PSD analysis are summarised as follows. Details can be found in [2, 3 and 4].

The root mean square gradient,  $Sdq$ , is the RMS-value of the surface slope within the sampling area, and is defined as (1).

$$Sdq = \sqrt{\frac{1}{(M-1)(N-1)} \sum_{j=2}^N \sum_{i=2}^M \left( \frac{z(x_i, y_j) - z(x_{i-1}, y_{j-1})}{\Delta x} \right)^2 + \left( \frac{z(x_i, y_j) - z(x_{i-1}, y_{j-1})}{\Delta y} \right)^2} \quad (1)$$

where  $z(x_i, y_j)$  is the height coordinate located in  $x_i, y_j$ ,  $M$  is the number of points in profile,  $N$  is number of profiles,  $\Delta x, \Delta y$  sampling distances.

The surfaces area ratio,  $Sdr$ , expresses the increment of the interfacial surface area relative to the area of the projected plane (2).

$$Sdr = \frac{\sum_{j=1}^{N-1} \sum_{i=1}^{M-1} A_{i,j} - (M-1)(N-1)\Delta x \Delta y}{(M-1)(N-1)\Delta x \Delta y} \quad (2)$$

The surface kurtosis,  $Sku$ , describes the "peakedness" of the surface topography, and is defined as (3), where  $Sq$  is the RMS value of topography. For Gaussian height distributions  $Sku$  approaches 3.0 when increasing the number of pixels. Smaller values indicate broader height distributions.

$$Sku = \frac{1}{MNSq^4} \sum_{j=1}^N \sum_{i=1}^M z^4(x_i, y_j) \quad (3)$$

PSD analysis transforms the profile from the spatial domain to frequency one using Fourier transformation. Transformation gives complex result. The power spectral density assigns an "amplitude" – magnitude of the complex number – to the frequency pair  $p_k, q_l$ . There are two possibilities of showing results. One is to represent the amplitude of PSD in the function of wavelength. The other prevalent method is logarithmic scale frequency-PSD amplitude visualization. In the second method the height frequency range of the curve can be approximated by a line. The slope of the line is in correlation with the fractal dimension of surface. Wavelengths smaller than the highest dominant wavelength plays a considerable role. PSD amplitude becomes constant – the self-affinity character of the surface disappears – in a lower wavelength range. The slope of fitted line ( $s$ ) to PSD curve has correlation with fractal dimension of surface according to (4).

$$Df = 4 + \frac{s}{2} \quad (4)$$

#### 4 RESULTS

Changes of  $Sdq$  and  $Sdr$  parameter in wear are summarised in Table 2 and Figure 4 and 5. Both parameters change dramatically. Some cases the change is higher than 100%.  $Sdr$  parameter is very sensitive for wear: its change is higher than 50% in all cases. In cases of A, B, G, H both parameters increases, although the wear process of A-H specimens are the same. The  $Sdq$  value after wear – using similar test set up – becomes similar. In case of A-H this value is in range 3.62-7.08°, although the original topographies have wide range (2.73-12.76°) of this parameter. Analysing the results of six-hour wear process the conclusion is the same.

Sign	$Sdq$ [°]		Change in %	$Sdr$ [-]		Change in %
	before wear	after wear		before wear	after wear	
2hPF_A	2.79	5.37	-92.47	0.06	0.36	-500.0
2hPF_B	3.12	3.62	-16.03	0.09	0.14	-55.6
2hPR_C	11.07	6.31	43.00	1.82	0.54	70.3
2hPR_D	13.35	7.08	46.97	2.69	0.69	74.3
2hNF_E	11.85	5.02	57.64	2.05	0.32	84.4
2hNF_F	12.56	5.20	58.60	2.33	0.35	85.0
2hNR_G	2.73	6.77	-147.99	0.06	0.62	-933.3
2hNR_H	2.90	5.41	-86.55	0.08	0.38	-375.0
6hNF_I	8.55	1.26	85.26	1.05	0.003	99.7
6hNF_J	9.23	1.30	85.92	1.24	0.004	99.7
6hNF_K	8.49	1.63	80.80	1.04	0.011	98.9
6hNF_L	8.55	1.14	86.67	1.05	0.002	99.8
6hNF_M	8.52	1.54	81.92	1.04	0.016	98.5
6hNF_N	8.24	1.47	82.16	0.97	0.011	98.9
Ch115PF_O	5.25	1.30	75.24	0.35	0.012	96.57
Bu115PWF_P	0.33	0.70	-112.12	0.0001	0.0002	-100.00

Table 2. RMS slope and surface area ratio before and after wear

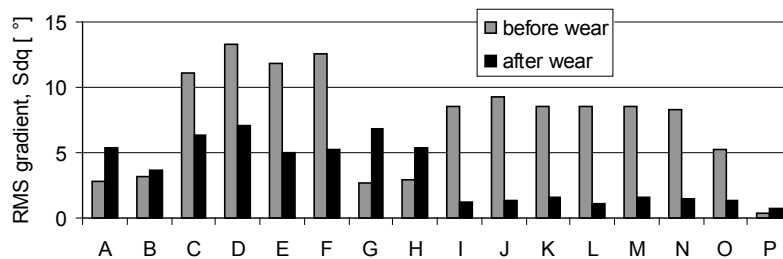


Figure 4. RMS slope before and after wear

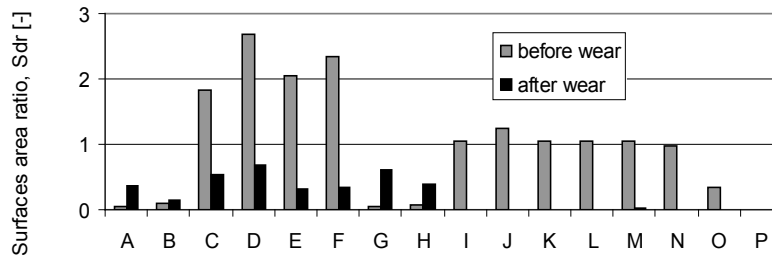


Figure 5. Surface area ratio before and after wear

It is also interesting that behaviour of  $Sdq$  and  $Sdr$  parameters is uniform. Examining the definitions of these parameters the experience is understandable. If the topography has higher RMS gradient it means, that enveloping surface is higher so  $Sdr$  parameter also has higher value. Because of the very sensitive character of  $Sdr$  in general case  $Sdq$  seems more effective.

Fractal dimensions of topographies before and after wear, as the results of analysis were presented in [5]. Now its correlation with other parameters is analysed. Table 3 summarises the results and Figure 6 shows the fractal dimension before and after wear, while Figure 7 shows the surface kurtosis.

Sign	$Df$ [-]		Change in %	$Sku$ [-]		Change in %
	before wear	after wear		before wear	after wear	
2hPF_A	2.78	2.80	0.72	3.14	12.00	-282.17
2hPF_B	2.88	2.76	-4.13	3.57	3.94	-10.36
2hPR_C	2.89	2.71	-6.17	2.00	2.26	-13.00
2hPR_D	2.80	2.67	-4.49	2.42	3.18	-31.40
2hNF_E	2.77	2.80	0.89	3.40	8.74	-157.06
2hNF_F	2.73	2.68	-1.60	5.02	4.54	9.56
2hNR_G	2.72	2.57	-5.58	2.18	2.88	-32.11
2hNR_H	2.84	2.65	-6.67	3.07	4.25	-38.44
6hNF_I	2.84	2.65	-6.82	3.20	3.05	4.69
6hNF_J	2.92	2.58	-11.65	3.08	3.77	-22.40
6hNF_K	2.87	2.52	-12.22	3.54	2.48	29.94
6hNF_L	2.92	2.79	-4.40	3.38	2.86	15.38
6hNF_M	2.79	2.99	7.19	3.80	5.83	-53.42
6hNF_N	2.80	2.76	-1.37	4.94	4.70	4.86
Ch115PF_O	2.78	2.43	-12.72	3.62	2.91	19.61
Bu115PWF_P	2.92	2.31	-20.88	3.94	2.51	36.29

Table 3. Fractal dimension and surface kurtosis before and after wear

As was concluded in [5] fractal dimension – in contrast with other parameters – have correlation with wear:  $Df$  decreased in examined wear processes. Only three cases were where  $Df$  increased, but topographies in these cases have deep grooves formed by wear particles.

Increase of  $Sku$  parameter was supposed before the tests, because of plateau-like character of mild wear surfaces. The results do not confirm this statement. The change of kurtosis was minimal, and in some cases the parameter decreased. Topographies of six-hour wear process (sign I-N) have kurtosis between 3.08–4.94 before wear. However the same process was carried out  $Sku$  changed between -53.42 and 29.94 %. No correlation with wear process was found. Only one interesting thing must be mentioned: change of kurtosis was significant (more than 50%) in three cases. In these cases fractal dimension was increased. It means that not only the fractal analysis, but parameter surface kurtosis is sensitive for deep grooves of topographies. The fourth power in definition of  $Sku$  explain this phenomenon.

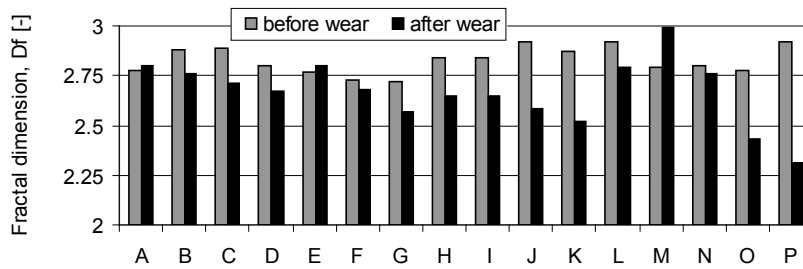


Figure 6. Fractal dimension before and after wear

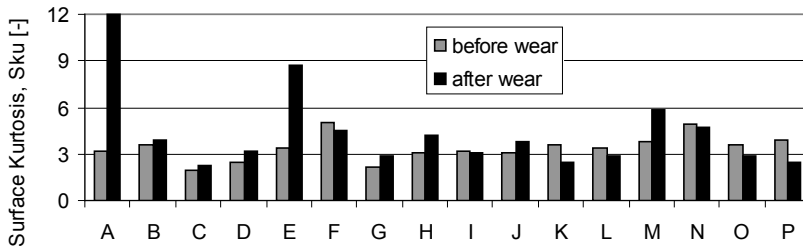


Figure 7. Surface kurtosis before and after wear

## 5 CONCLUSIONS

Results can be summarised as follows:

Root mean square slope ( $Sdq$ ) and areal ratio ( $Sdr$ ) parameters characterise similar features of topographies, but  $Sdr$  parameter is more sensitive for changes.

Fractal dimension ( $Df$ ) of surfaces was decreased in case of mild wear, but special surface features – such as deep grooves – increased its values.

Surface kurtosis ( $Sku$ ) has no correlation with wear process, but it is sensitive for appearance of deep grooves:  $Sku$  value drastically increased.

## References

- [1] Horváth S. 2D and 3D characterization of surface waviness; survey and analysis of its impact on operational characteristics. Dissertation, National Defence University 2008
- [2] Stout KJ, Sullivan PJ, Dong WP, Mainsah E, Luo N, Mathia T, Zahouni H. The development of methods for characterisation of roughness in three dimensions. University of Birmingham Edgbaston 1993.
- [3] Persson BNJ, Albohr O, Tratagliano U, Volokitin AI, Tosatti E. On the nature of surface roughness with application to contact mechanics, sealing, rubber friction and adhesion. J. Phys, Condens. Matter 2005;17:R1-R62
- [4] Blateyron, F.: New 3D Parameters and Filtration Techniques for Surface Metrology, Quality Magazine, White Paper, May 15, 2007
- [5] István Barányi, Árpád Czifra, Sándor Horváth: Power spectral density (PSD) analysis of worn Surfaces, Gépészet 2010 Proceedings of the seventh conference on mechanical engineering, Budapest, 2010. május 25-26, ISBN 978-963-313-007-0

# REVIEW AND CLASSIFICATION OF FRETTING FATIGUE TEST RIGS

J. De Pauw<sup>1</sup>, P. De Baets<sup>1</sup> and W. De Waele<sup>1</sup>

<sup>1</sup> Ghent University, Laboratory Soete, Belgium

**Abstract** There is no standard or generally accepted test rig for fretting fatigue experiments. Therefore, researchers adopt an existing concept, or build a new test rig that meets their specific requirements. However, too many different test rigs may be disadvantageous because the results of two different test rigs are hard to compare. The increasing amount of diversity is mainly caused by the lack of a recent literature survey on fretting fatigue test rigs. In 1994, *Hills* and *Nowell* described a few test rigs in *Mechanics Of Fretting Fatigue*. In this study, the authors made a classification of test rigs based on the contact geometry, which is determined by the test specimens, not by the test rig itself.

The authors of this article present a review of the available literature, and present a classification based on the properties of test rigs. Fretting fatigue test rigs are first divided in two categories based on the geometry of the test specimen: full scale and coupon scale test rigs. The latter are mostly used to perform research and are subdivided in categories based on increasing functionalities. This is the ability to apply a fatigue load, a constant normal force, and an alternating slip in the range of some micrometers. In time, from the fifties until now, progress has been seen in the design of fretting fatigue test rigs. More parameters can be controlled during experiments and more measuring techniques are incorporated. State of the art test rigs are classified in the last category with most functionalities, but still have imperfections. Future designers can use this article to classify their needs, or help to design a better test rig knowing the imperfections of the state of the art test rigs.

**Keywords** Fretting fatigue, test rig, coupon scale, full scale, classification

## 1 INTRODUCTION

Fretting fatigue occurs frequently in mechanical connection techniques such as bolted lap-joints, press fit connections, dovetail connections, splined couplings, ... Early failures of such connections can cause failure of the whole mechanical constructions. To prevent unexpected failures caused by fretting fatigue, a well-founded estimation of the lifetime is needed. Lifetime can be measured during experiments or calculated by theories that are validated by experiments.

Experiments are performed on a test rig that is capable to test fretting fatigue. However, there is no standard or generally accepted test rig to test fretting fatigue. Therefore, researchers copy literature designs, or design a custom test rig that meet their specific requirements. The proliferation of test rigs has negative consequences though. Results obtained from two different test rigs are very difficult to compare with each other. A slight difference in the compliance of the test rig has already a significant influence on the result in a fretting fatigue experiment. Next to the constructions of the test rigs, the test specimen geometry has a significant influence on the result of an experiment as well. Figure 1 shows the stress field during two experiments, only the height  $h$  of the fretting bridges is changed, which is always arbitrarily chosen. The stress field in both experiments is very different as well as the contact pressure distribution.

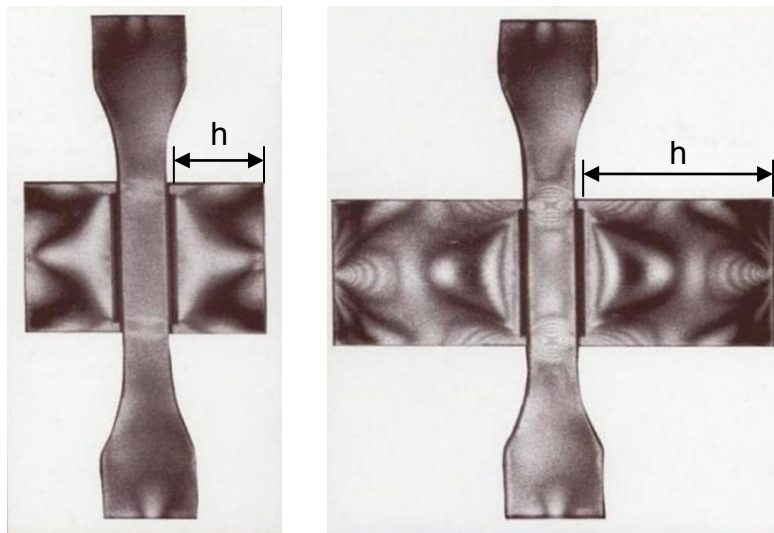


Figure 1. Photo elastic picture of the stress field, with different height  $h$  of the fretting bridges [1].

Without a standard, or recent overview of existing test rigs, researchers are forced to design their own test rig, increasing the number of test rig concepts. This problem was broached in 1990 during the first conference on fretting fatigue, *Standardization of fretting fatigue methods and equipment* [1]. However, twenty years later there is still no standard. The best overview of fretting fatigue tests known to the authors dates from 1994 in *Mechanics of fretting fatigue* [2] by *Hills and Nowell*. However, over the last 16 years there was a progress in test rigs both qualitative and quantitative that is not yet summarized.

The authors of this article give a classification of test rigs, based solely on the properties of the test rig. This in contrast with *Hills and Nowell* [2] who made a classification for fretting fatigue tests based on the specimen geometry rather than the performance of test rigs.

## 2 FEATURES OF A FRETTING FATIGUE TEST RIG

Fretting fatigue in one contact point is schematically shown in Figure 2. Two specimens, a fatigue specimen (specimen) and an indenter (pad) are preloaded onto each other with a constant force  $F_N$ . The indenter is alternately moving with an amplitude  $d$ , the amplitude of the resulting slip  $s$  is in the range of some (1..100) micrometer and fretting will occur between the pad and the specimen. Fatigue is introduced in the specimen by an alternating load  $F_{fat}$ .

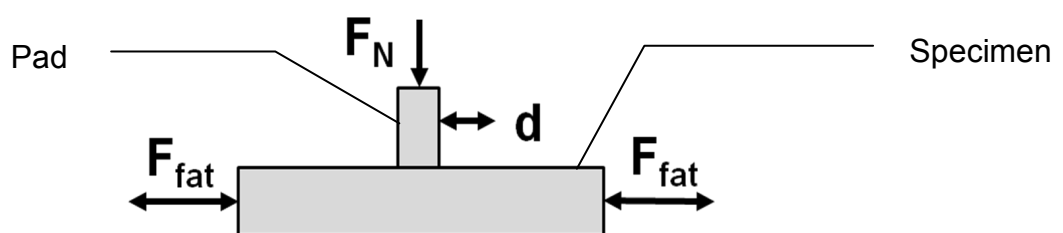


Figure 2. Schematic overview of fretting fatigue.

The schematic overview of Figure 2 describes fretting fatigue for one contact point. Most fretting fatigue experiments have multiple contact points for symmetry reasons. However, to perform a fretting fatigue experiment one needs to apply two forces and one slip in the contact area:

- A constant force  $F_N$
- A dynamic force  $F_{fat}$
- A relative slip  $s$

These features are not always independently controlled. For scientists who want to perform state of the art research it is interesting to control every parameter independently. If all the input parameters are known, a lot of experiments can be performed. However, industrial researchers don't know all the input parameters for this model. Therefore they perform experiments on full scale pieces and apply forces like in the real application. The interacting forces  $F_N$ ,  $F_{fat}$  and the slip  $s$  in one contact area are coupled with each other by geometry, just like in the real application.

The difference between full scale experiments and coupon scale experiments is the specimen geometry. The specimens in full scale experiments are real geometries like a dovetail connection, lap joint, etc. While the geometry of the specimens in a coupon scale experiment on the other hand is not related to a real problem. The geometry focuses on the contact area where fretting fatigue initiates, as shown in Figure 2.

Different test rigs are needed to perform full scale experiments or coupon scale experiments. During coupon scale experiments we want to measure and control as much parameters as possible, preferably independent ones. In a full scale experiment however, only those forces are applied that appear in the real application.

The classification of test rigs has a first subdivision between full scale test rigs and coupon scale test rigs. The next paragraph discusses and enumerates some full scale test rigs. Paragraph 4 focuses on coupon scale test rigs, further subdivision of test rigs will be expanded in this section.

### 3 FULL SCALE TEST RIGS

Full scale test rigs are mostly used in industrial research, to estimate the lifetime of a component. The geometry of the test specimen is (scaled) related to the real application.

The advantage of a full scale test is the similarity in contact mechanics, because contact geometry and stiffness are similar. Another advantage is that only the known forces are applied. Test rigs for full scale tests usually only need one actuator, with a simple controller.

The applied force on the full scale geometry results in one or more contact points where fretting fatigue can occur. In such a contact point there is a constant force  $F_N$ , a dynamic force  $F_{fat}$  and a relative slip  $s$ . However, these forces and slip are related to the applied force and cannot be controlled individually, nor be measured. Therefore, verification with coupon scale test is nonexistent. Even verification between two similar full scale test rigs is difficult, because the compliance of the specimens and the test rigs will determine the distribution of the normal force  $F_N$ , the fatigue force  $F_{fat}$ , and the relative slip  $s$ .

Full scale tests are more expensive than coupon scale tests, therefore full scale test are only used when economically justified, for example to predict the lifetime of connection techniques in aerospace industry. An ordinary airplane has several connection techniques that can fail due to fretting fatigue. The shell of an aircraft is constructed by aluminum sheets that are bolted or riveted together, these lap joints are sensitive to fretting fatigue [3]. In the engine of an aircraft there are two connection techniques that can fail due to fretting fatigue. A dovetail connection to connect the turbine blades onto the rotor (paragraph 3.1), and a splined connection to connect parts of the engine [4-6].

Another application where a full scale fretting fatigue test rig has been build comes from the oil and gas industry. To mine and transport oil and gas, pipelines are used. Pipelines are sometimes joined by a threaded connection that fails due to fretting fatigue [7], leading to costly repairs and expensive downtime. The aim of the full scale experiment is to determine the lifetime of such a connection accurately.

Full scale test rigs are also used to test connection techniques that are frequently used but still give problems, like press-fitted connections [8-11]. This connection technique is frequently used to connect a shaft with a bearing, a gear, a flywheel, etc. The last full scale test rig listed in this article is used to test the fretting fatigue properties of a leaf spring package that is used for cars [12].

An overview of some existing full scale test rigs is given in Table 1. This table indicates how the fatigue force  $F_{fat}$ , the normal force  $F_N$ , and the relative slip  $s$  are applied during an experiment. Most of the full scale test rigs have only one actuator to apply the dynamic fatigue force. The slip is always dependent of the applied force and the local geometry. How the normal force is applied depends on the application.

Table 1. Overview of how the interacting forces and slip are applied in full scale experiments

	<b>Fatigue force</b>	<b>Normal force</b>	<b>Slip</b>
<b>Dovetail connection</b>	Applied by actuator	Due to actuator	Due to geometry and fatigue force
<b>Bolted or riveted lap connection</b>	Applied by actuator	Pre stress bolt or rivet	Due to geometry and applied forces
<b>Wire rope</b>	Applied by actuator	Pre stress by dead weight	Due to geometry and fatigue force
<b>Wire rope connection</b>	Applied by actuator	Pre stress by dead weight	Due to geometry and applied force
<b>Press-fit connections</b>	Applied by electric motor and geometry	Press fit geometry	Due to geometry and applied forces
<b>Splined coupling</b>	Applied by actuator	Pre stress by spring system	Due to geometry and applied forces
<b>Threaded connections</b>	Applied by electric motor and geometry	Pre stress in threaded connection	Due to geometry and applied forces
<b>Leaf spring</b>	Applied by actuator	Pre stress of leaf spring package	Due to geometry and applied forces

The next two paragraphs give more details about two full scale test rigs. The first test rig is used to test dovetail connections, a typical connection technique in aircraft engines, steam turbines and other turbines. The second test rig is developed to test wire ropes that are used as overhead conductors.

### 3.1 Dovetail connections

Modern aircraft engines (turboprop) are based on a turbo machine, fluid energy is converted into mechanical energy by means of a blade. The blade transfers the energy onto the rotor through a dovetail connection. Due to the wedge-formed shape of the dovetail and the interacting forces on the blade, a slip arises between the blade and the rotor [13-15].

A full scale experiment of a dovetail connection is shown in Figure 3. The specimens have the shape of a dovetail connection. The only force that is applied during the experiment is  $F$ , working in vertical direction. There are two contact areas between the blade and the rotor, notice that this test rig has replaceable parts in the upper block. The dovetail connection is failed due to fretting fatigue, a crack initiated in the contact area, and propagated through the specimen (crack in Figure 3).

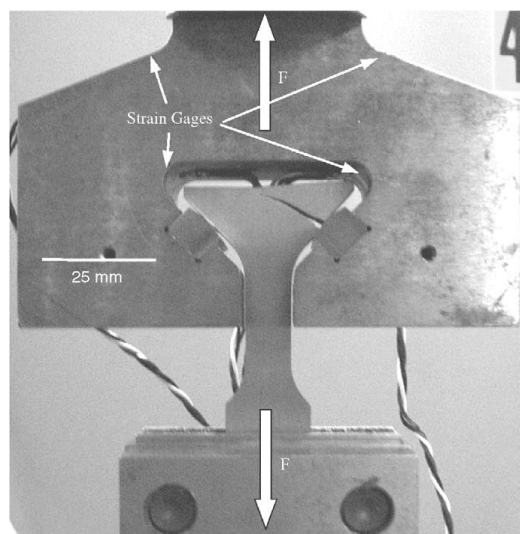


Figure 3. Dovetail fretting fatigue experimental setup with failed specimen [14].

### 3.2 Wire rope and wire rope fixture

The second full scale test rig discussed in this paper is developed to test an overhead conductor. Overhead conductors are just wire ropes that transport electricity. This test rig can be used to test other applications of wire ropes like a hoisting mechanism, a suspended bridge, a ski lift, etc.

The test rig exists of a 42 meter prestressed wire rope that is subjected to a dynamic loading by the shaker. The small wires in the wire rope will slip over each other leading to fretting fatigue failure in the wire rope. This problem can occur in the whole wire rope. However, most problems with fretting fatigue are seen in the suspension points of the wire rope. Clamping fixtures are placed around the wire rope and are securely tightened. The larger dimensions of the clamping fixture leads to a stiffer entity than the wire rope (Figure 5 left). This results in a discontinuity of the bending stiffness of the wire rope in the vicinity of such a fixture, and will result in fretting fatigue.

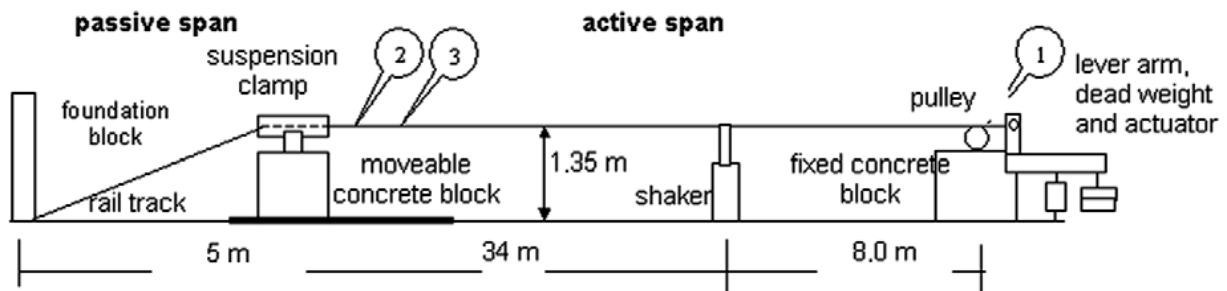


Figure 4. Schematic view of the fretting fatigue test rig for overhead conductors [16].

A heavily worn wire rope is shown in Figure 5 right. The outer layer of wires are worn and broken due to fretting fatigue between the wire rope and the clamping fixture. The underlying layer of wires is visible and shows elliptical wear marks due to fretting between two wires (trellis contact). Some of these wires are broken in the worn contact due to fretting fatigue (not visible on Figure 5).

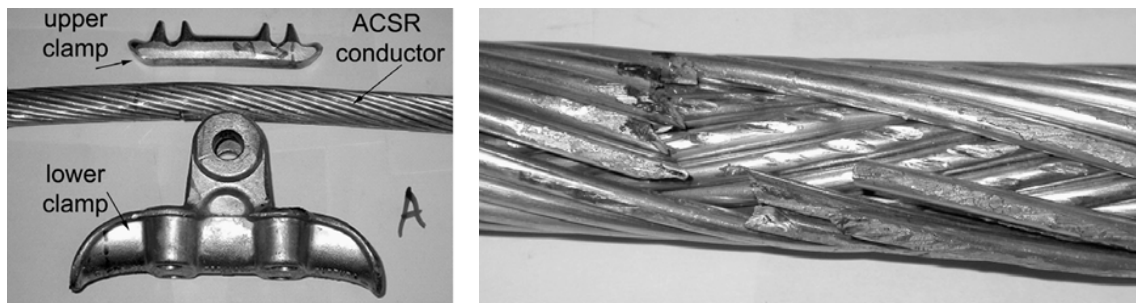


Figure 5. Clamping fixture not mounted on the wire rope (left) and a heavily worn wire rope (right) [16].

## 4 COUPON SCALE TEST RIGS

In contradiction to a full scale test rig, the specimens of a coupon scale test rig have no similarity with the real geometry of an application. Coupon scale testing is a common practice for material characterization and is used by academics to perform research.

Simple geometry specimens are ideal for material characterization tests regarding to fretting fatigue. It is assumed that all the specimens are manufactured and assembled equally, so the interacting forces in the vicinity of the contact area are the same. A second assumption is even more doubtful: when one has a ranking for materials on coupon scale it is assumed tacitly that an identical ranking applies to the real problem [2].

Academic researchers adopted the coupon scale technique for state of the art research. Coupon scale specimens have the advantage that all the dimensions can be chosen arbitrarily by the designer. Manageable specimens for laboratory testing have their benefits. However, the major advantage of a coupon specimen is the convenience to perform a parametric study on the dimensions of the specimen.

A well designed test rig has similar ease to perform parametric studies. Progress can be seen over time, the first types of coupon scale test rigs consist of one servo-hydraulic actuator and some screws to apply the forces. While most modern test rigs have multiple actuators to control the forces and slip independently in time.

The last advantage of coupon scale test rigs that will be cited here is the visibility of the contact. In most full scale test rigs it is impossible to see the contact area, nor the crack. For research however it is important to know the slip between pad and specimen and is it interesting to see the surface where cracks will occur. Crack propagation, and possible crack initiation, can then be studied with new field measuring techniques such as a thermal camera [17-19], an optical camera [20-22], a magnetic camera [23]...

#### 4.1 One actuator test rig

This section discusses test rigs that have one controllable actuator. This can be a hydraulic actuator, a piezo-electric shaker, any crank mechanism or other controllable drive unit. The bulk fatigue load  $F_{fat}$  is controlled by this actuator, all other applied external forces are set manually.

The normal force is mostly applied by a floating circular spring system, called a proving ring (Figure 6). The proving ring operates like a pre-stressed spring whereby the initial force is set by a setscrew and works based on the compliance of the spring. If the total length of the compressed parts doesn't change, the normal force stays constant during the experiment. This is not the case in fretting (fatigue) experiments, where fretting causes wear.

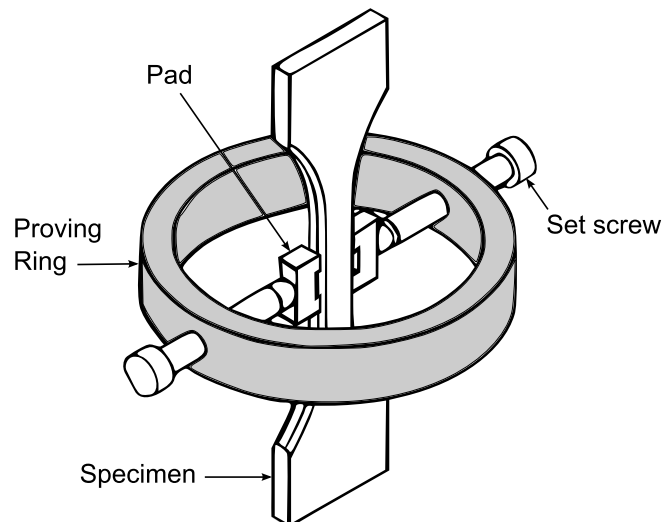


Figure 6. Fretting fatigue experiment whereby the normal load is applied with a proving ring [24]

If voluminous oxidized wear particles stay in the contact area they will cause an elongation of the compressed parts, and the proving ring. This results in a higher normal force  $F_N$  from the proving ring. On the other hand if particles escape from the contact area the pads will move towards the specimen due to wear. This is a shortening of the loading train that results in a decrease of normal force  $F_N$ . These mechanisms are undesirable if the normal force has to be constant. For example, *R.B. Waterhouse* used a proving ring with an unidirectional stiffness of about 12MN/mm, this resulted in a reduction of 15.5MPa when the relative distance of the two surfaces decreases 25 $\mu$ m [25].

Besides the fatigue force and the normal force, one should also apply a slip between the specimen and the pad. The relative displacement between the fatigue specimen and the pad is realized by the compliance of the specimens (fatigue specimen and pad) and the compliance of the test rig. The slip is always in phase with the fatigue loading and cannot be controlled independently. Two types of pad geometries will be discussed: floating fretting bridges (paragraph 3.1.1) and fixed fretting bridges (paragraph 3.1.2) as shown in Figure 7.

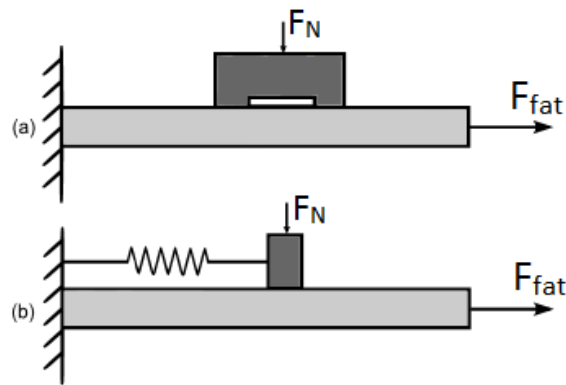


Figure 7. Floating fretting bridge (a) and Fixed fretting bridge (b).

#### 4.1.1 Floating fretting bridges

A floating fretting bridge is a pad that has two contact points with the specimen (Figure 7a). During an experiment two floating fretting bridges are mounted on one fatigue specimen for symmetry. Floating fretting bridges in combination with a proving ring (Figure 6) are frequently used because of their easy installation on an ordinary universal load frame.

Applying a fatigue load on the specimen will elongate the specimen. The initial contact points of one floating fretting bridge move apart, and a slip will occur in both contact points. The slip is in phase with the applied fatigue force, and cannot be controlled. The slip can be influenced prior to an experiment by adapting the geometry of the floating fretting bridges or the specimen. However, not all combinations of slip and fatigue load are possible.

Disadvantage of floating fretting bridges is the difficulty to compare results. A change in the geometry of the floating fretting bridges gives significant different results (see Figure 1). Other disadvantages of floating fretting bridges are the impossibility to measure the slip and the tangential force.

#### 4.1.2 Fixed fretting bridges

A fixed fretting bridge is fixed on the test rig, and has only one contact point with the fatigue specimen (Figure 7b). During an experiment two fixed fretting bridges are mounted on one fatigue specimen (Figure 8). Loading the specimen causes a displacement of the contact area. A slip will occur between the pad and the specimen. This slip is in phase with the applied fatigue force.

In contradiction to floating fretting bridges, fixed fretting bridges have the ability to measure the slip and the tangential force. The tangential force can be measured by strain gauges on the fixed fretting bridge which act as a calibrated spring [26].

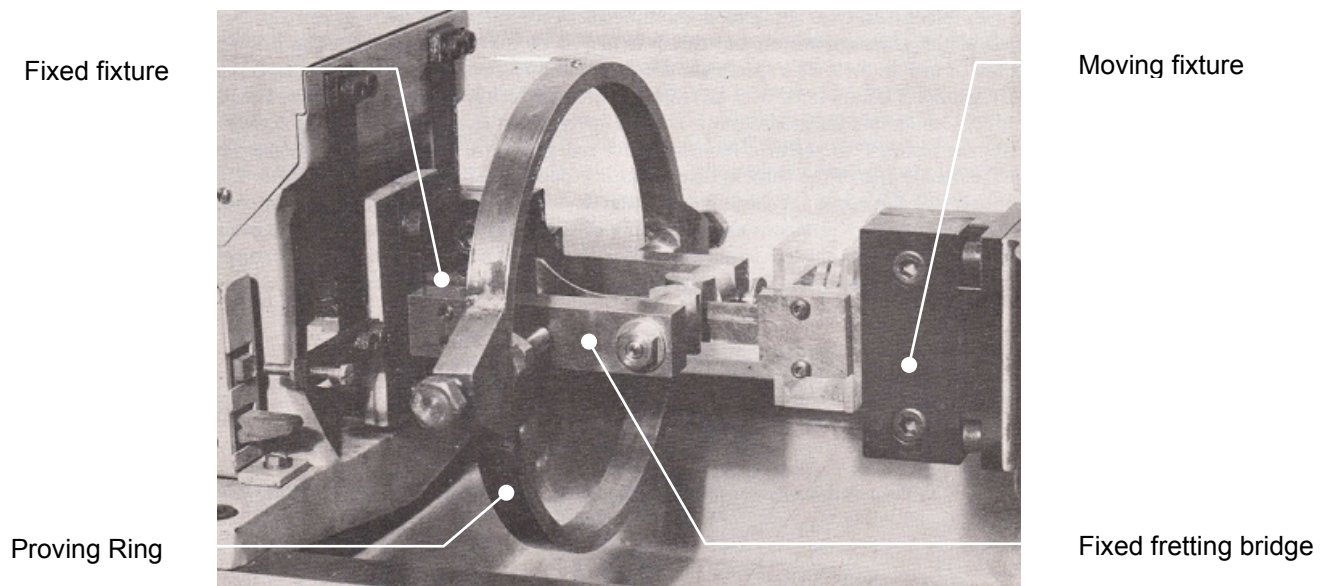


Figure 8. Fretting fatigue test rig with half fretting bridges and proving ring [25].

#### 4.2 One actuator test rig with adjustable compliance

A second type of coupon scale test rigs is based on one actuator, and has the ability to adjust the compliance of the test rig. The working principle is similar to fixed fretting bridges, Figure 7b. The only difference is that these test rig are designed to have an (continuous) adjustable compliance. This allows more combinations of slip and fatigue load. The slip is in phase with the fatigue load, but can be influenced prior to an experiment by adjusting the compliance of the test rig.

The mechanisms to adjust the compliance of the test rig are based on longitudinal springs [27] or cantilever beams [28-30]. A schematic drawing of the latter is shown in Figure 9. Two fretting pads are mounted on a stiff plate by linear bearings and load cells (LC4-LC7). The stiff plate is connected onto the rigid base by two cantilever beams. The support of the cantilever beams can be adjusted, so the stiffness of the test rig can be adjusted continuously prior to an experiment.

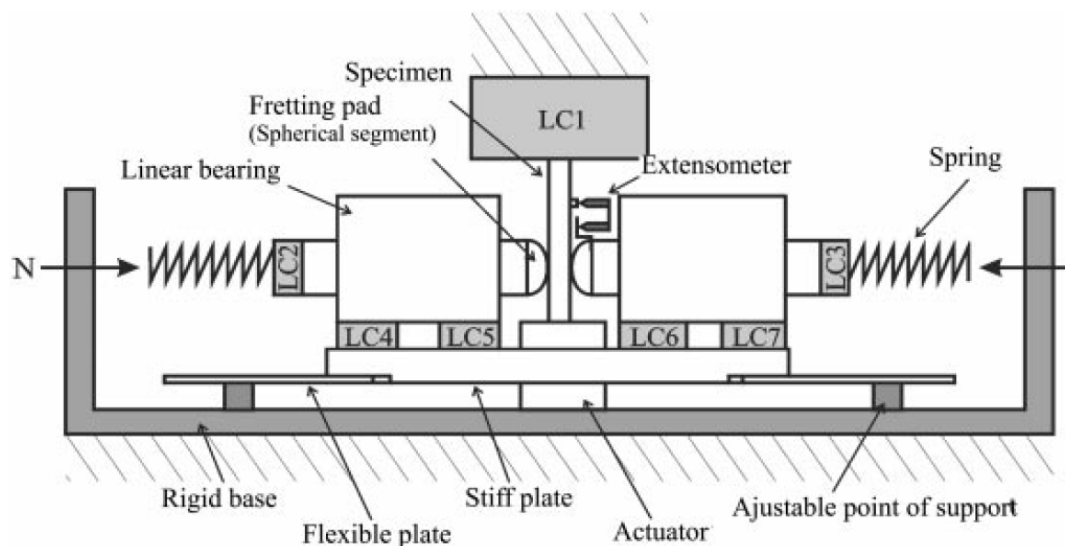


Figure 9. Fretting fatigue test rig with adjustable compliance, adjustable by support [30].

### 4.3 Two actuators test rig

The last type of fretting fatigue test rig that will be discussed in this paper is based on two actuators that independently control the fretting action and the fatigue action during experiments. In previously discussed test rigs these actions were always coupled by geometry and (adjustable) compliance of the test rig.

This type of test rig is first used by researchers at the University of Oxford [31] to investigate the influence of the fretting action and the fatigue action separately. Therefore the authors used a test rig whereby the fretting and fatigue action can be controlled independently. A schematic overview is shown in Figure 10 for one contact point.

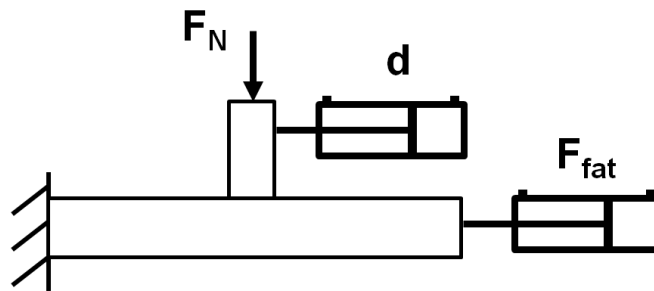


Figure 10. Schematic view of a fretting fatigue test rig with two actuators

A schematic view of a real test rig is shown in Figure 11. Two pads are used for symmetry reasons, and are installed on a fretting fixture (5). This fretting fixture is connected to a hydraulic actuator (1) by means of a structural frame (3). The fretting fixture is moved to control the slip between the pad and the specimen. However, the displacement of the fixture will depend on the displacement of the hydraulic actuator and the compliance of the structural frame. This compliance will ensure that the slip cannot be controlled accurately. The only literature that mentions the accuracy of the slip that they can apply is *Magadu et. al.* [32], who are able to control the slip in the range of 15µm.

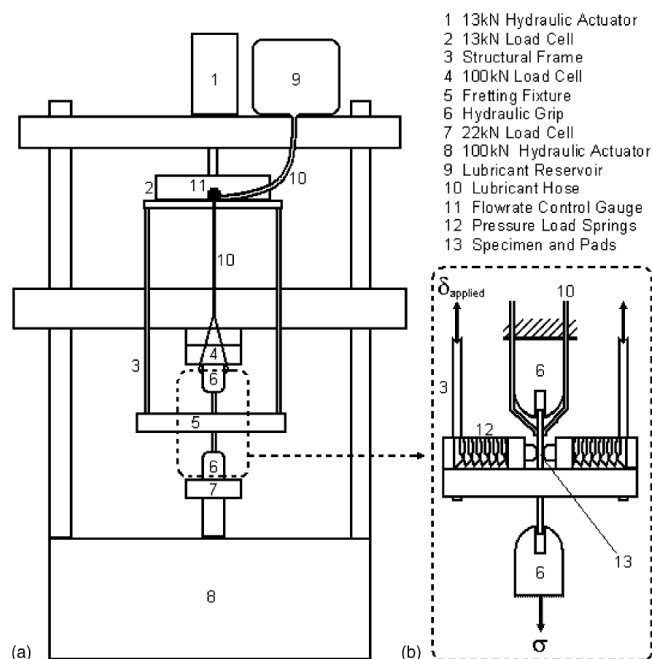


Figure 11. Schematic view of the test rig at Wright-Patterson AFB [33]

Table 2 gives an overview of five existing two actuators test rigs that are known to the authors, and lists the driving equipment for the fatigue force, normal force and slip. All the test rigs use a hydraulic actuator to apply the fatigue force. The slip in the test rigs is applied by a second hydraulic actuator. The difference between the listed test rigs is how the normal load is applied.

Table 2. Overview of some fretting fatigue test rigs based on two actuators

Research institute	Fatigue force	Normal force	Slip
Wright-Patterson AFB	Hydraulic actuator	Compliant springs	Hydraulic actuator and compliance test rig
University of Brasília	Hydraulic actuator	Hydraulic accumulator	Hydraulic actuator and compliance test rig
University of Oxford	Hydraulic actuator	Hydraulic actuator	Hydraulic actuator and compliance test rig
United Technologies Research Center	Hydraulic actuator	Hydraulic actuator	Hydraulic actuator and compliance test rig
University of Lyon	Hydraulic actuator	-	Hydraulic actuator and compliance test rig

## 5 CONCLUSION

A classification of fretting fatigue test rigs based on the properties of the test rigs is given in Figure 12. A first difference of test rigs is based on the specimens scale, full scale or coupon scale. Full scale test rigs are directly related to a real application, eight full scale rigs are listed in Table 1.

Further classification has been done for the coupon scale test rigs. Based on their capability to apply a slip  $s$ , tree categories are made. The first type, *one actuator test rig*, is not designed to control or influence the slip. The second type, *one actuator test rig with adjustable compliance*, can influence the slip in advance, but is not able to control the slip during the experiments. In both types of test rig, the slip is in phase with the fatigue force. The third and last type of coupon scale test rigs, *two actuators test rig*, can control the slip independently of the fatigue load. However, due to construction of the test rig, the slip cannot be applied accurately in the range of some micrometer, which is necessary to test fretting.

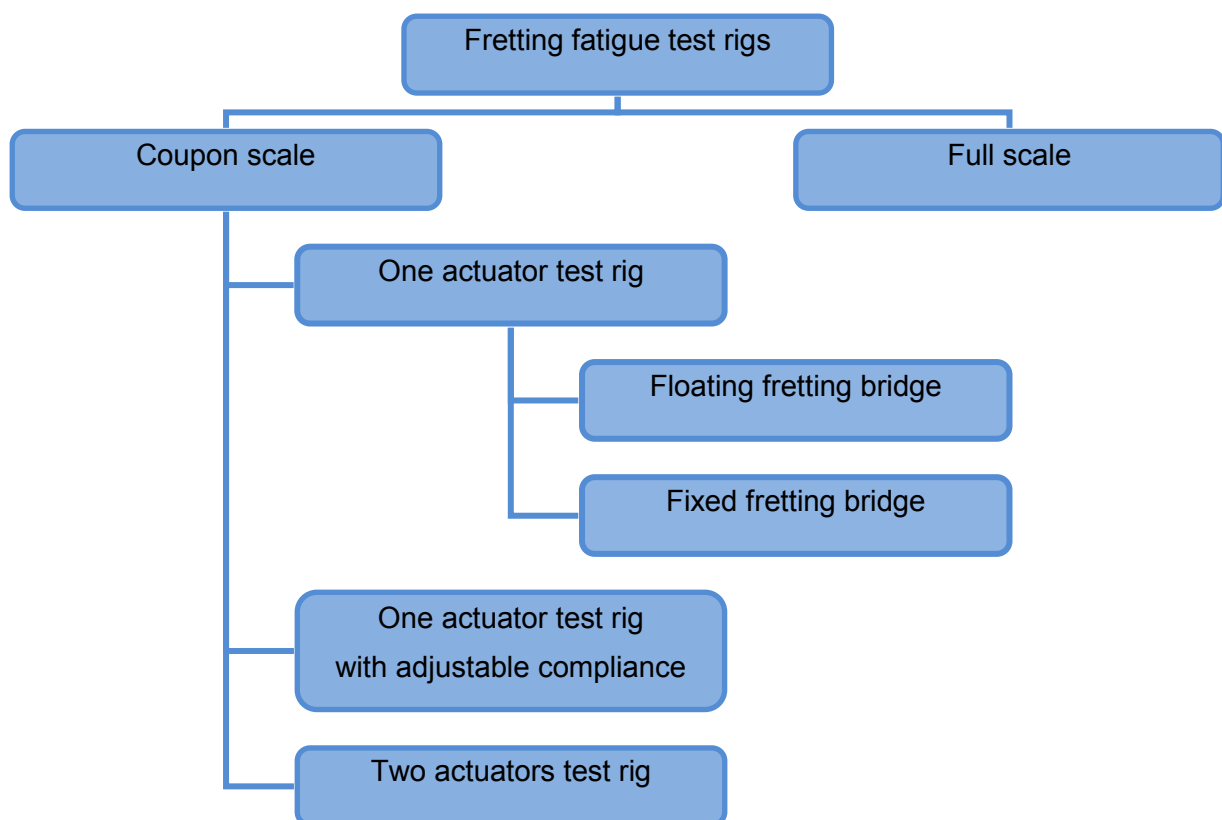


Figure 12. Classification of fretting fatigue test rigs.

## 6 NOMENCLATURE

d	relative movement of pad	$\mu\text{m}$
s	slip	$\mu\text{m}$
h	height fretting bridge	mm
$F_N$	normal force	N
$F_{\text{fat}}$	fatigue force	N
F	force	N

## 7 ACKNOWLEDGEMENTS

The authors would like to acknowledge the support of the IWT (Agency for Innovation by Science and Technology – n° SB-091510)

## 8 REFERENCES

- [1] M. H. Attia and R. B. Waterhouse, *Standardization of fretting fatigue test methods and equipment*, 1992.
- [2] D. A. Hills and D. Nowell, *Mechanics of fretting fatigue* vol. 30, 1994.
- [3] S. Wagle and H. Kato, "Ultrasonic wave intensity reflected from fretting fatigue cracks at bolt joints of aluminum alloy plates," *Ndt & E International*, vol. 42, pp. 690-695, Dec 2009.
- [4] D. Houghton, P. M. Wavish, E. J. Williams, and S. B. Leen, "Multiaxial fretting fatigue testing and prediction for splined couplings," *International Journal of Fatigue*, vol. 31, pp. 1805-1815, Nov-Dec 2009.
- [5] T. R. Hyde, S. B. Leen, and I. R. McColl, "A simplified fretting test methodology for complex shaft couplings," *Fatigue & Fracture of Engineering Materials & Structures*, vol. 28, pp. 1047-1067, Nov 2005.
- [6] S. B. Leen, T. H. Hyde, C. H. H. Ratsimba, E. J. Williams, and I. R. McColl, "An investigation of the fatigue and fretting performance of a representative aero-engine spline coupling," *Journal of Strain Analysis for Engineering Design*, vol. 37, pp. 565-583, Nov 2002.
- [7] L. Bertini, M. Beghini, C. Santus, and A. Baryshnikov, "Resonant test rigs for fatigue full scale testing of oil drill string connections," *International Journal of Fatigue*, vol. 30, pp. 978-988, 2008.
- [8] B. Alfredsson, "Fretting fatigue of a shrink-fit pin subjected to rotating bending: Experiments and simulations," *International Journal of Fatigue*, vol. 31, pp. 1559-1570, 2009.
- [9] R. Gutkin and B. Alfredsson, "Growth of fretting fatigue cracks in a shrink-fitted joint subjected to rotating bending," *Engineering Failure Analysis*, vol. 15, pp. 582-596, 2008.
- [10] T. Juuma, "Torsional fretting fatigue strength of a shrink-fitted shaft with a grooved hub," *Tribology International*, vol. 33, pp. 537-543, 2000.
- [11] D. H. Lee, S. J. Kwon, Y. S. Ham, and W. H. You, "Characterization of fretting damage in a press-fitted shaft below the fretting fatigue limit," in *Fatigue 2010*. vol. 2, P. Lukas, Ed. Amsterdam: Elsevier Science Bv, pp. 1945-1949.
- [12] M. L. Aggarwal, R. A. Khan, and V. P. Agrawal, "Effect of surface roughness on the fretting fatigue behaviour of EN45A spring steel," in *Proceedings of the Institution of Mechanical Engineers -- Part B -- Engineering Manufacture*. vol. 220: Professional Engineering Publishing, 2006, pp. 1325-1331.
- [13] P. J. Golden and T. Nicholas, "The effect of angle on dovetail fretting experiments in Ti-6Al-4V," *Fatigue & Fracture of Engineering Materials & Structures*, vol. 28, pp. 1169-1175, Dec 2005.
- [14] P. J. Golden and J. R. Calcaterra, "A fracture mechanics life prediction methodology applied to dovetail fretting," *Tribology International*, vol. 39, pp. 1172-1180, Oct 2006.
- [15] A. Kermanpur, H. S. Amin, S. Ziaei-Rad, N. Nourbakhshnia, and M. Mosaddeghfar, "Failure analysis of Ti6Al4V gas turbine compressor blades," *Engineering Failure Analysis*, vol. 15, pp. 1052-1064, Dec 2008.
- [16] C. R. F. Azevedo, A. M. D. Henriques, A. R. Pulino Filho, J. L. A. Ferreira, and J. A. Araújo, "Fretting fatigue in overhead conductors: Rig design and failure analysis of a Grosbeak aluminium cable steel reinforced conductor," *Engineering Failure Analysis*, vol. 16, pp. 136-151, 2009.
- [17] O. Plekhov, T. Pain-Luc, N. Saintier, S. Uvarov, and O. Naimark, "Fatigue crack initiation and growth in a 35CrMo4 steel investigated by infrared thermography," *Fatigue & Fracture of Engineering Materials & Structures*, vol. 28, pp. 169-178, Jan 2005.
- [18] D. Wagner, N. Ranc, C. Bathias, and P. C. Paris, "Fatigue crack initiation detection by an infrared thermography method," *Fatigue & Fracture of Engineering Materials & Structures*, vol. 33, pp. 12-21, Jan 2009.

- [19] W. Thomson, "On the dynamical theory of heat - with numerical results deduced from Mr. Joule's equivalent of a thermal unit and M. Regaut's observations on steam," *Royal Society of Edinburgh, Transactions of the Royal Society*, pp. 261–288, 1853.
- [20] S. Henkel, D. Holländer, M. Wünsche, H. Theilig, P. Hübner, H. Biermann, and S. Mehringer, "Crack observation methods, their application and simulation of curved fatigue crack growth," *Engineering Fracture Mechanics*, vol. 77, pp. 2077-2090.
- [21] B. Bruzek and E. Leidich, "Evaluation of crack growth at the weld interface between bronze and steel," *International Journal of Fatigue*, vol. 29, pp. 1827-1831, 2007/11//.
- [22] P. Cavaliere, A. D. Santis, F. Panella, and A. Squillace, "Thermoelasticity and CCD analysis of crack propagation in AA6082 friction stir welded joints," *International Journal of Fatigue*, vol. 31, pp. 385-392, 2009.
- [23] J. Hwang, J. Lee, and S. Kwon, "The application of a differential-type Hall sensors array to the nondestructive testing of express train wheels," *NDT & E International*, vol. 42, pp. 34-41, 2009.
- [24] K. K. Liu and M. R. Hill, "The effects of laser peening and shot peening on fretting fatigue in Ti-6Al-4V coupons," *Tribology International*, vol. 42, pp. 1250-1262, 2009.
- [25] R.B. Waterhouse, *Fretting Corrosion*. Oxford: Pergamon Press 1972.
- [26] K. Endo and H. Goto, "Initiation and propagation of fretting fatigue cracks," *Wear*, vol. 38, pp. 311-324, 1976.
- [27] R. Cortez, S. Mall, and J. R. Calcaterra, "Investigation of variable amplitude loading on fretting fatigue behavior of Ti-6Al-V," *International Journal of Fatigue*, vol. 21, pp. 709-717, Aug 1999.
- [28] S. Fouvry, K. Kubiak, A. M. Marechal, and J. M. Vernet, "Behaviour of shot peening combined with WC-Co HVOF coating under complex fretting wear and fretting fatigue loading conditions," *Surface & Coatings Technology*, vol. 201, pp. 4323-4328, 20 December 2006.
- [29] M. C. Gean and T. N. Farris, "Elevated temperature fretting fatigue of Ti-17 with surface treatments," *Tribology International*, vol. 42, pp. 1340-1345, Sep 2009.
- [30] Wittkowsky, Birch, Dominguez, and Suresh, "An apparatus for quantitative fretting testing," *Fatigue & Fracture of Engineering Materials & Structures*, vol. 22, pp. 307-320, 1999.
- [31] L. J. Fellows, D. Nowell, and D. A. Hills, "On the initiation of fretting fatigue cracks," *Wear*, vol. 205, pp. 120-129, 1997.
- [32] A. Mugadu, D. A. Hills, and D. Nowell, "Modifications to a fretting-fatigue testing apparatus based upon an analysis of contact stresses at complete and nearly complete contacts," *Wear*, vol. 252, pp. 475-483, 2002.
- [33] R. Magaziner, O. Jin, and S. Mall, "Slip regime explanation of observed size effects in fretting," *Wear*, vol. 257, pp. 190-197, 2004.

# DEGRADATION OF CARBON FIBER REINFORCED EPOXY COMPOSITES UNDER SLIDING IN AMBIENT AIR

H. Dhieb<sup>1</sup>, J.G. Buijnsters<sup>1</sup>, J.P. Celis<sup>1</sup>

<sup>1</sup> Katholieke Universiteit Leuven, Dept. MTM, Kasteelpark Arenberg 44, B3001 Leuven, Belgium

**Abstract** For many technical applications friction and wear are critical issues. Polymer composites reinforced by different components are currently widely used in various automotive and aerospace applications as well as structural engineering. However, the degradation of such composite materials in fretting contacts leads to change and loss of the material in use and the contact behaviour of these materials depend on the counter body, reinforcements, and operation time. In this paper, the wear and coefficient of friction of bulk epoxy and carbon fiber reinforced epoxy composite have been investigated under reciprocating sliding against alumina and stainless steel balls in ambient air. The effect of sliding direction with respect to the long and unidirectional carbon fibers has been studied. The coefficient of friction measured for the bulk epoxy against stainless steel and alumina is around 0.65, whereas the values measured for the epoxy reinforced with carbon fibers are significantly lower. It was found that sliding with stainless steel in a direction parallel to the fiber orientation results in a lower coefficient of friction than under sliding in anti parallel direction. The reduced wear volume of the composite is largely influenced by the carbon fiber reinforcement due the auto-protecting film formed on the contact area.

**Keywords** Carbon fiber reinforced epoxy composite, reciprocating sliding, friction and wear, material degradation

## 1 INTRODUCTION

Carbon fibre reinforced thermoset polymers are composite materials that are usually not applied for tribological purposes, although they have inherent great potential. When using such composites (e.g., in sports equipment, automotive, marine, and aerospace applications) one should bear in mind the sliding contact zone. Tribological properties of such materials in reciprocating contacts depend definitely on the properties of both matrix and reinforcement elements, and their interface. Research is thus needed to understand the degradation of the surface and subsurface of such materials. In that respect, tribochemical reactions and cracking occurring at the surface may be of large importance besides other mechanisms. Many researches have been done under sliding movement using the pin-on-disc system [1-5] as well as ring-on-block [6-8], ring-on-ring [9], disk-on-disk [10], wheel abrasion [11], face-contact-sliding [12], twin disc rings [13] and ball-on-prism [14] configurations to investigate the friction and wear behaviour and mechanisms like surface fatigue and abrasion of such kind of materials. As we mentioned before, the application fields of composite materials imply that contact vibrations can be the origin of material degradation. Up to now, research studies on the reciprocating movement of composites against different counter bodies have not been reported at all. In the multiple studies involving sliding movements, various reinforcements [15] and matrixes were investigated, such as short carbon fibres [4], glass fibres [2], graphite fillers [5], or a mix of different reinforcements [16]. The PEEK thermoplastic polymer is extensively used as a matrix, whereas the epoxy thermoset polymer is less well investigated. It is generally recognized that the most common types of wear of polymers are abrasion, adhesion and fatigue [17]. The carbon fibres increase the compressive strength and the creep resistance of the polymer matrix. It has been shown that the effect of fiber orientation is strongly dependent on the nominal contact pressure. It is evident that the abrasive wear behaviour of composites and specifically carbon fibre reinforced epoxy is complex and it is widely recognised that it needs more systematic investigation.

In this study, the friction and wear under reciprocating fretting contacts [18] were investigated. The wear tests were performed on a fretting/reciprocating sliding machine and the wear tracks on the samples and ball counter bodies were examined in detail. SEM and profilometry were employed to characterise the materials degradation. Our results provide valuable information of the evolution of the wear and the effect of fretting direction, and they help to understand the tribological behaviour of carbon fibre reinforced epoxy in contact with stainless steel and alumina counter bodies.

## 2 EXPERIMENTAL

The materials used in this study are bulk epoxy and carbon fiber reinforced epoxy. For the production of the bulk epoxy we have used standard DGEBA (Epikote 828) and Aradur 3486 (aliphatic polyamine) as a hardener (ratio epikote/hardener 100/30). For the carbon fiber reinforced samples, the resin was mixed, poured in a mould and cured at room temperature followed by an oven treatment. The cycle to cure those samples was 24 hrs at room temperature plus 8 hrs at 80°C. The reinforced epoxy sample contains 8 layers of unidirectional carbon fibre mixed with the epoxy to obtain 1 mm of thickness. The stack of pre-impregnated fibers is placed on a PTFE sheet on an aluminium base plate. It is covered with another PTFE layer and a 10-mm thick aluminium plate is put on top. The assembly is covered with bleeder fabric and a vacuum bag. Vacuum is applied through a tube that is incorporated in the sealing of the bag. A vacuum of 0.095 MPa is then applied for 15 min at room temperature to debulk. Following, the assembly is placed in an oven (while maintaining the vacuum) and heated to 90°C for 60 min and finally heated to 130°C for 90 min. After that, the assembly is taken out of the oven and the vacuum is released (Figure 1). The carbon fibre mixed with the epoxy is STS - 24K having the following specific properties: 24,000 filaments, 4,000 MPa tensile strength, 240 GPa tensile modulus, 1.7% elongation, 7- $\mu$ m diameter, and 1.75 g/cm<sup>3</sup> density. All the specimens were cut into the same dimension (20 x 20 mm<sup>2</sup>) for testing.

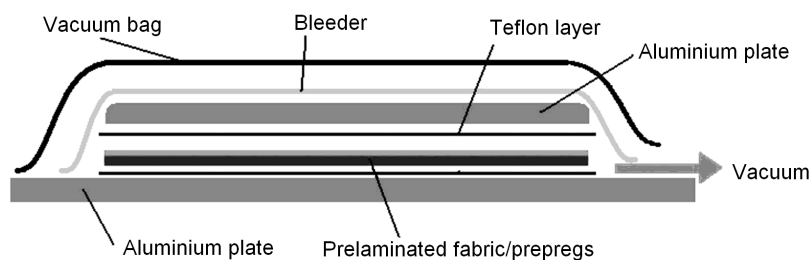


Figure 1. Carbon fibre reinforced epoxy's production set-up

Reciprocating tests were performed to investigate the coefficient of friction, the wear track and the wear volume lost. Stainless steel (AISI 316) and alumina balls, both with a diameter of 10 mm, were used as the counter body. All materials were degreased and cleaned prior to the fretting tests using acetone and ethanol. The reciprocating tests were carried out under ambient air conditions (temperature: 22 °C, relative humidity: 50%) and the total number of cycles varied from 10,000 to 200,000. A normal load of 9 N, a frequency of 3 Hz, and a displacement distance of 600  $\mu$ m were used for all tests. More details on the laboratory simulation of fretting and the applied test set-up can be found elsewhere [18]. Reciprocating sliding was analysed under dry condition through examining the wear tracks of the samples with scanning electron microscopy and a white light interferometer.

## 3 RESULTS AND DISCUSSION

SEM images of the worn bulk epoxy surfaces after 40,000 and 100,000 sliding cycles of sliding against the stainless steel ball are displayed in Figure 2. The relative directions of the sliding are indicated by the arrows in Figures 2a,b. The most damaged regions are situated near both edges of the wear tracks and they present many micro-cracks that appear perpendicular to the displacement (Figure 2d). These cracks are the result of the shear force during sliding. This fatigue wear causes micro-surface damage, which normally occurs at high temperatures. Another important aspect of the degradation process of the bulk epoxy material is the formation of debris in and around the wear tracks. Most of the debris is located outside the damaged area and, in particular, relatively large debris particles are observed at the very ends of the wear tracks. A specific form of debris or rollers is represented in Figure 2c. This form with different sizes is due to the rolling effect of the sample debris during sliding and probably consists of shear-deformed epoxy. It could reduce the shear stress, the coefficient of friction, and the contact temperature, which leads to a reduction of the damage. The formation of these rollers is considered an important process that plays a key role in enhancing the wear resistance. In general, the most recognized common types of wear of polymers are abrasion, adhesion, and fatigue [1].

SEM images of the wear tracks formed on the bulk epoxy after 40,000 and 100,000 sliding cycles against alumina balls are displayed in Figure 3. It is clear that the wear tracks differ from those produced with the stainless steel counter body (Figure 2). The material damage for the epoxy/alumina contact is significantly higher as can be concluded from the higher density of cracks and wear debris. In particular, the high number of rollers of accumulated epoxy in- and outside the wear track formed after 100,000 cycles (Figure 3b) is striking.

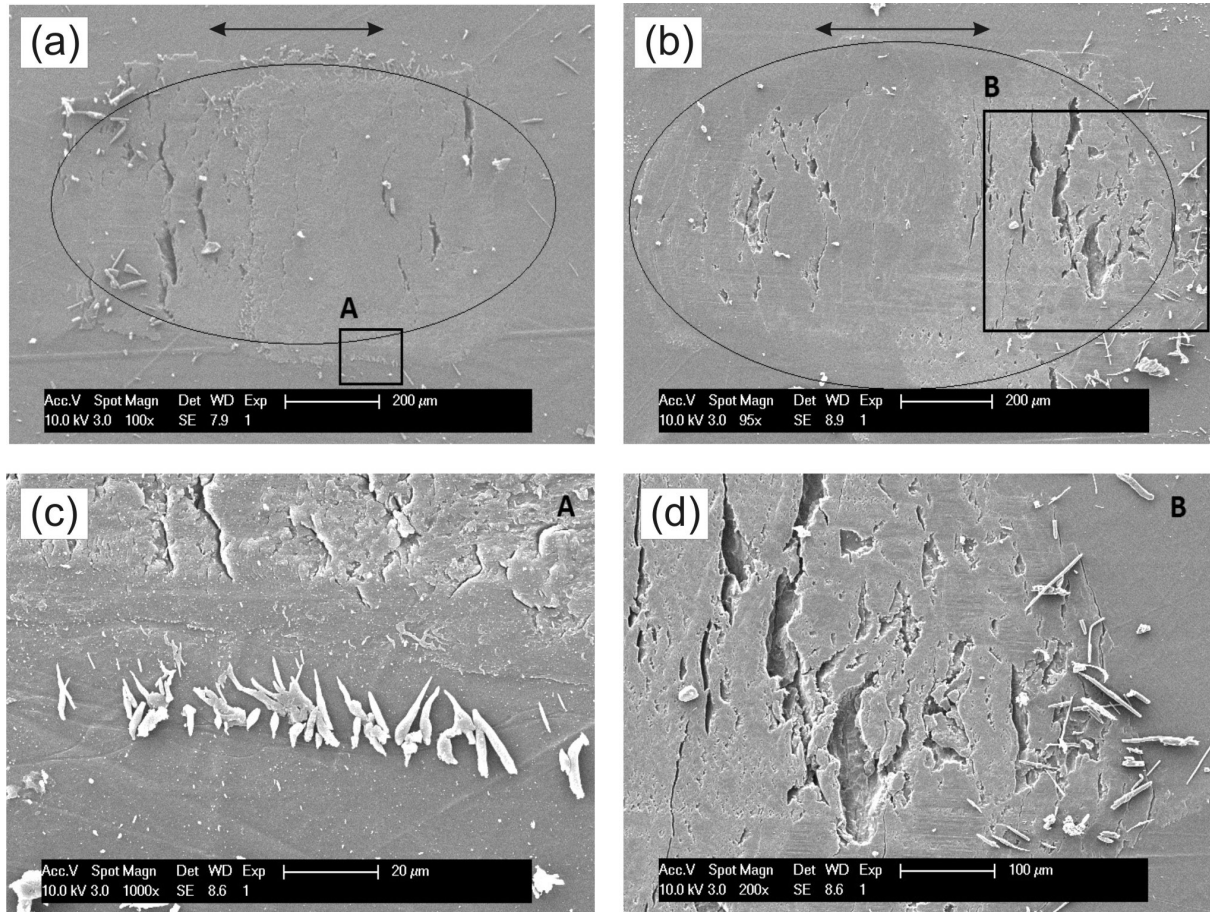


Figure 2. SEM images of the wear tracks of bulk epoxy sliding against stainless steel after (a) 40,000 cycles and (b) 100,000 cycles. (c) Zoom of debris outside the wear track (area A in Fig. 2a) and (d) zoom of cracks within the wear track (area B in Fig. 2b)

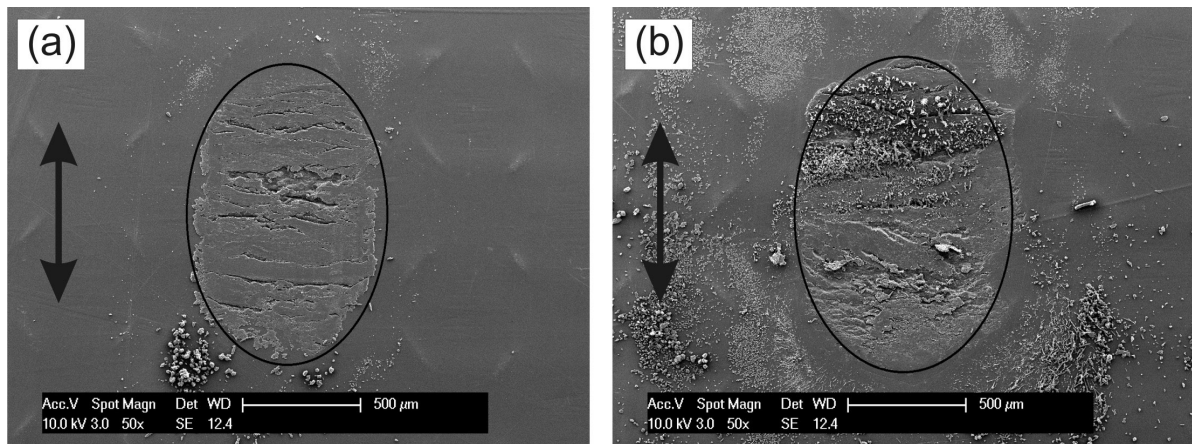


Figure 3. SEM images of the wear tracks of bulk epoxy against alumina after (a) 40,000 cycles and (b) 100,000 cycles

Figure 4 shows the wear tracks formed on the surfaces of the carbon fibre reinforced epoxy after 40,000 cycles against both the stainless steel and alumina counter faces. Tests have been worked out with a sliding direction parallel and anti-parallel to the orientation of the carbon fibre reinforcements (the latter orientation being indicated by the bundle of 4 parallel lines in Figure 4). Sliding against stainless steel (Figures 4a,b) results in a larger amount of wear debris (indicated by the black arrows) than for sliding against alumina (Figures 4c,d), irrespective of the sliding direction. Note that for the carbon fibre reinforced epoxy, the wear debris is mainly located at the circumference of the wear tracks, parallel to the direction of displacement. On the contrary, the wear debris is mostly located at the ends of the wear tracks for the bulk

epoxy (Figures 2 and 3). The composite displays a higher wear resistance against stainless steel when the fibres are oriented parallel to the sliding direction. For all cases, the matrix has been affected within the wear track, since individual fibers are exposed and, therefore, the direct contact area is decreased. This could result in a higher contact pressure and increased surface stress, which might affect the microstructure of the composite surface at the sliding contact as well.

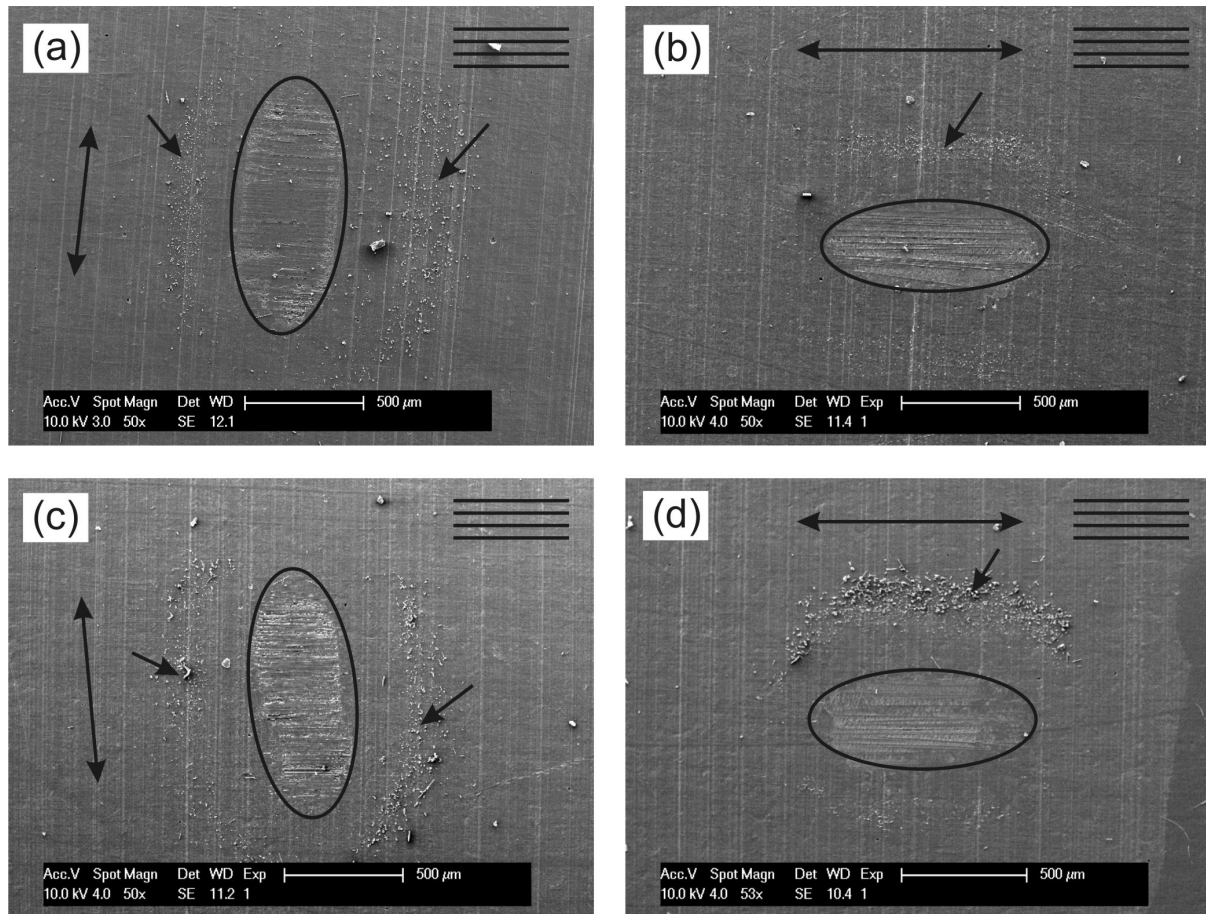


Figure 4. SEM images of the wear tracks of the carbon fibre reinforced epoxy after 40,000 cycles of reciprocated sliding against stainless steel with (a) anti-parallel and (b) parallel orientation, and alumina with (c) anti-parallel and (d) parallel orientation

The coefficient of friction for the different sliding contacts is presented in Figure 5. The coefficient of friction observed on the bulk epoxy is highest ( $0.65 \pm 0.03$ ) and is very similar and relatively constant throughout the whole reciprocating test of 10,000 cycles against either alumina or stainless steel. For the composite, the coefficient of friction strongly depends on the counter face material. It is high during the early stages of reciprocating sliding and reaches a value around 0.53 after about 500 to 1,000 cycles. On reciprocating sliding against alumina, the coefficient of friction is relatively high and it does not depend on the relative sliding direction. On the contrary, the relative sliding direction significantly affects the coefficient of friction recorded for sliding against the stainless steel counter face. It decreases to values as low as 0.25 after 10,000 sliding cycles with the sliding direction parallel to the orientation of the fibre reinforcements. In the case that the sliding is done anti-parallel to the fibre orientation, the coefficient of friction is somewhat higher. The coefficient of friction reaches lower steady-state values of  $0.27 \pm 0.05$  and  $0.11 \pm 0.01$  on sliding against stainless steel in the anti-parallel and parallel directions, respectively, after about 60,000 cycles (not shown). It is evident that the reciprocating sliding behaviour depends on the mechanical properties of, and possibly the tribochemical interaction with, the counter face material. Material originating from both the epoxy matrix and the fibre reinforcements might be transformed into a graphitic, low-friction tribolayer which will change the sliding contact behaviour. These kinds of lubricating surface layers are commonly observed for testing other soft and hard carbon-based materials, such as hydrogenated amorphous carbon [19]. In future work, micro-Raman spectroscopy and atomic force microscopy analysis will be employed to investigate the microstructural and topographical changes of the composite material at the sliding contacts as a function of test parameters and counter face material.

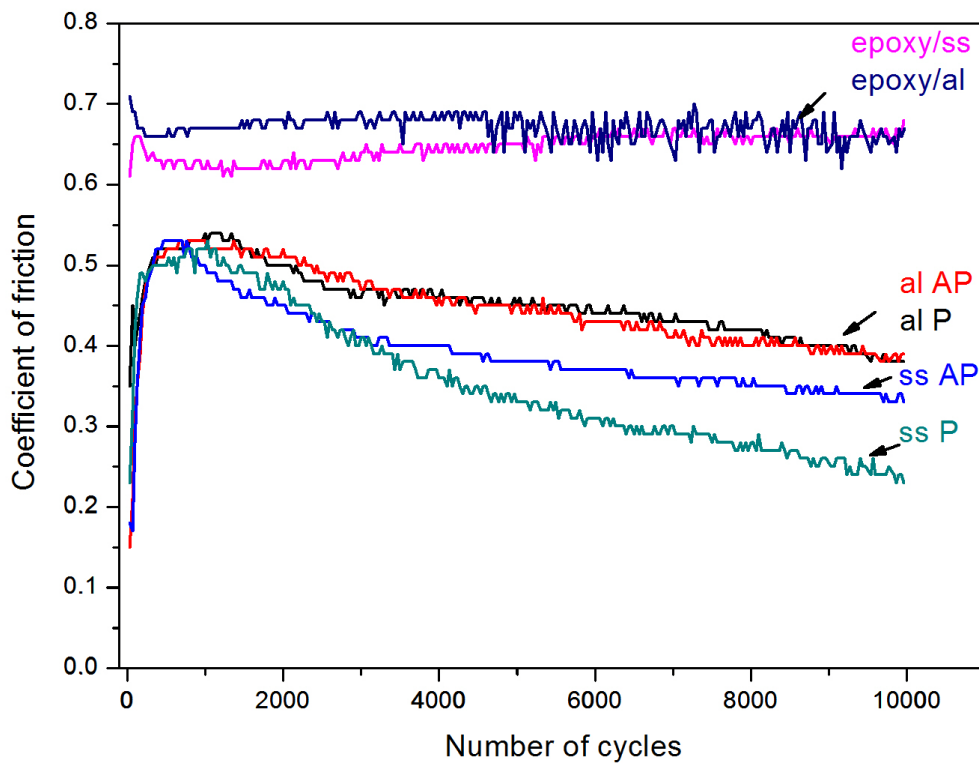


Figure 5. Representative evolution of the coefficients of friction recorded on bulk epoxy and carbon fibre reinforced epoxy sliding in parallel and anti parallel orientation against stainless steel and alumina counter bodies (al: alumina, ss: stainless steel, AP: anti parallel, P: parallel)

#### 4 CONCLUSIONS

The results of this study on bulk epoxy and carbon fiber reinforced epoxy composite against alumina and stainless steel balls in a reciprocating mode revealed some interesting phenomena related to friction and wear.

1. The carbon fiber reinforcements improve the tribological properties of the thermoset epoxy by reducing the coefficient of friction, the wear volume lost, and the wear track damage and debris formation.
2. The wear track of the carbon fiber reinforcement epoxy is smoother than the wear track of the bulk epoxy due to the formation of an auto-protecting surface layer which changes the surface contact behaviour.
3. The choice of counter face material has no significant effect on the coefficient of friction (i.e.,  $0.65 \pm 0.03$ ) for bulk epoxy material.
4. The choice of counter face material has an important effect on the coefficient of friction for the carbon fiber reinforced epoxy composite. It is always lower on sliding against stainless steel.
5. When alumina is used as the counter face, the sliding direction with respect to the orientation of the carbon fibers has no effect on the coefficient of friction. For stainless steel, the steady-state value of the coefficient of friction in parallel sliding direction ( $0.11 \pm 0.01$ ) is lower than in the anti-parallel direction ( $0.27 \pm 0.05$ ).

#### 5 ACKNOWLEDGEMENTS

The authors would like to thank the Flemish Science Foundation Flanders (FWO) for a fellowship (contract No. Senior- GP.007.10N) granted to JGB. This research is part of a research project done jointly by Universiteit Gent and Katholieke Universiteit Leuven and funded by the FWO-Flanders under contract n° F6/12-2008.

#### 6 REFERENCES

- [1] Davim, J.P., Cardoso, R., Effect of the reinforcement (carbon or glass fibres) on friction and wear behaviour of the PEEK against steel surface at long dry sliding, *Wear*, 266, 795-799, 2009.

- [2] Larsen, T., Andersen, T.L., Thorning, B., Horsewell, A., Vigild, M.E., Comparison of friction and wear for an epoxy resin reinforced by a glass or a carbon/aramid hybrid weave, *Wear*, 262, 1013-1020, 2007.
- [3] Sumer, M., Unal, H., Mimaroglu, A., Evaluation of tribological behaviour of PEEK and glass fibre reinforced PEEK composite under dry sliding and water lubricated conditions, *Wear*, 265, 1061-1065, 2008.
- [4] Chang, L., Zhang, Z., Tribological properties of epoxy nanocomposites. Part II. A combinative effect of short carbon fibre with nano-TiO<sub>2</sub>, *Wear*, 260, 869-878, 2006.
- [5] Suresha, B., Siddaramaiah, Kishore, Seetharamu, S., Kumaran, P.S., Investigations on the influence of graphite filler on dry sliding wear and abrasive wear behaviour of carbon fabric reinforced epoxy composites, *Wear*, 267, 1405-1414, 2009.
- [6] Jia, J.H., Zhou, H.D., Gao, S.Q., Chen, J.M., A comparative investigation of the friction and wear behavior of polyimide composites under dry sliding and water-lubricated condition, *Materials Science and Engineering A*, 356, 48-53, 2003.
- [7] Jia, J., Chen, J., Zhou, H., Hu, L., Chen, L., Comparative investigation on the wear and transfer behaviors of carbon fiber reinforced polymer composites under dry sliding and water lubrication, *Composites Science and Technology*, 65, 1139-1147, 2005.
- [8] Zhang, H., Zhang, Z., Friedrich, K., Effect of fiber length on the wear resistance of short carbon fiber reinforced epoxy composites, *Composite Science and Technology*, 67, 222-230, 2007.
- [9] Zhou, X.H., Sun, Y.S., Wang, W.S., Influences of carbon fabric/epoxy composites fabrication process on its friction and wear properties, *Journal of Materials Processing Technology*, 209, 4553-4557, 2009.
- [10] Lu, X., Wong, K.C., Wong, P.C., Mitchell, K.A.R., Cotter, J., Eadie, D.T., Surface characterization of polytetrafluoroethylene (PTFE) transfer films during rolling-sliding tribology tests using X-ray photoelectron spectroscopy, *Wear*, 261, 1155-1162, 2006.
- [11] Suresha, B., Chandramohan, G., Siddaramaiah, Samapthkumaran, P., Seetharamu, S., Three-body abrasive wear behaviour of carbon and glass fiber reinforced epoxy composites, *Materials Science and Engineering A*, 443, 285-291, 2007.
- [12] Yamamoto, Y., Hashimoto, M., Friction and wear of water lubricated PEEK and PPS sliding contacts Part 2. Composites with carbon or glass fibre, *Wear*, 257, 181-189, 2004.
- [13] Kukureka, S.N., Hooke, C.J., Rao, M., Liao, P., Chen, Y.K., The effect of fibre reinforcement on the friction and wear of polyamide 66 under dry rolling-sliding contact, *Tribology International*, 32, 107-116, 1999.
- [14] Werner, P., Altstadt, V., Jaskulka, R., Jacobs, O., Sandler, J.K.W., Shaffer, M.S.P., Windle, A.H., Tribological behaviour of carbon-nanofibre-reinforced poly(ether ether ketone), *Wear*, 257, 1006-1014, 2004.
- [15] Friedrich, K., Zhang, Z., Schlarb, A.K., Effects of various fillers on the sliding wear of polymer composites, *Composites Sliding and Technology*, 65, 2329-2343, 2005.
- [16] Zhang, G., Rasheva, Z., Schlarb, A.K., Friction and wear variations of short carbon fiber (SCF)/PTFE/graphite (10 vol.%) filled PEEK: Effects of fiber orientation and nominal contact pressure, *Wear*, 268, 893-899, 2010.
- [17] Myshkin, N.K., Petrokovets, M.I., Kovalev, A.V., Tribology of polymers: Adhesion, friction, wear and mass-transfer, *Tribology International*, 38, 910-921, 2005.
- [18] Mohrbacher, H., Celis, J.P., Roos, J.R., Laboratory testing of displacement and load induced fretting, *Tribology International*, 28(5), 269-278, 1995.
- [19] Buijnsters, J.G., Camero, M., Vázquez, L., Agulló-Rueda, F., Gago, R., Jiménez, I., Gómez-Aleixandre, C., Albella, J.M., *Diamond and Related Materials*, 19, 1093-1102, 2010.

## TURNING SPECIALITIES OF ZrO<sub>2</sub> CERAMICS

G. Fledrich, I. Pálincás, R. Keresztes, L. Zsidai, K. Petróczki

Institute for Mechanical Engineering Technology, Faculty of Mechanical Engineering,  
Szent István University, Gödöllő, Hungary  
www.geti.gek.szie.hu

**Abstract** In place of brittle ceramics used so far have appeared up-to-date so called tough ceramic materials resisting better against mechanical effects [6]. Such material is the zirconium-dioxide, too. The important advantage of hard-turning is the applicability of universal tool. Various outlines can be formed by a tool given. Machining ceramics in case of using traditional machining (turning, milling, drilling) requires special technological conditions (tools, machine-tools, technological parameters, etc.) which are developing presently [2]. We would like extending our research work in this course, too.

To clarify the machinability – turning – of ZrO<sub>2</sub> ceramics we developed a cutting force measurements for the applied CBN and PCD cutting tools. The forces were studied in the function of cutting speed and feed, the surfaces were analyzed by SEM and the cutting process was controlled by thermo-camera. The failure of cutting edges were also studied. The summarized results suggest the possible turning possibilities of ZrO<sub>2</sub> ceramics.

**Keywords** polycrystal diamond, cubic boron nitride, 3D-topography, heat ring, surface roughness, friction

### 1 INTRODUCTION

By industry development the demand is increasing for such materials to be applied at higher temperature beside at heavy physical and chemical load. The structural ceramics can have an important role exactly in this segment. The zirconium –dioxide is also such material [3]. The role of ceramics hard-machining is increasing presently [4]. The zirconium-dioxide deriving from its lower hardness and from other characteristics [1] is suitable to machine by tool having regular edge can become a potential material at piece or small- and medium series production. To ensure this it has to be known its cutting characteristics [5].

Our research work focusing a part of this in keeping with the recommendation of the company producing and developing zirconium-dioxide semi-finished products.

### 2 MATERIALS TESTED AND THEIR FORMS

The common properties of engineering ceramics are that they have outstanding physical and chemical characteristics in very high temperature range [7]. The ceramics tested by us have got high hardness (1250-1800 HV), because of this it can be cut by polycrystal diamond and cubic boron nitride tools. The material tested is zirconium-dioxide ceramics. The specimens used at turning tests were cylindrical, their diameters were 16 and 20 mm (Figure 1).



Figure 1. The zirconium-dioxide (Zn40) ceramics used at tests.

The ceramic properties tested [6].

	Dimension	
Material		ZN 40
Main component		ZrO <sub>2</sub> -MgO
Density	g/cm <sup>3</sup>	5,74
Bending strength	MPa	500
Compression strength	MPa	1600
Young modulus	GPa	210
Poisson - ratio		0,3
Vickers hardness HV0,5		1240
Thermal conductivity	W/mK	3
Linear coefficient of thermal expansion	10 <sup>-6</sup> K <sup>-1</sup>	10,2

Cutting tests

During turning the work-piece rotating movement is the main movement, the auxiliary movements are the turning tool movement in feeding and depth of cut directions. We have set the cutting speed by the work-piece revolution number.

To measure the axial and tangential components of the cutting force [8] we have used a measuring tool-head with strain gauge. We have used the Spider 8 measuring amplifier for the tests. We have connected four channels. We have coupled to the O-channel the revolution marker, we have measured the tangential and feeding forces on the 1 and 2 channels. The 3. channel served to measure the tool displacement, here we have connected an inductive displacement tele-transmitter restored by spring.

Heat affected zone tests.

The heat arising during cutting influences considerably the removal of stock process as well as influences very much the tool durability. We have also made shots with thermo-camera during cutting to study the heat affected zone formed.

**3 DISCUSSION**

During cutting we have measured the main and feeding forces affecting the tool. With the measuring-system capable to measure active forces-developed by us in the institute – we show some diagrams (Figure 2 and 3) in the followings. We present the main cutting force with thin line the feeding force with crossed line. We show the change of feed-rate with sections having circle end point.

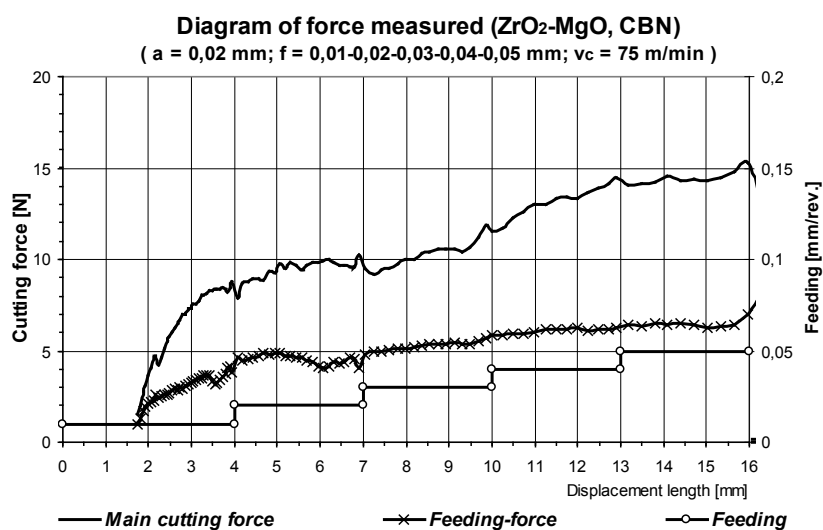


Figure 2. Diagrams of main cutting force and feeding force  
( $v_c = 75$  m/min.,  $a = 0,02$  mm;  $f = 0,01-0,02-0,03-0,04-0,05$  mm,  
ceramic: zirconiumdioxide, tool: CBN)

The zirconium-dioxide was cut with cubic boron nitride tool in the above. Figure 2. It can be seen that main cutting force and feeding force show increasing tendency with the increasing feed-rate.

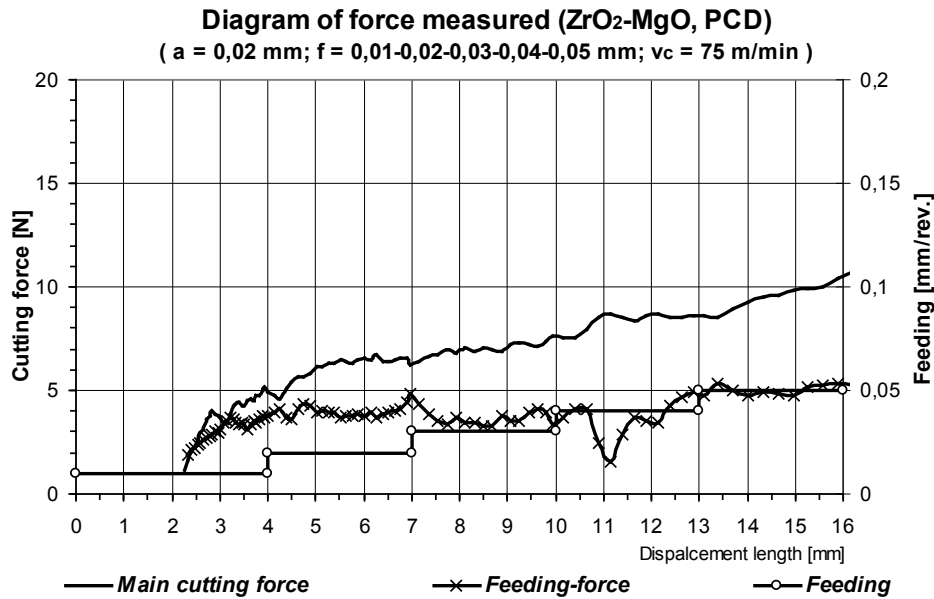


Figure 3. Diagrams of main cutting force and feeding force  
( $v_c = 75 \text{ m/min.}$ ,  $a = 0,02 \text{ mm}$ ;  $f = 0,01-0,02-0,03-0,04-0,05 \text{ mm}$ ,  
ceramic: zirconiumdioxide, tool: PCD)

In Figure 3 at the same conditions but cutting with polycrystal diamond resulted some different curves. The main cutting force increase is less rising in this case but it has got similar tendency, the feeding force following a short rising shows rather smaller increasing angular curve.

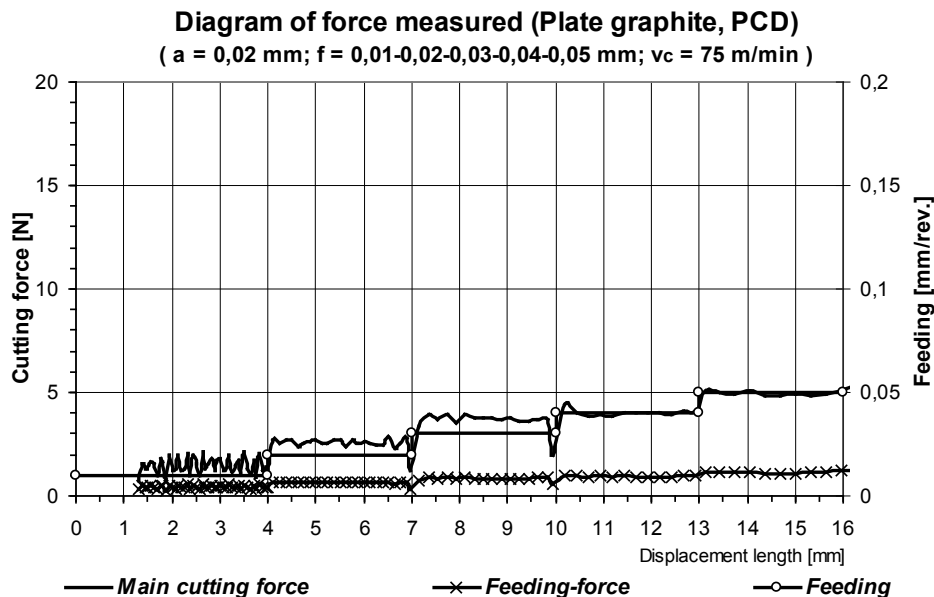


Figure 4. Diagrams of main cutting force and feeding force  
( $v_c = 75 \text{ m/min.}$ ,  $a = 0,02 \text{ mm}$ ;  $f = 0,01-0,02-0,03-0,04-0,05 \text{ mm}$ ,  
cast iron: plate graphite, tool: PCD)

We have cut plate graphite cast iron with PCD-tool similar with previous cutting data in case of Figure 4. We compared the known cast iron with zirconium-oxide unknown from turning standpoint is such way. The diagrams got are similar though with lower values. Difference can be experienced in the initial increasing

section. The change of forces are directly proportional. In case of ceramic the initial increase is steeper at both tool materials.

SEM photos of the cut surfaces can be seen in figure 5-7 in 2000 x magnification. The different surface effects of the CBN and PCD tools can be realized.

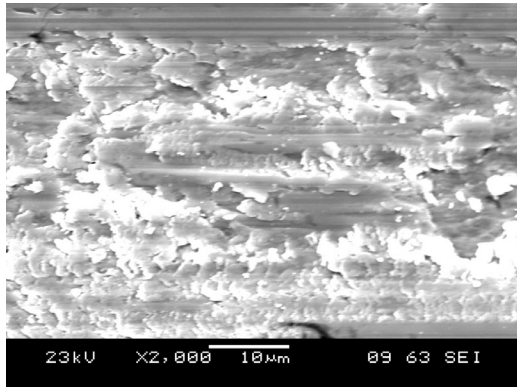


Fig. 5. Ceramic surface, machined with CBN.  
 $v_c=75$  m/min.,  $a = 0.02$  mm,  $f = 0.04$  mm/rev.  
 magnification x2000

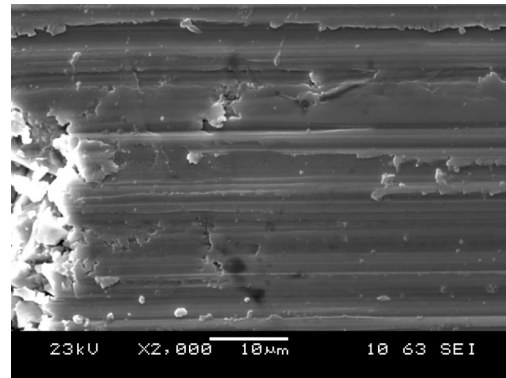


Fig. 6. Ceramic surface, machined with PCD.  
 $v_c=75$  m/min.,  $a = 0.02$  mm,  $f = 0.04$  mm/rev.  
 magnification x2000

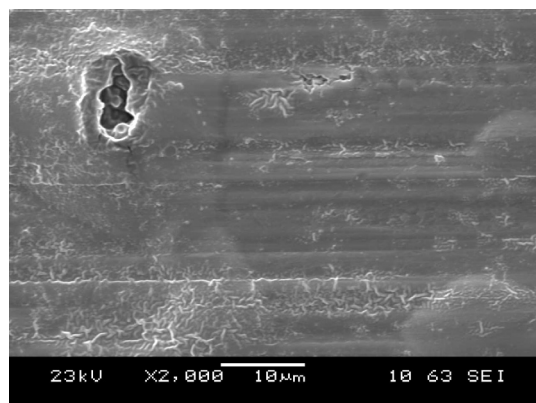


Figure 7. Grinded surface

The  $ZrO_2$  phase transformation tracks caused by mechanical effect can be seen in 2000x-magnification of the original surface grinded ( Figure 7.). In case of PCD-tool the rate of greater shell-like tears is similar to grinding. The amount of micro-cracks can be reduced based on the Figures. Less micro-cracks can be seen on surfaces turned compared to grinded in the Figures.

3D-topography pictures can be seen in Figure 8-10.

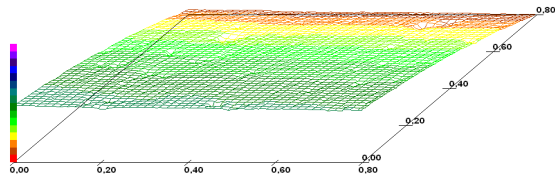


Figure 8. PCD tool turned  
 $v_c = 75$  m/min.,  $a = 0.02$  mm,  $f = 0.05$  mm/rev.

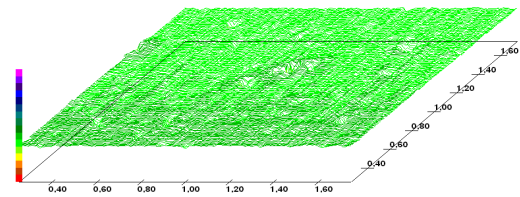


Figure 9. PCD tool turned  
 $v_c = 75$  m/min.,  $a = 0.02$  mm,  $f = 0.02$  mm/rev.

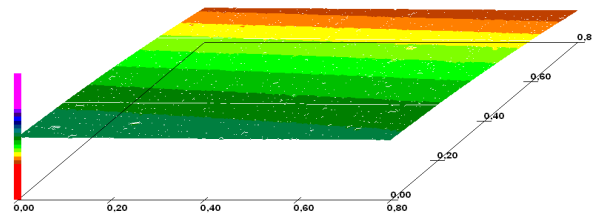


Figure 10. Grinded surface

In Figure 8-9. can be seen that the higher cutting speed ( $v_c = 75$  m/min.) resulted more favourable surface roughness than at lower cutting speed ( $v_c = 25$  m/min.).

From the point of applicability of cutting technology for ceramics, it is important to examine the friction behaviour of the different machined ceramic surfaces (grinded and machined surfaces with different cutting tools and technological settings) because the most common applications of such materials can be found among the slide bearing solutions.

In the dry friction tribological model system – steel pin on the machined ceramic ring surfaces - we have analyzed the friction force (coefficient) (Figure.11), and wear. Regarding the machining phenomena of the two tool materials, the PCD tool was selected to produce machined ceramic surfaces with different technological settings. In the tribological test system we have increased the normal load in three steps: starting with 50N ( $\sigma_{\text{Hertz-max}} = 391$  N, without wear) load the measurements were running for 5 minutes, then it was increased upto 100 N for 5 minutes and further 150N was applied to the seizure of samples.

Having S355 steel pin with grinded surface  $R_a 0,3$  on the different machined ceramic ring surfaces, we have found that the applied higher cutting speed ( $v_c = 75$  m/min) and lower feed ( $f = 0,01-0,02$  mm/ford) resulted lower friction between the steel and ceramic surface than it was with the original grinded ceramic surface. The original grinded ceramic surface has more but smaller sized “pits”, which can stick the steel worn particles, thus the friction process turns quickly to a steel/steel like contact having relatively high adhesion.

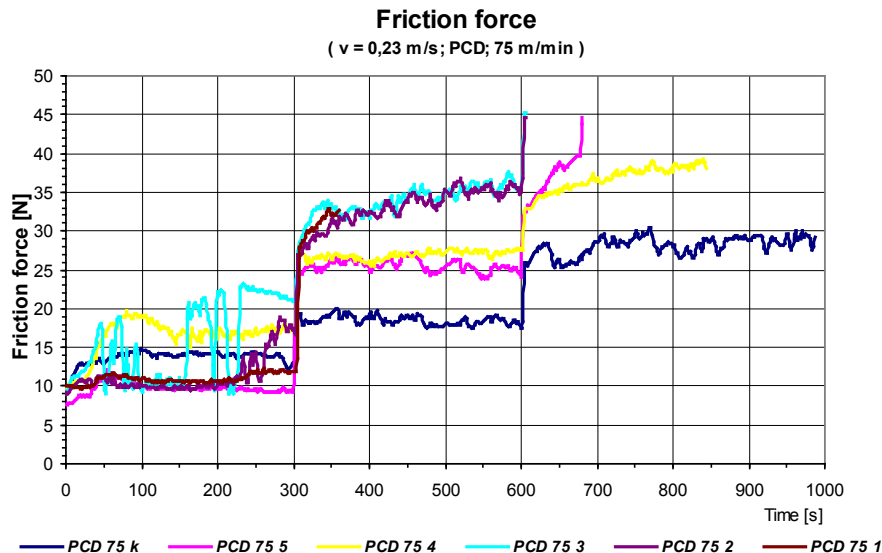


Figure 11. Friction force diagram  
(steel/grinded and machined ceramic surfaces)

### 3 CONCLUSIONS

Trend characterizing steel turning appears at using CBN turning tool, local cutting force maximum can be identified.

In case of PCD-tool at higher cutting speed more favourable surface roughness can be got, comparing to CBN-tool.

It is possible turning zirconium-dioxide semi-finished product. The condition of the starting surface has got definite importance how is possible to turn the surface point of view. The raw-product surface grinded has damaged the PCD-tools in case of all cutting parameters tested.

The hardness recommendation accepted for tools in technical literature (3-4 times higher hardness difference in favour for the tool) can not be used at raw-products grinded in case of zirconium-dioxide ceramics, Softer, 2 times higher hardness can be used.

Based on the tests can be established that given cutting speeds in case of increasing feedings at different tool-materials and workpiece materials show similar tendency, only in steepness is change. The phenomenon validity can be extended from the steel/carbide connection to the zirconium-dioxide/CBN friction, chip removal connection, too. The CBN and PCD-tools have resulted significantly different cutting forces. It can be stated that the cutting speed increase has resulted well measured increase in cutting force in case of diamond turning tool which has called forth significant heat evolution.

This is significantly unfavourable tribological connection.

The standard PCD –tool used did not result different surfaces regarding the surface roughness.

It can be stated on the basis of SEM photos that on the surfaces grinded phase transformations take place at microcracks. This results the higher cutting forces at turning in case of grinded surfaces. At surfaces turned phase transformation can not be seen. The surface cut by PCD –tool results favourable surface roughness.

We have found that it is possible to produce machined ceramic surface, which can offer better sliding properties against steel than the original grinded ceramic surface.

#### 4 NOMENCLATURE

a	depth of cut	mm
CBN	cubic boron nitride	-
f	feed	mm/rev
$F_c$	cutting force	N
HV	Vickers hardness	-
PCD	polycrystal diamond	-
$R_a$	surface roughness	$\mu\text{m}$
S355	structural steel	-
SEM	scanning electron microscop	-
$v_c$	cutting speed	m/min
$\text{ZrO}_2$	zirconium – dioxide (ceramic)	-
$\text{ZrO}_2\text{-MgO}$	zirconium – dioxide with magnesiumoxide (ceramic)	-
$\sigma_{\text{Hertz}}$	Hertzian stress	MPa

#### 5 REFERENCES

1. CURTIS, C.E.: Development of zirconia resistant to thermal shock. *J. Am. Ceram. Soc.* 30 180-196., 1947.
2. A. H. Fritz, G. Schulze (Hrsg.):Fertigungstechnik. 8. Aufl *Springer Verlag, Berlin* 279. o., 2007
3. H. SALMANG, H. SCHOLZE: Keramik, *Springer Verlag, Berlin*, 2007
4. SWAIN, M.V.; ROSE, L.R.F.: Strength Limitations of Transformation-Toughened Zirconia Alloys. *J. Am. Ceram. Soc.* 69 511-518., 1986.
5. MÉSZÁROS I., SZEPESI D.: Edzett acélok nagy pontosságú megmunkálása IV. *Gépgyártás XLVI.* évf. 4. sz. 29-33 old., 2006.
6. SZÉPVÖLGYI J.: Korszerű műszaki kerámiák, *Magyar Tudomány*, 4. sz. 7- 13 old., 1994.
7. CeramTec AG Innovative Ceramic Engineering Medical Products Division: *Broschüre* 2008
8. FARKAS G., KALÁCSKA G.:The effect of the different cutting tools on the micro-geometrical surface of engineering plastics. *Sustainable Construction & Design. 2010. Vol.1. p. 102-107.*

# IMPROVED HANDLING CHARACTERISTICS OF OFF-ROAD VEHICLES BY APPLYING ACTIVE CONTROL OF STEERING WHEEL TORQUE

J. Kis, L. Jánosi

Institute for Mechanical Engineering Technology, Faculty of Mechanical Engineering,  
Szent István University, Gödöllő, Hungary

**Abstract** Driving speed of agricultural mobile machines have been increased in the recent years, raising serious questions about vehicle handling characteristics considering the high center-of-gravity, multi-mass configuration and rear-wheel-steering of these vehicles. The next generation of steering systems on off-road vehicles will incorporate a steering column mechatronic subsystem which will generate tactile feedback for operator. This paper presents our research work to utilize steering wheel torque to improve off-road vehicle handling characteristics.

**Keywords** agricultural mobile machines, rear wheel steering, off-road vehicles, haptic feedback, handling

## 1 INTRODUCTION

To gain productivity the weight and speed of off-road vehicles, particularly agricultural mobile machines is continuously increasing. Operation on the field (or in some circumstances at least retain mobility) and have safe and comfortable vehicle handling on public roads have contra verse requirements on vehicle design [6] Good example for the contra verse requirements is the tire design and pressure of agricultural tires. The design of the steering system is also a result of a suboptimal compromise between road transport and field operation. Some vehicle have articulated steering Figure 1/b which allows only very limited speed, because of the steering kinematics. Self propelled forage harvester or combine harvesters are equipped with rear wheel steering, which have several benefits for the field operation in terms of header operation, and also in machine design in terms of body clearance. This concept has also serious drawbacks in terms of vehicle handling in transport mode, because of the stability problems with rear wheel steering.

In Steer-by-Wire (SBW) systems there is no mechanical or hydraulic link between hand wheel and road wheels. The hand wheel angle is measured by redundant rotary sensors, processed by an electric control unit to obtain road wheel angle, and calculates also the set value for the actuator control. [3] This concept enables decoupling the motion and the forces of the road wheels from the hand wheel motion and torque, which makes possible to implement various driver supporting control systems. Using an active force feedback device on hand wheel unit, the SBW system can provide various type of haptic signals for the operator.

In this paper we investigate the stability conditions for the heavy-duty agricultural vehicle with rear wheel steering. Considering of a SBW system with active force feedback, we present one method to emulate synthetic torque on hand wheel, which corresponds to the ideal aligning moment of a virtual front wheel steered vehicle. The paper will provide information about the calculation of the state feedback gain, and the stability of the modified system. The concept uses the state variables of the vehicle motion, which can be estimated on various ways, and these methods are not part of this paper.

## 2 INFLUENCE OF MODEL PARAMETERS ON STABILITY

### 2.1 Vehicle model

For the investigation of the rear wheel steering system, and the handling behavior of the heavy-duty agricultural mobile machine we use a linear single track model. The model and the resulting differential equations are derived in and analyzed for the front wheel steering system but there is limited information about pure rear wheel steering systems [2,4,7].

The model shown on Figure 1/a is body with 3 degree of freedom, whereby motion in z-plane is allowed. The differential equations for lateral and rotational motions are:

$$m(\dot{r} + \beta)v = F_{SR} + F_{SF} \quad \dot{r}l = a F_{SF} - b F_{SR}$$

The model is valid below 0.4g lateral acceleration, and below 5 degree lateral tire slip. We investigate the vehicle under these conditions in road transport mode. Assuming a constant velocity along x axis the state variables of the model can be reduced to the rotational speed  $r$  and slip angle  $\beta$ . There are two lateral tire forces acting on the chassis, whereby longitudinal components are ignored.

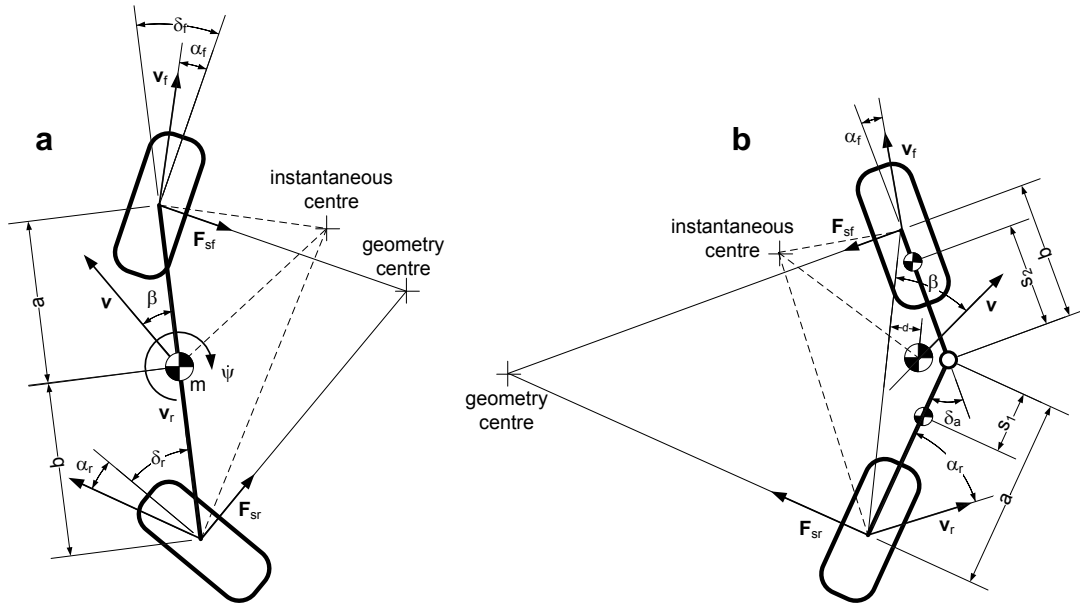


Figure 1: Linear single track models for front/rear and articulated steering

Because vehicle behavior is function of tire lateral force and moments, therefore model accuracy is significantly influenced by the accuracy of tire models. There are widely accepted nonlinear tire models, e.g. the “magic formula” to cover different aspects of tire-road interactions. Due to small lateral slip, in our analysis we use a simple linear relationship between the lateral force and lateral slip, and aligning moment and lateral slip. The constant parameter used in the model is the cornering stiffness ( $C_{F,R}$ ). In our analysis we don't consider the effect of suspension flexibility on lateral tire forces, and so the elasto-kinematic trail, because we investigate a system with no suspension and very rigid steering linkage (hydraulic cylinders acting directly on the wheel). We ignore the fact also that most of the mobile machines equipped with rear wheel steering are designed with large castor angle and mechanical trail. The model consider only the effect of the pneumatic trail on aligning moments.

$$F_{SF} = \alpha_F C_F \quad F_{SR} = \alpha_R C_R$$

Using Figure 1/a we can obtain the equations for the tire lateral slip angles from rotation and slip angle:

$$\alpha_F = \delta_F - \frac{a r}{v} - \beta \quad \alpha_R = \delta_R + \frac{b r}{v} - \beta$$

Combining the equation from above we can set up the differential equations for the single track model in the form where the derivatives of state variables are on the left hand side:

$$\dot{\beta} = \frac{(v \delta_R - \beta v + b r) C_R + (v \delta_F - \beta v - a r) C_F - m r v^2}{m v^2}$$

$$\dot{r} = - \frac{(b v \delta_R - b \beta v + b^2 r) C_R + (-a v \delta_F + a \beta v + a^2 r) C_F}{v l}$$

Using these equations we can obtain the state equations of the system in matrix form  $\dot{x} = A x + B u$ .

$$\begin{bmatrix} \dot{\beta} \\ \dot{r} \end{bmatrix} = \begin{bmatrix} -\frac{C_R + C_F}{m v} & \frac{b C_R - a C_F - m v^2}{m v^2} \\ \frac{b C_R - a C_F}{l} & -\frac{b^2 C_R + a^2 C_F}{v l} \end{bmatrix} \begin{bmatrix} \beta \\ r \end{bmatrix} + \begin{bmatrix} \frac{C_F}{m v} & \frac{C_R}{m v} \\ \frac{a C_F}{l} & -\frac{b C_R}{l} \end{bmatrix} \begin{bmatrix} \delta_F \\ \delta_R \end{bmatrix}$$

The system state variables are  $x_1=\beta$   $x_2=r$  and the inputs are the steering angles  $\delta_{F,R}$ . The differential equation system in matrix form.

## 2.2 Stability of rear wheel steered vehicles

Why pure rear wheel steering is not used in passenger cars has several reasons. One is that the tire aligning moment acts on opposite direction, and changes direction in transient situation. Therefore mechanical force feedback can not be realized. The other reason is, that because of the flexibility of the steering system and the suspension, an elasto-kinematic steering angle created, if lateral force is present. The opposite aligning moment increases this angle, therefore there is no stable operating point for this situation.

Driving the vehicle on steady-state path, the realized elasto-kinematic steering angle reduces the lateral force, which has an impact on the rear axle cornering stiffness and so on over steering behavior of the vehicle.

## 2.3 Modeling the mechanical steering system

To compare front- and rear wheel steering, the single track vehicle model is extended with the model of the steering system. In this model the inertia, viscous friction and (as an external disturbance) hand wheel steering torque are modeled, and it can be regarded as a feedback system. The differential equation used for the steering system model:

$$\ddot{\theta} J_S = -\tau_{VISC} + \tau_{EX} - \tau_{AL}$$

The viscous friction is proportional to the angular speed of the steering system. This parameter can be part of the control system and can represent a virtual friction to reduce system oscillations. The aligning moment depends only on the pneumatic trail and lateral force. The kinematic relationship between hand wheel angle and road wheels are modeled with fixed ratio  $i_S$ .

$$\tau_{VISC} = \dot{\theta} d_S \quad \tau_{AL} = \frac{t F_S}{i_S} \quad \delta_F = \theta i_S$$

Combining the equations from above, and expressing the angular acceleration the differential equation of the steering system:

$$\ddot{\theta} = - \frac{\dot{\theta} v i_S^2 d_S - v \tau_{EX} i_S^2 + (-\beta t v - a r t) C_F i_S + t \theta v C_F}{v i_S^2 J_S}$$

Substituting the rear wheel steering angle in the differential equations of the single track vehicle model:

$$\dot{\beta} = - \frac{(\beta v - b r) i_S C_R + ((\beta v + a r) C_F + m r v^2) i_S - \theta v C_F}{m v^2 i_S}$$

$$\dot{r} = \frac{(b \beta v - b^2 r) i_S C_R + (-a \beta v - a^2 r) C_F i_S + a \theta v C_F}{v i_S I}$$

This gives the state equations for the front wheel steering system in the following form:

$$\begin{bmatrix} \dot{\beta} \\ \dot{r} \\ \dot{\theta} \end{bmatrix} = \begin{bmatrix} -\frac{C_R}{mv} - \frac{C_F}{mv} & \frac{bC_R}{mv^2} - \frac{aC_F}{mv^2} - 1 & 0 & \frac{C_F}{i_S mv} \\ \frac{bC_R}{I} - \frac{aC_F}{I} & -\frac{b^2 C_R}{vI} - \frac{a^2 C_F}{vI} & 0 & \frac{aC_F}{i_S I} \\ \frac{tC_F}{i_S J_S} & \frac{atC_F}{v i_S J_S} & -\frac{d_S}{J_S} & -\frac{tC_F}{i_S^2 J_S} \end{bmatrix} \begin{bmatrix} \beta \\ r \\ \theta \end{bmatrix} + \begin{bmatrix} 0 \\ 0 \\ \frac{1}{J_S} \end{bmatrix} \tau$$

The state equation for the rear wheel steered vehicle :

$$\begin{bmatrix} \dot{\beta} \\ \dot{r} \\ \ddot{\theta} \end{bmatrix} = \begin{bmatrix} -\frac{C_R}{mv} - \frac{C_F}{mv} & \frac{bC_R}{mv^2} - \frac{aC_F}{mv^2} - 1 & 0 & \frac{C_R}{i_S mv} \\ \frac{bC_R}{I} - \frac{aC_F}{I} & -\frac{b^2 C_R}{vI} - \frac{a^2 C_F}{vI} & 0 & -\frac{bC_R}{i_S I} \\ \frac{tC_F}{i_S J_S} & \frac{atC_F}{vi_S J_S} & -\frac{d_S}{J_S} & -\frac{tC_R}{i_S^2 J_S} \end{bmatrix} \begin{bmatrix} \beta \\ r \\ \dot{\theta} \end{bmatrix} + \begin{bmatrix} 0 \\ 0 \\ \frac{1}{J_S} \end{bmatrix} \theta$$

The difference between the two system matrix (A) are marked bold. We can see the negative feedback of the hand wheel angle on the yaw rate change and the angular acceleration, which cases the system instability.

In the following section we will analyze the stability of this system in function of different model parameters using the eigenvalues of the system matrix. It is known, that at given model parameter set, if all the eigenvalues of A have negative real parts the system is stable. Figure 2 shows the eigenvalues of the front and rear wheel steered system at changing model parameters.

Figure 2/a shows the effect of increasing ground speed on the system pole locations. Both pole pairs are slowing down, and the damping of the system is not changing. Because of the increasing phase lag the system poles get positive real parts, and at 25 m/s the system get unstable. Figure 2/b shows the effect of decreasing rear tire cornering stiffness. The damping of the faster pole pair is decreasing, due to the decreasing aligning moment. The slower pole pair get into the unstable region because of the over steering.

It is obvious if the pneumatic trail get reduced (Figure 2/c) the controllability of the system decreases, which shows over damped poles at not changing viscous friction. If speed increases a higher viscous fraction value is required to keep vehicle stable (Figure 2/d). This is one of the concept used in the following section to modify vehicle handling characteristics. Figure 2/e shows the system poles of the rear wheel steered vehicle at increasing speed. It is obvious that this system is unstable, because it has one real poles in the right hand plane.

### 3 ALTERING VEHICLE HANDLING CHARACTERISTICS

In this paper a concept will be presented to alter vehicle handling using an active force feedback device which will generate virtual aligning moment for the operator to keep the vehicle stable. In the following model we assume, that the wheels are controlled by an electromechanical actuator, which can “keep-up” with the hand wheel dynamics, disregarding the control effort problem in this model.

#### 3.1 Haptic feedback modeling

The haptic feedback is realized with a brushless DC motor and toothed belt transmission. The haptic feedback contains inertia, viscous friction, a ratio to hand wheel and a ratio the steered wheels. The torques acting on the motor shaft are:

$$\ddot{\phi} J_H = i K_M + \frac{\tau_D}{i_H} - \dot{\phi} K_F$$

The generated back electromagnetic force (BEMF) using the motor parameters:

$$v_B = \dot{\phi} K_B$$

The electrical differential equation with impedances for the brushless dc motor:

$$v - v_B = i R + \frac{di}{dt} L$$

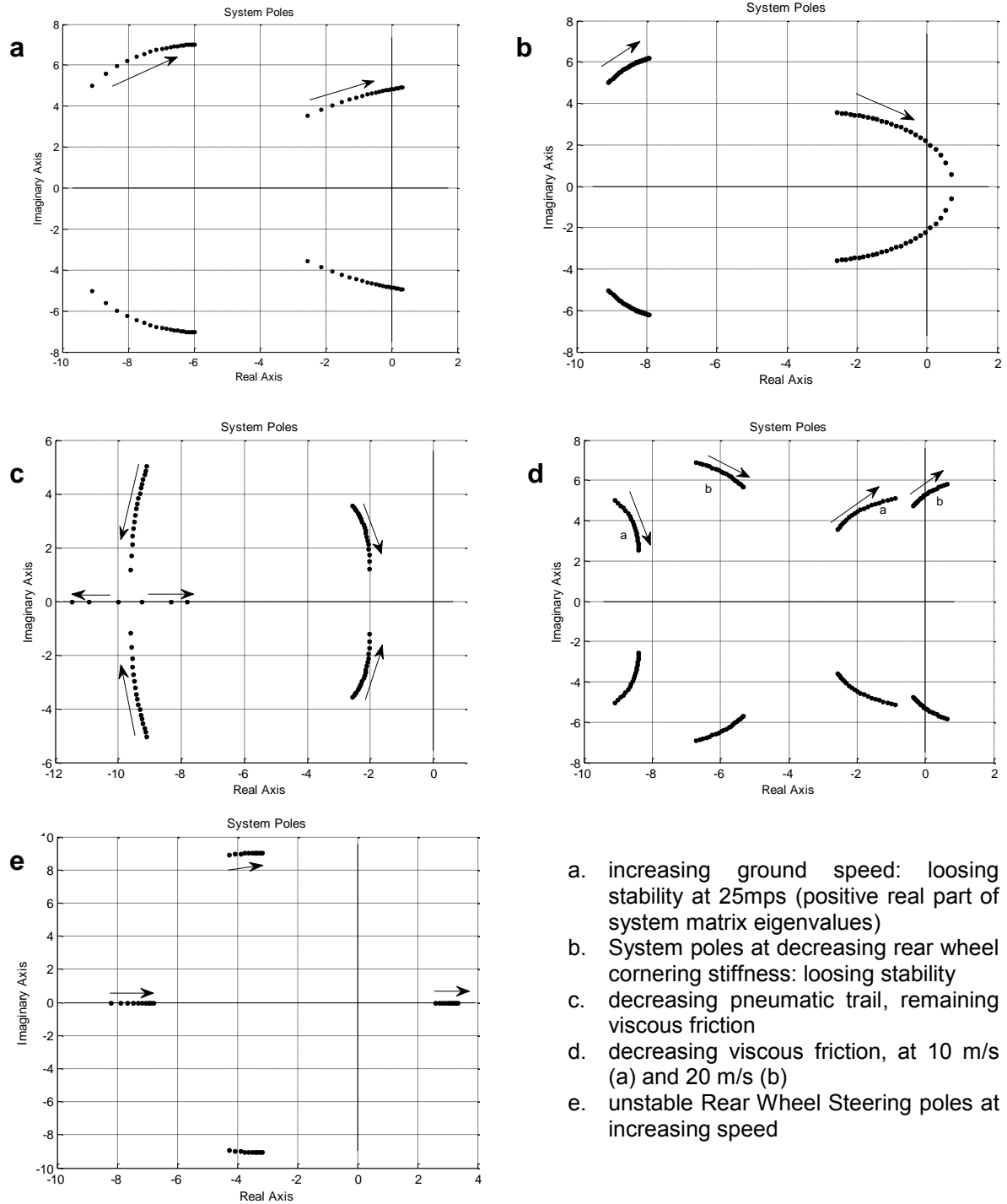


Figure 2: System pole locations with changing model parameters.

Combining the mechanical and dynamic differential equations we get for the haptic feedback:

$$\ddot{\phi} = \frac{i i_H K_M - \dot{\phi} K_F i_H + \tau_D}{J_H i_H}$$

$$\frac{di}{dt} = \frac{i R + \dot{\phi} K_E - v}{L}$$

The state equations for the haptic feedback device:

$$\begin{bmatrix} \dot{i} \\ \ddot{\phi} \\ \dot{\phi} \end{bmatrix} = \begin{bmatrix} -\frac{R}{L} & -\frac{K_B}{L} & 0 \\ \frac{K_M}{J_H R} & -\frac{K_F}{J_H} & 0 \\ 0 & 1 & 0 \end{bmatrix} \begin{bmatrix} i \\ \dot{\phi} \\ \phi \end{bmatrix} + \begin{bmatrix} \frac{1}{L} & 0 \\ 0 & \frac{1}{J_H i_H} \\ 0 & 0 \end{bmatrix} \begin{bmatrix} v \\ \tau_D \end{bmatrix}$$

Because of the limited dynamics of the whole system, in the simulation we ignore the inductive impedance. And therefore we can reduce the number of state variables to angular speed and angle position. The reduced state equations are:

$$\begin{bmatrix} \ddot{\phi} \\ \dot{\phi} \end{bmatrix} = \begin{bmatrix} -\frac{K_B K_M}{J_H R} - \frac{K_F}{J_H} & 0 \\ 1 & 0 \end{bmatrix} \begin{bmatrix} \dot{\phi} \\ \phi \end{bmatrix} + \begin{bmatrix} \frac{K_M}{J_H R} & \frac{1}{J_H i_H} \\ 0 & 0 \end{bmatrix} \begin{bmatrix} v \\ \tau_D \end{bmatrix}$$

The input of the haptic feedback is the armature voltage which is controlled by the state feedback controller.

### 3.2 Explicit calculation of feedback gain for emulated front wheel steering

The control system is shown on Figure 3. There are several methods for optimal design for the feedback gain, e.g. the concept of the linear quadratic regulator (LQR). It will give optimal solution for full state feedback at given transient and steady-state constrains.

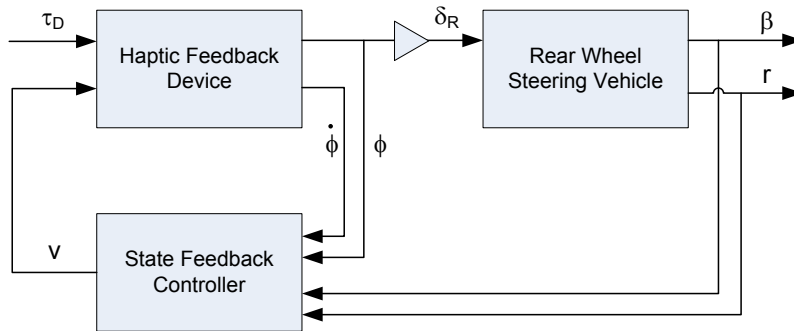


Figure 3: State feedback controller for rear wheel steered vehicle (without steering actuator dynamics) based on emulated front wheel aligning moment and added viscous friction

We follow a different method by explicit calculating the feedback gain, because we would like to emulate a steering system which has a front wheel steering. So the system may work suboptimal compared to the LQR design but gives the operator the feeling of an front wheel steered vehicle. The controller has to calculate the necessary voltage to create realistic steering torque:

$$v = \frac{\tau_M R + \phi K_B K_M}{K_M}$$

The emulated hand wheel torque can be calculated on the virtual aligning moment on the front wheels in case of an front wheel steering plus the synthetic viscous friction in the system, which is used to modify system dynamics.

$$\tau_M = \frac{\tau_{AL}}{i_H i_M} - \tau_{VISC}$$

Substituting into the electric equation we get for the voltage:

$$v = \frac{\left( \frac{t C_F \left( -\frac{\phi}{i_H i_S} - \frac{a r}{v} - \beta \right)}{i_H i_M} - \phi K_F \right) R + \phi K_B K_M}{K_M}$$

After modifying the equation above we can describe the four feedback gains for all four state variables:

$$v = \left\{ K_B - \frac{K_F R}{K_M} \right\} \phi - \left\{ \frac{t C_F R}{i_H^2 i_M i_S K_M} \right\} \dot{\phi} - \left\{ \frac{t C_F R}{i_H i_M K_M} \right\} \beta - \left\{ \frac{a t C_F R}{v i_H i_M K_M} \right\} r$$

Some parameters of the control system are given by vehicle geometry or electrical components (a, b, R, etc.) State variables are directly or indirectly measurable like yaw rate, lateral acceleration angular speed, angle. Other parameters like cornering stiffness must be estimated by online system identification algorithms. The results of the simulation on unit hand wheel torque is shown on figure 5.

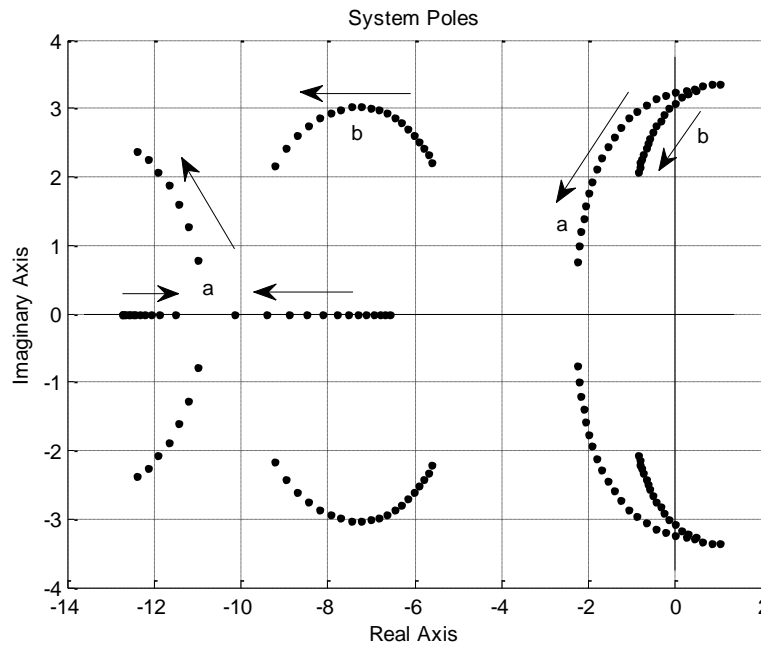


Figure 4: System poles of the single track model with haptic feedback at increasing damping at 10 mps(a) and 20 mps(b)

#### 4 CONCLUSIONS

Off-road vehicles with rear wheel steering have acceptable handling only at lower speeds. This behavior can be significantly improved by using active haptic feedback systems. The presented method of explicitly calculating the feedback gain to emulate front wheel steering feedback can improve the stability of system. This is shown on Figure 4, whereby the closed loop poles of the system with increasing damping at different ground speed are on the left hand plane, If appropriate synthetic viscous friction has been set.

Further work is necessary to consider a road wheel actuator with finite dynamics, analyze the effect of the state estimation and parameter identification. The presented concept must be also verified on real vehicle.

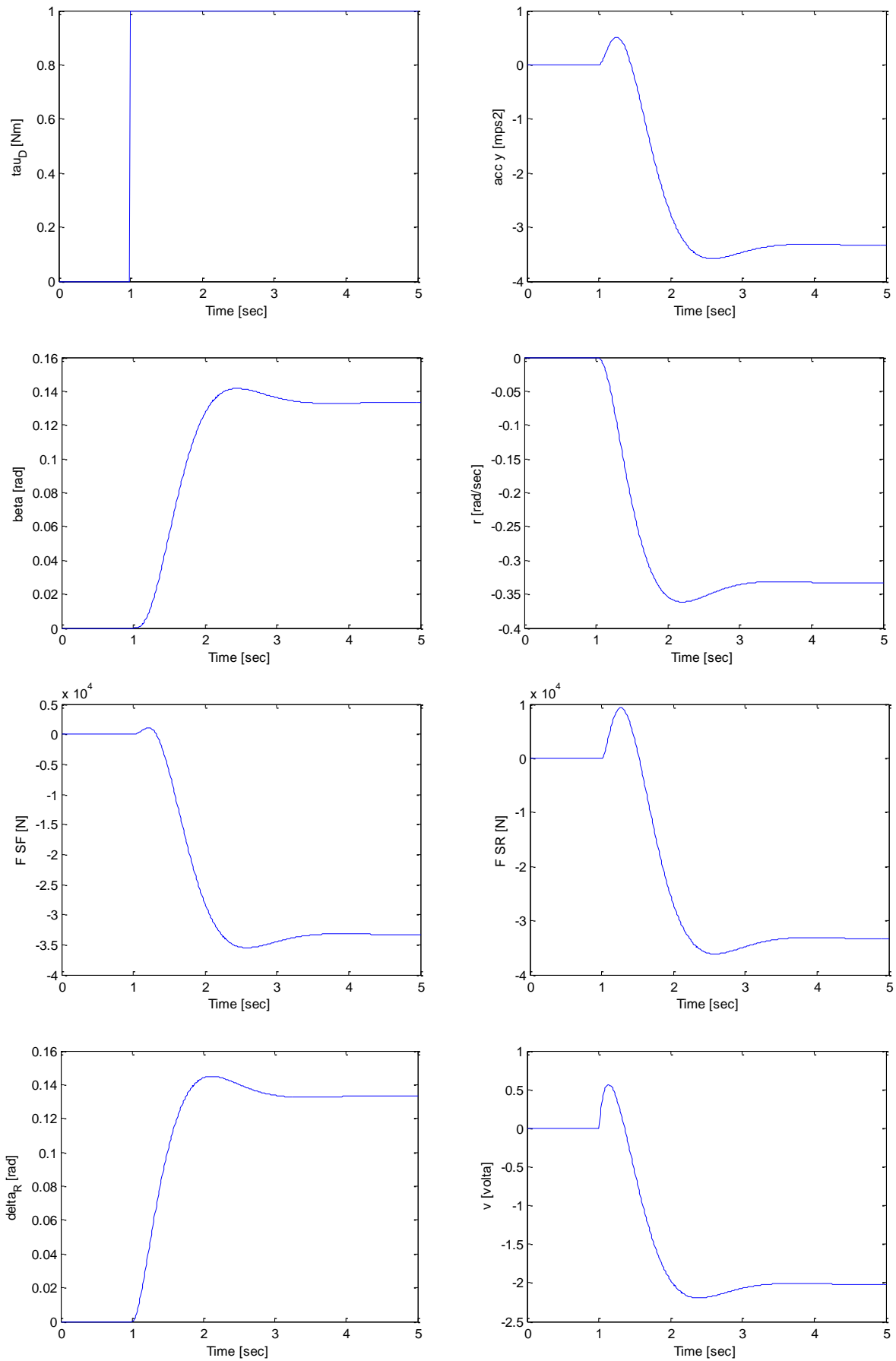


Figure 5: Step response of the system to unit hand wheel torque

## 5 NOMENCLATURE

$F_{SF,SR}$	Lateral tire force	N	$\tau$	Torque on hand wheel	Nm
$C_{F,R}$	Cornering stiffness	N/rad	$i_S$	Steering ratio	-
$\alpha_{F,R}$	Tire slip angle	rad	$\phi$	Motor shaft angle	rad
$\delta_{F,R}$	Steering angle	rad	$J_H$	HapticFeedback inertia	kgm <sup>2</sup>
a,b	acc to fig. 1	m	$i$	Current	A
r	Yaw rate	rad/s	$K_M$	Motor torque constant	Nm/A
$\beta$	Slip angle	rad	$K_F$	Viscous constant	Nms/rad
v	Ground speed	m/s	$K_B$	BEMF constant	Vs/rad
v	Voltage	V	R	Resistance	Ohm
I	Inertia	kgm <sup>2</sup>	$i_H$	Haptic ratio	-
$\theta$	Hand wheel angle	rad	$i_M$	Force feedback ratio	-
$J_S$	Steering inertia	kgm <sup>2</sup>			

## 6 REFERENCES

- [1] Janosi, L., & Kis, J. (2010.). Steer-by-Wire Technology: Steering wheel as new, intelligent Human Machine Interface. *VDI-MEG. Conference Agricultural Engineering*. (pp. 7-14.). Düsseldorf: VDI Verlag.
- [2] Jazar, R. N. (2008). *Vehicle Dynamics: Theory and Applications*. NY: Springer.
- [3] Kopetz, H. (1997). *Real-Time Systems: Design Principles for Distributed Embedded Applications*. London: Kluwer Academic Publishers.
- [4] Odenthal, D. (2002). How to make Steer-by-Wire Feel like Power Steering. 15th Triennial World Congress, Barcelona, Spain: Elsevier IFAC.
- [5] Switkes, J., Rossetter, E., & Gerdes, J. (2006). Handwheel Force feedback for Lanekeeping Assistance: Combined Dynamics and Stability. *Journal of Dynamic Systems Measurement and Control* v.128, no. 3, 532-542.
- [6] Tapazdi, T., Kis, J., & Laib, L. (1997). Does the Concept of the trailer with propelled Axles Experience a renaissance. *VDI-MEG. Conference Agricultural Engineering*. (pp. 55-58.). Düsseldorf.: VDI-Verlag.
- [7] Yih, P., & Gerdes, J. (2005, oct. 25). Modification of vehicle handling characteristics via steer-by-wire. *IEEE Transactions on Control Systems Technology*, pp. 965-976.

# DEVELOPMENT ENVIRONMENT FOR HAPTIC FEEDBACK DEVICE ON MOBILE AGRICULTURAL EQUIPMENT

L. Jánosi, J. Kis

Institute for Mechanical Engineering Technology, Faculty of Mechanical Engineering,  
Szent István University, Gödöllő, Hungary  
www.geti.gek.szie.hu

**Abstract** The steering wheel equipped with a tactile feedback is a human machine interface (HMI), capable to present sophisticated feedback information for the operator. Haptic stimulation is superior in interpretation speed by humans compared to audio-visual information. In this paper we present the concept of haptic feedback on vehicle and the ongoing research activities at the Department of Mechatronics to develop flexible technology to retrofit production machines with steer-by-wire capability to collect data representing the interactions in different application context (road and field modes).

**Keywords** haptic feedback, steering wheel, off-road vehicles

## 1 INTRODUCTION

In the last decade numerous scientific results has been presented to the engineering community in the topic of Steer-by-Wire technology (SBW). Despite the fact that the more complex mechatronics providing the by-wire functionality raises several safety related questions, also open exciting new opportunities for off-road vehicles not existing before.

The topic SBW can be discussed in numerous aspects: For example the advanced sensor/actuator components, the administrative regulation of by-wire systems, the failure-tolerant communication to interconnect components and the redundant system design are all large topics alone [1], [2]. We would like to focus in this presentation on the new, exciting functions, which could be realized by the Human-Machine-Interfaces (HMI) of the SBW systems.

Driving speed of agricultural mobile machines have been increased in the recent years, raising serious questions about vehicle handling characteristics considering the high center-of-gravity, multi-mass configuration and rear-wheel-steering of these vehicles. The next generation of steering systems on off-road vehicles will incorporate a steering column mechatronic subsystem which will generate tactile feedback for operator.

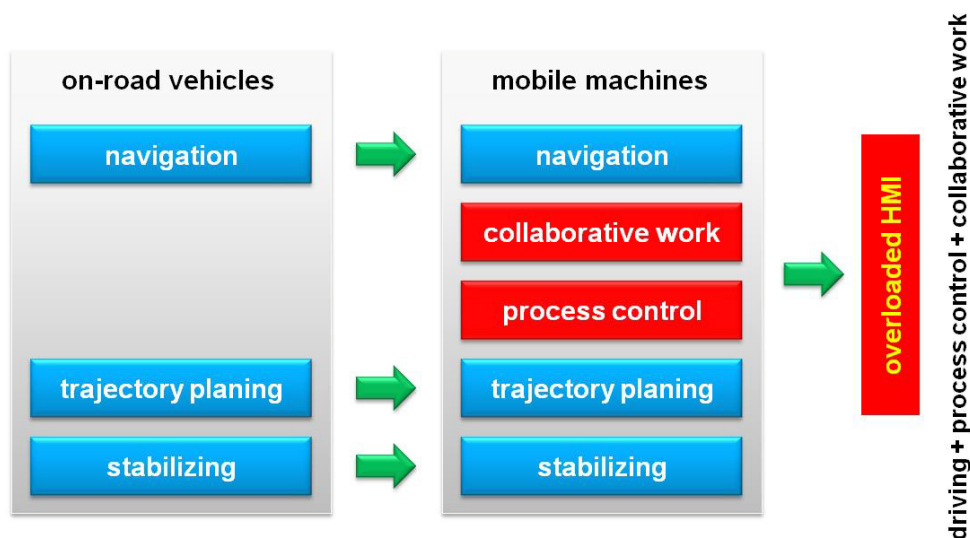


Figure 1. Operator's Control Functions: the „5 level model”

The steering wheel and its force-feedback actuator should be recognized as a new operator interface which enables the representation of feedback information on a new way.

Considering the “operator – steering – vehicle” as a closed loop control system, quality of the control system performance significantly can be improved or degraded by the quality of the steering wheel feedback [5]. The force or pressure sensed by the human hand – to so called haptic stimulus - get a significantly faster interpretation in our brain compared to the acoustic or visual information.

The HMI's of today's agricultural equipment are based mostly on visual information and some acoustic warning signals. These channels are overloaded and a new signal representation could be very useful to unload these channels. There are several HMI devices in the cockpit, where an intelligent feedback signal could be used: hydraulic levers with force feedback, or speed handles with traction feedback, etc.

## 2 5 LEVEL MODEL OF OPERATOR ASSISTANCE SYSTEMS IN AGRICULTURAL EQUIPMENT

The haptic feedback signals of the vehicle steering should be analyzed as part of the 'big picture', as sub domain of the Operator Assistance System in agricultural mobile equipment. Analogy with passenger car exist, considering the Driver Assistance Systems (Fahrer Assistanz Systeme - FAS).

In passenger cars the functions of supporting electronics can be linked to hierarchy levels of driver's controlling functions: navigation, trajectory selection and vehicle stabilizing [3]. The navigation systems are on the topmost level, helping to locate the vehicle and selecting optimal route. Recent advance in automotive electronic systems provide support for the driver to keep vehicle inside the lane, and to keep safe distance in busy traffic. Stabilizing of the vehicle needs the shortest response time from the driver, and this is very well supported today by electronic systems in the car. (advertised with acronyms like ABS, ESP, ASR, etc.)

Using this analogy, similar hierarchy levels can be defined on agricultural mobile equipment also Figure 1. These levels should be extended with two more hierarchy levels compared to passenger car, which are unique on mobile equipment: Collaborative task execution and process control. Collaborative task execution is very common on field work, whereby operators must synchronize the motion and processes of several machines (e.g. Forage Harvester + Transport Equipment). In the collaborative field maneuvers safety is extremely critical to avoid equipment damage or serious injuries. As we know, there are no product features or electronic systems available to support operator in these functions.

The majority of the mobile agricultural equipments are “rolling factories”, whereby the complex processes have to be controlled: settings must be changed according to changing field conditions, to achieve the requested product quality and equipment productivity. These processes are also supported some by electronic systems, mostly by visualizing process key figures or reloading preset values of machine settings. Navigation task on mobile equipment is supported by GPS based precision farming systems. The trajectory decision and speed control are also supported by GPS based automatic steering, which functions are state-of-the-art on today's production machines.

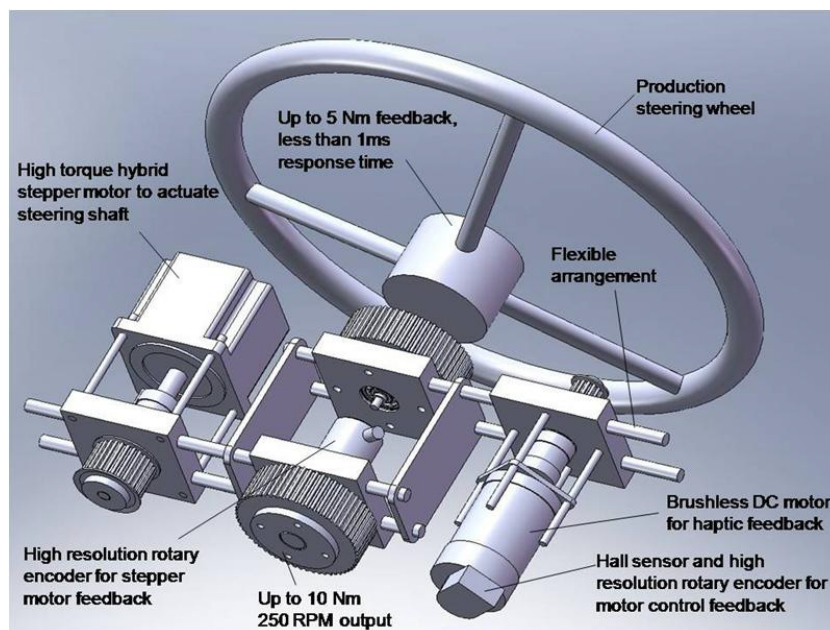


Figure 2. Haptic feedback signal testing equipment

The vehicle stability and controllability gets even more important. Increasing productivity means often higher transport speed and higher vehicle weight on public roads. We should consider the fact, that these vehicles will have higher center of gravity, low lateral stiffness of tires (terra) and no real suspension, even some have rear-wheel steering. This represents a rising risk, which can be significantly reduced by electronic systems, supporting the operator in stabilizing the vehicle. The numerous complex controlling task requires new information channels to be established, in order to provide safe way to feed information to the operator. Haptic feedback signals of the steering system regarded as one of this opportunities.

### 3 HAPTIC FEEDBACK RESEARCH METHODS AND TOOLS

Flexible research platform was designed to analyze the human-machine interaction and the vehicle dynamics, in accordance with the above mentioned physical and artificial feedback signals. The toolset can be placed on any kind of vehicle, with or without power steering.

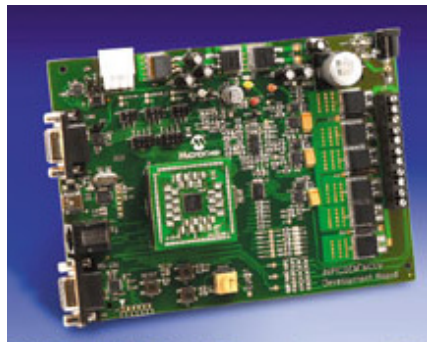


Figure 3. The dsPICDEM™ MCLV Development Board

The Figure 2 is showing the schematic of the tool used in the HMI experiments. The steering wheel position and driving torque is controlled by a brushless dc motor (BLDC) and timing belt transmission which is free from backlash. The four quadrant power electronics servo system (Figure 3 and Figure 4) incorporates the experimental feedback logic software.

The steering shaft is driven also by a high torque servo with timing belt. The high torque is required because also vehicles with no hydraulic support are going to be analyzed.

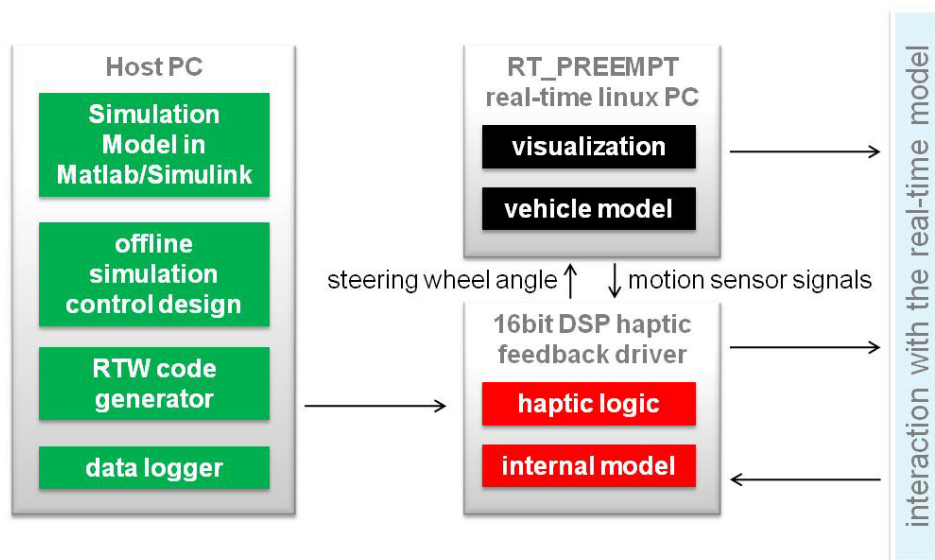


Figure 4. Human-in-the-Loop simulation tool chain

The motion of the steering wheel and the steering shaft are independent, therefore ratio, torque and timing could be programmed according to the analyzed effect. In case of locked clutch in the transmission, makes the ratio between steering wheel and steering shaft fixed and experiments with superposition torque control can be executed.

#### 4 FEEDBACK SIGNALS REPRESENTED BY THE HUMAN MACHINE INTERFACE

As mentioned in the previous section, the steering wheel regarded as a Human Machine Interface, can present several signal types to the operator. Let us overview first the signal types and their possible use in control of agricultural mobile machines.

Some of the possible emulated signals are of physical nature, and can be derived from the tire-soil/road interaction or vehicle dynamics. Some others are artificial feedback signals, like warnings or guiding signals. Physical or artificial feedbacks are programmable, and can be activated or suppressed dependent on the work-environment context, driving situation or user preferences.

##### 4.1 Emulated aligning moment and tire side forces

It has been proven [4], that intentional modification of the steering wheel torque has a positive impact on vehicle stability. State-of-the-art control technology used extensively in driver assistance systems like ESP [7], which is able to estimate state variables of vehicle motion, using signal processing algorithms (based on Kalman filtering), and set of low-cost sensors (wheels speed, lateral acceleration). This state information derived from the internal model can be used to calculate simulated aligning moment of the wheels.

This information of vehicle dynamics fed to the operator by emulating with the steering wheel haptic feedback (Illustrated in Example 1). Aligning moment can be also decreasing if wheel slip increases; this gives information about front wheel traction.

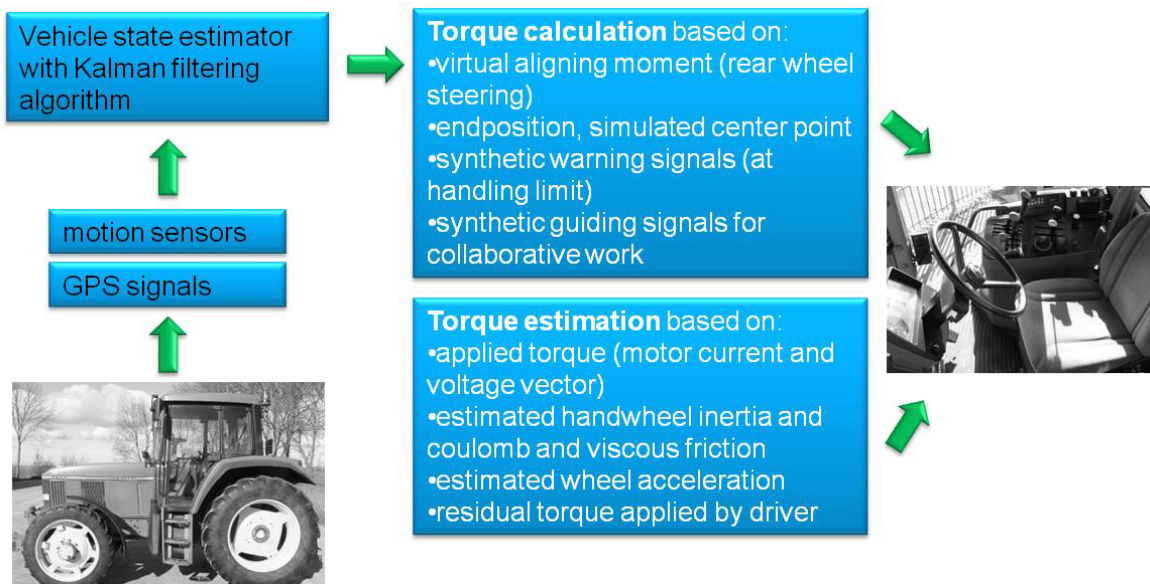


Figure 5. Control concept for Haptic Feedback

In certain operational context it is advantageous; if operator is able to realize if the turning torque of the wheel is rapidly increasing. In case of ploughing, guiding vehicle in furrow, or hitting an object, lateral forces on tire are transmitted to the steering wheel, and are interpreted by the operator as guiding or warning signals.

Off-road vehicles using hydrostatic steering lacks on steering feedback, which have a negative impact on vehicle handling, especially at higher speeds. An active steering feedback have an advantage, that only positive effects are emulated which can improve response time and quality, cornering predictability, center point feeling and reduce overshooting and unwanted steering torque oscillations. Feeling of the applied steering torque and or aligning moment support the operator to control vehicle in turning (Figure 5). This is one the most important haptic information on the steering wheel, which should be emulated by the active force feedback device. The aligning moment is present until steering wheel and the wheels get back to a neutral position, which is very useful (and safe) for vehicles, which have hard to see rear wheels. The emulated steering provides information about traction conditions, side forces, friction coefficients or slip. If the driver gets closer to traction limit the emulated aligning torque decreases.

##### 4.2 Warning and guiding signals

Warning signals are of great importance, because haptic information is realized significantly faster than audio or visual signals. Collision avoidance or other operator actions requiring fast response should be placed on steering wheel actuator, for example as vibration. This could be combined with guiding signals, which gives the operator a proposed direction of safe steering wheel motion.

Guiding signals offers several application possibilities (see application on passenger cars [6]): proposed driving direction based on GPS position, or local sensors. The driver can override anytime the guiding signals, and system will go back to the original proposed direction. The guiding signal feels like a magnetic conveyor. The guided direction could be a GPS based straight running, returning to steering wheel zero position or “centre point feeling”. The last one could be interesting, if no aligning moment available or vehicle have any visible steered wheels.

Guiding signals can be used efficiently in collaborative working environment, whereby motion of machine-chains should be synchronized. In this case a guiding steering torque presented in both vehicle. If a handle with active feedback available, also speed could be synchronized.

#### 4.3 Steering wheel used as hand force sensor

The steering wheel is able not only measure the position-velocity-acceleration, but also measures torque using current sensing of the motor drive. If velocity information and the driving torque available changes of inertia and reactive torque can be estimated. This information is used to determine the operator fitness or availability. If an automatic steering device available, often operators don't hold the steering wheel, which represent a risk.

For most of the working machines (forklift, forage harvester) is essential to identify operator presence for safety, and for this mostly a simple switch is built in the seat. This simple sensor cannot identify if the driver is inactive, e.g. sleeping. The haptic feedback on the steering can be used to integrate an intelligent driver presence sensing algorithm.

The power electronics have build in current sense components, and the driving torque can be calculated very accurately, without using any additional sensors. Using the known calibrated rotational inertia of the system and the motor driving/braking torque, the hand force of the operator can be estimated. If no steering force required, on stand or driving on a straight line, the steering wheel can use a modulated “ringing” signal to check, if driver's hands are still on the steering wheel.

Changing the steering ratio dynamically can improve the steering-kinematics. Unique functions can be implemented, like backing-up with trailer where a virtual relocation of the steered wheel from front to back is possible. Implements using three point hitch can be also regarded as a new option for relocation of the virtual steered wheels and create optimal new steering kinematics.

#### 4.4 Hardware-in-the-Loop simulation

Figure 6 a-b shows the steering wheel angle and controller internal model outputs at different model settings. If lower damping (angular speed dependent viscous friction) is used the system response (yaw rate, slipping angle) oscillate (Figure 6/a-d), which is close to the handling experience with passenger cars on public roads. Increasing the damping these oscillations on the steering wheel can be reduced (Figure 6/e-f) and so the optimal value for comfort and safety can be achieved.

Figure 6/g shows an implementation of the above mentioned soft-end feel. Figure 6/h shows both soft-end implementation and an example for the synthetic warning signals at assumed handling limits (yaw rate).

### 5 CONCLUSIONS

Haptic feedback is an interesting new opportunity to improve functionality of agricultural mobile machines. There are numerous options to implement physical type of signals, like aligning moment, to increase safety and vehicle handling.

There is also a new and interesting opportunity to design synthetic haptic feedback to present fast, and not yet existing warning signals for the operator. Using the presented development environment and the human-in-the-loop simulation tools further investigation of the human-machine interaction must be analyzed.

The haptic feedback can be used in the same time as an intelligent sensor to detect driver presence and ability. This opportunity must be investigated further involving ergonomist expertise.

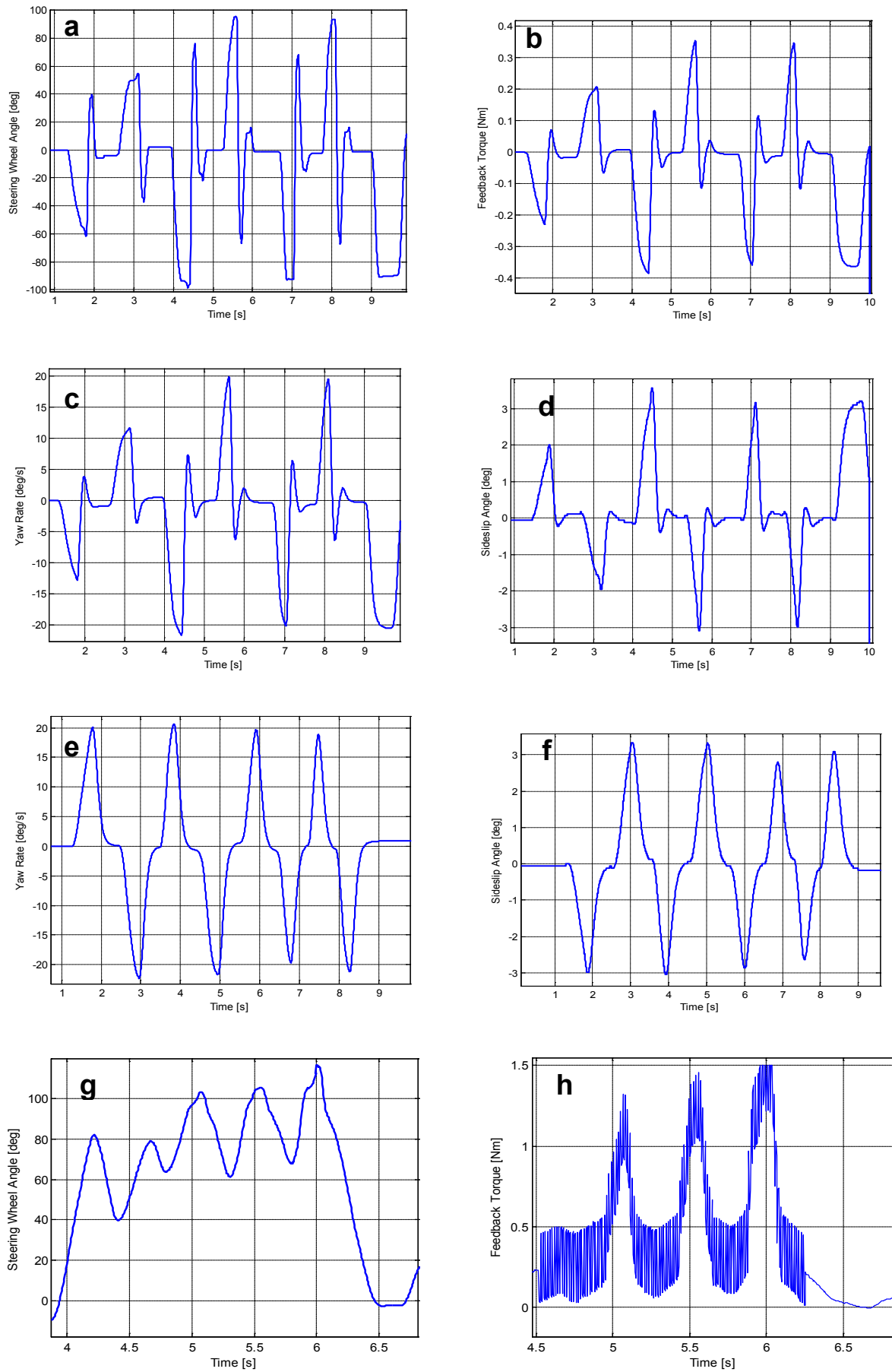


Figure 6: Human-in-the-Loop test results with different parameter set

## 6 REFERENCES

- [1] Amberkar, Sanket. „A Control System Methodology for Steer by Wire Systems.” Reprinted From: Steering and Suspension Technology Symposium 2004. Michigan: 2004 SAE World Congress, 2004.
- [2] Kopetz, Hermann. Real-Time Systems: Design Principles for Distributed Embedded Applications. London: Kluwer Academic Publishers, 1997.
- [3] Winner, Hermann, Hakuli, Stephan and Wolf, Gabriele. Handbuch Fahrerassistenzsysteme. Wiesbaden : Vieweg, 2009.
- [4] Odenthal, Dirk. „How to make Steer-by-Wire Feel like Power Steering.” 15th Triennial World Congress, Barcelona, Spain: Elsevier IFAC, 2002.
- [5] Schmidt, Gerrit. Haptische Signale in der Lenkung: Controllability zusätzlicher Lenkmomente. Braunschweig: Technischen Universität Carolo-Wilhelmina zu Braunschweig, Dissertation, 2009.
- [6] Switkes, J.P., E.J. Rossetter, és J.C. Gerdes. „Handwheel Force feedback for Lanekeeping Assistance: Combined Dynamics and Stability.” Journal of Dynamic Systems Measurement and Control v.128, no. 3, 2006: 532-542.

# ABRASIVE WEAR OF DIFFERENT HOT-DIP GALVANIZED MULTILAYERS

L. Szabadi, G. Kalácska, L. Pék, I. Pálkás

Institute for Mechanical Engineering Technology, Faculty of Mechanical Engineering, Szent István  
University, Gödöllő,  
www.geti.gek.szie.hu

## Abstract

More and more steel constructions are provided with zinc coatings as durable protection against corrosion. Hot-dip galvanizing process is widely used in Europe considering its favourable characteristics. Lately beside the corrosion resistance demand of hot-dip galvanized coatings as a new requirement is the abrasive wear resistance. The industrial floor boards, agricultural walking grids get heavy abrasion effect. The abrasive wear resistance of zinc coatings with multilayer structure is not tested yet, less known domain.

**Keywords:** hot-dip galvanized, diffusion, abrasive wear, gradient material structure.

## 1 INTRODUCTION, APPLICATION FIELDS OF COATING HOT-DIP GALVANIZED, THEIR PRODUCING AND THE COATING CHARACTERISTICS

The hot-dip galvanizing technology is used for durable resistance against of surfaces of iron- and steel constructions and of goods sold by the piece, its protection effect depends decisively on the thickness of a layer [1]. Its main application fields suggested is the surface protection against atmospheric load in all corrosivity grades as well as to protect the metal structures of indoor ventilated spaces. Its application expands continuously because of its reliable protective effect, the process industrial-scale applicability, its comparatively high productivity and low need for human labor demand. Continually increasing proportion of steel constructions manufactured in Europe-yearly more than 6 million ton-are covered by coatings hot-dip galvanized. Nowadays the products get also mechanical loads beside corrosion effects at industrial filters, industrial, agricultural, public square pavement grids hot-dip galvanized meaning new and at the same time expanding application fields. At surfaces hot-dip galvanized exposed to abrasive wear, sand and breakstone spreading there is an application demand for today wear- and friction resistant coatings. Comparing test data regulated relating to wear resistance there are not available neither in technical literature nor in the data-base of companies producing and developing coatings. These data are indispensable to develop technology improving wear resistance.

Two basic groups developed hot-dip galvanizing [2]. The most characteristic phase of individual processes are the dip into the metal bath exists at each group, however there are significant differences between individual solutions considering the preceding surface preparation and subsequent treatments. There is no difference between the two process groups considering the zinc-layer forming which takes place by the same physical-chemical processes. They so called continuous technologies belong to the first group, during which the product to be galvanized "as spliced" continuously with suitable speed passes through on the technological system.

The continuous broad strip-, narrow strip- and wire galvanizing processes have similar methods essentially. The strip surfaces are oxide relieved in a closed technological system, their materials are heated up then are guided into zinc-bath where the coat develops.

The so called periodic technologies belong to the second group. At there the products get treatment by individually or in groups. The surface is here also pre-treated then this is followed with hot-dip galvanizing. Covering steel constructions belong to this group, too.

The pure zinc is readily-formed and soft metal. The Zn hardness- 55-70HBS [3] is far below of the mild steel hardness -120HBS-, thus its wear resistance is also significantly smaller. In case of alloyed steels this difference can be still significantly greater. The structure of zinc-layer is determined decisively by the

chemical composition and texture of steel base-metal, the zinc-bath temperature, the dip duration, the zinc-bath alloying elements, the surface condition and thickness of the workpiece as well drawing out speed and the lifting method of the workpiece to be coated [4]. During dip-hot galvanizing an intermetallic, multi phase zinc layer develops on the products surfaces. The last step of technological treatment is the galvanizing when at about 450°C temperature the zinc atoms diffuse into the clean metal surface and produce atomic (cohesion) bond infiltrating into the metal-crystalline, namely they form an alloy with iron, on the zinc-iron boundary surface zinc rich Fe-crystallines develop. This forms essentially the “adhesive-bridge” between the zinc coating and the iron plate. The further alloy layers are based on this which iron content decreases progressively to the outer layer and in case of optimal steel quality also cease to exist. The coating thickness is about 80-100 µm. Figure 1. shows the zinc layer structure.

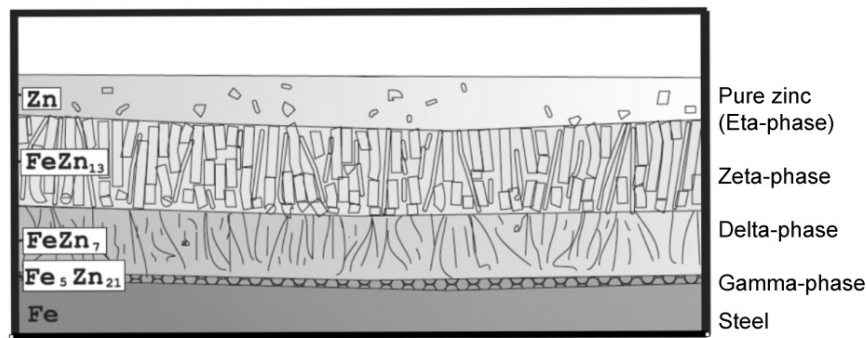


Figure 1. The zinc layer structure and the individual phases.

The gradient material structure developed during diffusion is not homogeneous, its composition changes in the function of thickness.

## 2 METHOD AND RESULTS

### 2.1 Specimens tested

We have chosen S235JRG2 steel as specimen material used for abrasive tests, which is the most definite base metal for example of pavement grid. As this material is desoxidized with aluminium- and not with silicium – and the mechanism of layer developing is determined first of all by the amount of silicium to be in steel, therefore it can be hot-dip galvanizing outstandingly. We have taken into account at deciding the specimens dimension the tool form of the abrasion tester, as well as those positions and the geometrical dimension of the container containing the abrasive medium ensuring abrasion. Figure 2 shows the dimension of specimen galvanized.

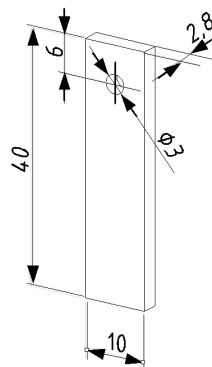


Figure 2. Specimen dimension.

Two types of coating were tested in the function of friction length, speed and pressure of abrasive medium.

- Technigalva: The determining components are the zinc (Zn), aluminium (Al), lead (Pb) and nickel (Ni) of the zinc-bath. The coating was made by dry periodic technology.
- Technigalva heat treated: The specimens were heat treated in order to the coating should have zinc-iron alloy phases in the total cross-section.

The abrasion resistance of coatings depends on its hardness, therefore it is needed to measure the micro-hardness. The micro-hardness tests showed that the Techigalva coatings had 48HVM in average, while the heat treated coating had 106 HVM in average. The testing points on the specimen's surface can be seen in figure 3. we have selected 10 – 10 test speciemens and after measuring each ones the registered hardness values were averaged that are summarized in Table 1.

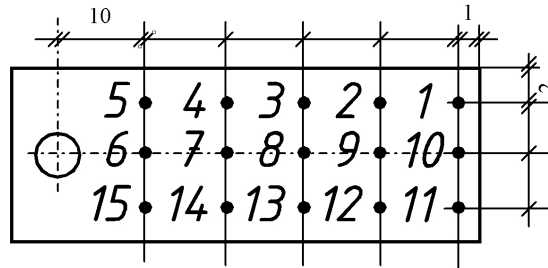


Figure 3. The hardness measuring points on the specimen's surface

Table 1. the measured micro Vickers hardness values

Measuring point	„Technigalva” sample [HV M]	„Heat treated Technigalva” sample [HV M]
1	48,7	98,2
2	50,7	97,3
3	45,9	114,2
4	46,8	92,5
5	49,7	96,3
6	45,9	89,5
7	51,8	101,4
8	49,7	105,4
9	45,9	108,2
10	54,0	112,2
11	45,9	112,2
12	42,5	103,5
13	41,7	96,3
14	43,3	91,2
15	44,7	91,2

Figure 4. and 5. show the SEM-pictures made from coatings, introducing the distinguished layers and EDS sampling areas. Certain layers, phases can be separated very good in the thousand-fold magnification. We have also carried out EDS (Electron Detector System) tests.

EDS spectra result are summarized in table 2., the measured graphs can be seen in Figure 6.

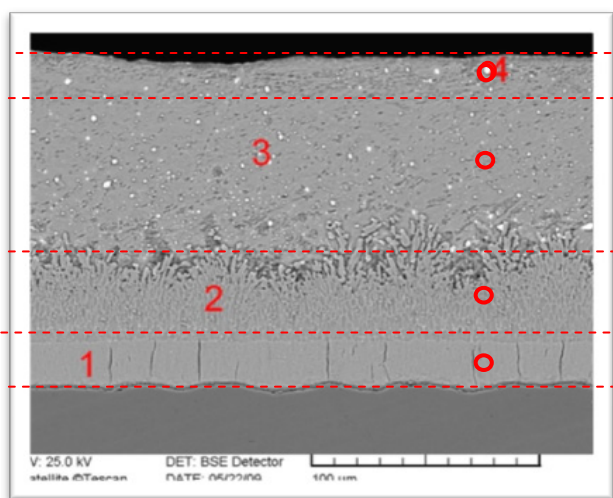


Figure 4. 1000X-magnification of Technigalva specimen zinc coating, (numbered layers with indicated EDS zone)

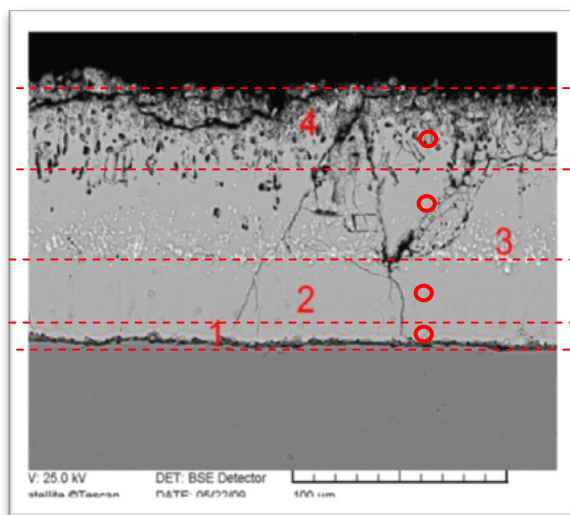


Figure 5. 1000X magnification of specimen heat treated zinc coating, (numbered layers with indicated EDS zone)

Table 2. EDS spectra result of Fe, Zn and Pb values (%)

Technigalva „T”				Heat treated Technigalva „H”		
Layer	Fe (%)	Zn (%)	Pb (%)	Fe (%)	Zn (%)	Pb (%)
1	16,4	83,6	-	47,5	52,5	-
2	10,1	89,9	-	16,3	87,7	-
3	-	100	-	19,6	79,6	0,8
4	-	21,2	78,8	17,9	82,1	-

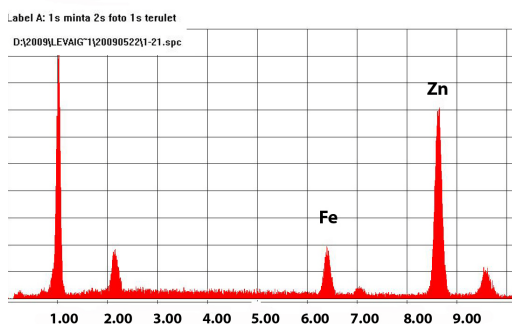


Figure 6. EDS spectra of Technigalva layer, phase Gamma (1)

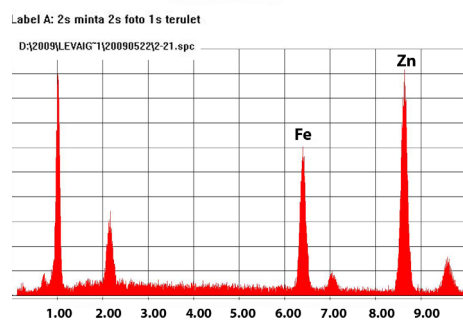


Figure 7. EDS spectra of heat treated Technigalva layer, phase Gamma (1)

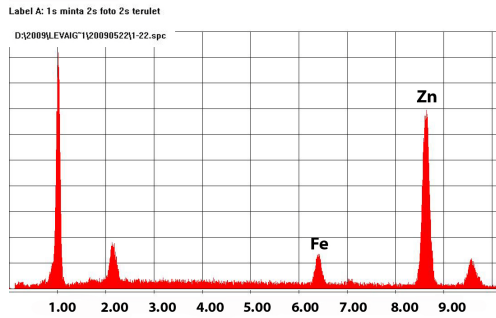


Figure 8. EDS spectra of Technivalva layer, phase Delta (2)

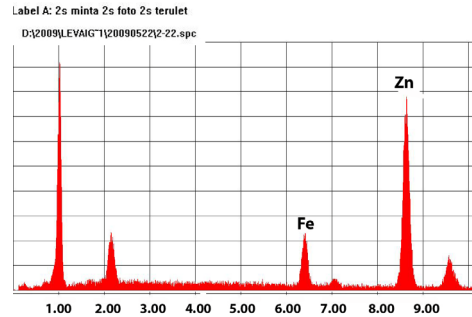


Figure 9. EDS spectra of heat treated Technivalva layer, phase Delta (2)

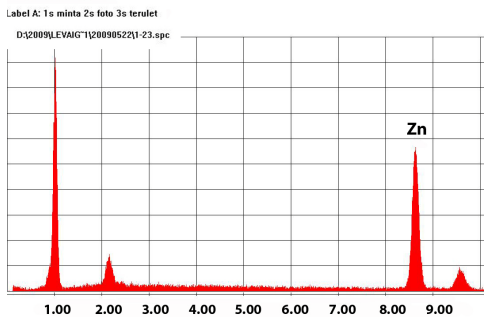


Figure 10. EDS spectra of Technivalva layer, phase Zeta (3)

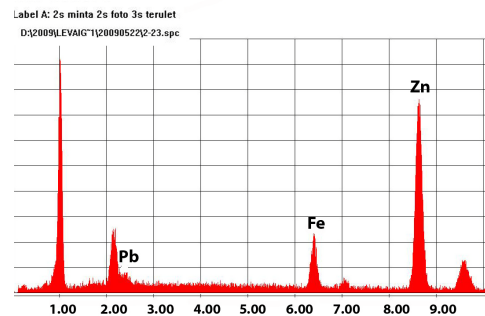


Figure 11. EDS spectra of heat treated Technivalva layer, phase Zeta (3)

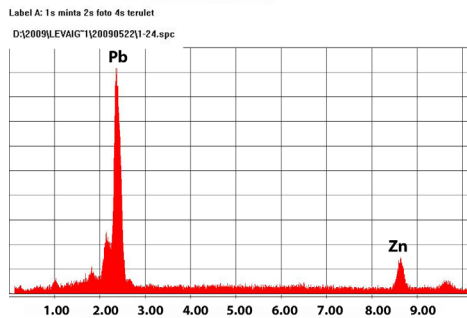


Figure 12. EDS spectra of Technivalva layer, phase Eta (4)

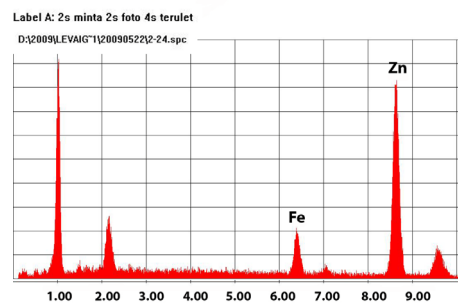


Figure 13. EDS spectra of heat treated Technivalva layer, phase Eta (4)

## 2.2 Abrasion test with “sand-slurry” equipment

The “sand-slurry” principle is well known in the VI. test category of tribological modeling. Several versions are wide-spread but they agree that for example in a sand with grain composition given - as in abrasive medium – a specimen moves in circular orbit generally with speed given. Great number of specimens can be measured at the same time in abrasive medium given as well as it can be well define but beside in different conditions with the abrasion tester developed in the Institute for Mechanical Engineering Technology. The results got made possible the evaluation according to various standpoints, too. Figure 14. shows the abrasion tester developed.

The electric motor shaft connects to a worm-gear which gear transmission in 22,58. The working shaft can be found at the exit side of the worm-gear on which 3 pcs. arm cross-clamps can be found – in different heights related to the base plate (Figure 15.) The specimens to be abraded can be fixed in suitable position on this. To one tool, to each arm 3 pcs. altogether 6-6 pcs. specimens can be fixed. Important characteristic of the cross-clamps is that the specimens can be fixed with each other in  $90^\circ$  included position, at their sides in pairs altogether 6 various positions related to the centre of gyration. The tools are set turned away to one another on the working shaft in top view the circle is divided to  $30^\circ$  sectors. The container containing the abrasive medium can be put into an outer container in case of demand, which can be filled with cooling-heating water to the thermal dynamics of measuring procedure can be regulated.

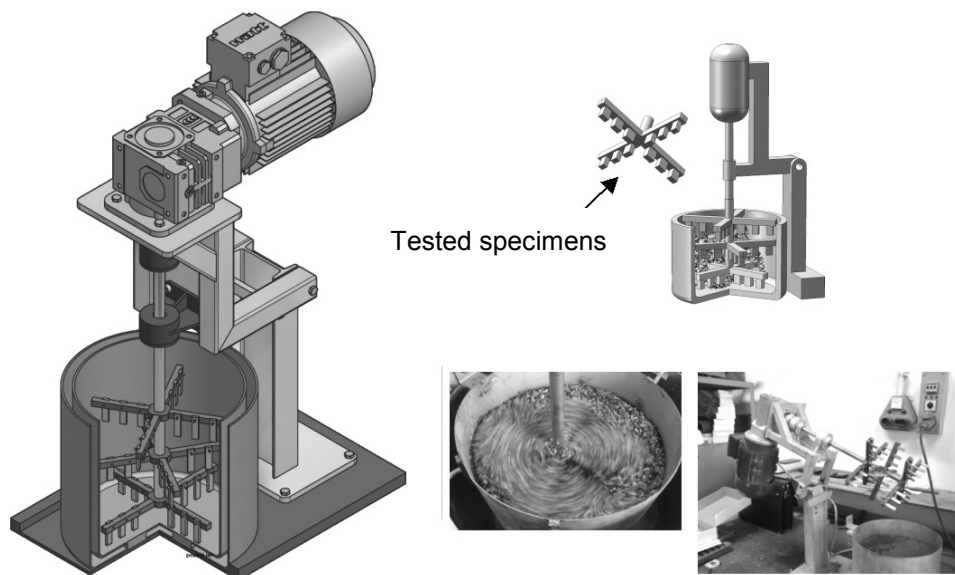


Figure 14. The abrasion with specimens mounted.

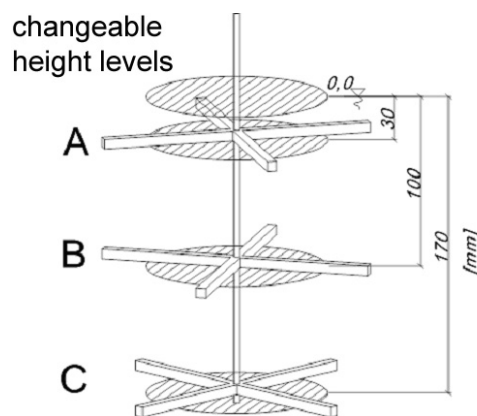


Figure 15. Specimens placed on three levels.

The abrasive medium was 0/8 OK – type ballast stone. Its average aggregation density in dry condition is  $1,7 \text{ ton/m}^3$ . There is no practically clay-sludge content as it is produced from washed, granulated gravels by knapping. The grain fraction is between 2 and 8 mm.

The specimens to be in different radiuses move with various different peripheral speed in the abrasive medium and the height position results different surface pressure ratios (Figure 16). The abrasion tester makes possible exceptional complex evaluation in the function of these variables.

### 2.3 The abrasion and speed connection

We have measured the abrasion of the 6 pcs. heat treated and 6 pcs. not heat treated specimens placed in all three levels (A,B,C) after seven various abrasion time. The surface pressures in standing (not rotating) condition:

$p_1$  (A level) = 153,83 Pa

$p_2$  (B level) = 521,82 Pa

$p_3$  (C level) = 902,41 Pa

Testing speed range: 14 – 40 m/min

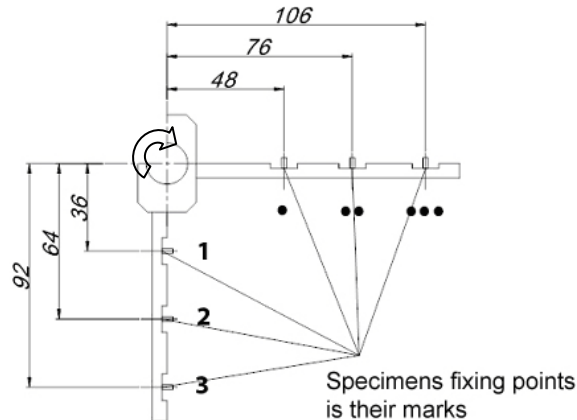


Figure 16. Position of specimens on different radiuses.

The specimens covered different length with different peripheral speed moving on various radiuses. After averaging the abrasion results measured at each specimen, repeating three times the measuring series the same incline could be seen at the lines to be adaptable to the plot at heat treated and not heat treated specimens, too. Based on these the speed independence supposed were proved by mathematical – statistical methods, by covariance analyses at all three levels at heat treated and not heat treated specimens, too. The abrasion values of all specimens to be in the different levels can be presented with a single regression straight line.

This means that the abrasion values do not depend on the abrasive speed in the speed domain tested (Figure 17. and 18). There is no significant difference between the specimens moved with various speeds but placed at the same level.

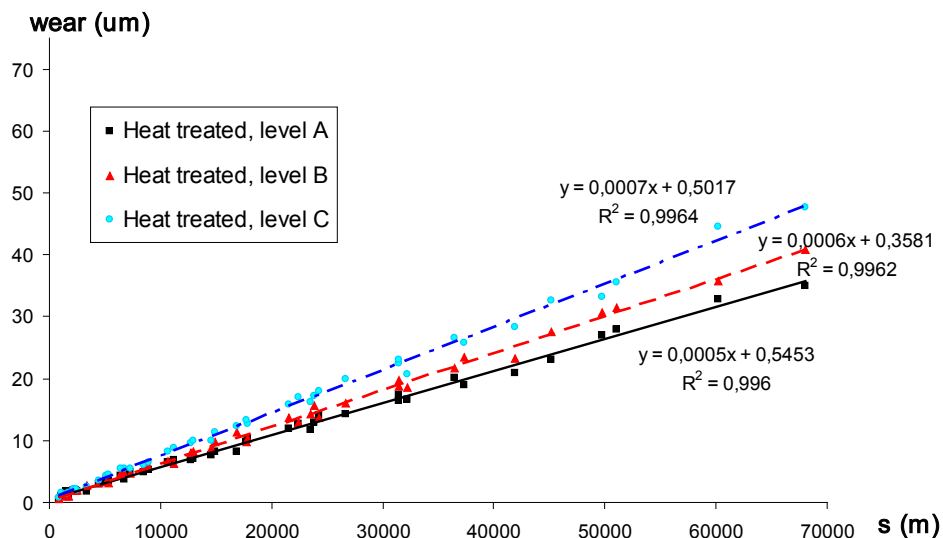


Figure 17. Abrasion values of heat treated specimens on "A", "B" and "C" level ( $h_1$ ,  $h_2$  and  $h_3$  depth)

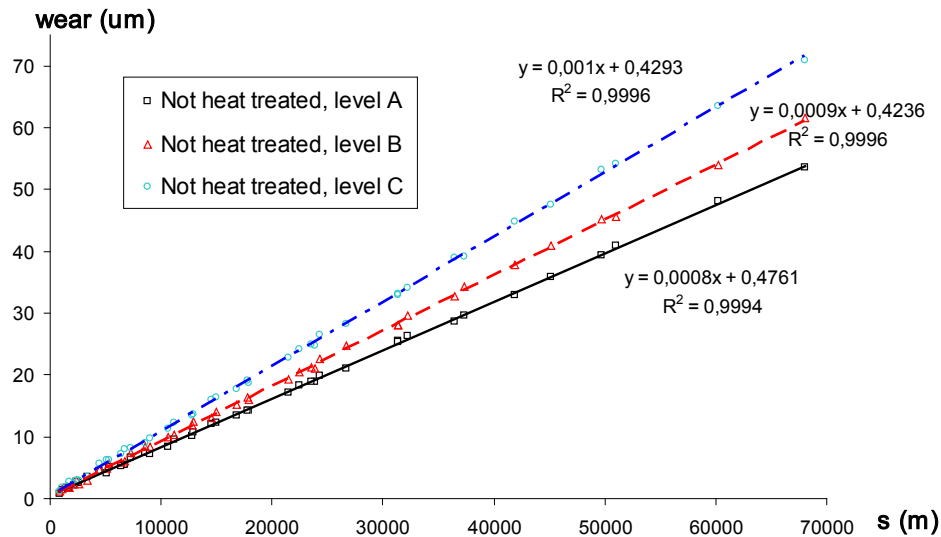


Figure 18. Not heat treated specimens abrasion values on “A”, “B” and “C” levels.

## 2.4 Connection between surface load and abrasion

The specimens placed on the “A”, “B” and “C” level get different surface loads because of this the abrasion values measured on “A”, “B” and “C” levels has to be compared. According to the hypothesis the abrasion values depend on the load. It can be approximated with linear trend-line the appropriate data to different levels on the diagrams, the matching is close in each case. The data appropriate to different levels can be separated visibly however if there is significant difference between them it has to be examined by regression analysis. The worst case is where there is the smallest difference: this is the “A” and “B” level data of the specimens heat treated. The calculations carried out proved that there is significant difference between the abrasion values of specimens fixed on “A” and “B” level. This means that the amount of surface load has significant effect on the abrasion values in the system tested. In case of higher load the specimens have got higher abrasion.

## 2.5 Comparing the layer structure of coating and abrasion values

The abrasion measured as a resulting effect on the surface of specimens means the continuous decreasing of coatings with layer structure. In Figure 19. and 20. can be seen how changes the percentage rate of decisive chemical elements in certain layers of heat treated specimens. The chemical composition's changing does not influence the abrasion intensity. According to data tested by EDS spectroscopy the percentage rate of chemical elements in the layers of not heat treated specimens is formed otherwise, but this compound does not influence the abrasion intensity of certain layers.

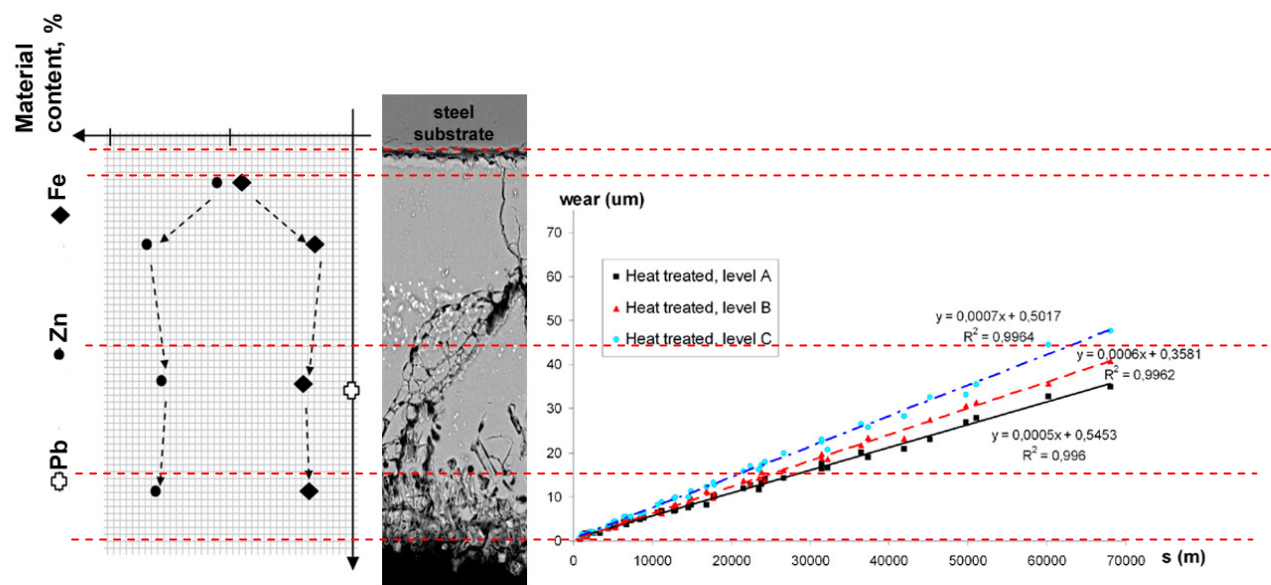


Figure 19. Heat treated specimens abrasion and the connection of layer structure.

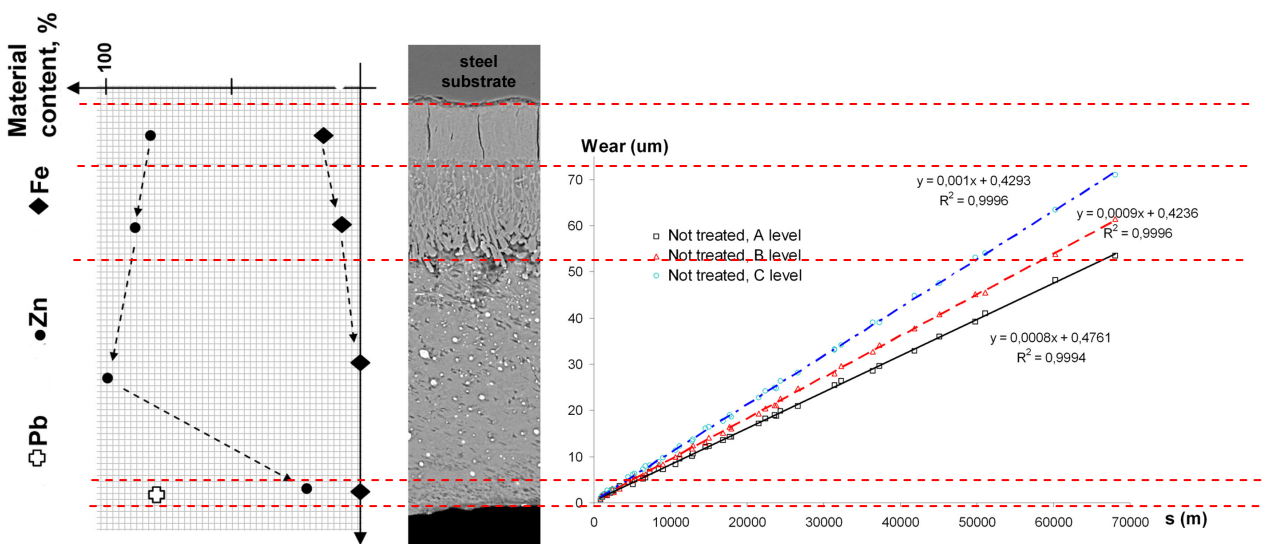


Figure 20. Not treated specimens abrasion and layer structure

### 3 CONCLUSION

- The multilayer coatings of hot-dip galvanized abrasion intensity in the test-system does not depend on the friction speed neither at heat treated nor at not heat treated specimens, but it depends on the medium pressure and on the resistance of medium deriving from that.
- The heat treatment improves the abrasive resistance. The higher hardness results higher abrasive resistance improvement.
- SEM-pictures and EDS spectroscopy proved that heat treatment results different gradient layer structure and composition.
- The linear abrasion dynamics of hot-dip galvanized layers tested does not depend on that, which layer comes to friction connection with abrasive medium. The inner gradient friction character did not effect the abrasion intensity measured, but the resultant of different gradient structure has different abrasive resistance.

### 4 REFERENCES

- [1] Arenasa M. A., Damboreenea J. Medranob J., A., J., García B. A., Rodríguez R. (2002): Corrosion behaviour of rare earth ion-implanted hot-dip galvanised steel. Surface and Coatings Technology, Volume 158-159, Page 615-619
- [2] Magyar Tűzihorganyzók szövetsége: Szakmai Ismeretek, Dunaújváros, Dunatáj Kiadó Kft., Dunaújváros, 1997 (Association of Hungarian Hot Dip galvanizing Companies. Professional Knowledge. In Hungarian)
- [3] Dr. Zorkóczi Béla: Metallográfia és anyagvizsgálat, Tankönyvkiadó Budapest, 1975. (Metallurgy and Material Testing. In Hungarian)
- [4] Magyar Tűzihorganyzók szövetsége, Tűzihorganyzás, CD-kiadvány, 2008. (Association of Hungarian Hot Dip galvanizing Companies. Galvanizing Technologies. In Hungarian)

# INVESTIGATION OF FRICTION HYSTERESIS USING A LABORATORY-SCALE TRIBOMETER

P. D. Neis<sup>1,2</sup>, P. De Baets<sup>2</sup>, Y. Perez Delgado<sup>2</sup> and N. F. Ferreira<sup>1</sup>

<sup>1</sup>Federal University of Rio Grande do Sul, Brazil

<sup>2</sup>Ghent University, Laboratory Soete, Belgium

**Abstract** The current paper addresses the characterization of dynamic friction by using a laboratory-scale tribometer. A special post-processing script in MatLab has been developed in order to analyse the data from the experiments. A sine wave signal for the velocity is imposed, with three different frequencies and, consequently, acceleration and deceleration rates. A friction material from brakes, with nominal contact area of 254 mm<sup>2</sup>, was subjected to sliding against a commercially available brake disc (gray cast iron, diameter of 256 mm). Some technical details and adjustments from the designed tribometer are showed and the results from the experiments are discussed. A friction hysteresis has been observed for all experimental curves, which exhibit loops in elliptical shape. A negative slope has been encountered for the curves when the imposed frequency is 1 Hz and 2 Hz, while for the highest frequency (4 Hz) the slope is positive. The laboratory-scale tribometer, associated to the post-processing stage, is capable to successfully be used to characterize friction hysteresis effect.

**Keywords** friction, tribometer, hysteresis

## 1 INTRODUCTION

In the last decades, demand for high-accuracy positioning and tracking systems has been considerably increased in the machining and assembly industry. Not accurate information about the friction behavior can severely deteriorate control systems performance in the form of higher tracking errors, larger setting times, hunting and stick-slip phenomena [1]. Many parameters can influence the friction: material, surface roughness, apparent contact area, contact pressure, relative sliding velocity, ambient conditions, mechanical system parameters and the acceleration/deceleration rate [2].

The current paper addresses the influence of the last factor on the friction behavior of mating materials. A laboratory-scale tribometer has been modified in order to incorporate evaluations in different acceleration/deceleration rates of the slider against the disc. These modifications relate to changes in the control program of the machine (in Simulink) and the development of a post-processing script in MatLab for analysis of the results.

## 2 DYNAMIC CHARACTERIZATION OF FRICTION

For friction dynamic characterization, as during the changes in sliding velocity, a linear reciprocating tribometer is used. Typically, this equipment consists of a linear actuator (electrical or pneumatic), a displacement sensor, a load cell and a compartment where the friction elements are installed (Figure 1).

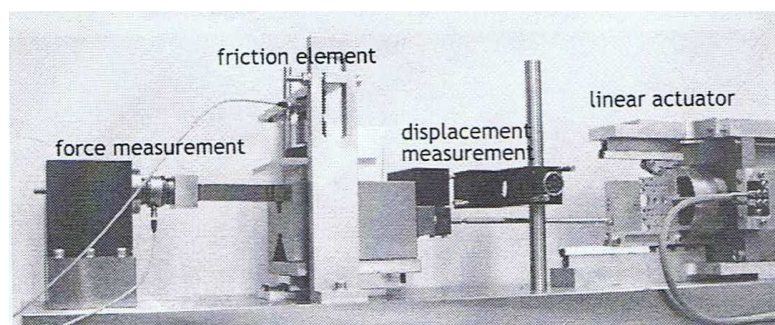


Figure 1. Linear Tribometer in Catholic University of Leuven [3]

By means of a reciprocating tribometer is possible to simulate the geometry and motions experienced in many types of rubbing components whose normal operation results in periodic reversals in the direction of relative sliding. Friction coefficient is produced for forward and backward movements of the stroke. This equipment is very useful for studying static coefficient of friction, when the direction changes [4]. In this type of machine, the maximum frequency is inversely proportional to the set stroke. According to a manufacturer [5], their reciprocating tribometer achieves frequency of 2 Hz for a maximum stroke of 35 mm. But for strokes lower than 2 mm, frequencies up to 120 Hz can be achievable by using such equipment.

Figure 2 presents some typical results from linear reciprocating tribometer. In this graph, the large dots represent the steady-state friction-velocity curve and the friction hysteresis is shown by the loops a,b,c,d, and e, corresponding to the frequencies 0.1,0.25,0.5,1 and 5, respectively. Notice that in this graph the loops exhibit an elliptical shape for the friction hysteresis.

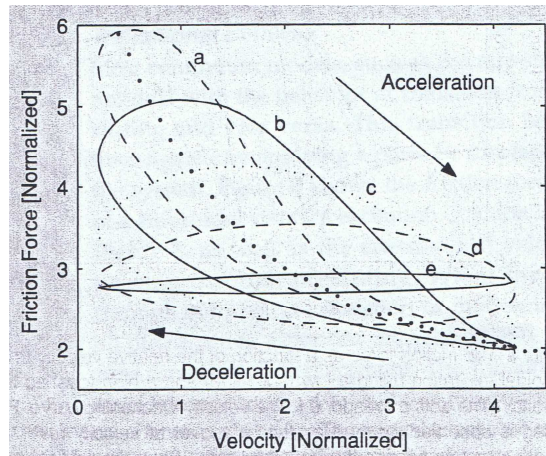


Figure 2. Dynamic characterization of friction force [1]

Other common shapes for the friction force vs. velocity curves (Figure 3) during friction hysteresis behaviour are known as loops clockwise and counter-clockwise loops [6].

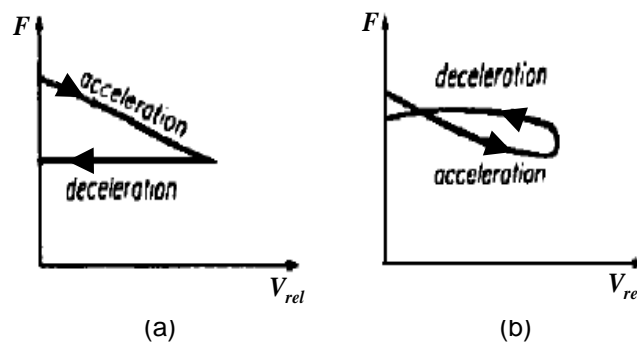


Fig. 3. Friction force-relative speed relations: (a) clockwise loops; (b) counter-clockwise loops (adapted from [6])

According to the literature [1,2], friction hysteresis effect is associated with the instantaneous real contact area, which is not only a function of the instantaneous relative sliding velocity, but also of the time available for the system to adapt to the situation corresponding to the actual sliding speed.

### 3 EXPERIMENTAL APPARATUS

Figure 4 shows the experimental apparatus used in the current research, where both the rotating and actuator systems of the tribometer are presented.

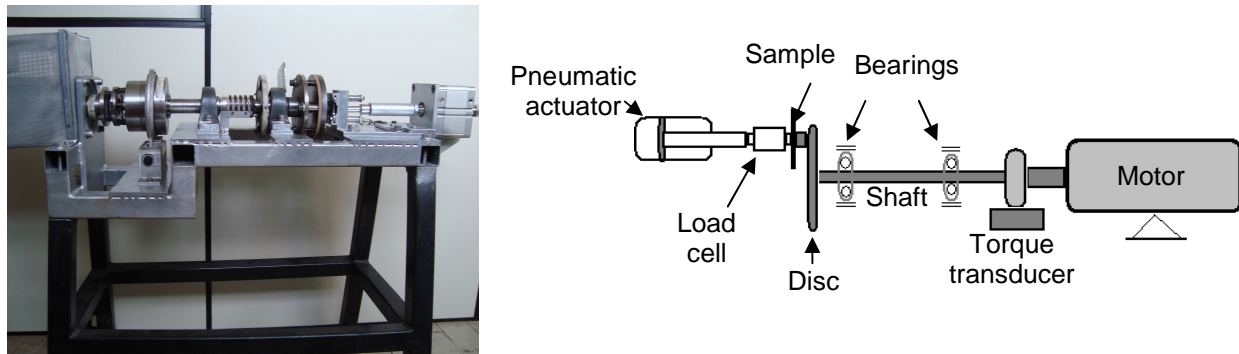


Figure 4. Experimental apparatus: (a) photograph and (b) scheme of the tribometer

The laboratory-scale tribometer (Fig. 4) has been designed to match the range of contact pressure and sliding speed as those in real car brakes, according to a previous study [7]. In this equipment, the sample has a small size in order to allow versatility during the tests and reduce the costs.

Regarding to the load/actuator system, the tribometer can operate in two different modes:

- I) Constant force mode: the normal force on the disc, which is done by means a pneumatic actuator, is kept constant over time during the tests. At the same time, the braking torque remains free to vary according to the changes in the coefficient of friction.
- II) Constant torque mode: the braking torque is kept constant over time during the tests. This is done by a closed loop process that controls the applied force at each fraction of a second. A feedback from the current torque is performed by means of a torque transducer installed on the tribometer shaft.

Regarding to the rotating system, the tribometer can operate in three modes:

- I) Constant drag mode: rotation speed of the disc is kept constant over time during the tests.
- II) Disc deceleration mode: the rotation speed of the disc decreases at a pre-set rate as the braking proceeds, similar to the braking process in cars and the tests performed on brake dynamometers.
- III) Wave mode: this option allow us to characterize friction dynamics, such as friction hysteresis in velocity. For doing that, a sine or squared wave signal for the velocity is imposed by the servomotor of the tribometer (Figure 5). Different acceleration and deceleration rates can be tested by altering the frequency of the imposed velocity.

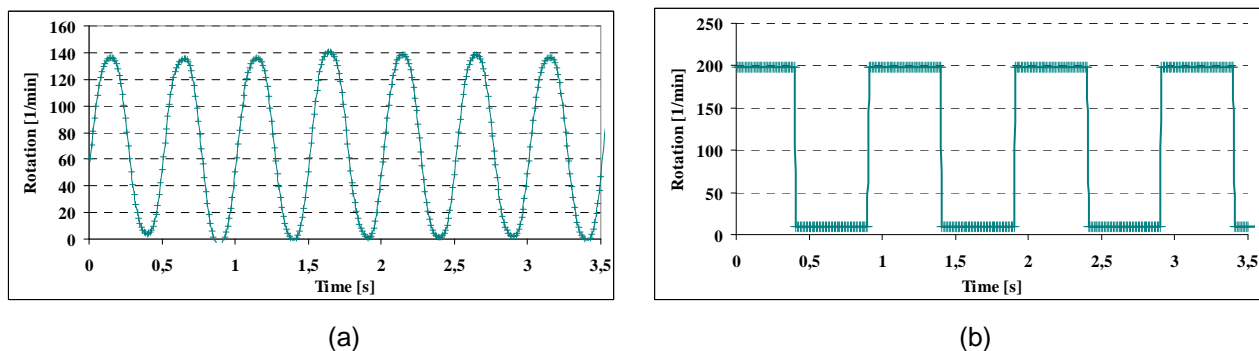


Figure 5 – Type of waves for the velocity in the wave mode: a) Sine wave; b) Squared wave.

Table 1 summarizes the general characteristics of the described machine, where the range of frequencies for the imposed velocity in the wave mode (0 to 4 Hz) is shown. These frequencies are valid between 0.1 to 200 rpm and for a maximum load of 400 N. When using 4 Hz, a rotation speed higher than 200 rpm or a load higher than 400 N may put the motor inverter in “over-torque limit” due to the high starting torque required from the servomotor.

Table 1. General characteristics of the tribometer

Normal load	0 to 4200 N
Motor power	11 kW
Sliding radius	27 to 54 mm
Rotating disc speed	0 to 4500 rpm
Disc diameter	159 mm
Frequency for the imposed velocity in the wave mode	0 to 4 Hz

## 4 SET UP OF THE TESTS

### 4.1 Matlab script for post-processing

Due to the high dynamic involved in the current tests, performed with wave mode, both hardware and software filters (type “pass-band”) have been removed. A calibration procedure has been previously done in order to determine the torque due to the inertia of the tribometer shaft during the accelerations and decelerations. These curves are used in a post-processing script, developed in MatLab. During post-processing stage, the signal noises are filtered (Fig. 6-a) and the friction torque (net torque) is determined by subtracting the total torque, measured during the experiments, by the torque due to the inertia in the tribometer shaft (Fig. 6-b).

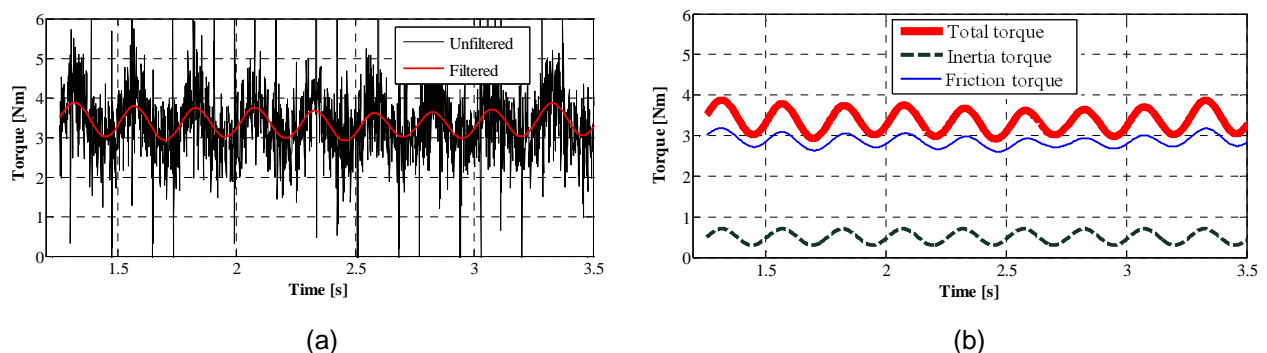


Figure 6. Post-processing the data: a) filtering the signal; b) determining the friction torque.

### 4.2 Samples preparation

Table 2 shows the formulation of the newly formulated sample used in this study. All the constituents were weighed using an analytical balance and mixed for 10 min by using a commercial blender.

Table 2. Formulation of the sample

Constituents	Content in wt%
Binder	43
Metal	0.6
Friction Modifiers	15
Filler	17
Fibers	20
Others	4.4

The final mixture was loaded into a cylindrical mold. Post-curing was carried out at a constant temperature of 180°C by placing the samples in a preheated. This friction material is currently in development process to become a commercial brake pad for light vehicles by a manufacturer in Brazil.

Sample was machined in a circular shape with nominal contact area of 254 mm<sup>2</sup> (Fig. 7). As counter surface, a commercially available brake disc (gray cast iron, diameter of 256 mm, thickness of 6 mm) has been used.



Figure 7 - Sample geometry.

### 4.3 Operating Parameters

In order to eliminate transient effects, such as running-in, a pre-run sliding of 1h duration (constant load and speed of 150 N and 1.5 m/s, respectively) has been done prior the tests. Table 3 shows the operating conditions used in each experiment, where a sine wave signal has been set for the imposed speed.

Table 3. Operating parameters

Test Number	Frequency [Hz]	Acceleration/deceleration rate [mm/s <sup>2</sup> ]	Max speed [mm/s]	Min speed [mm/s]
1	1	100	50.4 (12 rpm)	4.2 (1 rpm)
2	2	200	50.4 (12 rpm)	4.2 (1 rpm)
3	4	400	50.4 (12 rpm)	4.2 (1 rpm)

A normal constant load of 400 N was adjusted during all tests, resulting in a nominal pressure of 1,57 MPa, whose value is equivalent to a typical braking condition that occur in light vehicles [7]. Data acquisition sampling rate was set in 1 kHz and 10s of duration for each test.

## 5 EXPERIMENTAL RESULTS

Figure 8 shows the friction hysteresis behaviour for the test number 1, corresponding to the frequency 1 Hz. A negative slope of -0.0012 has been encountered for this curve, where this parameter was determined by subtracting  $\text{cof}_2$  by  $\text{cof}_1$ , divided by the difference between the maximum and minimum rotation (rpm).

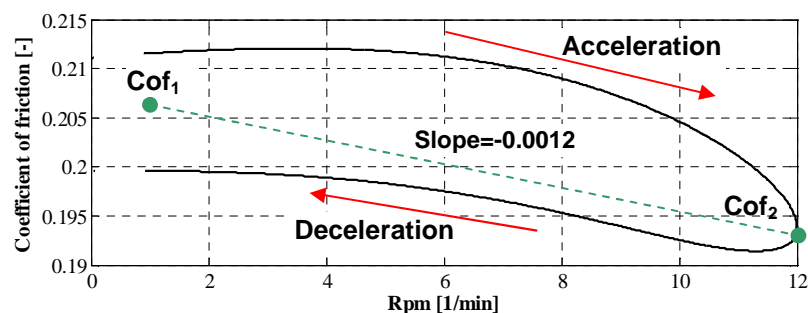


Figure 8. Friction hysteresis for the test 1

Figure 9 shows the friction hysteresis curve for the test number 2, corresponding to the frequency 2 Hz. Comparing the slope of this curve to those from the test 1, not significant difference has been encountered.

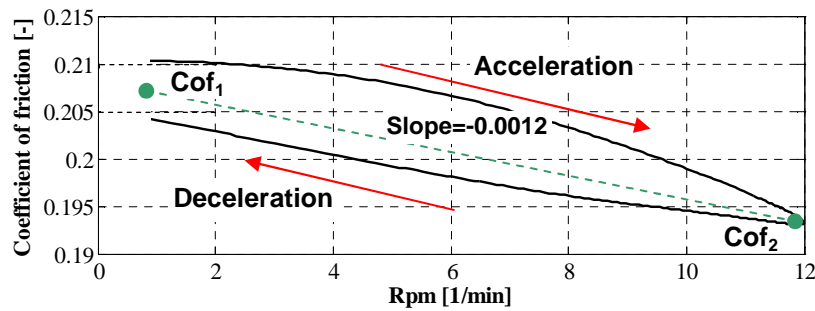


Figure 9. Friction hysteresis for the test 2

Figure 10 shows the friction hysteresis curve for the test number 3, corresponding to the frequency 4 Hz. Unlike the previous results, a positive slope of +0.0011 has been encountered for this curve.

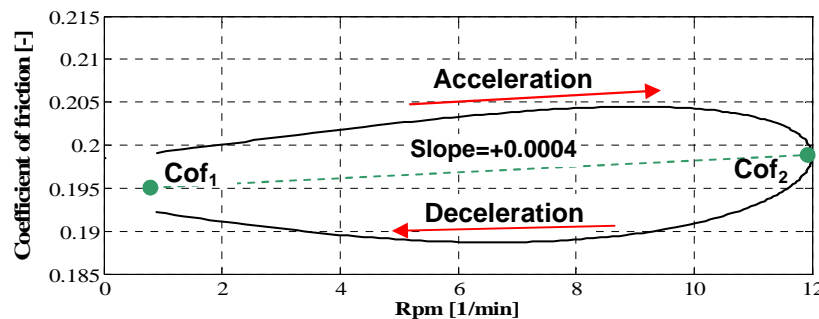


Figure 10. Friction hysteresis for the test 3

All experimentally obtained curves (Figs. 10, 11 and 12) reveal an elliptical shape for the friction hysteresis. This behavior is similar to those found by [1], which were previously shown in the Fig. 2.

Table 4 summarizes the experimental results for all tests. Notice that the curve slopes change the signal (negative to positive) only when the frequency is considerably increased, as in the test 3 (4 Hz). It seems that the influence of changes in acceleration/deceleration rates on the friction is strongly non-linear, since no significative differences in the curve slopes have been observed for the frequencies 1 Hz and 2 Hz, as during the tests 1 and 2, respectively.

Table 4. Experimental results

Test Number	Cof <sub>1</sub>	Cof <sub>2</sub>	Slope
1	0.206	0.193	-0.0012
2	0.207	0.194	-0.0012
3	0.195	0.199	0.0004

A lower coefficient of friction has been encountered in the beginning of the sliding process (parameter Cof<sub>1</sub>) for the test 3. A possible explanation for this phenomenon is found in the non-uniform surface conditions (mainly the surface roughness) of the cast iron disc and also variations in local chemical composition, causing the friction to change during disc rotation. In depth analysis of these effects will need further research effort that is beyond the scope of the present study.

## 6 CONCLUSIONS

A friction hysteresis has been observed for all experimental curves, which exhibit loops in elliptical shape. A negative slope has been encountered for the curves when the imposed frequency is 1 Hz and 2 Hz. On the

other hand, for the highest frequency (4 Hz) the slope is positive. This general behavior is similar to those published by [1].

The laboratory-scale tribometer allow us to test a wide range of acceleration and deceleration rates. For this reason, this equipment associated with the post-processing script currently developed, is capable to successfully be used to characterize friction hysteresis effect.

## 7 NOMENCLATURE

Cof <sub>1</sub>	average of coefficient of friction in the minimum rotation (1 rpm)	-
Cof <sub>2</sub>	average of coefficient of friction in the maximum rotation (12 rpm)	-

## 8 ACKNOWLEDGEMENTS

Authors are grateful to Financial support of FWO project G022506 and Erasmus exchange program - Euro Brazilian Windows II.

Special thanks also to Jonas Giacomeli by the technical support supplied.

## 9 REFERENCES

- [1] F. Al Bender; J. Swevers, *Characterization of Friction Force Dynamics*, IEE Control Systems Magazine, 2008.
- [2] F. Van de Velde, P. De Baets, *Comparison of Two Stick-Slip Tester and Recommendations for Repeatable And Significant Stick-Slip Testing*, Tribotest Journal 3-4, 1997.
- [3] F. Al-Bender, H. Van Brussel, T. Janssens, K. De Moerlooze, *Experimental Characterization of Friction*, Brochure about the facilities in the Faculty of Engineering in Katholieke Univesiteit Leuven, Belgium.
- [4] ASTM G133 - 05(2010), *Standard Test Method for Linearly Reciprocating Ball-on-Flat Sliding Wear*, 2010
- [5] Nanovea tribometers, *Company website*. Available in : <<http://www.nanovea.com/Tribometers.html>>, Access at 15th of Dez 2010.
- [6] B.N.J. Person, *Sliding friction: physical principles and applications*, Springer, Berlin. ISBN(1998) 3-540-63296-4.
- [7] M. B. Infantini, *Variáveis de desempenho dos sistemas de freios*. Master dissertation, 96 pages. Federal University of Rio Grande do Sul, Brazil, 2008.

# DEVELOPING SMALL-AIRCRAFT SERVICE AND RE-CONSTRUCTION OF LANDING-GEAR LEG SUPPORT

R. Lefánti, G. Kalácska, I. Oldal, K. Petróczki

Faculty of Mechanical Engineering, Szent István University, Gödöllő, Hungary  
[www.geti.gek.szie.hu](http://www.geti.gek.szie.hu)

## Abstract

The programs of air-operation and service in the aviation engineering - within this at light-aircraft too - take place according to rigorous regulations [6, 7]. There are such machine units and parts which regulation are incomplete, for instance such is the landing-shaft seating. We have developed a new maintenance model based on the traditional ones, which offers new information exchange modul for e.g. weak point re-construction and uses paper based documentation and modern remote maintenance as well. Beside the new model we have worked out a renewing solution of the often failed landing-gear leg support applying field and laboratory test and FEM modelling to fill up as an engineering example for the information modul of the new maintenance model.

**Keywords:** small-aircraft, re-construction, FEM model

## 1 INTRODUCTION

The programs of air-operation and service in the aviation engineering - within this at light- aircraft too - take place according to rigorous regulations [6, 7]. Its reason is to increase the safety of aviation and the aircraft reliability. For the sake of these such operating and service programs have been worked out by both the manufacturer and the aviation authority, and nevertheless the maintenance personnel of airworthiness that those programs to be suitable for the technical requirements and regulations alike. There are such machine units and parts which regulation are incomplete, for instance such is the landing-shaft seating. This paper written from our research work reviews briefly the problem and analyses of the landing-shaft and its development.

## 2 REPEATED BREAKDOWN

As a practical problem the silent-bloc (elastic longitudinal-seating support) at the attachment of landing-shaft in a Cessna 172-type aircraft manufactured in the years of 1970 broke down repeatedly, many times. The characteristically repeated breakdown allows to come to conclusion that this is one blot (weak-point) of the aircraft. This aircraft is often used to train learner pilots generally taking place on grassy runway (the landings and take offs, however the quality of the grassy runway is not ideal in every event). These facts mentioned contribute on a large scale to the breakdown of silent-bloc. The Cessna 172-type is put into circulation with two construction landing-shafts [1]. One type has got rectangular cross-section, of uniform strength part reminding of solid arched plate-spring. The other type has got circular ring cross-section uniform strength part (tubular shaft). The breakdown mentioned is characteristic to the latter type.

In case of breakdown metallic contact can take place between the landing-shaft and the support (inasmuch the elastic element totally got ruined). In this case the depth of damage on the landing-shaft (for example scratch, knockout) can be at most 0.01 inch. If this happens the landing-shaft has to be replaced.

The condition mentioned is very dangerous considering the aviation safety because the silent-bloc serving to support the landing-shaft and to elastic damping, does not perform its task so the degree amount of damping and support is not appropriate. It can happen such event that the breakdown is not recognized in time, so the stress in the material increases at certain parts of the landing gear and in the framework as the effect of operation load changes. This situation is extremely accidental.

The deterioration of PUR-seating at Cessna 172-type means the blot (weak-point) to be repaired by reconstruction. Signs referring to breakdown could be observed in the setting - in place, too (Figure 1.). The plastic between the outer steel-bush of silent-bloc and the landing-shaft almost crumbled away because of repeated load. Figure 2. shows the damaged part in disassembled position. It can be seen in the Figure 2. that the original PUR-seating totally deteriorated. The inner part of the PUR bush extenuated, cracked and the material protruded towards the outer flange of the silent-bloc, surely here it could freely deformed.

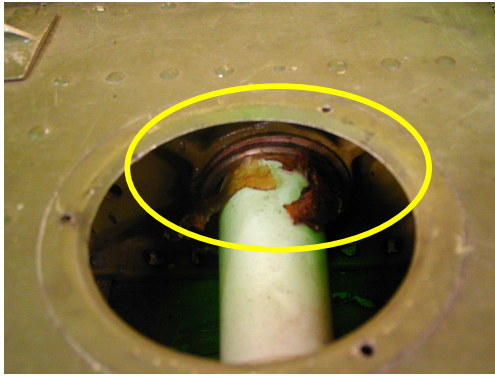


Figure 1. The damaged machine element installed position



Figure 2. The damaged machine element in disassembled position

### 3 THE SERVICE INSTRUCTION AND ITS LACK, OBJECTS.

The outer support has to be checked at Cessna 150-type after each 1000 hour or every 3 year, at 172-types after each 1000 hour but only at plate spring constructions concerning the landing-shaft. The manufacturer doesn't take measures in no kind of instructions concerning the service of elastic support (seating) in case of pipe cross-section landing-shaft [1]. The landing-shaft seating susceptible to breakdown means risk from aviation safety standpoint. The question can be raised with good reason whether the blot (weak point) can be replaced with solution containing new, up-to-date materials, where the operation load doesn't result returning breakdown.

Objects:

- To propose replacing the original PUR material with elastic seating by other plastic or by plastic mating.
- Further aim is to determine that characteristic load and limit based on which it is necessary checking the machine-element given, independently that just in which period is the aircraft service. It reaching the value determined it is proposed to supervise the machine-element, maybe its replacement. By this characteristic parameter the incomplete service instruction can be completed.

### 4 RECONSTRUCTION EXAMINATION OF LANDING-GEAR LEG SEATING

Figure 3. shows the process of the complex testing and evaluating of the machine-element deteriorated. We have marked the main activity points in the Figure. These are:

- Determining the material models;
- Measuring the load in real conditions;
- Preparing the mechanical finite-element analysis;
- To carry out rapid fatigue-wear tests in laboratory conditions;
- Preparing the mechanical finite-element analysis;
- Evaluating the results.

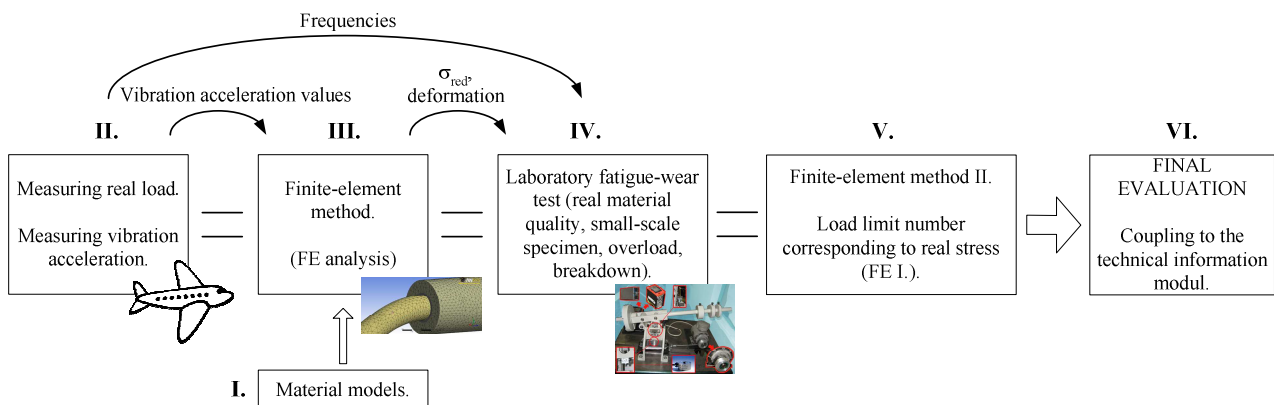


Figure 3. Complex testing, evaluating system

#### 4.1 Determining original material and material desired for tests.

The elastic seating material resulting manifold breakdowns corresponds in mechanical properties to the cast polyurethane basic material presently in circulation as PUM 70A symbol.

Considering that the PUM 70A-type basic material characteristic breakdown is the fatigue and the wear because of this the PUM 60A and PUA 90A basic materials have been chosen as replacing materials having near similar elastic but better fatigue and wear and tribological properties.

To determine the mechanical and strength properties of the materials tested are needed to carry out further tests. Because of these hardness, tensile - and compression tests were carried out on these basic materials. The results and evaluation of the tests gave the input parameter of the FE - analysis.

#### 4.2 System suitable for measuring the real load.

It is a very complex task to measure the loads befalling to the aircraft to the landing-shaft and from this to the silent-bloc. Several procedures are widely used in practice to measure the stresses and strains in a construction [2, 4].

We have developed and made a measuring-system capable to measure acceleration/vibration-acceleration determining the load befalling to the certain machine-element (Figure 4.).

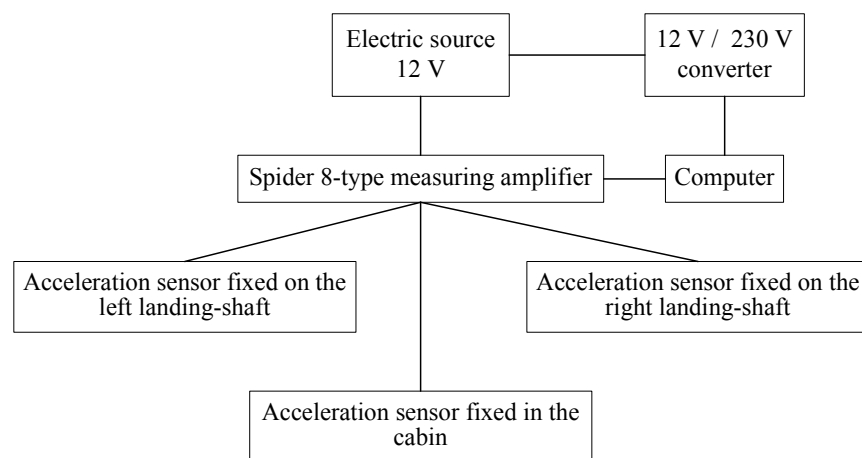


Figure 4. Sketch of the measuring-system suitable measuring accelerations arising in the light-aircraft

We have got permission and technical assistance after consulting with the operator to fix the acceleration sensors on the aircraft as well as the appliances needed to carry out the measurements.

On the spot of measurements the airport has got concrete cover and grassy fields can be found. Five-five landings and take offs were made on the concrete cover and grassy fields. The flights took place according to the regulations required by aviation authority and by the operational instructions of the light aircraft.

##### 4.2.1 Evaluating the acceleration results

From the acceleration results measured in the framework and in the landing-shafts the results measured in the framework were used in further examinations and use for mechanical modelling. The reason of this is that to complete the mechanical model later the connection between the landing-shaft and the silent-bloc is not rigid surely the landing-shaft has got elasticity/damping by which the model to be prepared should be enlarged. This would make more difficult to complete the model as the elasticity/damping of the landing-shaft is unknown. Because of this we disregarded the results measured on the landing-shaft. The connection between the framework and the outer bush of the silent-bloc is rigid and the sensor in the cabin was fixed at such place (real seat frame) which has got proper rigid contact with the framework.

Among the measuring directions at the vertical „z” direction it could be unambiguously separated the various characteristic aeronautic conditions.

That six sections can be seen in Figure 5. which can be separated during measuring and flight.

The names of certain sections:

- I. Landing process, in the air;
- II. Moment of landing;
- III. Section of decelerating taxiing on the field;
- IV. Section of accelerating taxiing on the field;

- V. Section after the moment of take off;
- VI. Take off process in the air.

The examination of sections after these happened separately. We used Fourier transformation (FFT) examining the sections. As a result of FFT we got vibration acceleration-frequency values from the vibration acceleration-time functions [5].

This guaranteed for us that we could determine the repetition member (frequency) of load belonging to the characteristic acceleration values. An example picked out of Fourier transformation can be seen in Figure 6. The characteristic acceleration values are marked in the Figure so, as an exposed value (A), as well as a characteristic section (B).

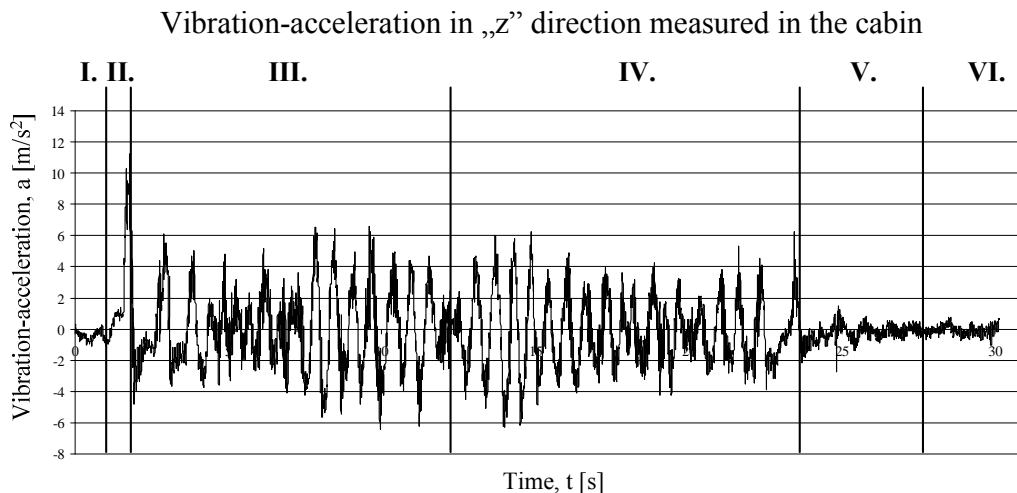


Figure 5. Characteristic sections of vibration-acceleration in „z” direction in the function of time measured in the cabin

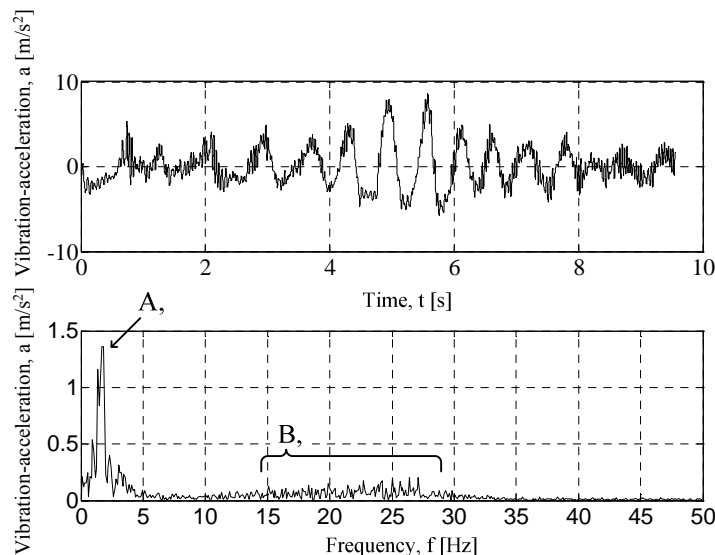


Figure 6. Time-function of acceleration measured in the aircraft and FFT frequency spectrum, in the section of decelerating taxiing on the field, „z” direction

It can be stated by knowing the results that the breakdown of the silent-bloc then happens sooner if the load is accompanied with much higher repetition number.

Knowing this it can be established that fact the critical sections considering the silent-bloc are the decelerating/accelerating taxiing on the ground (III., IV. section) and not the moments of landing as well as take off. The characteristic values of acceleration and frequency of decelerating/accelerating taxiing on the ground had to be applied for the further examinations.

### 4.3 Mechanical examination of the landing-shaft with simulation

The measurements with real time carried out on the aircraft and their results as well as the results of material testing give due base to carry out mechanical simulation examinations (Finite-element method, FEM) on the landing-shaft silent-block unit. The aircraft industry is among those domains applying FEM in practice [3]. We have used the Ansys Workbench 11 program for the FEM simulation. Some steps of using the program are shown in Figure 7. and 8.

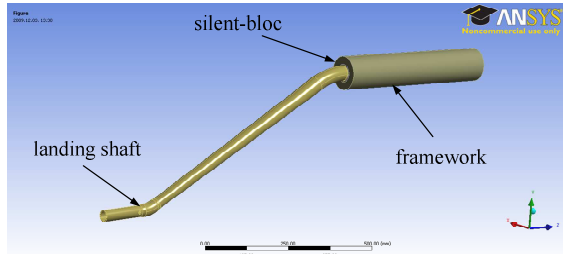


Figure 7. The geometric model

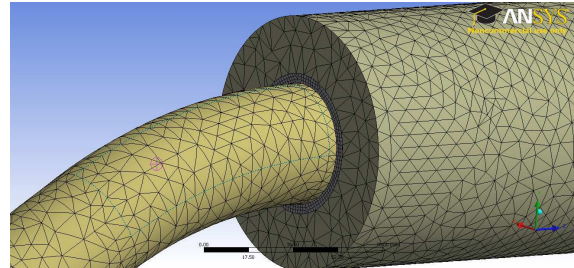


Figure 8. Making the mesh for the model

During the program we have completed the real model of the landing-shaft and silent-bloc. Among the parameters to be set for the run of the simulation the various material properties and the acceleration values in different directions measured occurred.

By executing the simulation we determined the reduced stress arisen in the plastic bush of the silent-bloc as well as the magnitude of deformations.

The characteristics determined appeared as input parameters at the laboratory rapid fatigue test.

### 4.4 Laboratory fatigue test

We have made an equipment for laboratory fatigue test capable to clamp a small- scale specimen to model the ruin of the silent-block. The construction and form of the equipment had to be capable carrying out rapid fatigue tests with construction materials in a reproducing system that the load should be suit the experiences at real measurements respectively with the FET calculations.

The DIN 50322 standard gave the basis of the test, within we took the 6. testing category into consideration, namely the model test with specimens having simple shape.

The directions of strain and load agrees with each other at real construction. The direction of strain and load however is perpendicular at the laboratory fatigue-test equipment. This doesn't disturb the laboratory comparing tests, the reproducing capability - as a characteristic of 6. category -. The amount of the fatigue work introduced into the specimens and the other load parameters can be controlled.

The theory of fatigue test was given by the "Locati" rapid fatigue test applied for steels. During the test the material to be fatigued is exposed to  $10^5$  repeated load at each increasing load level. During these loads the material tested is ruined [8].

The fatigue test applied by us differs from the previously mentioned that we adapted the test theory to high elasticity elastomer.

The fatigue of the specimen to be tested is carried out with a carriage making straight line reciprocating motion, on the other hand the specimen is pressed by a load vertically to steel base plate (Figure 9.). This is a complex mechanical and tribological fatigue where the contact surfaces also deform and also rub (stick) as in the real landing-shaft seating.

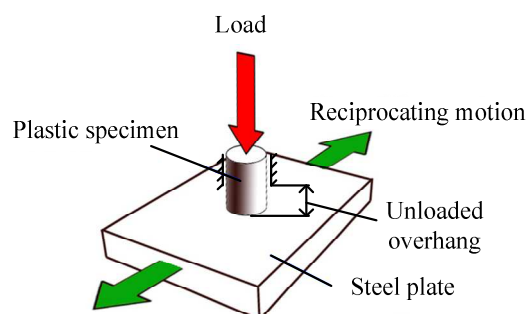


Figure 9. The specimen loads

The equipment built and its parts can be seen in Figure 10. The equipment was suitable to carry out the needed rapid fatigue tests.

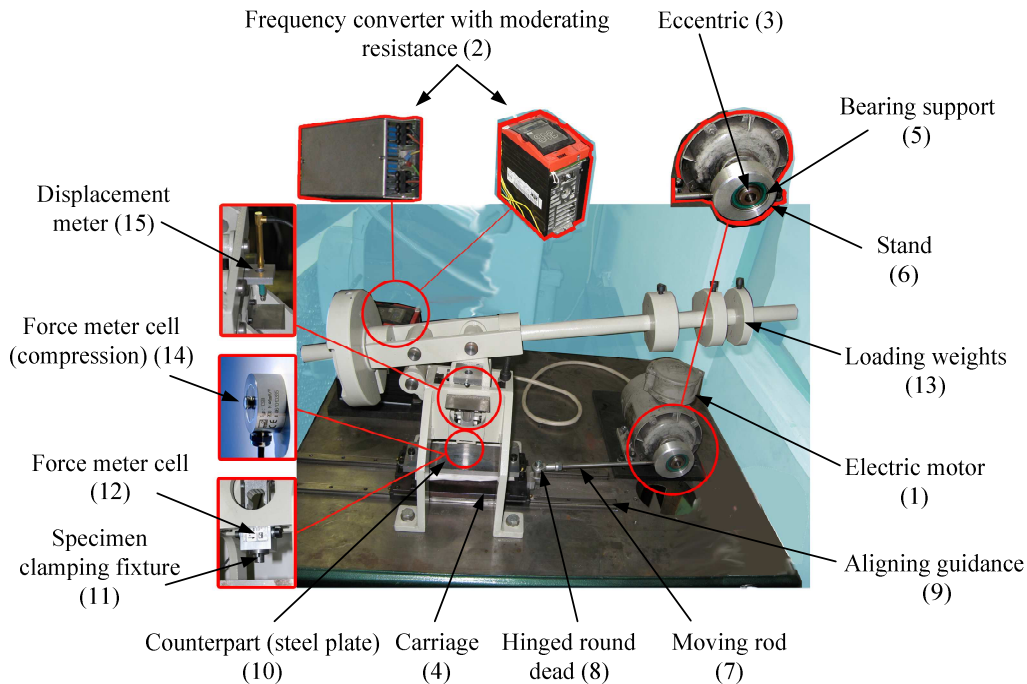


Figure 10. Equipment for fatigue-tribological tests

The results got from real time measurements carried out on the aircraft as well as got from FET-simulation gave the parameters to be set during fatigue tests on the equipment for fatigue test These are:

- The amplitude of the counterpart (10) movement with the help of eccentric (3);
- The frequency of the counterpart (10) movement with the help of the electric motor (1) and with the frequency converter (2);
- Vertical load with the help of loading weights (13);
- The length of unloaded overhang of the specimen from the specimen clamping fixture (11).

It could be established from the evaluation after carrying out laboratory measurements that in case of materials tested the functional reliability is the most favourable at PUA 90A. This is followed by PUM 70A then by PUM 60A.

#### 4.5 Connection of the measuring results and of the real load repetition number (cycle- number)

During laboratory fatigue tests also bending and shear stress develop on the specimen beside vertical direction normal force because of this reduced stress has to be taken into consideration as a defined characteristic. It has to be determined the reduced stress in the specimen at load level given to decide the fatigue characteristic from measuring results of the silent-block elastic seating manufactured from the material tested. To determine this we have carried out mechanical modelling (FET).

After finishing the mechanical model we have determined fundamentally that:

- Bending and shear develop in the specimen beside compression.
- The  $\sigma_{red}$  value is multiple of the value calculated from compression at given load level and overhang length because of complex stress of the specimen. The fatigue test took place thus substantially at higher stress level comparing to operation condition.

We have obtained the following result using the results of real time aircraft measurements, the results of laboratory rapid fatigue tests furthermore the results of mechanical modelling (FET) of laboratory fatigue test:

- The elastic seating made of PUM 60A type plastic will be ruined probably at 2980 landings and take offs calculating with 20% factor of safety expecting 3727 take offs. The suspension of the landing-shaft and itself the silent-bloc have to be examined at reaching the limit number determined whether the breakdown started or ensued.
- The machine part original material corresponds to the PUM 70A commercial product. During our tests we established that with PUM 70A material higher service life and fatigue number of cycles can be reached than with PUM 60A- material. The basic material according to our tests is further suitable fulfilling its task, too. The results of fatigue-abrasion tests however come to the conclusion

that the elastic section of bed endures undoubtedly 2980 landings and take offs. At reaching the silent-bloc has to be checked whether the breakdown ensued or began. By this proposal such aggravation comes to the new service system which increases the safety. Further more the deficiency of the plant service instruction can be supplied with this information.

- The PUA 90A material is also suitable for the part as basic material. The results come to the conclusion that still greater improvement (higher service-life) can be reached than with PUM 70A material.

## 5 CONCLUSIONS

Summing up it can be established that we have created a complex measuring and evaluating system destined for executing reconstruction planning of a real construction. As a result of our research work we have determined a limit number suitable to give a reliability limit concerning the elastic seating of the landing-shaft (at a certain constructional condition) of the aircraft-type. We have hopes of helping the more safety aircraft operation with this completed reconstructional planning and with the complex evaluating process.

## 6 REFERENCES

- [1] Cessna 172 Series Service Manuals & Parts Catalogs: DVD kiadvány, 2010.
- [2] Dömötör F.: A rezgésdiagnosztika elemei. Budaörs: SKF Svéd Golyóscsapágy Rt., 1996.
- [3] Fodor T. - Orbán F. - Sajtos I.: Végeelem - módszer. Elmélet és alkalmazás. Budapest: Szaktudás Kiadó Ház, 2005.
- [4] Janik J.: Gépüzemfenntartás. Dunaújváros: Dunaújvárosi Főiskolai Kiadó, 2001.
- [5] Nagy I.: Állapotfüggő Karbantartás, Műszaki Diagnosztika I., Rezgésdiagnosztika. Paks: Delta-3N Kft., 2006.
- [6] Decree (2003): 2042/2003/EK.
- [7] Decree (2008): 859/2008/EK.
- [8] Veress E.: Technológiai anyagvizsgálati módszerek. Magyar nyelvű szakelőadások a 2000 - 2001-es tanévben, Babeş-Bolyai Tudományegyetem Vegyészmérnöki Kar. Románia, Kolozsvár: Erdélyi Magyar Műszaki Tudományos Társaság, 2001.

# MACHINABILITY OF ENGINEERING POLYMERS

R. Keresztes, G. Kalácska, L. Zsidai, Z. Dobrocsi

Institute for Mechanical Engineering Technology,  
Faculty of Mechanical Engineering, Szent István University, Gödöllő, Hungary  
[www.geti.gek.szie.hu](http://www.geti.gek.szie.hu)

**Abstract** Nowadays parts made of up-to-date engineering plastics are used more and more in mechanical engineering practice. These machine-elements are produced most frequently by injection molding or by one cutting process. The injection molding technology are used generally for great number of pieces, in case of serial production while cutting processes are preferred to piece (unit) or smaller number production. We used lathe and measured the main- and feeding-directional cutting force at different engineering polymers (cast PA6, POM C and UHMW PE, HD 1000). We compared these results with the tensile properties of the materials. The analysis made can be well used in practice.

**Keywords:** turning force components, lathe, force measuring, main cutting force, tensile stress,

## 1 INTRODUCTION

Among cutting processes the turning takes place often. During turning engineering plastics many problems can arise. Among these one is the splint (continuous chip) forming which can cause accident and can cause failure maybe the total ruin, fracture of the cutting tool. Because of this it is important to set the proper cutting parameters by which it is possible forming elemental or transitional (easily fracture) chip, too. It is also important to know during cutting the amount of the main cutting force. Knowing this the load of cutting tool can be made more constant as well as the remnant stress in the material chipped can be reduced to minimum in case of proper cutting parameters. The tensile properties of the materials is also important and we analysed the tensile stress – strain curves of the polymers. We plotted the quotient of the specific cutting resistance and the yield stress in the function of the chip cross section with the all machining parameter groups.

## 2 TESTING METHODS, INSTRUMENTS

The cutting is a machining method during which the required shape of the workpiece is formed by removing the surplus material layer in smaller – bigger particles (chip) with a suitable tool. Relative displacement is needed between the tool and workpiece for chip removal, for cutting movement. We measured the tensile properties of the materials.

### 2.1 Equipment used for tests

The CNC-lathe, type EMCO COMPACT 5, was used for tests. The equipment can be found in the laboratory of Institute for Mechanical Engineering Technology its programming takes place of G-codes. The photograph of the workpiece clamped as well as the shank with strain-gauges clamped into tool-box and the turning tool can be seen in Figure 1.

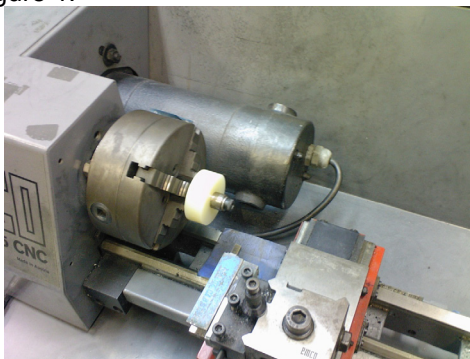


Figure 1. The lathe and the workpiece clamped

The tool clamping structure used for measuring the forces can be seen in Figure 2. The first section of the Figure shows the 3D-model.

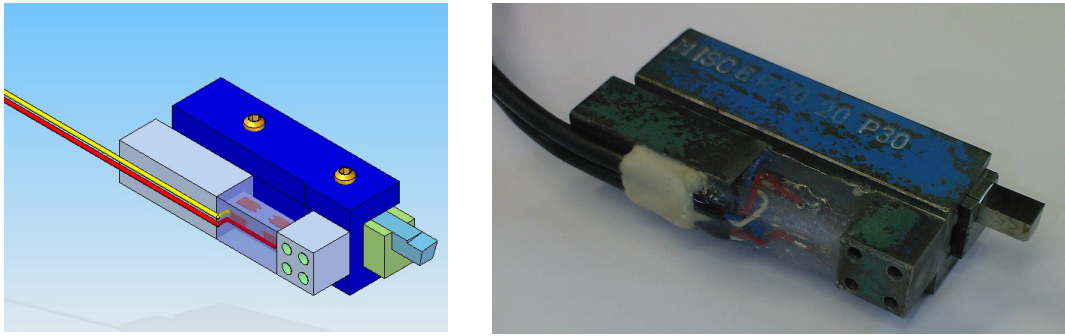


Figure 2. The force measuring shank model and its real picture

2-2 pcs. strain gauges are fixed at every side. Coupling the strain gauges into total (full) – bridge those is a possibility measuring the forces arising in two directions. To measure the main cutting force  $F_v$  (tangential) arising from the movement in vertical plane of the tool and  $F_f$  feeding (axial) force arising from the movement in horizontal plane. A second tool-box is fixed to 4 pcs. threaded holes on the measuring-shank into which the real cutting tool is fixed. The strain gauges measure the tangential (lower – upper) and the feeding (right side – left side) forces connect to a Spider-8 type measuring amplifier through wires, which amplifier convert the analogous signals into digital than transmits to the computer. With the help of Catman 3.1 program data measured can be seen. The frequency of measuring and data collecting is 25 Hz. We measured the tensile properties of the materials according to MSZ EN ISO 527 standard with a type of INSTRON 5581 tensile machine and we prepared the tensile stress – deformation curves of the polymers. From these diagrams we determined the yield stresses of the materials. The figure (Fig. 3) shows the tensile machine.

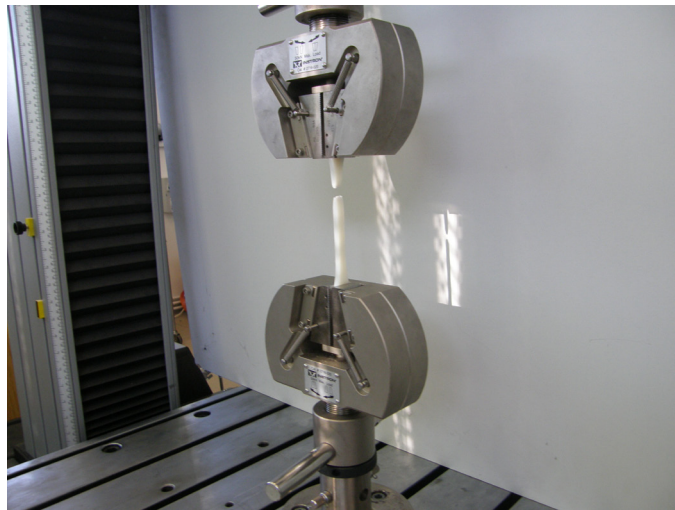


Figure 3. The tensile machine and the workpiece clamped

## 2.2 Materials tested

The materials tested are those polymer basic types that are often used in engineering practice to manufacture machine-elements. Table 1 shows the name of product, the whole name and the marks accruing on lather diagrams. The specimens prepared for cutting are shown the first part of Figure 4 and the tensile specimens are shown the second part.

Table 1. Name and mark of plastics

Serial number	Product name [6]	Whole name	Own mark
1.	DOCAMID 6G H	Cast polyamide 6, (Magnesium)	PA 6G Mg
2.	DOCAMID 6G	Cast polyamide 6, (Natrium)	PA 6G Na
3.	DOCACETAL C	Polyoximethylene / Polyacetal	POM C
4.	DOCALENE	UHMW – Polyethylene	HD 1000

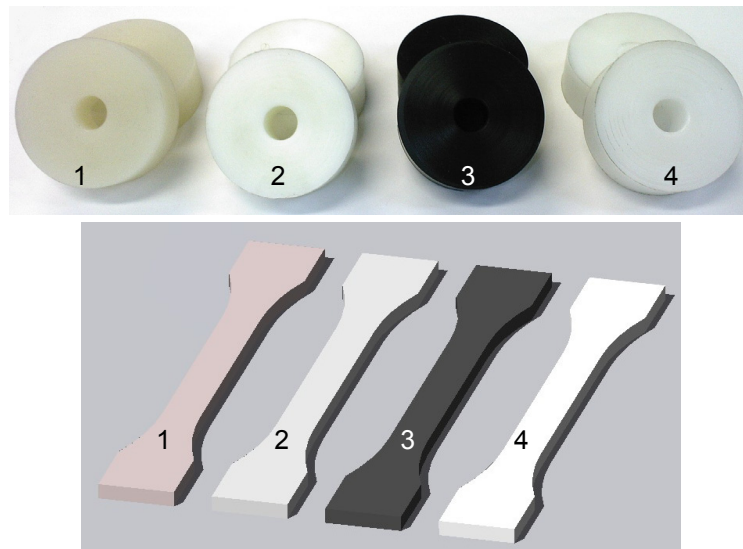


Figure 4. Specimens prepared for machining and for tensile tests

In the Table 2. the more important properties of polymers tested can be seen summarized.

Table 2. More important properties of plastics

Polyme r	Strength [MPa]	Toughnes s (Charpy) [kJ/m <sup>2</sup> ]	Sliding characteristi c ( $\mu$ )	Thermo- duricity [°C]	Hardness	Density [kg/dm <sup>3</sup> ]
<b>PA 6G Na</b>	77 - 110	112	0,15 - 0,5	-40 - 140	Rockwell 85 – 98 HRC	1,15 – 1,6
<b>PA 6G Mg</b>	77 - 110	112	0,15 - 0,5	-40 - 140	Rockwell 85 – 98 HRC	1,15 – 1,6
<b>POM C</b>	70 – 80	8	0,25 – 0,45	5 – 120	Rockwell 86 – 90 HRC	1,4
<b>HD 1000</b>	20 – 24	no fracture	0,2 – 0,3	-80 – 110	Shore 60 – 65 D	0,96

#### Cutting parameters

Feeding/rev.:  $f = 0.025, 0.05, 0.1, 0.2$  mm/rev.  
 Depth of cut:  $a = 0.1, 0.25, 0.5, 1, 2$  mm  
 Cutting speed:  $v = 50, 100, 200$  m/min

#### Tensiling parameters

Speed:  $v = 50$  mm/min  
 Humidity: RH = 50 %  
 Temperature:  $T = 23$  °C

### 2.3 Forming of the cutting tool

The cutting angles of high-speed steel (HSS Co5) turning tool have been determined on the basis of technical tables. The relief angle:  $\alpha_0 = 10^\circ$ , the rake angle:  $\gamma_0 = 5^\circ$ . The grinding of turning tool was carried out on profile-grinding machine using diamond grinding wheel. The ready made turning tool can be seen in Figure 5.

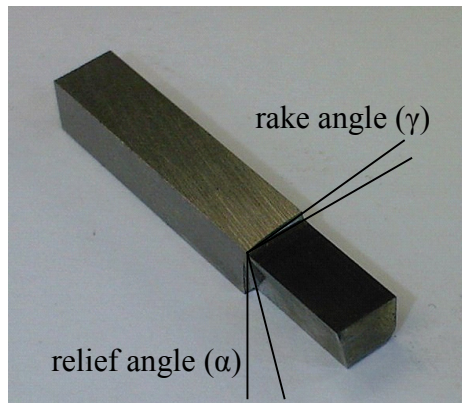


Figure 5. The bit of turning tool used.

### 3 TEST RESULTS AND THEIR EVALUATIONS

We have measured two-way forces during tests. The tangential-directional main cutting force and the axial feeding-directional force. We have grouped the materials by depth of cut, by feeding within on these by cutting speed. Unite these in one file we have got four series main cutting force and the same series feeding-directional cutting force diagrams. We have made one-one diagram by parameter from these. Figure 6. and 7. show one-one sample diagram. The cutting force given (main or feeding directional) as well as the feeding ( $f[\text{mm/rev.}]$ ), depth of cut ( $a[\text{mm}]$ ) and the cutting speed ( $v[\text{m/min.}]$ ) appear in the diagram title. The force values  $[\text{N}]$  given appear on the vertical axis, the cutting time  $[\text{s}]$  appears on the horizontal axis. We have presented all four materials in one diagram, so it can be well comparing that at same cutting parameters how great force befalls onto the cutting tool at various materials. Each colour marks one material according to mark explanation under the diagram. Continuous line shows the test results. The dotted line shows the average during measuring time given. Its value can be seen beside the line.

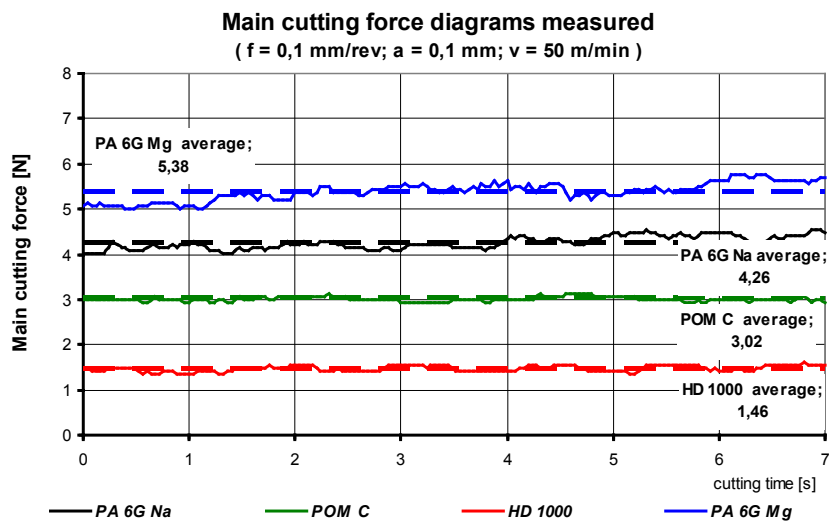


Figure 6. Main cutting force value at materials tested at cutting parameters given.

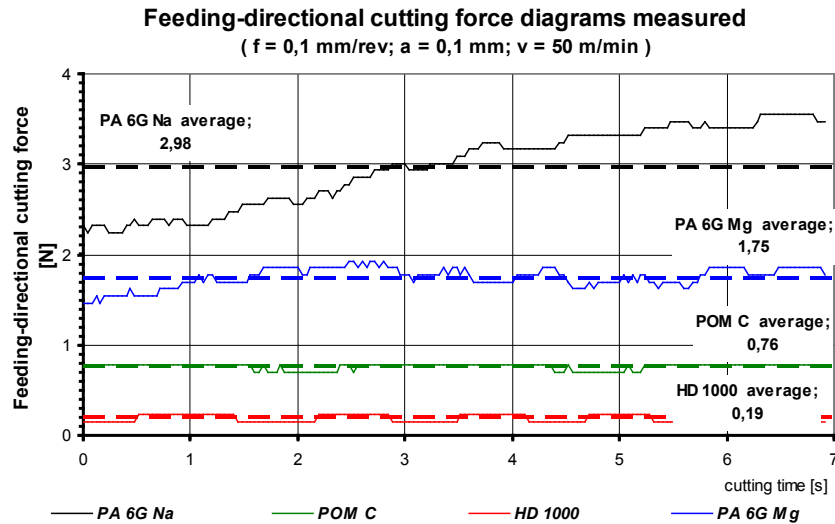


Figure 7. Feeding-directional cutting force at materials tested at parameters given.

As each workpiece tested had the same directions the measuring time period was continuously changing because of various feeding and cutting speed values. Therefore we have 7 s –time taken into account at most measuring. In case of certain cutting parameters this value could not be reached, therefore at these parameters the cutting time was reduced to 4 at one case 2 s respectively. The next diagram we have presented the main –and feeding- directional cutting forces in the function of depth of cut and of feeding from average values belonging to parameters given according to the following sample (Figure 8). Similar evaluations were done for each material types.

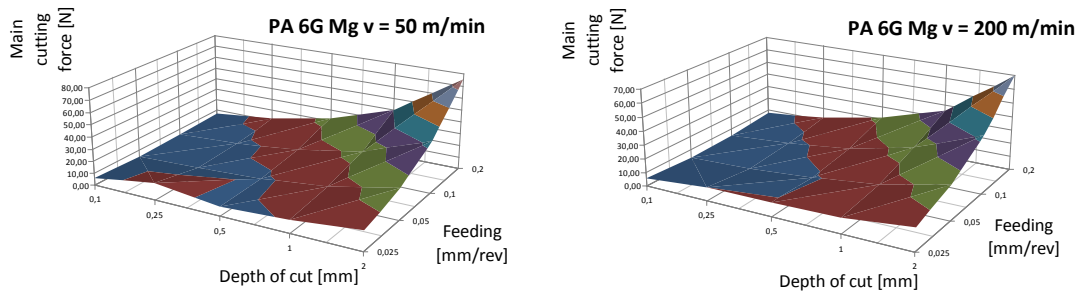


Figure 8. The value of main cutting force in the function of depth of cut and of feeding, PA 6G Mg

### 3.1 Specific cutting resistance

Cutting materials the specific cutting resistance ( $k_s$ ) is an important factor. The following sample shows its change in the function of depth of cut and of feeding (Figure 9).

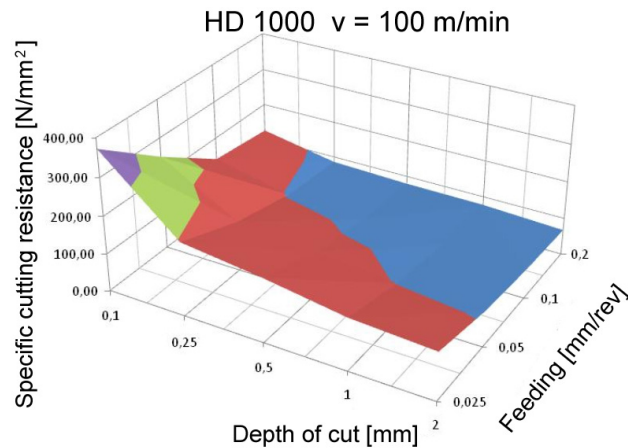


Figure 9. The value of specific cutting resistance in the function of depth of cut and of feeding, HD PE 1000

According to the relation to be found in the literature the main cutting force is the function of the specific cutting force (or resistance) and of the chip area. As during measuring we have also measured the main cutting force, the chip area was given because of parameters set, so the value of the specific cutting force can be got by transposing the original relation.

$$F_v = k_s \cdot A = k_s \cdot a \cdot s \Rightarrow k_s = \frac{F_v}{a \cdot s} \rightarrow \left[ \frac{N}{mm^2} \right] \quad (1)$$

The material tested and the cutting speed used occur in the title of sample diagram. Beside the depth of cut and feeding the specific cutting resistance (y-axis) in  $N/mm^2$  unit can be found on the datum lines.

### 3.2 Chip pictures (photographs)

The chip removed during machining have been collected and photographs have been made. Based on these the types of chips formed can be examined. Figure 10. shows the chip pictures (splint, continuous chip, transitional platelike, elemental) in the function of feeding and depth of cut at 50 m/min cutting speed at POM C material. It can be established those parameters at materials in case of which chip type meets well the practical requirements.

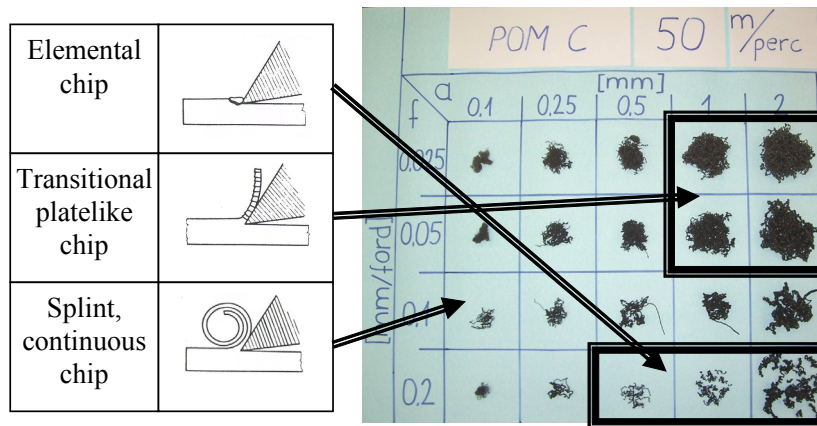


Figure 10. The forming of chip picture in the function of depth of cut and of feeding, POM C

### 3.3 Tensile strength and specific strain

During the test the pulling force ( $F$ ) and strain ( $\Delta L$ ) is registered. From these data we have determined the tensile strength values and specific strain.

$$\sigma = \frac{F}{A} \rightarrow \left[ \frac{N}{mm^2} \right] \quad (2)$$

$$\varepsilon(\%) = 100 \cdot \frac{\Delta L_0}{L_0} \rightarrow [\%] \quad (3)$$

As an example Figure 11 shows the tensile diagram of POM C, where tensile strength is plotted against specific strain. While the different colors belong to different test samples the black dashed line expresses the average of six measured samples. Later the averaged curves were taken into account for further evaluations.

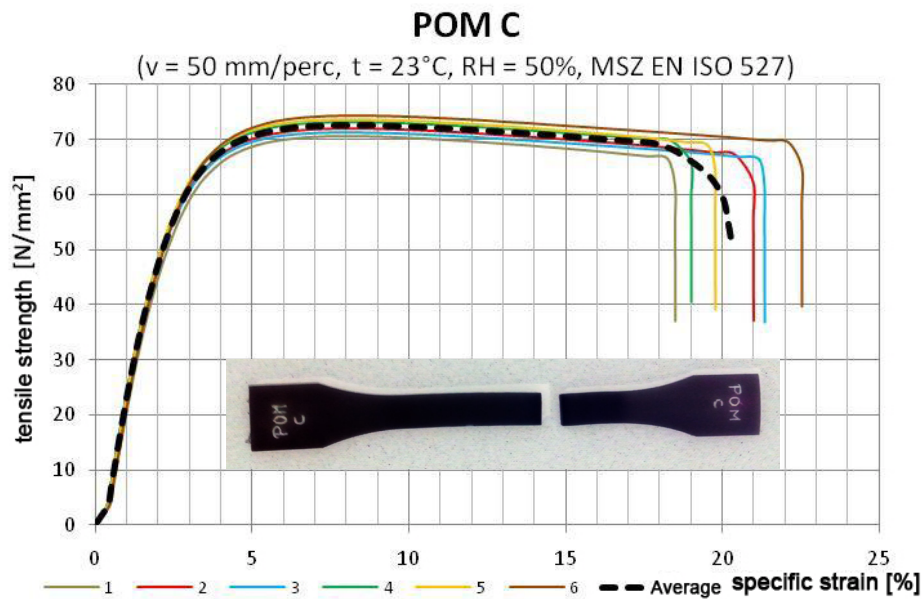


Figure 11. Tensile curves of POM C

Figure 12. shows the yield stress values determined from tensile tests. We found that PA 6G Mg material had the highest yield strength.

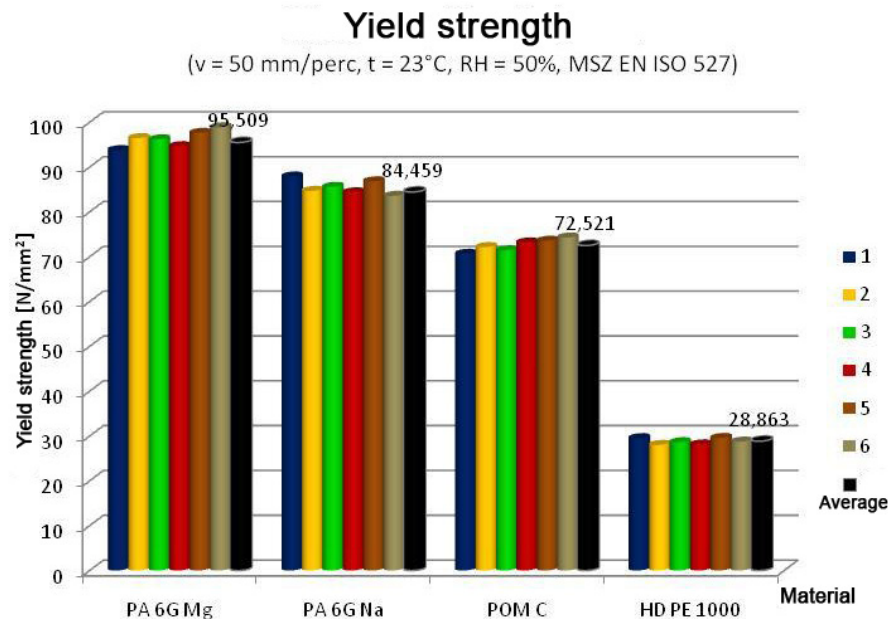


Figure 12. Yield strength of the different samples

### 3.4 Quotient of specific cutting resistance and yield strength

We divided the specific cutting resistance ( $\text{N/mm}^2$ ) (according to the set parameters -  $a$ ,  $f$ ,  $v$  -) with the yield stress values:

$$\frac{k_s}{\sigma} \rightarrow [-] \quad (4)$$

These quotient values were plotted against the product of “ $a$ ”- cutting depth and “ $f$ ”- feed, namely the chip’s cross section ( $A_c$ ,  $\text{mm}^2$ ). Figure 13. shows as an example the UHMW-PE HD 1000 material. The quotient is dimensionless number. All of those graphs were constructed for each materials.

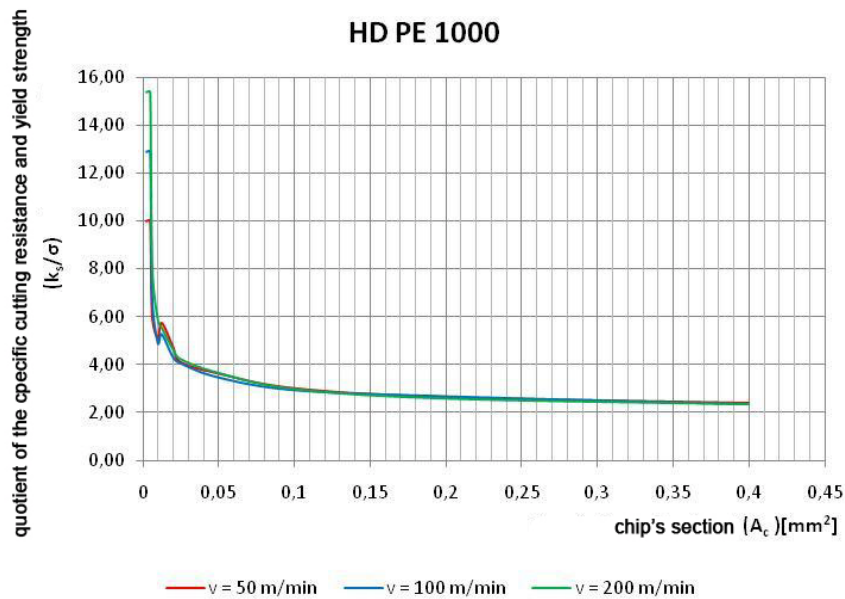


Figure 13. The quotient of the specific cutting resistance and yield strength against the chip's section for HD PE 1000

#### 4 CONCLUSIONS

- It can be established from the test results that PA 6G Mg –material proved to be the toughest from both the cutting force and the specific cutting resistance point of view. The specific cutting force decreases substantially by increasing the cutting parameters (feeding, depth of cut). Taking into account the chip type formed it can be said that it is a hardly machineable material. Using the lower feeding (0.025 mm/rev) is suggested.
- The PA 6G Na polymer shows a little lower toughness from the cutting force point of view, on the other hand in case of the specific cutting force it shows already more important change, approximately it reduces into third. Its value with the increasing of feed and depth of cut does not decrease such amount as in case of Mg-containing material. At cutting the small feeding (0.025 mm/rev) and the greater depth of cut (1-2 mm) is suggested.
- At POM C –material could be observed the further decrease of cutting – and specific cutting force. Both decreased into half approximately, but in case of latter, similarly finding PA 6G Na –material, neither here decreased such amount with increasing the feeding and depth of cut as at Mg –containing material. From the standpoint POM C had got the most favourable chip picture among the engineering plastics taking part in tests. Comparing to PA 6G –materials here is suggested the use of greater feeding with increasing depth of cut which results more favourable chip type forming, too.
- The smallest cutting forces can be measured at HD 1000 –polymer. It can be well observed at the value of the specific cutting resistance that this material has got the lowest toughness. From the standpoint of turning this is not a favourable material as regarding the chip type formed is split (continuous chip) in great part of cases tested. The analysis made can be well used in practice. The favourable values of feeding, of depth of cut and of cutting speed, within the ranges tested, can be set for cutting materials tested and for the favourable chip picture.
- We measured the tensile properties of the materials according to MSZ EN ISO 527 standard with a type of INSTRON 5581 tensile machine and we prepared the tensile stress – deformation curves of the polymers. From these diagrams we determined the yield stresses of the materials. We plotted the quotient of the specific cutting resistance and the yield stress in the function of the chip cross section with the all machining parameter groups.
- The specific cutting resistance values of the engineering polymers practically are not available. Only the mechanical properties are highlighted in producers' data sheets. Based on my research work knowing the tensile values of the material the specific cutting resistance can be estimated in case of a given machining settings. These can ease significantly the cutting calculations and the proper technological setup and determine the type of chip produced with a given setup. In the engineering practice the obtained new information formerly were not available, but now the commonly used engineering polymers have special machining database connecting the cutting forces, tensile values, chip formations and removal into one technological datasheet.

## 5 REFERENCES

- [1] Antal – Fledrich – Kalácska – Kozma: Műszaki műanyagok gépészeti alapjai, Műszaki műanyagok gépészeti alapjai, Minerva-Sop Bt. Sopron, 1997
- [2] Angyal B., Dobor Lné., Palásti K. B., Sipos S. – A Forgácsolás és Szerszámai – Műszaki Könyvkiadó, Budapest, 1988
- [3] Frischerz, Dax, Gundelfinger, Häffher, Itschner, Kotsch, Staniczek – Fémtechnológiai Táblázatok – B+V Lap- és Könyvkiadó Kft., 1997
- [4] Dr. Kalácska Gábor - Műszaki Műanyag Féltermékek Forgácsolása - Quattroplast Kft., Gödöllő, 2005.
- [5] Nagy P. S. – Szerszámgépek, gyártórendszerek – BDMF jegyzet, Budapest, 1997
- [6] [www.quattroplast.hu](http://www.quattroplast.hu)

# ROUGHNESS MEASUREMENT PROBLEMS IN TRIBOLOGICAL TESTING

V. Rodriguez<sup>1</sup>, J. Sukumaran<sup>1</sup>, M. Ando<sup>2</sup>, P. De Baets<sup>1</sup>

<sup>1</sup> Ghent University, Laboratory Soete, Belgium

<sup>2</sup> Szent István University, GÉTI, Hungary

**Abstract** In tribological measurement of thermoplastics against steel the surface roughness has a potential effect in dictating the frictional behavior of the material. In most cases the roughness of the specimen is measured before and after the test, where it affects the friction force and influences the mechanism involved. The roughness of the material is not the exact value and it has a deviance which depends upon the machining process used in preparing the surface. Generally, the direction of machining has an influence on the topography of the surface in case of turning, milling and drilling but in case of pressed components the direction has no effects. In order to maintain ideal test condition the surface roughness of the test materials has to be consistent for the given number of samples. Even though the test specimens are machined in the same machine with same parameters there are number of parameters involved in deciding the consistency of the surface roughness. The roughness of the surface are defined by number of parameters such as Ra, Rz and few 3D parameters in such a case narrowing down to a specific constant is vital. The results from the roughness is not made from one measurement were an average and deviance from several measurement decides that if two ideal samples has same or different roughness.

**Keywords** : roughness comparable, machined surface, Ra, Rz.

## 1 INTRODUCTION

The influence of surface roughness has an important role in tribology, because most off the time the friction and wear in two solids sliding against each other are encountered in several day-to-day activities [1]. Usually the surface description in the scientific articles is not appropriate and thus an overview is made on identifying the suitable basic surface parameters.

Surface texture is the repetitive or random deviation from the nominal surface which forms the three dimensional topography of the surface. Fig. 1. Show different representations of surface roughness having the same Ra- value (Ra~0.64)[2].

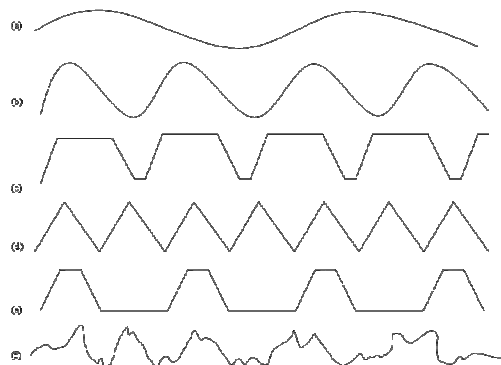


Figure 1. Various surface profiles having the same Ra value [Ra~ 0.64].

Roughness (nano-and microroughness) are formed by surface irregularities of short wavelength, characterized by peaks (asperities) (local maximum) and valleys (local minimum) or varying amplitude and spacing that are larger than molecular dimensions. These create the predominant surface pattern, which exhibits those surfaces features intrinsic to the manufacturing process.

Numerous techniques are used to quantitatively measure surface roughness which includes optical methods like optical interference and light scattering and mechanical methods, such as oblique sectioning and stylus profilometry.

Surface roughness most commonly refers to the variations in the height of the surface relative to a reference plane. It is measured either along a single line profile or along a set parallel line profiles (surface maps). It is usually characterized by one of the two statistical height descriptors advocated by the American National Standards Institute (ANSI) and the International Standardization Organization (ISO). According with those statistical height descriptors they defined this parameters like, five extreme-value height descriptors are defined as follows:  $R_a$  is defined as the distance between the highest asperity and the mean line:  $R_v$  is defined as the distance between the mean line and the lowest valley:  $R_z$  is defined as the distance between the averages of five highest asperities and the five lowest valleys; and  $R_{pm}$  is defined as the distance between the averages of the five highest asperities and the mean line. The reason for taking an average value of asperities and valleys is to minimize the effect of unrepresentative asperities or valleys which occasionally occur and can give an erroneous value if taken singly.  $R_z$  and  $R_{pm}$  are more reproducible and are advocated by ISO. In many tribological applications, height of the highest asperities above the mean line is an important parameter because damage may be done to the interface by the few high asperities present on one of two surfaces; on the other hand, valleys may affect lubrication retention and flow.

The selection guide lines for the roughness value in respect to the function and manufacturing process is certainly not complete nevertheless the basics can serve as a reference (Fig. 2., the surface roughness is  $R_a$  in this case) . The overview shows that sliding surfaces with very low roughness value ( $R_a < 0.4$ ) often require a surface finish after turning or cutting, e.g grinding.

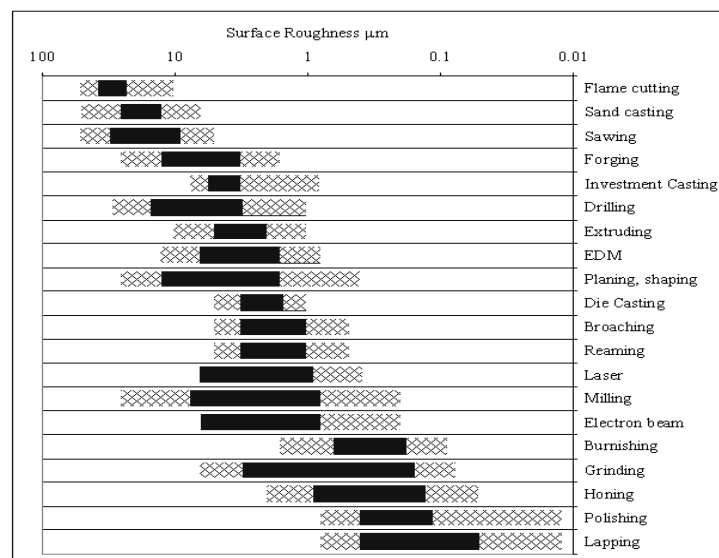


Figure 2. Limited selection of guidelines for surface roughness in respect to function and manufacturing process.

According with others studies [3] all the plastics tested against steel showed low coefficient of friction when mating rough surfaces but this also depends upon the external parameters like contact pressure and force. In different engineering plastics against steel showed that the plastics is characterized by a roughness of  $R_a = 0.05 - 0.10 \mu\text{m}$  is mean that is a smooth surface and the steel material is characterized by a roughness of  $R_a = 0.10 - 0.30 \mu\text{m}$  is mean that is a rough surfaces [4].

Materials	Smooth surface / coefficient	rough surface / coefficient
PA6-S355	$R_a = 0.05 - 0.2 / \mu = 0.2 - 0.4$	$R_a = 0.5 - 1.5 / \mu = 0.4 - 0.6$

In tribological application the surface roughness has significant effect on the friction force and wear. The aim of the article is to illustrate the appropriate values and methods from the surface measurements and on deciding the usage of parameters like Ra to Rz.

## 2 SURFACE ROUGHNESS OF SPECIFIC SURFACE AND STATISTICAL DISTRIBUTION

In the surface roughness measurement it is very difficult to measure at the same place every time and thus different values produced as a result of measurement. The working conditions in the machining process changes from time to time due to tool wear, dynamic phenomenon of chip formation, resonance of the machine and possible thermal shock. Describing roughness parameter of a specific surface one has to accept that a deviance exist all the time. Usually there are several independent parameters which has an effect on the surface roughness, so the Gaussian (normal) distribution can be used to resolve the deviance. When somebody use for example  $Ra=3.2$  necessary to use an interval also ( $Ra=3.2\pm0.2$ ). The size of the interval for the deviance basically depend on the machining process (condition of the tool, parameters of the machining) and the material (steel, polymer, aluminium).

A steel plate (S355) was ground and measured for the roughness on 24 different points (Table 1.), and the Fig. 3. shows the group of different values from the measurement in the whole group. The distribution of the values shows normal shape, because the peak is in the middle, and no other peaks can be found at the left or right side, and there is only one peak in the whole roughness group.

Table 1. Ra values of the grinded S355 plates

0,441	0,533	0,615	0,631	0,653	0,699	0,716	0,792
0,515	0,602	0,616	0,633	0,658	0,704	0,737	0,792
0,524	0,607	0,628	0,636	0,669	0,712	0,749	0,819

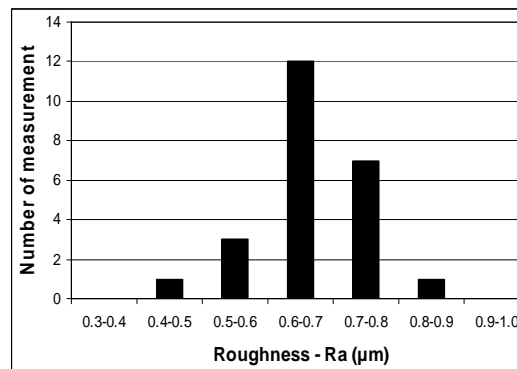


Figure 3. Roughness values of grinded plate.

Fig. 4. Shows the calculated Gauss-curve based on the 24 measurement. The average point ( $Ra = 0.653$ ) and the  $\pm 2\sigma$  points ( $Ra = 0.467$  and  $Ra = 0.840$ ) is also marked in the figure.

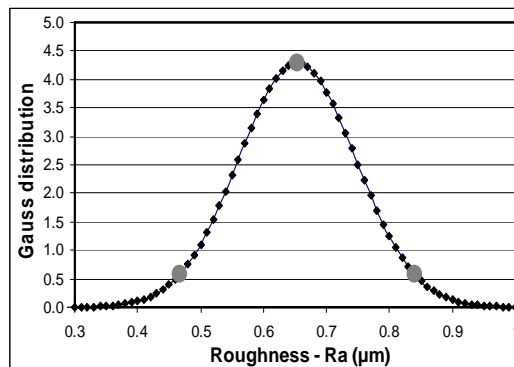


Figure 4. Gauss distribution base on 24 measurements.

The  $\pm 2\sigma$  points show the limit, which 95% of the test results falls between the two points. In our case only one value is out of this range, which represents 4.2%. Table 2. contains the values which belong to different sigma criteria to explicitly show the values which are present outside the range.

Table 2. Effect of the sigma limits.

Sigma	Level	Ra interval ( $\mu\text{m}$ )	Average $\pm$ %	Result out of the range	
$\pm 1\sigma$	68%	0.560-0.746	$0.653 \pm 14.2\%$	8 ps	33.3%
$\pm 2\sigma$	95%	0.467-0.840	$0.653 \pm 28.4\%$	1 ps	4.2%
$\pm 3\sigma$	99.7%	0.374-0.933	$0.653 \pm 42.6\%$	0 ps	0%

In normal technical practice an error of 5% is acceptable, which is accommodated inside the  $\pm 2\sigma$  range. Some specific fields  $\pm 3\sigma$  is also used, however, the application of  $\pm 1\sigma$  (also from the diagrams) are incorrect and leading to misunderstanding.

### 3 EFFECT OF THE MACHINING DIRECTION

Most of the machining process creates the roughness profile with respect to the direction of machining and the type of machining process itself has a direction factor on the surface profile. For example in case of turning or grinding the measured value dramatically changes when the measurements are made parallel or perpendicular to the feed direction. Milling has also this effect, but the differences of the values are relatively less. Some machining process exist which has minimal effect on the direction such as finishing sander or fine polishing. In case of polymers the pressing also has no directional effects of the roughness.

Fig. 5. Shows the surface roughness in case of grinding (different feed rates). Even though the samples are machined with same machining parameters a clear difference is seen between the parallel and perpendicular measurements seen from the Ra and Rz values which are not close to each other. In case of milling (Fig. 6.) both the group from parallel and perpendicular measurements are also seems separated but the differences are relatively less. The values in case of milling ten times bigger then the grinding, for this, the nominal values cannot be used to describe the parameter.

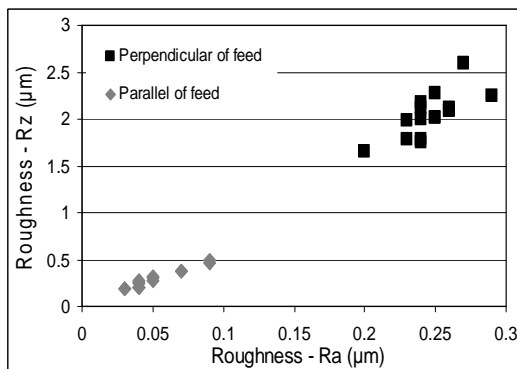


Figure 5. Effect of the measuring direction in case of grinding.

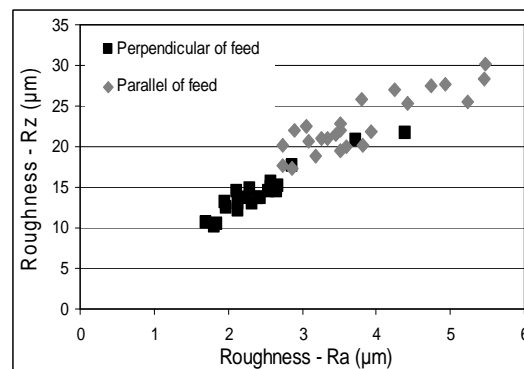


Figure 6. Effect of the measuring direction in case of milling.

The Fig.7. Shows the measurements from a pressed polymer sheet where is no difference in the sample surface on both the directions (the grey and the black dots are in one cluster). The two groups in fig is because of the different material of the two samples. It is also interesting that pressed surface has ten times smoother surface than the grinding. In tribology it is well known that in polymer-steel contacts, smoother surface helps to the adhesion characteristics. Using finishing sander also produces smooth surface without directional effect. On the Fig. 8 the dots are in the same group.

#### 4 RELATIONSHIPS BETWEEN RA AND RZ NOMENCLATURE

From the previous figures it is seen that Ra and Rz parameters are not dependant on each other but on the other hand they are not completely independent as well, because they are calculated values from the same primary profile. In most cases it is necessary to convert the two values, for this some approximate method are exist.

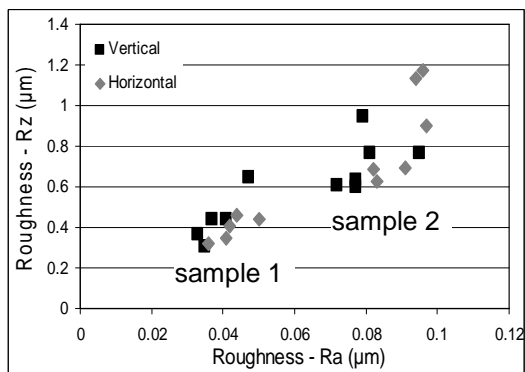


Figure 7. Effect of the measuring

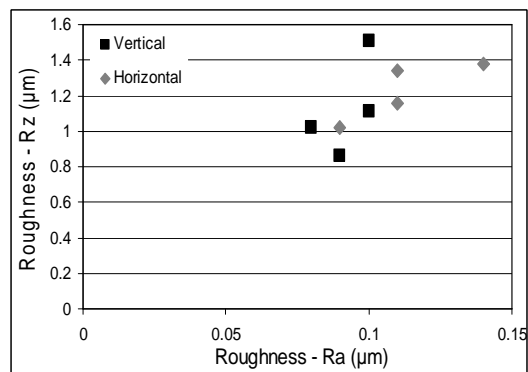


Figure 8. Effect of the measuring

direction in case of polymer pressing. direction in case of using finishing sander.

One well known factor is  $Rz=4 \cdot Ra$  which cannot be used all the time. The basic problems is that this equation is not sensitive to the Gaussian distribution. In the real application if the engineer choose  $Rz=15$  (from the drawing) but from the machined part we can measure just Ra, we should use an other equation ( $Ra=Rz/7.5$ ) to get  $Ra=2$  which means the machining process produces values between  $Ra < 2$ , that means Rz will be less than 15. On using the first equation ( $Rz=4 \cdot Ra$ ), we get  $Ra=3.75$ , but on the Fig. 9. it is clearly sene if we measure  $Ra=3.7$  under the machining, we can easily measure  $Rz=15-27$ , which is not appropriate. So if Rz is unknown we should use  $Rz = 4 \cdot Ra$ , but if Ra is unknown we should use  $Ra=Rz/7.5$ . This two equation are the borders of the commonly used machining process. But for specific machining this borders could change. Table 3. contain the equations of the borders for different parameters.

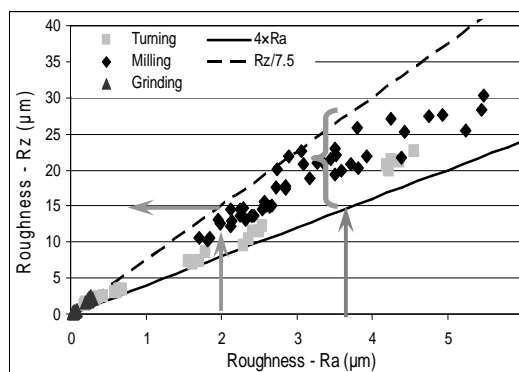


Figure 9. Connection between Ra and Rz in case of different machining.

#### 5 HOW CAN COMPARE TWO DIFFERENT SURFACE

In a set of values from the measured surface parameters it is possible to calculate the mean and the standard deviation, but to decide to the values are same the f-test and t-test should be used.

These calculations does already exist but the aim is to sort out the correct one between several parameters ( $R_a$ ,  $R_z$ ...) and directions effects. From the different values of  $R_a$  and  $R_z$  correlation cannot be made to make a certain surface. Fig 10. and Fig 11. show the results of different grinded steel plates in parallel and perpendicular directions. As you can see there is difference in the values of  $R_a$  and  $R_z$  between the perpendicular and the parallel measurements. Measurements parallel of the machining has less influence so the difference rather belongs to the results from the measurements in the perpendicular direction (Fig. 12).

Table 3. Relationships between the surface parameters.

Unknown parameters	Measured parameters	Border
$R_a$	$R_z$	$R_a = \frac{R_z}{7,5}$
$R_a$	$R_q$	$R_a = \frac{R_q}{1,4}$
$R_z$	$R_q$	$R_z = \frac{R_q}{0,3}$
$R_z$	$R_a$	$R_z = 4 \cdot R_a$
$R_q$	$R_a$	$R_q = 1 \cdot R_a$
$R_q$	$R_z$	$R_q = 0,15 \cdot R_z$

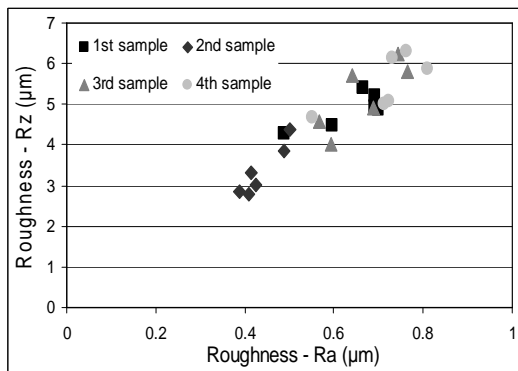


Fig. 10. Different grinding samples (perpendicular of feed).

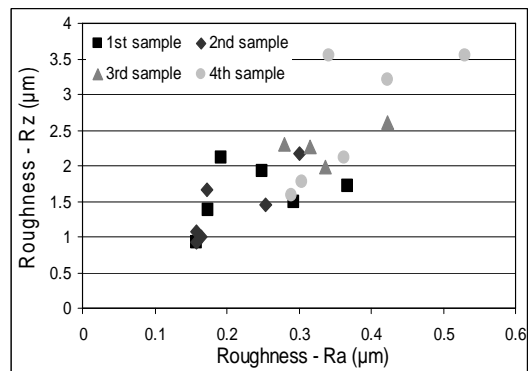


Fig. 11. Different grinding samples (parallel of feed).

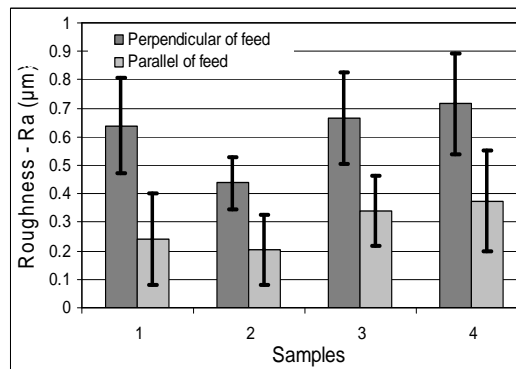


Figure 12. Roughness of different samples and directions.

At first the t-test shows that the deviances of the plate are the same (usually this is true, because of the same machining process). If the t-test is good, f-test show the results are different or same. In our case the second sample is different from the others, the other three are same. From the experiments it is clear that using the values of Ra or Rz are almost same to compare different surfaces. The parallel values are much closer then the perpendicular. In case of parallel the difference is just between second and fourth samples. It is important to know the two surface are same and better to use the statistical method for identifying the parameters (Ra, Rz...) which can be used as a reference in the further experiments. In our case the second sample was regrinding to achieve the same surface.

## 6 CONCLUSION

In tribological experiment surface roughness is one of the important parameter. Because of that a comparable a specific surface roughness is needed. Unfortunately, sometimes even with the same machine and tool results in different surfaces. In the roughness measurement it is possible to calculate the average but it is also important to calculate the standard deviation. Direction effect is vital considering the roughness measurement. In case of turning and grinding the parallel and the perpendicular values are completely different. In case of milling also has direction effect but relatively less because the values are closer to each others. Some machining techniques have no directional effect (finishing sander, pressing).

Between the surface roughness parameters (example Ra and Rz) exist some approximate method to change each other, but this methods are sensitive to the directions. To compare two surface the f-test and t-test should be used. Easy way is to not compare all the parameters, but just the one perpendicular to the feed. Result of the statistical method practically are the same in case of the different surface roughness parameters (Ra, Rz...). If the samples surfaces are not the same it is worth to remac hine the different sample.

## 7 REFERENCES

- [1] Van Beek Antoni. "Advanced engineering design". Delft University of technology mechanical engineering. Edition 2006. Pg 138-141.
- [2] Bhushan Bharat. "Modern Tribology Handbook". Volumen One. September 2000. Pg 49-50.
- [3] Quaglini Virginio. "Influence of counterface roughness on friction properties of engineering plastics for bearings applications". Materials and design. Italy 2009. Pg 1650-1658.
- [4] Yamaguchi. Y, "Tribology of plastics materials" Tribology series. Volumen 16. 1990 Elseiver.

# EFFECT OF VELOCITY ON ROLL/SLIP FOR LOW AND HIGH LOAD CONDITIONS IN POLYMER COMPOSITE

J. Sukumaran<sup>1</sup>, M. Ando<sup>2</sup>, V. Rodriguez<sup>1</sup>, P. De Baets<sup>1</sup>

<sup>1</sup>University of Gent, Department of Mechanical Construction and Production, Sint-Pietersnieuwstraat, 41, 9000 Gent, Belgium

<sup>2</sup>Szent István University, GÉTI, Páter Károly utca 1. 2100 Gödöllő, Hungary

**Abstract** In the last decade polymer composites are often used without lubrication on both low and high speed applications. Some of the application areas are marine, automotive and agriculture used as bearings and cams where roll-slip is the dominant mechanism. Limited studies are made for composites relating such applications where rolling/sliding condition influences the tribological behavior of the material. Investigating the roll-slip phenomenon for identifying the influence of velocity on frictional behavior can mark a boundary to map the use of composites with respect to its application. Moreover, the design of the material can be optimized to match the operating conditions. In the current research the polymer composite (with polyester matrix) has been tested under rolling-sliding condition for two different loads with 61N and 210N and with different speeds ranging from 10 rpm to 700 rpm. Ideal conditions in terms of roughness, slip ratio, surface temperature and ambient temperature were maintained to reduce the frictional heating. Using a 20% slip ratio the behavior of the material was observed for the tribological characteristics where the rate of increase of friction force follows an exponential pattern with increasing speeds. Nevertheless, on testing with high speeds a steady rate of increase in the friction curve was observed. Friction behavior of composites under different speeds is briefed with the microstructural characteristics for low and high loads.

**Keywords** Rolling/sliding, polyester composites, friction force, effect of velocity

## 1 INTRODUCTION

Composite are adopted as a solution to new materials in the bearing industry for dry running applications in-order to avoid complex lubricating system [1]. Fiber composites are the preferred materials in such applications for the versatility in fibre orientation, fibre usage and volume fraction of the composite which can be altered according to the requirement [2]. The fiber composites are preferred for their relatively high young's modulus. Apart from the fibbers and resins, fillers are added as a lubricant to have better frictional behaviour [3- 5]. Internal lubricant such as PTFE is generally used as friction modifiers. Low coefficient of friction, resistance to stick-slip and high anti-adhesive property of PTFE makes it a suitable material as friction modifiers in bearings [6, 7]. It was also found that the fiber orientation normal to the sliding direct has produced favourable friction conditions [8].

The influential parameters mostly investigated in a tribological system of polymer composites are the velocity and the load governed by the visco-elastic property of the material[8]. Even though standard rules dictate the tribological behaviour, the system as a whole does not permits to have the same results for the similar materials at same test condition [3]. Previous research by El Syed et al [1] with fiber reinforced polymer composites has produced high coefficient of friction for low pv ratio which is explained by the softening behaviour of the composite. Contradicting behaviour on the tendency of the friction co-efficient was observed by Su et al on investigation PTFE composites [6]. The friction coefficient varies inevitably independent to the applied load where materials tested at high speeds have low coefficient of friction due to the polishing effect. Apart from the load and the velocity the frictional heating plays a vital role by having a deposit of transfer layer in the counterface material and thus reducing the coefficient of friction.

The deposit of transfer layer is a system and the material dependant, early research by El-Tayeba et al on polyester composites with sugarcane fibre and glass fibre has dissimilar results due to the back transfer of polymers in one of the materials by adhesion process [9]. Since a clear boundary has not been characterized between the presence of transfer layer and the back transfer, the material interaction rather seem to be uncertain. The current research has the underlying principle of interaction between composite-metal pairs rather than composite-composite pairs. And this is maintained by avoiding the phenomenon of transfer film and isolating the temperature variable (By having approximately a constant contact temperature along the test).

In the tribological system the most commonly occurring phenomenon is sliding and most of the researches correspond to pure sliding condition where adhesion plays a vital role. Apart from sliding the rolling

phenomenon exhibits in certain engineering components like gear, cams and rollers which tend to have roll-slip. This rolling to sliding at the same time has deformation as the additional mechanism to complicate the investigation. Only few researches have been conducted on polymer-metal and polymer-polymer contacts [10-13] thus leading to a situation of testing the interaction between composite-metal pair on rolling/sliding conditions.

## 2 EXPERIMENTAL

### 2.1 Materials

A combination of thermoset composite against steel is used for the current investigation. Commercially available polyester fiber reinforced polyester (Orkot) is used in place of the thermoset composite and 40CrMn tool steel is used as a counterface material. Orkot (Trelleborg AB) is a specially designed material used for bearings, the composite comprises polyester fabric with thermoset resin and PTFE as a internal lubricant. The material properties for the thermoset composite and the counterface material are given in Table 1. The used composite samples are in the form of a ring where a holder is used under press fit to fix the test material to the setup on running against solid counterface material. The composite ring has 8mm width and 5mm thickness. The diameter of the contacting surface for the composite and the counterface material is 90.12 & 74.93mm.

Table 1. Properties of the used materials.

Properties	40CrMn	Orkot
Yield strength [MPa]	415	55
Young's modulus [GPa]	205	3.3
Impact Strength (Charpy) [kJ/m <sup>2</sup> ]	590	122
Hardness	220 HB	100 Rockwell M
Maximum allowable service temp. [°C]	-	130

### 2.2 Test device

Although standards are available to study the frictional behaviour of materials for sliding phenomenon, the involvement of rolling in some cases urges the materials to be tested for roll-slip. A twin-disc is the apt model to investigate the contact between composite-metal pairs during rolling/sliding condition. For the current investigation the modified twin-disc setup at Laboratory Soete is used to test composite against tool steel for a specific slip ratio which is achieved by the difference in the diameter of the test disc and the counterface material disc. The required slip ratio is obtained by having different diameter of steel disc ( $d_1$ ) and composite disc ( $d_2$ ), which can be calculated with (1):

$$s = \left( \frac{d_2 - d_1}{d_1} \right) \cdot 100 \quad (1)$$

Torque meter attached to the shaft of the steel disc is used to measure the friction torque. Moreover, the temperature of the contact surface is measured using an infrared sensor and the normal load is induced by loading dead weights to the pivoted arm. Figure 1. shows the twin-disc setup used for testing the composite-metal pair.

All the measurements were recorded using online data acquisition system. Materials are tested with 20% slip ratio for five different speeds ranging from 10 rpm to 700 rpm for low load and high loading condition. A special program is developed (using labview) to test the material for different speeds. Initially a running-in is made for 16 minutes preceded by the measuring cycles where a specific time for conditioning is introduced for changing the speeds. Conditioning is done in order to avoid the transition during change in speed. In regards to the temperature measurement, the infra red sensor is located 180° C away from the instant of contact.

The friction from the bearings and seals of the machine has an influence on the measured friction torque and hence to have precise results a reference torque under no load condition is supplemented from the friction-torque obtained during loading. Moreover, the friction force is calculated from the friction torque and the diameter of the test disc (2).

$$Friction\ force\ (N) = \frac{T(Nm)}{r(m)} = \frac{"Measurments" - Average\ of\ "reference\ Torque"}{radius\ of\ the\ steel\ wheel} \quad (2)$$

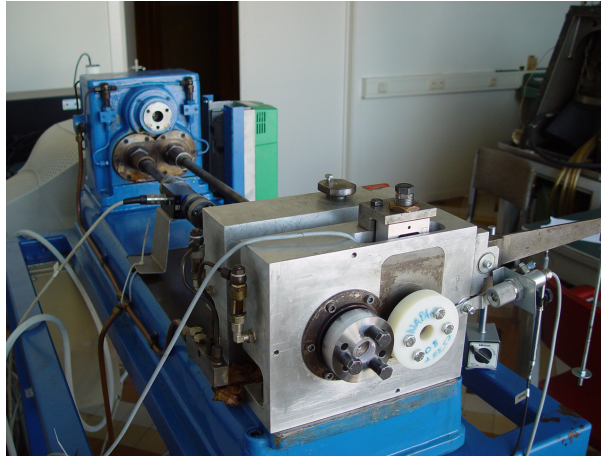


Figure 1. Shows the twin disc FZG test setup

Both the metal and composite samples were cleaned before and after the measurements. The contact surface of the counterface material is cleaned with metal sponge, acetone and alcohol (Loctite 7061), the same is used for the composite material except for the metal sponge which could change the surface parameter of the composite. Micrograph of the contact surface is taken at all intervals using a SFX microscope (Olympus) and a video camera (QICAM). Change in roughness of the contact surface is measured after every interval using a roughness tester (Homel).

### 3 RESULT AND DISCUSSION

Material behaviour on Hertzian non-conformal contacts plays a vital role in deciding the material behaviour for specific applications. Polyester composites were run against tool steel countersurface to test the tribological behaviour on rolling/sliding condition. Obtained results are the average of five measurements at every point in the curve. A deviation approximately 10% was observed which is very good in case of tribological testing. Five different speeds with 10, 100, 200, 450 and 700 rpm are used together with 61N (maximum pressure is 77.23 MPa) and 210N (maximum pressure is 143.30 MPa) loads to study the tendency of friction force. The friction force increases as the load is increased likewise the increase in speed tends to increase the friction force. Figure 2. illustrates the friction force as a function of speed for both low and high load condition.

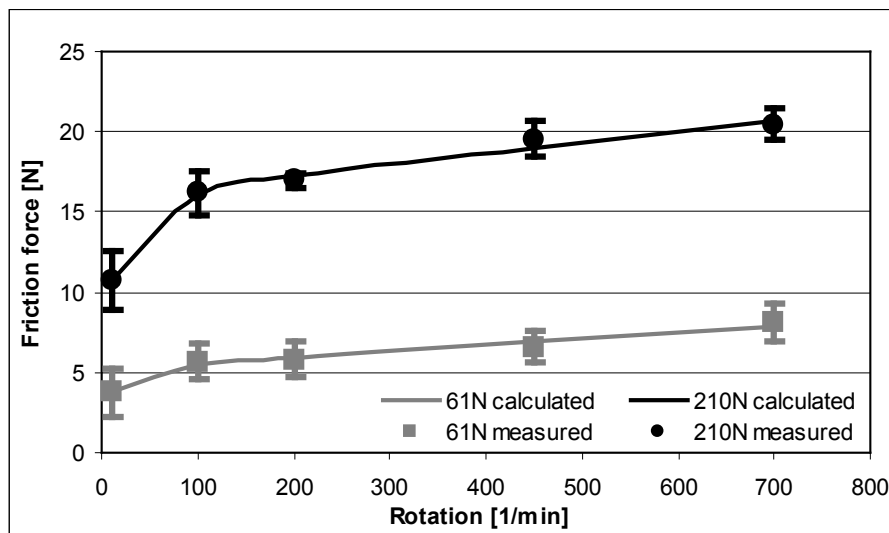


Figure 2. Friction force as a function of speed

The points in the plotted graph represent the experimental values and the curves are from the calculated functions. It is seen that the friction force is relatively less on low speeds and found to be rapidly increasing until a critical value (approximately 100-150 rpm) and saturates further to follow a linear increase to the corresponding speed. The rapid increase in friction force on low speeds is effective in high load condition relative to low load. The rapid increase in low speed can be explained with the time dependant strain

response of the polymer in the reinforced composite. The overall tendency of the curve shows exponential behaviour of the materials on testing against steel. It is interesting that the friction force increases by approximately 51% from 10 to 100 rpm on low and high load condition. In case of high speeds between 100 to 700 rpm the friction force increases just 26% at high loads and 42% in low load. This tendency might have been produced by having large rolling resistance, and there is also some effect due to the stronger adhesion during high loads.

Table 2. illustrates the functions for the curves and their  $R^2$  values where a linear increase in case of high load is seen and simultaneously the rate of increase in friction force is relatively more. But the high nominal values on changing to high speed since 100-700 rpm is 26% which means, the material on high load is less sensitive to the speed relative to the low load.

Table 2. illustrates the functions for the curves and their  $R^2$  values

M238 and PA6	Equation	$R^2$ value
61 N (77.23 MPa)	$F = 3.367 \cdot (1 - e^{-0.0897 \cdot n}) + 0.004 \cdot n + 1.718$	0.8602
210 N (143.30 MPa)	$F = 6.895 \cdot (1 - e^{-0.0256 \cdot n}) + 0.007 \cdot n + 9.082$	0.9656

### 3.1 Effect of the temperature

Most of the studies on friction force are evaluated based on the temperature effects but in fundamental research isolating a variable gives much more valuable information to design the system and the material accordingly. In the current research the effect of temperature has been eliminated by using limited time of contact. Figure 3. (a) & (b) shows the measured temperature as a function of speed where an increase in temperature of 2°C is observed in both low and high load condition. In previous research on rolling/sliding contacts of polymers the temperature increases over 80°C which has potent effect on the friction force but in our case the maximum attained temperature was 26 °C which has relatively less effect to consider friction heating to decide the tendency of the frictional curve. In most of the cases the tendency of the temperature curve is linear to the increasing speed but within a very limited range so to consider it as a major change in the temperature is not viable. Within the two degree increase in temperature higher temperature was observed in low loading condition. Temperature also has an effect on forming transfer layers in the counterface material, which was not observed in our case due to less friction heating and limited contact period. The transfer layer tends to have a condition where composite is tested against composite but in our case by avoiding such a phenomenon a real interaction between composite and metal are studied.

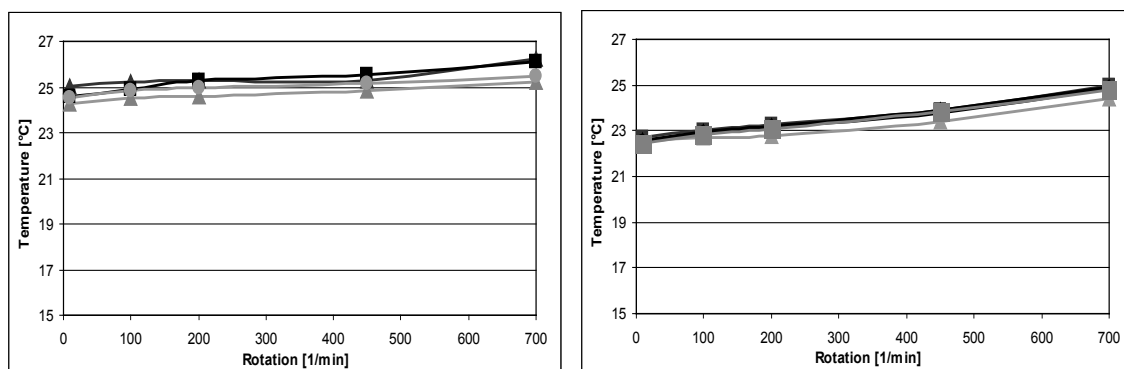


Figure 3. Measurements on temperature Vs speed (a) low loading condition (b) high loading condition

The deposition of transfer material on the counter face is critical which relies on the parameters like load and velocity activated by thermal effects. In most cases the transfer layers are very well present and in few cases the transfer layer cannot be seen due possible melting from the counterface material and transferred back to the polymer surface by adhesion. In the current research such complications were avoided and the result deliberates the influence of velocity without the aid of composite. Studies have proven that a deposit of atomic layer of plastic occurs during the first contact [14]. Nevertheless, even with an atomic layer of polymer on the counterface material the influencing factor affecting the friction force should be negligible.

### 3.2 Micrograph

Images were made on the contact surface using Olympus SRZ microscope before and after the testing. It is seen in Figure 4. (a) that a clean surface of the composite is seen before testing without any pits or

damages. But, on the other hand images shown in Figure 4. (b) & (c) from the tested surface displays pits and abraded surface.

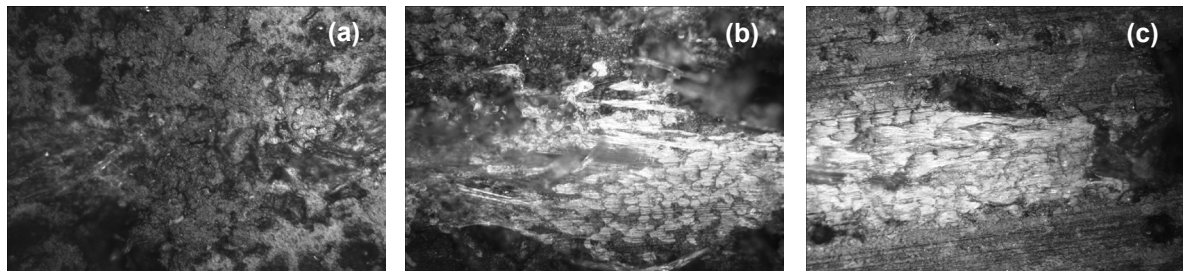


Figure 4. shows the contact surface of the composite (a) before contact (b) low load (c) high load

The scale like appearance on the contact surface is due to the aberration of thermoset leaving the matrix to expose and the pits are the places where the fibers tends to break leaving craters on the contact surface. Composite being the less hard material than the tool steel is expected to have considerable change in surface topography relative to the steel surface and hence the imaging is done only on composite surface. It is also seen from the image that the machine mark from the steel is impregnated in the composite. Comparing the image from both the loads not much difference is seen in the surface topography.

#### 4 CONCLUSIONS

Composite – metal pair which has recently captured the bearing industry for dry running application has complex mechanism involved in briefing the friction behaviour of these materials. Results from previous researches focuses on sliding but roll-slip does occur in such composite-metal pairs in applications like bearings, gears and cams. Experiments for roll-slip phenomenon under different velocities in low and high load condition produce similar results with a change in the tendency of the friction curve along the test period. The friction force increases rapidly under low speed until 100rpm and above that until 700 rpm the friction force increases linearly with increasing speed. Along the test cycle a combination of exponential and a linear behaviour of the friction curve was produced. Moreover, for the observed tendency the material is less sensitive to the changing speed in case high load. For this result there is a minimal effect of the contact temperature (less than 2°C changing) because of the special test method and the environment. There was no goal to examined the wear but from the beginning the are some craters on the composite surface.

#### 5 NOMENCLATURE

F - friction force

T - friction torque

$F_n$  - normal load

R - radius of the steel wheel

$d_1$  - diameter of the steel wheel

$d_2$  - diameter of the composite wheel

PTFE – polytetrafluorethylene

#### 6 REFERENCES

- [1] El-Sayed A.A., El-Sherbiny M.G., Abo-El-Ezz A.S., Aggag G.A., Friction and wear properties of polymeric composite materials for bearing applications, *Wear*, 184(1), 45–53, 1995.
- [2] Srivastava V.K., Pathak J.P., Friction and wear properties of bushing bearing of graphite filled short glass fibre composites in dry sliding, *Wear* 197(1-2), 145–150, 1996.
- [3] Quintelier J., Online wear monitoring of polymer matrix composites with advanced measurement techniques, Ph.D Thesis, Gent University, 2007.
- [4] Kishore, Sampathkumaran P., Seetharamu S., Thomas P., Janardhana M., A study on the effect of the type and content of filler in epoxy–glass composite system on the friction and slide wear characteristics, *Wear*, 259(1-6), 634–641, 2005.

- [5] Zhang X, Pei X, Wang Q. Friction and wear properties of combined surface modified carbon fabric reinforced phenolic composites. *European Polymer Journal* 44, 2551–2557, 2008.
- [6] Su F., Zhang Z.Z., Guo F., Men X.H., Liu W.M., Friction and wear properties of fabric/phenolic composites with plasma treated-hybrid glass/PTFE fabric, *Composites Science and Technology*, 67(6), 981–988, 2007
- [7] Burris DL, Sawyer WG. A low friction and ultra low wear rate PEEK/PTFE composite, *Wear* 261, 410–418, 2006.
- [8] Suresh B, ShivaKumar K, Seetharamu S, SampathKumaran P. Friction and dry sliding wear behavior of carbon and glass fabric reinforced vinylester composites. *Tribology International* 43, 602–609, 2010.
- [9] El-Tayeba N.S.M., A study on the potential of sugarcane fibers/polyester composite for tribological applications. *Wear*, Volume 265(1-2) 25, 223-235, 2008
- [10] Hooke C.J., Kukureka S.N., Liao P., Rao M., Chen Y.K., The friction and wear of polymers in non-conformal contacts, *Wear*, 200(1-2), 83–94, 1996.
- [11] Kukureka S.N., Chen Y.K., Hooke C.J., Liao P., The wear mechanisms of acetal in unlubricated rolling – sliding contact, *Wear*, 185(1-2), 1–8, 1995.
- [12] Gordona D.H., Kukureka S.N., The wear and friction of polyamide 46 and polyamide 46/aramid-fibre, composites in sliding–rolling contact, *Wear*, 267(1-4), 669–678, 2009.
- [13] Chena Y.K., Modib O.P., Mhaya A.S., Chrysanthou A., O’Sullivan J.M., The effect of different metallic counterface materials and different surface treatments on the wear and friction of polyamide 66 and its composite in rolling–sliding contact, *Wear*, 255(1-6), 714–721, 2003.
- [14] S Bahadur. The development of transfer layers and their role in polymer Tribology. *Wear* 245 (1-2), 92-99, 2000.

# THE SYMMETRICAL BEHAVIOUR OF CARBON NANOTUBES JUNCTIONS

T. I. Pataki; Z. Szakál

Institute for Mechanical Engineering Technology, Faculty of Mechanical Engineering,  
Szent István University, Gödöllő, Hungary  
www.geti.gek.szie.hu

**Abstract** We have been developing a mathematical model to predict the mechanical behaviour of carbon nanotubes under loads having different types of structures. In this paper we would like to introduce the behaviour of carbon nanotubes junctions under tensile strain. With an example we display that in a structure the junctions are very important intensifier component. We show the difference between the symmetrical and non-symmetrical junctions. We give an answer, which junctions are symmetrical and which ones are not symmetrical. Under tensile strain the “Y” junctions have different behaviour, if they are symmetric, or not.

**Keywords** nanotube, mechanical strain, symmetrical, simulation

## 1 INTRODUCTION

We have found two kinds of examples to the tensile tests of carbon nanotubes in the technical literature. In both cases samples fixed between the needles of microscopes were pulled by atomic force, in one case nanotube bunches [1], in another case multiwall carbon nanotube [2-3]. Beside of test difficulties problem was also the unknown exact structure of the samples tested, it couldn't be known that the measuring concerned for what exactly.

Several research fellows tried to determine the stress-strain diagrams by theoretical way [4-8]. The basic of the methods are always that the atomic forces can be determined as a derivatum of the potential function determining the energy of chemical bounding. The empirical Brenner-potential is used [9] for this now days nearly every-where. The reseats got however differed fairly from time to time there were also differences withes more scales for example in the values of tensile strength calculated [4-8]. The differences derived from the different applications of the Brenner-formulas. Several research fellows noticed namely that as long as the Brenner-formulas can be applied excellently to determine the state of equilibrium at the calculation of atomic forces there are already problems as on the derivate function there are break point and sudden incline changes which can not be explained with the behaviour of chemical bondings. First of all eluding by different ways of this problem caused the great differences at between strength calculated with the Brenner-potential. The best solution to this problem was given by eliminating mathematically the break point the sudden incline changes on the derivate formulas so that in the meantime it remained unchanged the possibility of looking for the equilibrium too. [10]

We have produced a computer program for the simulation algorithm of carbon nanotube structures tensile test in this paper to be able to run in case of great numbers of atoms. We made possible to determine the basic strength properties first of all for nanotube junctions [11-15] and networks [16-18] recommended as never carbon nanostructures by according to newest researches. That is important because in case of carbon nanostructures one of the most interesting characteristic is the high strength and the similarly unusual interesting electric behaviour [19-20].

## 2 SIMULATION ALGORITHM OF TENSILE TEST

As we calculate also the bonding forces between atoms as derivate of energetic potential function of chemical bondings we think necessary to make known the Brenner- formulas [9]. In this way the energetic potential is described with a rejecting ( $V_R$ ) and an attractive ( $V_A$ ) member between i-atom and j-atom to be in  $r_{ij}$ -distance from each other:

$$V(r_{ij}) = V_R(r_{ij}) - \bar{B}_{ij} V_A(r_{ij}) \quad (1)$$

where the members are given with the help of  $D_e S$ ,  $\beta$  and  $R$  material factors.

$$V_R = \frac{D_e}{S-1} e^{-\sqrt{2S}\beta(r-R)} f_{ij}(r_{ij}) \quad \text{és} \quad V_A = \frac{D_e S}{S-1} e^{-\sqrt{2/S}\beta(r-R)} f_{ij}(r_{ij}) \quad (2)$$

The  $f_{ij}$  correction function is a formula given by mathematic polynomes. It has got twofold role: partly cuts the attractive and rejecting effects outside a range (rather long) given partly because of its parametric shape the formulas can be matched to measuring results, both functions show their effects at departing from the equilibrium. [10] it was solved by introducing this that there are no break points and sudden incline changes on the derivative of the Brenner-formulas.

It is taken into account the effect of local surroundings of atoms (first and second coordination sphere) and the different angles of bondings with the help of  $B_{ij}$ -factor:

$$B_{ij} = \left[ 1 + \sum_{k(\neq i,j)} G(\theta_{ijk}) f_{ik}(r_{ik}) \right]^{-\delta} \quad (3)$$

where  $\theta_{ijk}$  is the angle of i-j and k-bondings,  $G$  given with  $a_0, c_0, d_0$  material factors respectively:

$$G(\Theta) = a_0 \left[ 1 + \frac{c_0^2}{d_0^2} - \frac{c_0^2}{d_0^2 + (1 + \cos \Theta)^2} \right] \quad (4)$$

The factor in (1) formula:

$$\bar{B}_{ij} = (B_{ij} + B_{ji})/2 \quad (5)$$

The steps of simulation algorithm of tensile test:

We have developed a computer program for the algorithm:

1. Giving the carbon nano-structure with the Table of appropriate point coordinates of atoms, unloaded, static condition.
2. Moving the atoms to be in the place of load in the load direction with small distance. (The displacement degree is so small it doesn't disturb the equilibrium calculations of the next step.)
3. Calculation of the new equilibrium (minimizing the Brenner-formula): confirming the atoms to be in the place of fixation and displaced in the previous step, the atoms between them are relaxed until to be calculated the equilibrium.
4. Calculation of bonding forces.
5. Repeating the previous three steps until the structure is damaged or niptures (if certain bonding in the structure reaches critical bond length, which is 1.7 Å).
6. Naturally it is sufficient to calculate the bonding forces at the weakest place (cross section) as this place however will be knows only during pulling because the forces can be expediently calculated from the tables put down after the steps, too. Finally we represent the resultant of bonding forces added vectorial at the weakest cross section in the function of elongation and this will be the tensile-test diagram.

After carrying out the chechings needed we started out research work by running the algorithm on a nanotube-structure. The aim of the research work is to carry out tensile-tests of carbon nano-structures with a lot of atoms mentioned in the introduction by the new simulation means. This structure is a Y-junction which branches are built up from zig-zag type nano-tubes in this case. Here we could determine that the angular arrangement between branches is  $120^\circ$ . We show the snaps of pulling-simulation in Figure 1. On the left Figure we show a basic starting structure. In the middle already the axial pulled structure can be seen. On the right Figure we displayed the moment before damage. The most loaded bonding in this structure reaches the critical bond-length at this moment (1,7Å). (Figure 2.)

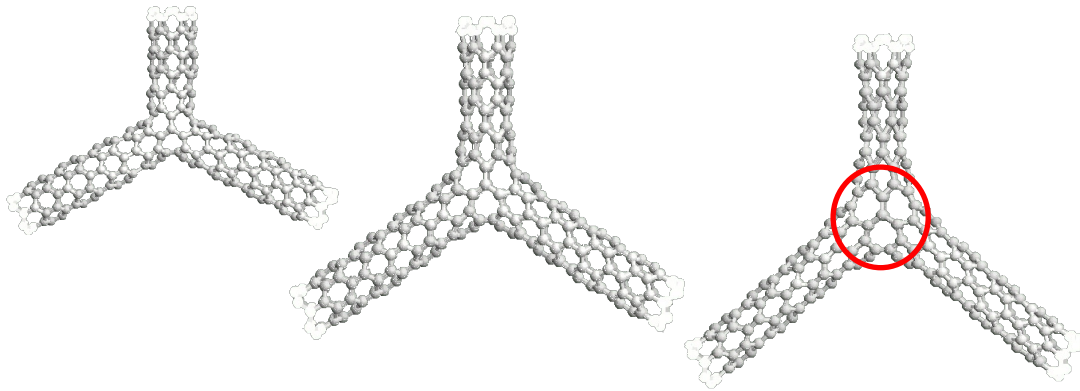


Figure 1. Snaps from the symmetric Y-junction pulling

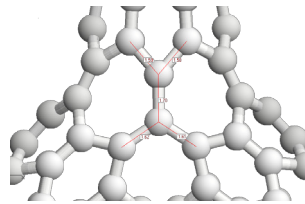


Figure 2. Critical bond-length (1.7 Å) inside of node

We show the results of runs carried out on asymmetric structure in Figure 3 and 4, where the tensile-test snaps of carbon nanotube Y-junction can be seen. The pulling takes place in the axial direction of tubes. According to the first appreciation still only can be decided that this structure will not rupture inside of node the bonding nomely here start to elongate in the greatest amount.

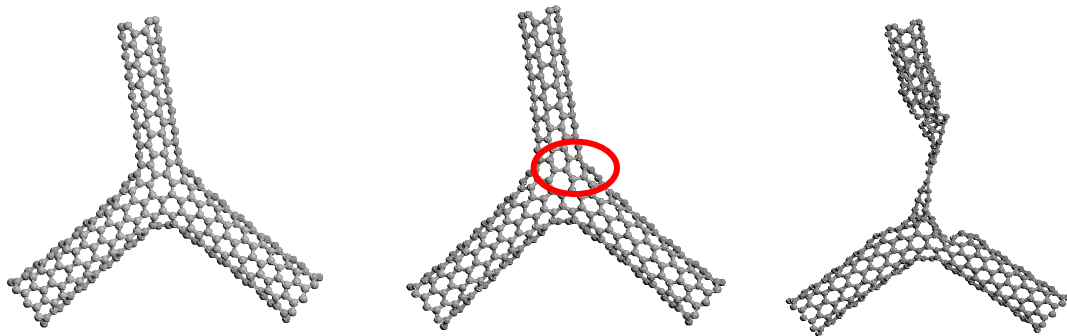


Figure 3. The critical bond-length and the damage on an asymmetric junction respectively

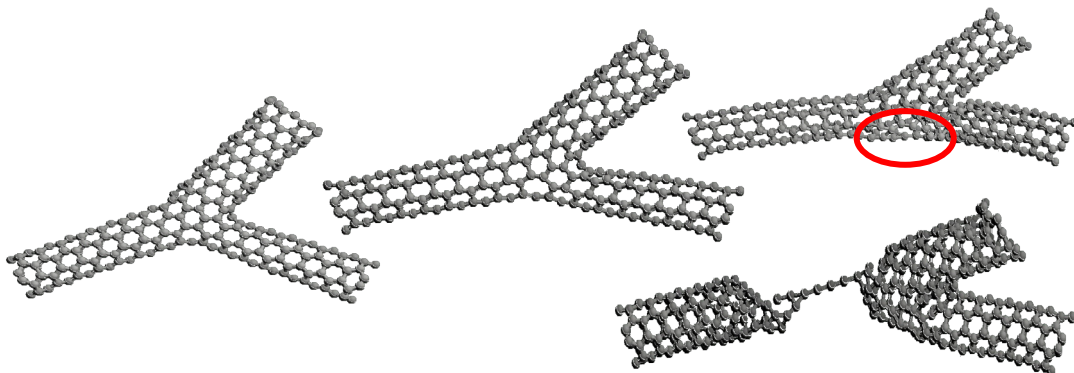


Figure 4. The critical bond-length and the damage on an another asymmetric junction respectively

## 2.2 Symmetric calculating method

During examining nanotube junctions lights was thrown that the symmetry has got a great effect to its strength properties

This paper sums up the results reached in the theme concerning the searching of axial symmetries of planar configurations and examining the similarity of 2D-al configurations.

### 2.2.1. Method

We search the symmetric axis of the configuration examined that we are scanning the plane with the hot direct lines passing through of the centre of gravity.

During scanning we set out from that theses whereas all symmetrical axes have to pass through on the centre of gravity. We carry out a calculation method for all direct line passing the centre of gravity which results we put down. By evaluating of data got this way we select the spot of approximating and exact symmetry. We display the results presenting in diagram. During evaluating the diagram we examine the local maximum values.

During our research work we have drawn up a symmetry searching algorithm, (Figure 5.) which by it is known in technical literature and can be applied in case of configurations with multiple complex outline, too.

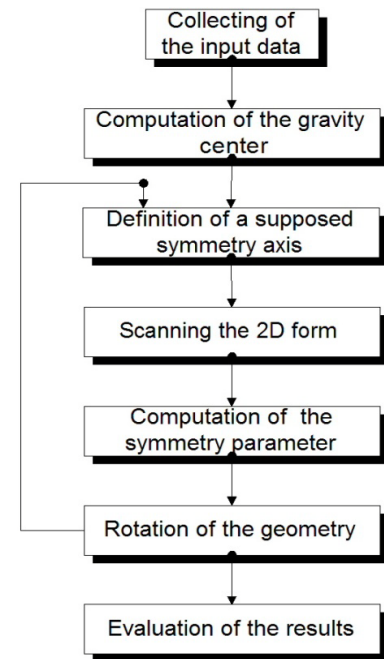


Figure 5. The algorithm

### 2.2.2. Calculating the symmetry-parameter

The  $Z$  symmetry-parameter shows the approximation to the axial symmetry in numerical form. This is a number between 0 and 1, it can be a certain grade of the symmetry characteristic. We introduce the following  $Z_k$  parameter for the definition referring to the  $k$ . scanning level:

The calculation of  $Z_k$  is simple in that case when on one scanning one-one intersection derives on the both sides of the axis. With the Figure Z. symbols:

$$Z_k = 1 - \frac{abs(b - j)}{b + j} \quad (6)$$

Where:

b: marks the left-hand side distance measured from symmetry axis of the perimeter section.

j: marks the right-hand side distance measured from the symmetry axis of the perimeter section.

The  $Z_k$  is designed so if the section of configuration with the measuring direct line given is exactly symmetrical to the axis supposed, then  $b=j$ , this  $Z_k=1$ . The better the configuration approximate to the symmetric the move it will be nearer the  $Z_k$  to 1 (figure 6).

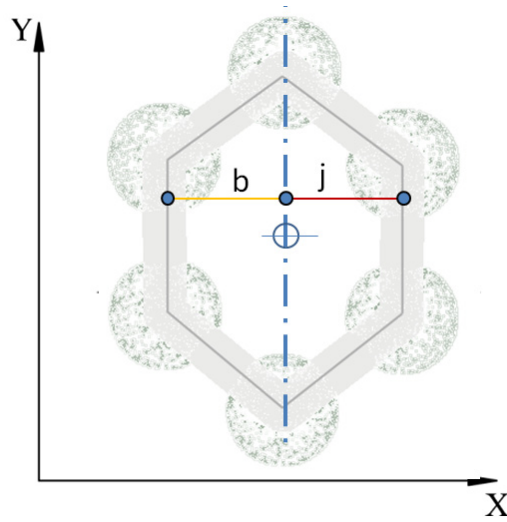


Figure 6. Explanation of measuring section

The more unfavourable situation is regarding to symmetry when the measuring section hasn't got a match on the opposite side of the axis, that is  $b > 0$  and  $j = 0$ , or  $b = 0$  and  $j > 0$ , then  $Z_k = 0$ , the smallest value.

As in the (6) connection the quotient of geometric dimension occurs,  $Z_k$  is a nondimensional number, its value does not depend on geometrical size.

If on a scanning level there are more than two intersections (with Figure 7. markings  $b_1, b_2, \dots, b_n; j_1, j_2, \dots, j_m$ ) then we place the  $b_i$  and  $j_i$  values into pairs and we form the  $Z_k$  value with (6) connection from this. If I suppose that more intersections are on the left-hand side:  $n > m$ . then the planning into pairs has to be made so, that beginning from  $b_{m+1}$  the  $b_i$  ( $i = m+1, \dots, n$ ) pair should be always  $j_i = 0$  ( $i = m+1, \dots, n$ ). The  $Z_k$  value in general case is the average of expressions formed of pairs calculated according to (6).

$$Z_k = \frac{1}{n} \sum_{i=1}^n \left( 1 - \frac{\text{abs}(b_i - j_i)}{b_i + j_i} \right) \quad (7)$$

The Z parameter formed, from the  $Z_k$  average of symmetry parameter

$$Z = \frac{\sum_{k=1}^N Z_k}{N} \quad (8)$$

where:

N: marks the number of scanning levels from timely  $Y_{\max}$  to  $Y_{\min}$ . As we form Z value by averaging according to (z), (8), Z keeps the original characteristic of  $Z_k$  values:

- Z can take up values in (0,1) interval ,
- $Z = 1$  is the most favourable (exact) case of symmetry,
- $Z = 0$  is the most unfavourable case regarding to symmetry,
- The values between 0 and 1 correspond to the approximate symmetry all the better the nearer is Z value to 1.
- Z is a nondimensional number and its value does not depend on the dimension of plane figure only it depends on its shape.

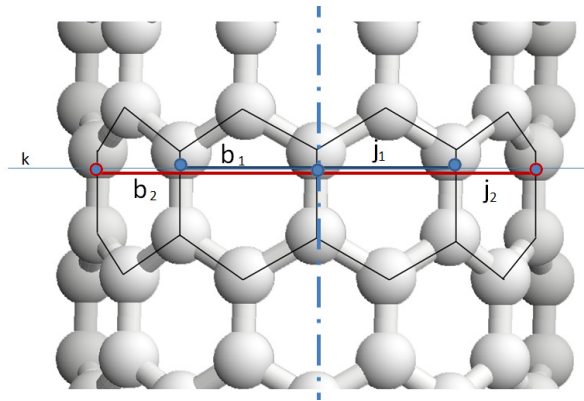


Figure 7. The explanation of  $Z_k$  parameter in case of optional complication.

### 3 CONCLUSIONS

We have developed a method to examine nanotube junctions.

Based on this method the nanotubes can be divided into two groups based on the symmetry theory, into symmetric and asymmetric configurations. It is possible to search the symmetry axis of the junction by a one axial symmetry reaching method. We search for such configurations with theoretical tensile-test of nanotubes that are optimized against pulling load. The structure of nanotube junctions have got near such strength properties than the tubes connected to it.

We have established that the symmetric and asymmetric junctions behave differently to the effect of mechanical loads. The symmetric junctions get damaged inside of node while the asymmetric junctions get damaged at the node and of the nanotube border. We have determined a quick and exact calculating method to distinguish at these nanotube structures. This program determines exactly whether the nanotube structure is symmetrical or asymmetrical.

### 4 REFERENCES

- [1] Yu MF, Files BS, Arepalli S, Ruoff R. Tensile loading of ropes of single nanotubes and their mechanical properties. *Phys. Rev. Lett.* 2000; 84:5552-5555.
- [2] Demczyk BG, Wang YM, et. al. Direct mechanical measurement of the tensile strength and elastic modulus of multiwalled carbon nanotubes. *Mater. Sci. and Eng. A* 2002; 334:173-178.
- [3] Yu MF, Lourie O, Dyer MJ, Moloni K, Kelly TE, Ruoff RS. Strength and breaking mechanism of multiwalled carbon nanotubes under tensile load. *Science* 2000; 287:637-640.
- [4] Fu CX, Chen YF, Jiao JW. Molecular dynamics simulation of the test of single-walled carbon nanotubes under tensile loading. *Sci. in China E* 2008; 50:7-17.
- [5] Mylvaganam K, Zhang LC. Important issues in a molecular dynamics simulation for characterising the mechanical properties of carbon nanotubes. *Carbon* 2004; 42:2025-2032.
- [6] Agrawal PM, Sudalayandi BS, et. al. Molecular dynamic simulations of the dependence of C-C bond lengths and bond angles on the tensile strain in single-wall carbon nanotubes, *Comput. Mater. Sci* 2008;41:450-456.
- [7] Duan WH, Wang Q, Liew KM, He XQ. Molecular mechanics modelling of carbon nanotube fracture. *Carbon* 2007; 45:1769-1776.
- [8] Belytschko T, et.al. Atomistic simulations of nanotube fracture. *Phys. Rev. B* 2002; 65:235430-1-8.
- [9] Brenner DW. Empirical potential for hydrocarbons for use in simulating the chemical vapor deposition of diamond films. *Phys. Rev. B* 1990; 42:9458-9471.
- [10] Zsoldos I., László I.: Computation of the loading diagram and the tensile strength of carbon nanotube networks, *Carbon* 2009; 4:1327–1334

# COMPARING STRENGTH PROPERTIES OF NATURAL AND SYNTHETIC RUBBER MIXTURES

T. Renner, L. Pék

Institute for Mechanical Engineering Technology, Faculty of Mechanical Engineering,  
Szent István University, Gödöllő, Hungary  
www.geti.gek.szie.hu

**Abstract:** During in our research work we examine the condition of developing elastomer – metal connection at manufacturing machine – and car industry hybrid parts. As a first step we have carried out comparison tests relating to the strength properties of synthetic – and natural rubber mixtures. During tests we have compared four mixtures used often in the practice (NR, NBR, EPDM, CR) in three characteristic hardnesses (43 Sh<sup>0</sup>, 57Sh<sup>0</sup>, 72Sh<sup>0</sup>). In addition to hardness we have measured the elongation at rupture and the density, too. As a continuation of our tests we researched what connection is between the surface roughness of metal plate and the elastomer – metal bonding formed.

**Keywords:** rubber mixtures, latex, hybrid parts, strength properties

## 1 INTRODUCTION: CHARACTERIZING THE MIXTURES EXAMINED

The natural rubber is the most often used type of mixture of the rubber industry nowadays which is produced from the milk-like fluid (from latex) of certain tropical trees. The latex is a colloid state dispersion, the rubber is precipitated (killed) by acetic – or formic acid from it then is washed, pressed, dried or smoked [2]. After these the quality classification takes place then it is packed in to bales and according to the so called „green book” it is put into commercial circulation. This handbook was accepted by the International Federation of Rubber Producing Nations in 1960 which is a standard publication in classifying rubbers up to present days. The introduction of SMR-system (Standard Malaysian Rubber) in 1965 meant further development which standardized the mass, packing, etc. of rubber bales. By this possibility arose to classify the SMR-type based on two important characteristics.

a./ according to starting basic material:

- latex basis,
- waste coagulum basis,
- latex + waste coagulum basis,

b./ according to viscosity:

- stabilized viscosity,
- non-stabilized viscosity

So the bulk processing of rubbers according to exact receipt was possible. [1]

The properties of natural rubber mixtures are the followings:

- high static tensile strength (15-22 MPa),
- high elongation (600-900%),
- excellent elasticity at low temperature (up to – 10°C doesn't change substantially)
- poor ozone and degradation stability,
- good confectionability because of excellent crude adhesion.

The degradation causes cracks on the rubber products however by receipt solutions and up – to – date auxiliary products they can be repaired considerably, so mixtures can be produced to be best suitable for the application required.

Example to the composition of a natural rubber based mixture. (Table1) [3].

Table 1.

Naming	Mass-rate [%]
Natural rubber	75,1
Wood-tar	1,5
Resin oil	0,8
Stearine acid	1,1
Zinc-oxide	18,8
Sulfur	2,3
Other accelerators	0,5

The **butadiene-acrylic-nitril** (NBR) rubbers are also often applied types, their greatest advantage is they have got good resistance against mineral oils and aliphatic solvents, because of this various sealings, pipes, oil-resisting technical products are made of them. Their technical properties depend on the acrylic-nitril content substantially thus by increasing this their heat resistance increases but their cold-resistance, elasticity decreases [1].

The **ethylene-propylene** (EPDM) rubber is a low density synthetic elastomer ( $850-900 \text{ kg/m}^3$ ), its hardness can be changed between wide limits ( $20-99\text{Sh}^0$ ). Their production is complicated, their mixing needs great attention whether it is made on bowl or in closed mixer. Their confection is difficult in consequence of poor cold-adhesion, to form appropriate metal binding needs special materials [5]. Their vulcanizing is slower whether it is made with peroxides or with sulfur + accelerator vulcanizing system, than the natural rubber. Despite a lot of difficulties they are very widely used materials, rubber boots, pipes, profile straps are made of them.

Characteristic properties:

- very good heat-resistance (up to  $150^0\text{C}$ ),
- ozone – proof,
- excellent electric insulating capability (average volumetric resistance about  $10^{10} \text{ Ohmcm}$ ).

One of the most important characteristic is the insulating resistance of the electric insulators and of rubber mixtures. The ratio of the D.C. voltage connected to the material and the current value read after 1 min. of the connection means the insulating resistance. The 1 min. value is an agreement it serves the simplification of measurings and the comparability.

However it has to be kept in one's mind that the value got is not identical with the real insulating resistance of the material, which is the ratio of the voltage and of the leakage current.

The **chloroprene** (CR) rubber has got high density ( $1300-1350 \text{ kg/m}^3$ ), it is widely used synthetic rubber in the practice. Their cost price is high, in exchange for this it has got several favourable characteristics:

- weather – and ozone – proof,
- medium heat-resistance ( $90-100^0\text{C}$ ),
- self-extinguish effect, its oxygen index is 40-50,
- resists mineral oils.

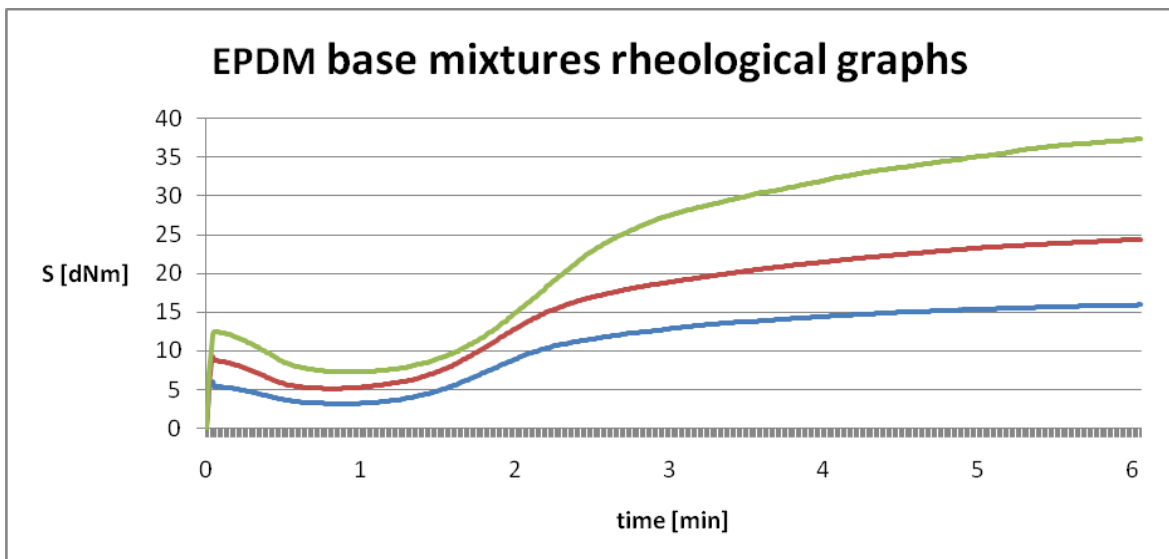
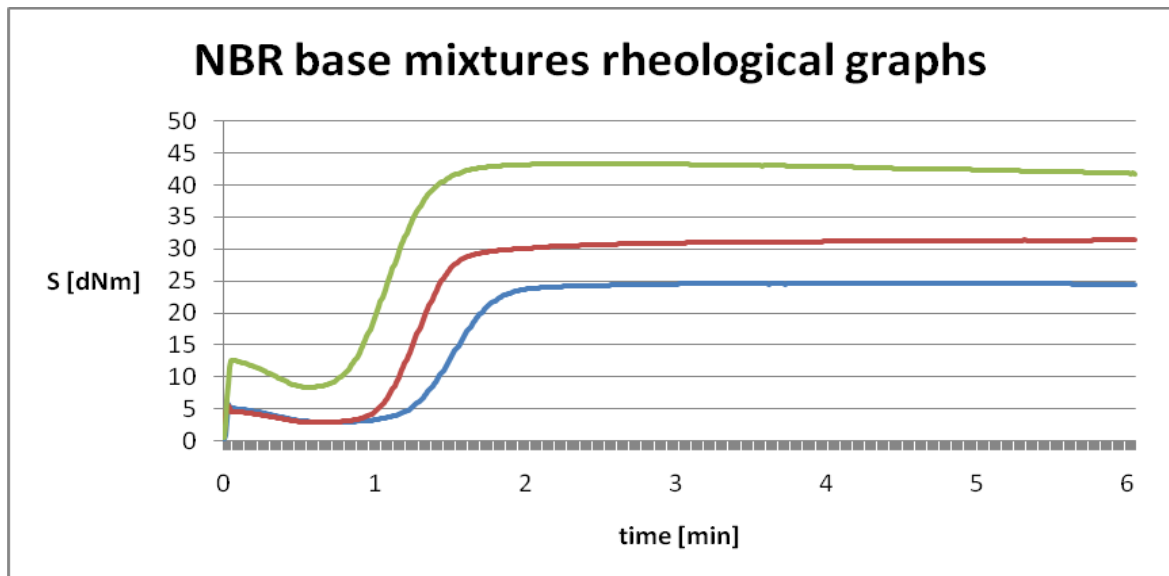
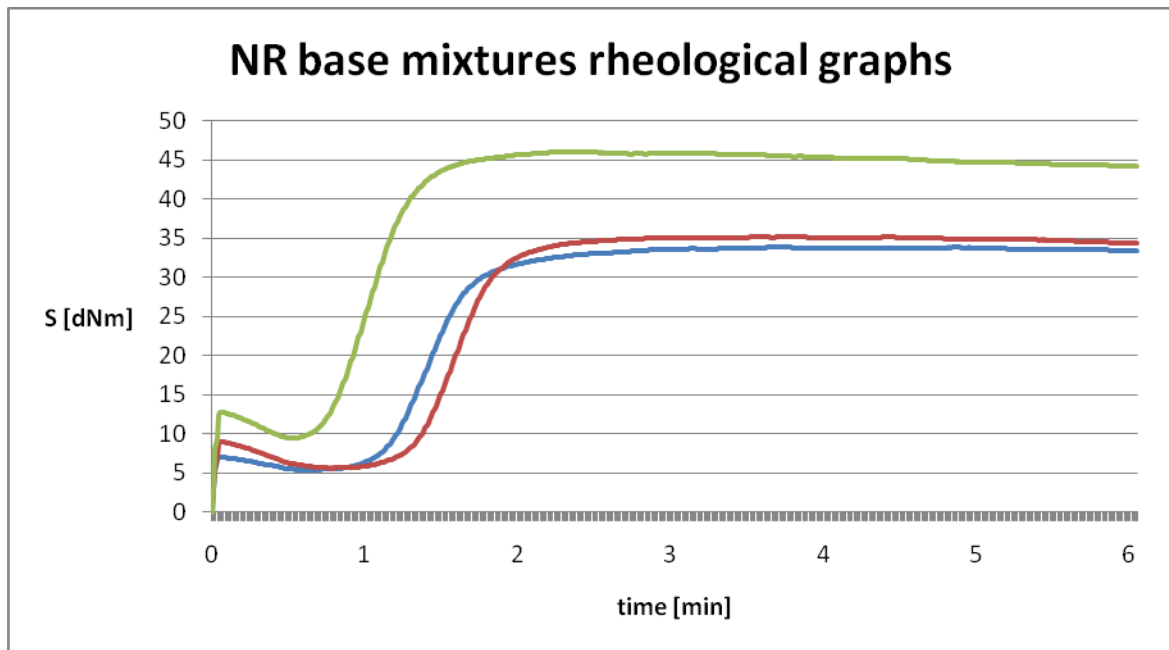
The so called oxygen index gives a very good picture from a mixture burning characteristic, which shows that what is the smallest amount oxygen in a nitrogen – oxygen mixture at room temperature at which the burning remains after setting on fire. [1].

Its application field is mainly pipes, belt conveyor slings.

## 2 PRESENTING THE RESULTS OF STRENGTH TESTS.

In order to compare the strength characteristics we have made mixture samples from all four materials, then we decided the vulcanizing optimum. The aim of deciding the optimum was that the values got during measurings should be the best results to be produced from the mixture given. It is not all the same that a mixture given in which vulcanizing state is examined and as the vulcanizing speed of the mixture compared is different for this examination was needed by all means. We have carried out examinations with S100 Monsanto Rheometer for this aim which results contains the No 1. diagram. The principle of the measuring is that a standardized rotor with 1,67 Hz frequency, oscillates with  $3^0$  amplitude in a heated chamber with determined geometry. The equipment measures the moment needed to drive the rotor in the function of time [1]. Figure 1. shows the graphs made with the equipment.

Key words: blue:  $43 \text{ Sh}^0$ , red:  $57\text{Sh}^0$ , green:  $72\text{Sh}^0$ ,  $170^0\text{C}$ , 6 min.



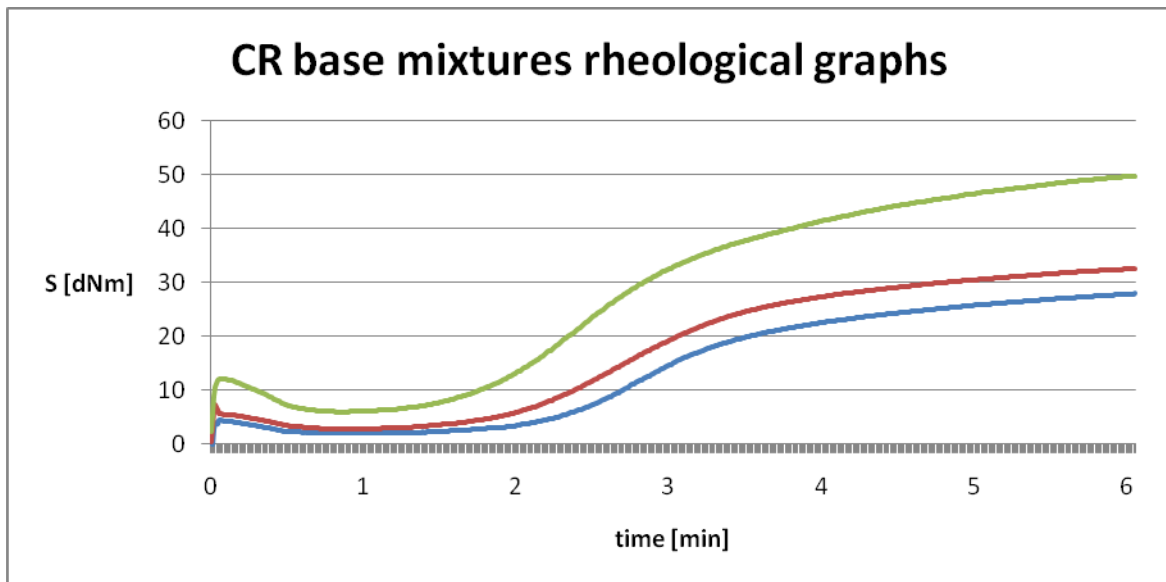


Figure 1. Rheological graphs

The O spatial-mesh point is ordered to moment curve minimum, the maximum to the moment curve maximum. As the maximum point can be defined with difficulty because of this according to the accepted practice the vulcanizing time of the material is considered that time ( $t_{90}$ ) belonging to the 90% rising calculated from the moment curve minimum (according to measurements the tensile strength maximum is here, too). The time got  $t_{02}$  belonging to the 20% rising calculated from the minimum mark.

We summed up the corner – numbers in the No. 2 table from which the vulcanizing time can be determined to be read from the graphs.

Table 2

Mixture	$S_{min}$	$S_{max}$	$t_{02}$	$t_{90}$
NR 43 Sh	5,98	33,7	0,95	1,96
NR 57 Sh	7,41	37,14	0,9	1,77
NR 72 Sh	8,63	41,36	0,81	1,62
NBR 43 Sh	2,88	24,63	1,00	1,82
NBR 57 Sh	2,87	31,44	0,89	1,58
NBR 72 Sh	8,38	43,4	0,71	1,4
EPDM 43 Sh	3,15	16	1,12	4,17
EPDM 57 Sh	5,1	24,4	1,07	4,46
EPDM 72 Sh	7,26	37,36	1,27	4,67
CR 43 Sh	1,98	27,91	1,61	4,79
CR 57 Sh	2,78	32,52	1,4	4,59
CR 72 Sh	5,96	49,74	1,3	4,7

We have vulcanized specimens for hardness tests for various times from the materials made and we have carried out hardness tests (No.3 table). The table shows the  $Sh^0A$  hardnesses in the function of vulcanizing time.

It can be seen well from the results of No.3 table that the materials change their hardness differently in the function of vulcanizing time. The NBR mixtures vulcanize similarly as the NR mixtures, but the last two elastomer-groups are "slower" substantially. The specimen for tensile test had to be manufactured to longer time at latters.

We have vulcanized sheet-specimens before tensile test from all materials for the times marked in table No.3. After this we carried out the tensile test according to the DIN53504 standard, and we display the results in the Figure.2. and Figure 3. series [4].

The tensile test parameters:

Type of tensile test machine: LLOYD LR 300

Breaking rate [mm/min]: 500

Cross section of sheet-specimen [mm<sup>2</sup>]: 12 (2x6mm)

Ambient temperature [°C]: 23

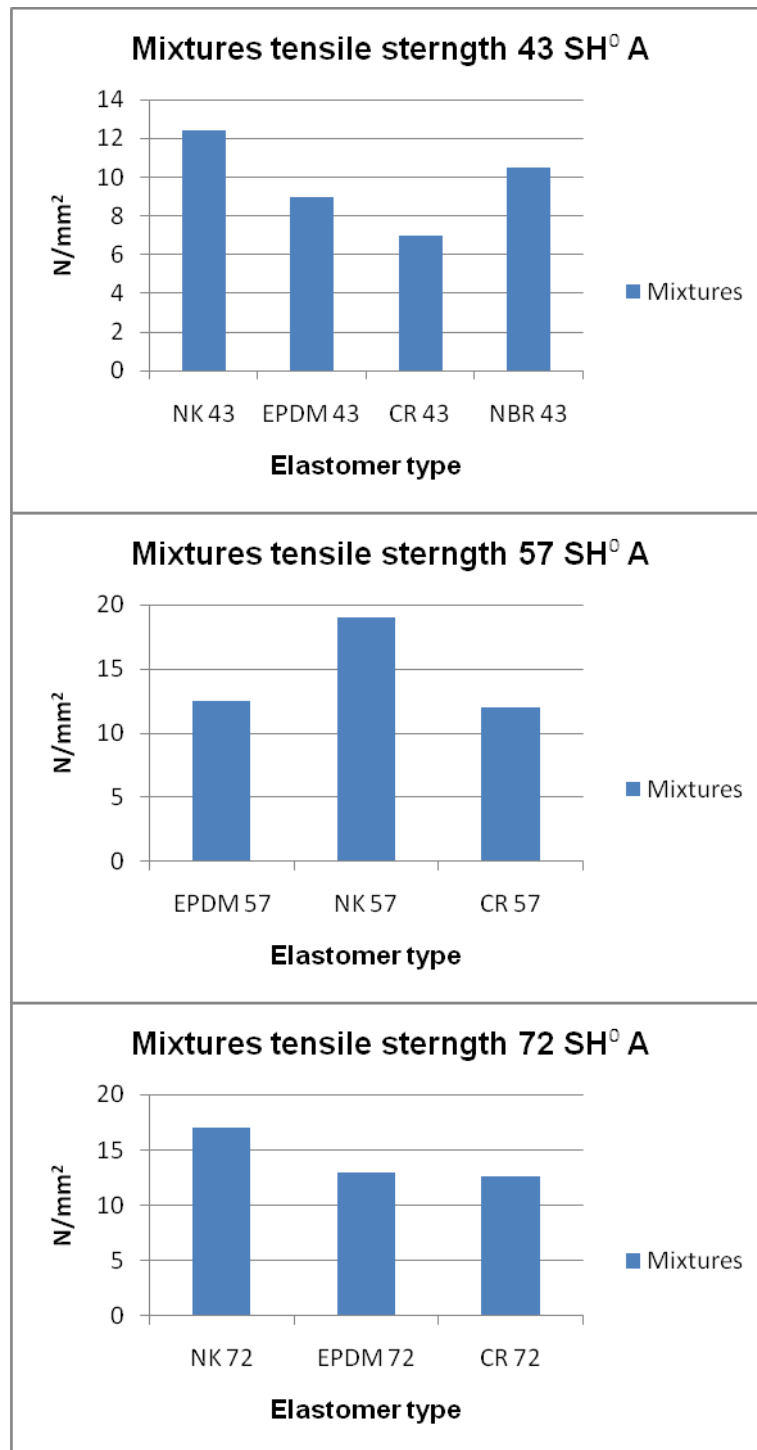
Relative humidity [%]: 40

Table 3

	6 min	8 min	10 min	12 min	14 min
NR 43	42	42	42	42	41
NR 57	56	56	56	55	55
NR 72	72	72	72	72	71
NBR 43	44	44	44	44	43
NBR 57	58	58	58	58	57
NBR 72	70	71	71	71	71
EPDM 43	40	42	44	45	45
EPDM 57	50	52	54	55	55
EPDM 72	70	72	72	72	72
CR 43	40	42	44	45	45
CR 57	50	53	54	57	57
CR 72	70	71	72	72	73

### 3 THE SURFACE ROUGHNESS EFFECT ONTO ULTIMATE TENSILE LOAD.

The forming of elastomer – metal bonding in industrial scale nowadays is realized by glue produced only in industrial circumstances. The general rules of bonding has to be kept at application of these materials that is after chemical cleaning mechanical metal preparation follows, then the glue spraying and finally the vulcanizing. As a continuation of our research work we have examined the effect of surface roughness onto the ultimate tensile load in the second phase. We carried out the measurings with metal plate fitted with 23 mm diameter M6x18 mm threaded shank, which we treated steel shot spraying material with different times. After this we carried out trial vulcanizing and we measured the ultimate tensile load. We show the results with the help of diagrams. The Figure 3 shows the formation the ultimate tensile load and the  $R_a$  average surface roughness in the function of spraying time in case of steel shot spraying material, while the No.4 diagram shows the same using corundum.



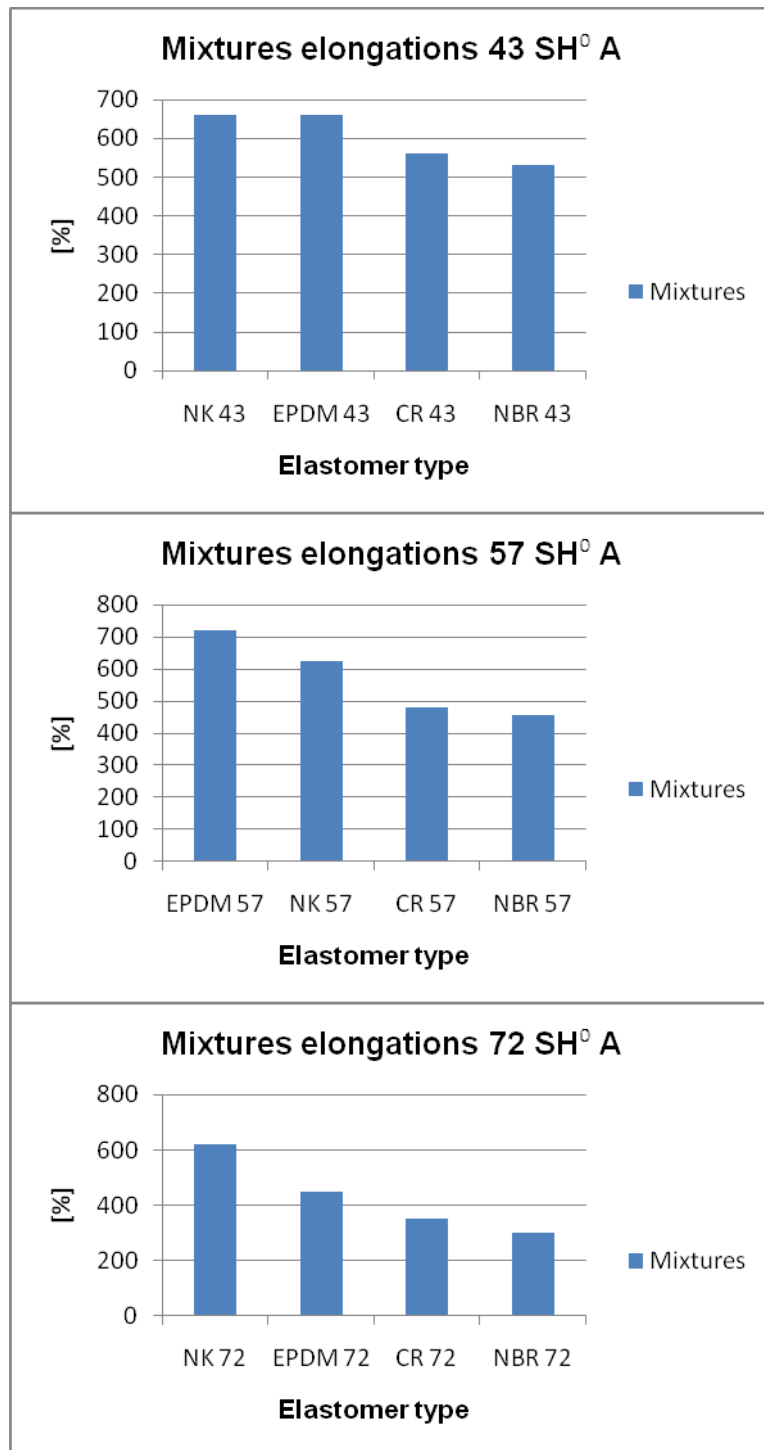


Figure. 2. Mechanical properties

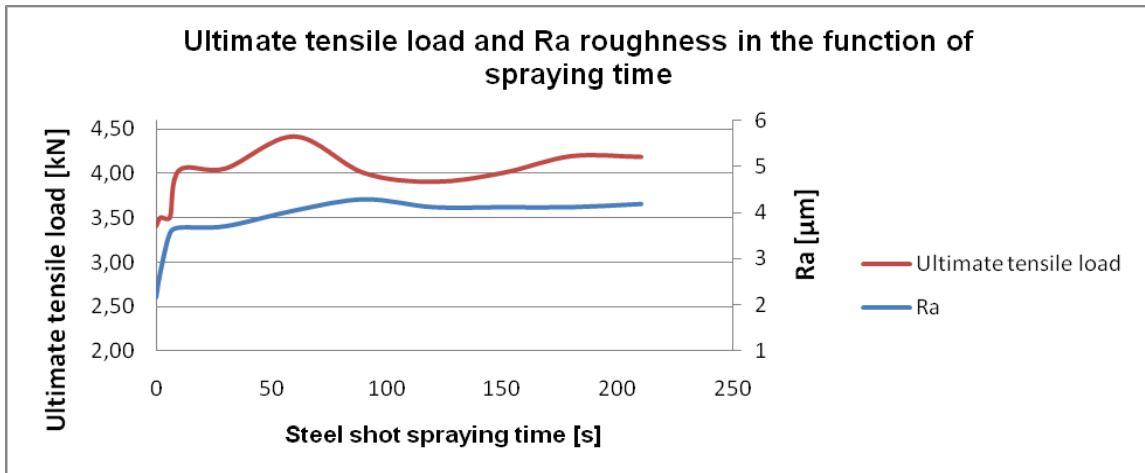


Figure 3. Effect of the steel shot spraying time

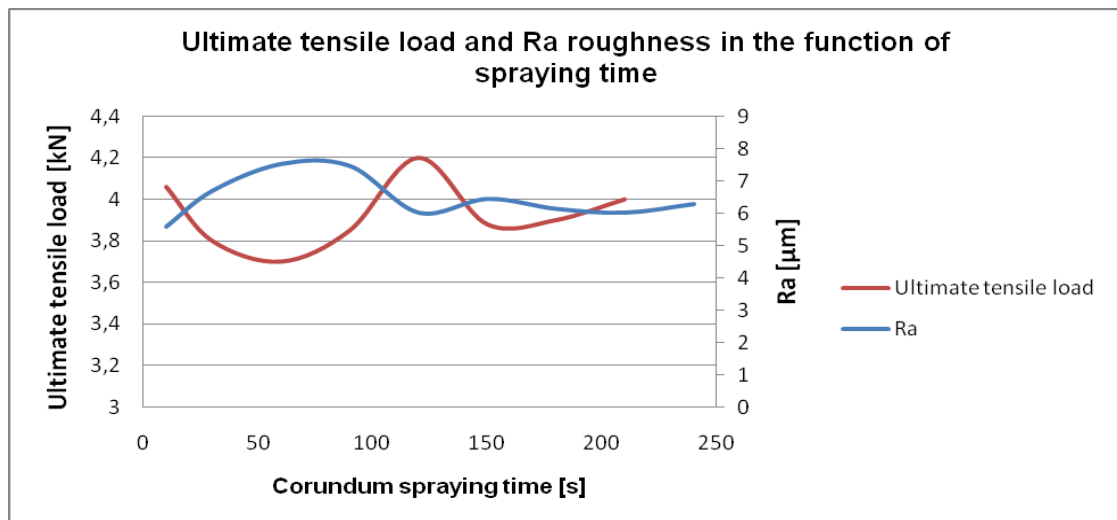


Figure 4. Effect of the corundum spraying time

#### 4 CONCLUSIONS

- It can be seen at the representation in diagram form of the strength results that the strength values increase with the growth of hardness however the elongation decreases.
- It can be established characteristically that the up-to-date synthetic elastomers strength values are similar to the natural rubber mixtures, thus the most important deciding standpoint is the manufacturing capability, taking into account the resistance of products.
- The EPDM rubber mixtures have got visibly very high elongation, at softer mixtures surpass the natural mixture from time to time, too.
- It is evident from the results of surface roughness examinations that the  $R_a$  average surface roughness is not suitable to characterize unambiguously the preparation of metal plates because of this as a further development we are going to carry out 3D –al examinations on the metal surfaces prepared and chemical examinations on the specimens cut into half and on the bonding boundary surfaces respectively.

#### 5 REFERENCES

- [1] Dr. Bartha Zoltán: Gumiipari kézikönyv. TAURUS-OMIKK, Budapest, 1988
- [2] Dr. Pék Lajos: Anyagszerkezetten és anyagismeret. Dinasztia Kiadó, Budapest, 2000
- [3] A. Springer: Gumi technológia. Műszaki Könyvkiadó, 1957.
- [4] [www.gak.de](http://www.gak.de)
- [5] [www.plastverarbeiter.de](http://www.plastverarbeiter.de)
- [6] Műanyag és Gumi. 44. évfolyam 6.szám 260p.

# NOVEL CYLINDER POSITIONING SYSTEM REALISED BY USING SOLENOID VALVES

L. Földi, Z. Béres, E. Sárközi

Institute for Mechanical Engineering Technology, Faculty of Mechanical Engineering  
Szent István University, Gödöllő, Hungary, [www.geti.gek.szie.hu](http://www.geti.gek.szie.hu)

**Abstract** This paper presents a novel control design, developed to realise fast and accurate position control of a pneumatic actuator using inexpensive on/off solenoid valves. In contrast to conventional control methods, the proposed control method operates chatter free, based on air compression. The control principle was developed by investigating the dynamics of a pneumatic actuator with an identified mathematical model. This new approach is applied to a pneumatic double acting cylinder, controlled by a pair of 5/3 way directional single solenoid valves. The described closed-loop circuit copes with the discontinuities associated with the valve's switching dynamics, and relatively long response time. The experimental apparatus uses an analogue displacement encoder for metering the piston's position and velocity, and doesn't incorporate pressure sensors thus ensuring a low cost system design. The results of experiments with various step responses show that the proposed control method performs well. The measured steady-state position errors are equal to the used potentiometer's travel resolution, which is 0,01 mm. Therefore this novel control and the related pneumatic system design could be a cost effective alternative to the servo-pneumatic positioning systems.

**Keywords:** Position Control, Solenoid Valve, Pneumatic Cylinder, Control Method, Actuator

## 1. INTRODUCTION

In order to achieve linear motion, pneumatic, electromagnetic and hydraulic actuators are typically used. Due to their advantageous characteristics in position control applications the latter two are more widespread. Though using hydraulic actuators high velocity and great force is achievable, and their position control can also be relatively easily solved, a handicap is that the leaking of hydraulic fluids might contaminate the workpiece. Electromagnetic actuators on the other hand are clean and reliable in their operation but often require a mechanical transmission, both to convert high speed and low torque to a more useful combination and to convert rotary motion to linear motion. While linear motors overcome the need for transmission, they can be expensive [9].

Pneumatic actuators have several advantages: they are fast, cheap, have an outstanding power-to-weight ratio, are easily maintainable and they don't contaminate the work piece. The challenge to the use of pneumatic drives is that due to piston friction and the characteristics of compressed gas flow their behaviour is non-linear. As a result their industrial use is only widespread in applications which require linear motions between end positions.

In the last decade such industrial controllers became available which have adequate computing capacity for real-time usage. Thus there is now opportunity to develop pneumatic systems which don't require costly proportional valves for positioning and hence the usage of the more cost-efficient solenoid valves became possible (Figure 1.). These simple on/off valves are cheap and easily maintainable. Their drawback however is that as yet the required control method is not appropriately elaborate: the solutions offered in the scarce publications on the topic consist of applying conventional control methods (PID, sliding mode, fuzzy logic) or their hybrid versions, with varying success.

A review of the papers on the topic is given in Table 1, where the applied control methods, the number of required valves and the highest positioning accuracy is shown. Even though it is not indicated in the table, in some cases certain speed or force decreasing solutions (eg. throttle valve, reduced pressure) were used, which naturally may have an effect on the operating range of the positioning system and the steady-state error. The employed valve's switching time is also omitted from the table.

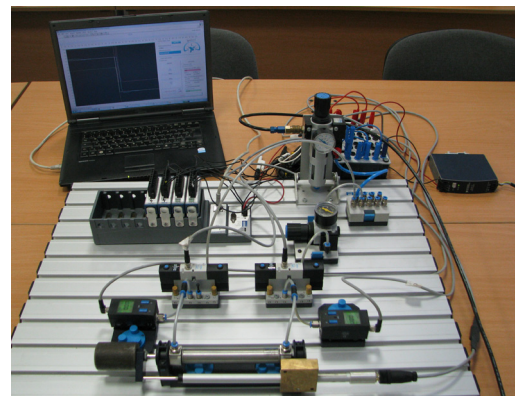


Figure 1. The experiment apparatus

<i>Number in References</i>	<i>Authors</i>	<i>Control method</i>	<i>Number of required valves</i>	<i>Positioning accuracy</i>
[9]	Thomas, M.B.; Maul, G.P.; Jayawiyanto, E.	Modified PD + PWM control	3	±0,1 mm
[1]	Ahn, K.; Yokota, S.	MPWM + neural network (LVQNN)	8	±0,2 mm
[7]	Parnichkun, M.; Ngaecharoenkul, C.	hybrid of fuzzy and PID + PWM control	1	±3,5 mm
[6]	Nguyen, T.; Leavitt, J.; Jabbari, F.; Bobrow, J.E.	Sliding mode control	4	±0,1 mm
[8]	Shih, M.-C.; Ma, M.-A.	Fuzzy + modified differential PWM control	2 + Proportional pressure valve	±0,075 mm
[5]	Messina, A.; Giannoccaro, N.I.; Gentile, A.	Individual control + PWM	2	±0,1 mm
[3]	Barth, E.J.; Zhang, J.; Goldfarb M.	Individual linear continuous + PWM	2	N/A
[2]	Akdağ, F.N.; Kuzucu, A.	Sliding mode control	2	±0,05 mm
[10]	van Varseveld, R.B.; Bone, G.M.	PID with friction compensation + PWM	2	±0,21 mm

Table 1. A review of the papers on the topic

## 2. MATHEMATICAL AND SIMULATION MODEL

We carried out the design work of our proposed control strategy based on an identified simulation model [4] of the actual apparatus. In order to develop this system we applied equations number (1) and (2); using these we can express the mass flow filling the chambers of the cylinder as follows:

$$\dot{m}_1 = A_1 \cdot p_{\text{sup}} \cdot \sqrt{\frac{2}{R \cdot T}} \cdot \psi_{(p_1/p_{\text{sup}})} \quad (1)$$

$$\dot{m}_2 = A_2 \cdot p_2 \cdot \sqrt{\frac{2}{R \cdot T}} \cdot \psi_{(p_{\text{atm}}/p_2)} \quad (2)$$

The outflow functions ( $\psi$ ) in the equations are one of the major causes of the nonlinear behaviour of the pistons. Knowing the mass flows, the pressures in the cylinder's chambers can be expressed through the gas law's derivative with respect to time:

$$\dot{p}_1 = \frac{1}{V_1} \cdot (\dot{m}_1 \cdot R \cdot T - p_1 \cdot \dot{V}_1) \quad (3)$$

$$\dot{p}_2 = \frac{1}{V_2} \cdot (p_2 \cdot \dot{V}_2 - \dot{m}_2 \cdot R \cdot T) \quad (4)$$

Using the pressures and knowing the physical parameters of the piston the mechanical equation complemented with the mass loads is as follows. Again, a term causing non-linearity appears: friction ( $F_f$ ).

$$m \cdot \ddot{x} = p_1 \cdot A_1 - p_2 \cdot A_2 - |F_f| \cdot \text{sign}(\dot{x}) - m \cdot g \cdot \sin \alpha - j \cdot (\dot{x})^2 \cdot \text{sign}(\dot{x}) \quad (5)$$

The last term in the equation is the pipe friction loss which, according to our observations is a significant factor in practice but is ignored in the specialised literature we made use of. This friction loss was taken into consideration with a friction factor ( $j$ ) multiplied by the square of velocity.

Using the presented equations we were able to construct the proposed control system's simulation model in Matlab/Simulink software. After completing the identification process of the model's parameters, we were able to effectively analyse some of the conventional control methods. As a result we decided to elaborate a novel control strategy, which copes with the discontinuities associated with the valve's switching dynamics, and relatively long response time.

### 3. CONTROL METHOD

Designing the control method we determined to apply two solenoid valves (one for each chamber), the biggest benefit of which is that the number of control signals is thus raised to the second power.

<i>Number of variation</i>	<i>Signal of solenoid valve 1</i>	<i>Signal of solenoid valve 2</i>	<i>Movement of the cylinder piston</i>
1	fill	empty	positive direction, fast
2	fill	close	positive direction, slow
3	fill	fill	immobile
4	close	empty	positive direction, uncontrolled
5	close	close	first immobile, then uncontrolled
6	close	fill	negative direction, slow
7	empty	empty	accidental direction, uncontrolled
8	empty	close	negative direction, uncontrolled
9	empty	fill	negative direction, fast

Table 2. Available variations using two solenoid valves

Out of the variations presented in Table 2, we ignored the uncontrolled ones (where pressure in both chambers changes in an uncontrolled way) which thus leaves us with five useful solenoid valve variations. However, in order to stop the movement of the cylinder piston in variation number 3, a complementary element had to be introduced (due to the asymmetric construction of the cylinder we used). Using a pressure regulator, the positive chamber was filled with supply pressure decreased in proportion to the surfaces of the piston. As a result a balance of force was reached based on equation number (5).

As a first step we started out from a graph representation, where time and position were placed on the axes. This way the most important control parameter, the error (difference between a measured process variable and a desired set-point) can be visualized easily if we represent both the ideal and the actual position values (reference signal and measured output respectively) plotted against the elapsed time.

Based on the scale of the error we might form predictions as to which valve variation has to be realized by the control method in order to decrease the absolute value of the error.

<i>Number of control signal</i>	<i>Relation between reference signal and measured output</i>	<i>Desired piston movement</i>	<i>Number of variation in Table 2</i>
1	$r \gg y_m$	positive direction, fast	1
2	$r > y_m$	positive direction, slow	2
3	$r \approx y_m$	immobile	3
4	$r < y_m$	negative direction, slow	6
5	$r \ll y_m$	negative direction, fast	9

Table 3. Realized valve variations

The variations in Table 3 can be easily indicated in the graph representation we have already created (Figure 2.), since control signal number 3 has to take effect within the close vicinity of the ideal position, namely in a predefined tolerance band where further changing of position is unnecessary. Nearby, above and below this band we can assign the zones where the piston is relatively close to the ideal position, thus slow movement is required (control signals number 2 and 4). Outside these bands those parts of the stroke length are situated which are relatively far from the ideal position, hence a fast piston movement is needed in order for a fast decrease in the absolute value of the error to take place (control signals number 1 and 5).

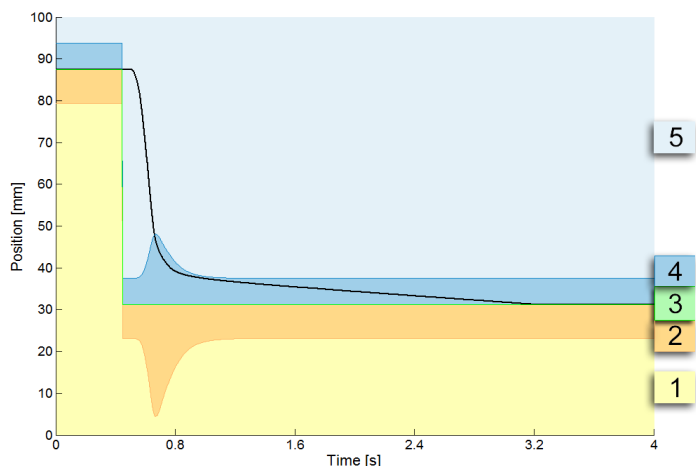


Figure 2. Control Strategy

Since the width of the tolerance band is a parameter given during utilization, the control method only has to determine the width of bands number 2 and 4 in a given moment. By rendering the respective valve variations to the given bands, the solenoid valves can be controlled harmoniously and in an essentially discrete way, with few valve switches, i.e. chatter free.

In order to determine the width of the bands we can set up the following equation based on the work-energy theorem:

$$0 - \frac{1}{2} \cdot m \cdot v^2 = - \left( \frac{p_b \cdot A \cdot (q + z)}{R \cdot T} \cdot R \cdot T \cdot \ln \frac{p_a}{p_b} \right) \quad (6)$$

Of the terms of the equation  $p_a$  and  $p_b$  are the initial and final pressures of the closed chamber,  $q$  is the distance needed to stop the piston while  $z$  is the remaining distance. Setting up the equation we regarded the process to be isothermal, thus we overestimated the necessary distance to stop the piston, this way compensating for the losses which appear in the positioning system.

After reducing the values regarded as constants and expressing  $q$  from the equation, we come to the following relation:

$$q = c_2 \cdot v^2 - z \quad (7)$$

The equation shows that the ideal deceleration distance of the piston ( $q$ ) changes according to a second-degree function of piston speed. It follows that the widths of the deceleration bands of the piston have to be adjusted in a given moment proportional to the square of the measured output's first derivative; at this point a proportional coefficient ( $c_2$ ) has to be introduced. Furthermore, it is also necessary to set a constant  $c_1$  bandwidth which guarantees the slow movement near the ideal value.

As the next step, we have to assign the adequate control signs to the bands. This is done in a similar way to the operation of a relay, by sign functions, which decide whether the piston's measured output is below or above the band limit set. Summing up the values of these sign functions we arrive at 4 discrete numeric values which unequivocally determine which band the measured output falls into (e.g. we get -3 if it is below all band limits, i.e. in band number 1). By assigning the adequate control signs to these numeric values and to the tolerance band around the ideal position we achieve a control method which satisfies the criteria set.

In accordance with notations of control engineering, the mathematical description of the control method is as follows:  $r$  stands for the reference signal, while  $y_m$  is the measured output,  $t$  means tolerance and  $F;C;E$  are respectively the filling, closing and emptying switch states of the first and second solenoid valves:

$$\begin{aligned} & \text{sign} \left\{ y_m - \left[ r - (c_1 + c_2 \cdot (\dot{y}_m)^2) \right] \right\} + \text{sign} (y_m - r) + \text{sign} \left\{ y_m - \left[ r + (c_3 + c_4 \cdot (\dot{y}_m)^2) \right] \right\} = k \\ & \text{if } |y_m - r| < t, \text{ then} \quad \Rightarrow \quad \text{cont} = [F;F] \\ & \text{if } |y_m - r| > t, \text{ then} \quad \left\{ \begin{array}{l} \text{if } k = -3 \Rightarrow \text{cont} = [F;E] \\ \text{if } k = -1 \Rightarrow \text{cont} = [F;C] \\ \text{if } k = 1 \Rightarrow \text{cont} = [C;F] \\ \text{if } k = 3 \Rightarrow \text{cont} = [E;F] \end{array} \right. \quad (8) \end{aligned}$$

The constants  $c_3$  and  $c_4$  figuring in the equation have the same function as the already known  $c_1$  and  $c_2$  constants; their introduction into the equation is necessary because of the asymmetric setting options which reflect the asymmetry of the cylinder.

The behaviour of the system is calculable and compared to the examples in the specialized literature the command signal operates at a lower frequency; thus, due to the smaller amount of gas let into the environment the efficiency of the overall system is increased. It is worth noting that the system is capable of adjusting itself to the reference signal even if per chance we have chosen too high parameters at the control settings. In this case the balance of force required to stop the cylinder piston sets in earlier than necessary, but since we only fill one of the chambers (see bands number 2 and 4) in the other chamber the pressure will slowly decrease, which is a consequence of the ever-present cylinder loss. The force arising from this pressure difference will always slowly move the piston to its ideal position. This is advantageous because this way, as far as the positioning systems most significant quality factor, the steady-state error is

concerned, we can say that our system operates without predefined working-positions. Another great advantage is that in spite of the low frequency and delays of the solenoid valves we are able to make the piston stop with a high accuracy thanks to the slow movement around the reference signal.

#### 4. APPARATUS

The circuit diagram of the pneumatic positioning system is presented on figure number 5. As an actuator we applied a Festo DSNU-20-100-PPV-A P606 cylinder of 100mm stroke length, to which we attached a Festo MLO-POT-225-LWG analogue displacement encoder, which has a 0,01 mm travel resolution. The applied encoder is a potentiometer which provides a voltage signal in proportion to the displacement. In order to move the cylinder we applied two Festo VSVA-B-P53C-H-A2-1R2L 5/3 way solenoid valves, but we only used one output connection each and the remaining output ports were plugged. We measured the mentioned solenoid valve's ON and OFF switching time at 6 bar supply pressure; in case of switching on it was 14 ms (Figure 3.) while at switching off 36 ms (Figure 4.).

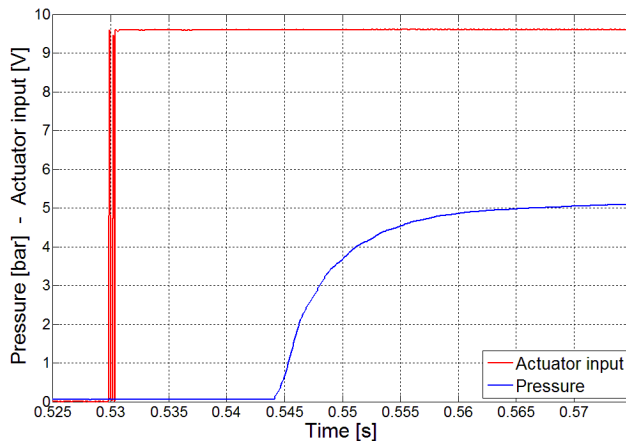


Figure 3. Valve switching – On

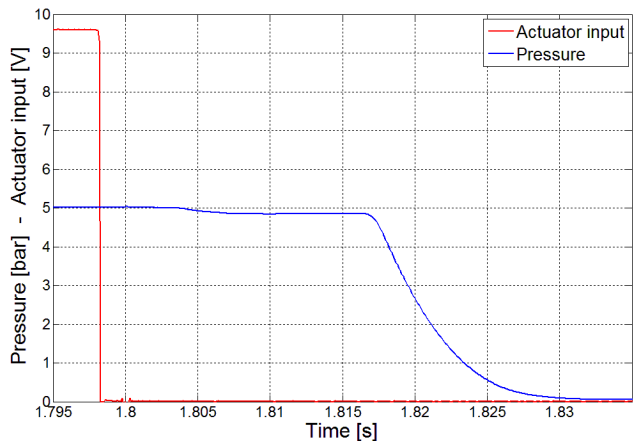


Figure 4. Valve switching - Off

A further constituent is a Festo D:LR-1/8-0-MINI pressure regulator, and we also connected a Festo SDE1-D10-G2-H18-C-PU-M8 pressure sensor to both chambers to serve as feedback, which however we did not use in the control process in order to minimize the number of sensors necessary for the operation of the system. This system was constructed to test the planned control method but by changing the different elements of the scheme, it can be freely scaled to achieve a faster operation or the movement of heavier loads.

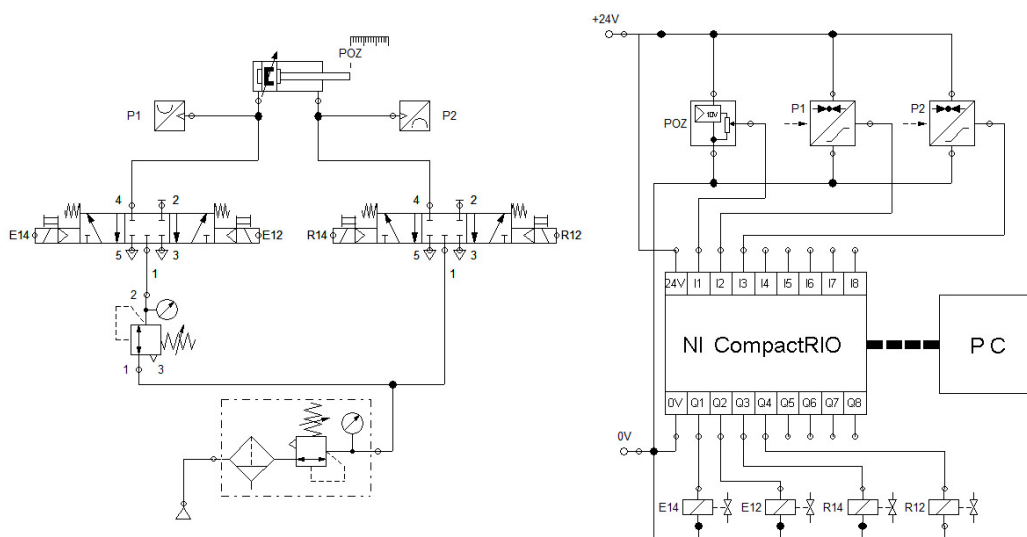


Figure 5. The circuit diagram of the pneumatic positioning system

The major elements of the electronic system are a 0-24 V direct current power supply (NI PS-15), an electronic instrument board (Festo), a NI CompactRIO™ (cRIO 9073) programmable automation controller and the already mentioned electro-pneumatic elements (displacement encoder, pressure sensors and solenoid valves). The applied NI CompactRIO™ programmable automation controller is a modular system; out of its modules we used the analogue-to-digital converter (NI 9201), for a dual purpose. On the one hand we applied it in the controlling process to measure the voltage signal (which is in proportion to the

displacement) provided by the displacement encoder. On the other hand we used it in collecting data about the voltage signals corresponding to pressure values (expressed in bars) provided by the analogue pressure sensors. We controlled the two solenoid valves with the help of the digital output module (NI 9472). The communication between the CompactRIO™ and the computer was ensured by an Ethernet connection. We realised the real-time control based on equation number (8) by applying the FPGA module of CompactRIO™ programming it in the LabVIEW 2009 software.

## 5. MEASUREMENT RESULTS

The testing of the compiled system was done by determining the quality factors of the control method. During this process we have determined the settling time for step responses from end positions, overshoots and steady-state error graphically based on measurement results. Under settling time we conventionally understand the time required for the measured output to finally reach the  $\pm 5\%$  vicinity of the reference signal.

The moved load was  $m=0.542$  kg, the value of supply pressure in the case of the negative chamber was  $p_2=6.105$  Pa, and accordingly the decreased supply pressure of the positive chamber was

$$p_1 = \frac{A_2}{A_1} \cdot p_2 = 5,04 \cdot 10^5 \text{ Pa}$$

. The measurements were carried out at room temperature.

The control setting parameters were  $c_1=18$  [mm],  $c_2=950$  [-],  $c_3=18$  [mm],  $c_4=250$  [-]; based on previous experiences with the system the width of the tolerance band was set to be  $\pm 0.025$  mm, we regarded the position as adequate within this range.

First we tested the dislocations of the cylinder piston in the positive direction, i.e. when the piston was moving outwards of the cylinder.

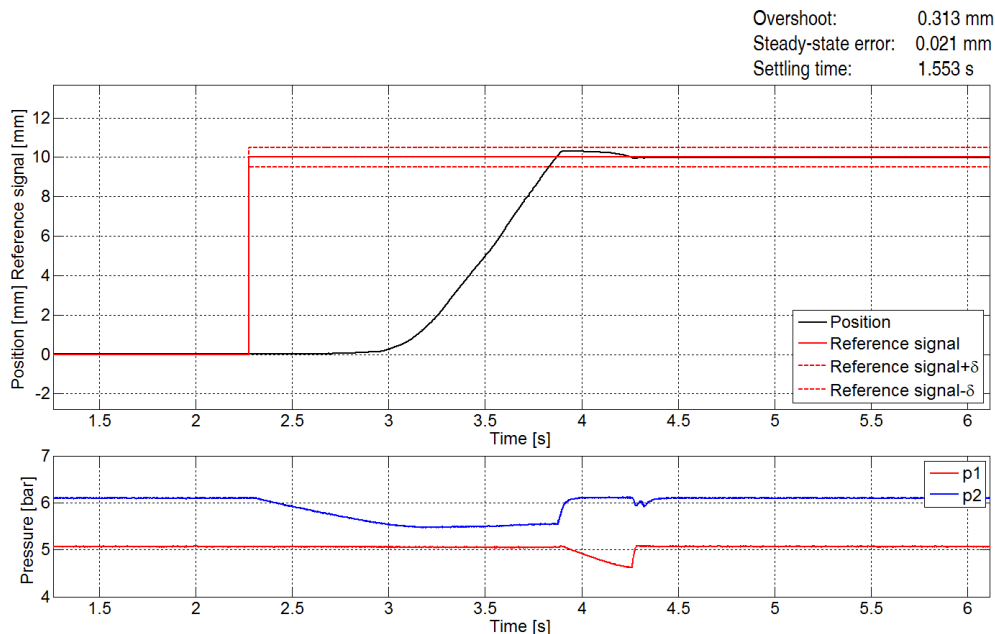


Figure 6. Step response - 0-10 mm

In Figure 6. we examined a settling onto the 10 mm reference signal from initial position, which is 10% of the stroke length of the cylinder. At such a small change of position the control system works in the deceleration zone (2) all the way through, i.e. the speed of the displacement of the piston is only dependent upon the cylinder loss. It is visible that the settling time is under 2 seconds, the overshoot can be considered minor. The steady-state error is greater than the resolution of the displacement encoder, but it nevertheless remained within the tolerance band and is still better than most of the best values to be found in the specialised literature.

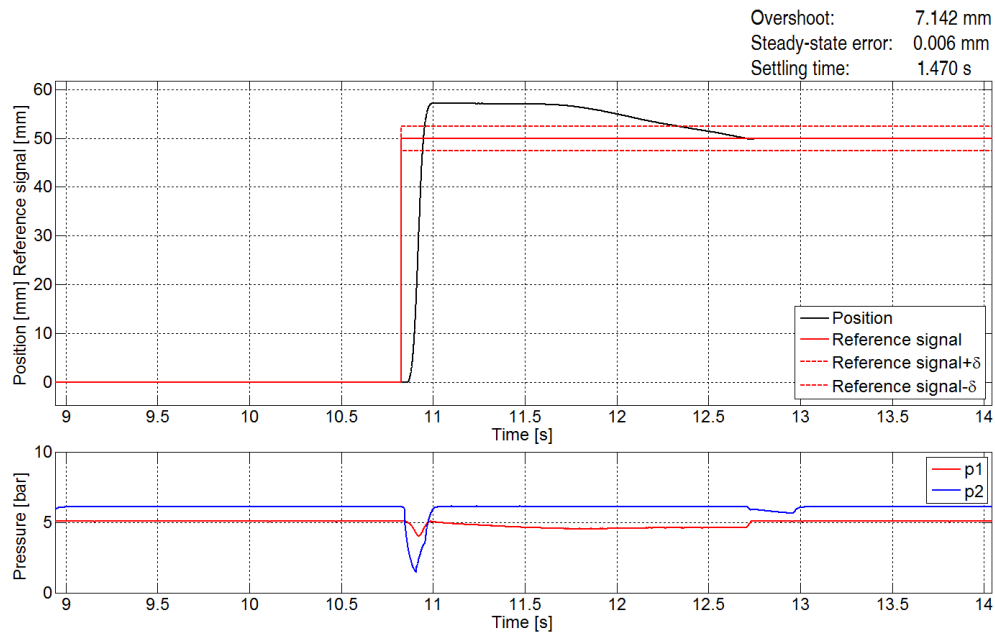


Figure 7. Step response - 0-50 mm

The evaluation of the second test (Figure 7.) sheds light on the limits of our positioning system, given that in the case of the settling to the 50 mm reference signal a significant overshoot was observed. This is the consequence of the fact that the chamber filling at the adjusted supply pressure is fast and because of this the acceleration of the low-friction cylinder piston is too great to be followed by the control system. This is the consequence of the operating limits of valves with long switching time. The deceleration of the piston movement, i.e. the closing of the ventilated chamber begins later than would be ideal, which is why the significant overshoot and the same settling time appear. It is important to be noted though, that all these do not influence the positioning accuracy, i.e. the steady-state error is equivalent to the travel resolution of the displacement encoder.

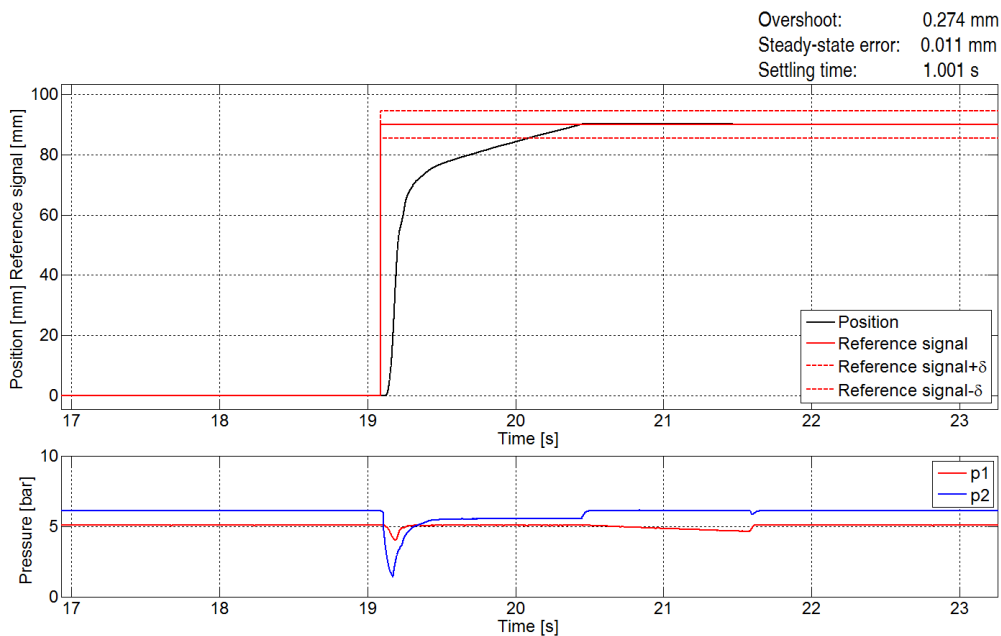


Figure 8. Step response - 0-90 mm

At the third measurement (Figure 8.) we have examined a displacement which is long compared to the stroke length of the cylinder by setting the reference signal at 90 mm. It is visible that in the case of large step size the control method is able to follow the dynamics of the cylinder, the overshoot is minimal while the settling time is 1 second. The steady-state error is again equivalent to the travel resolution of the displacement encoder.

After this we examined the movement of the piston in the negative direction, namely when it moves backwards into the cylinder.

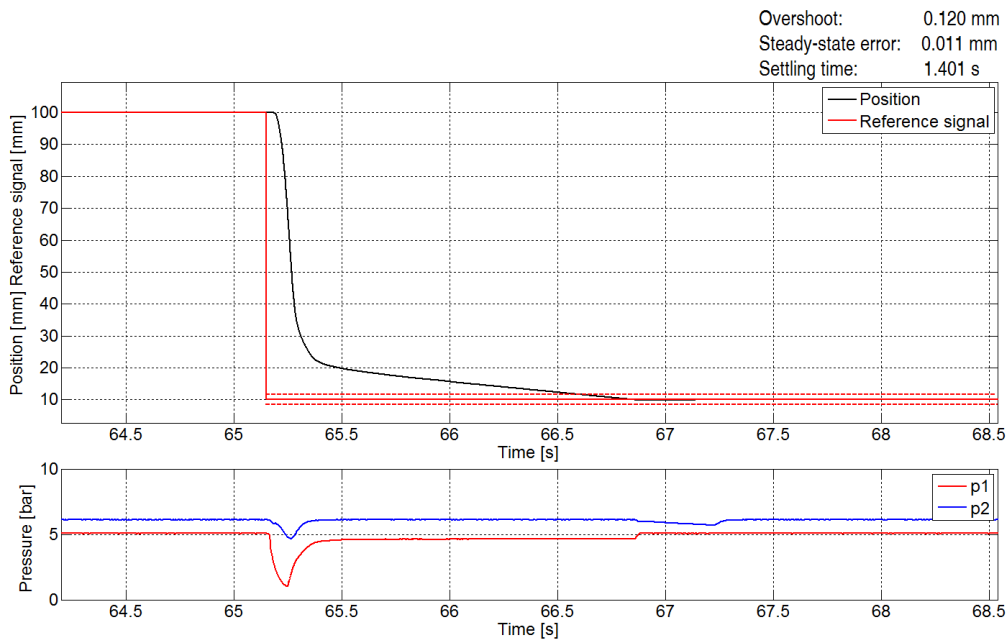


Figure 9. Step response - 100-10 mm

In the course of the fourth test at Figure 9. we can see a displacement similarly great to the previous experiment, but in the negative direction. The overshoot is minimal, and the settling time is still under 2 seconds. The steady-state error is once again equivalent to the resolution of the displacement encoder.

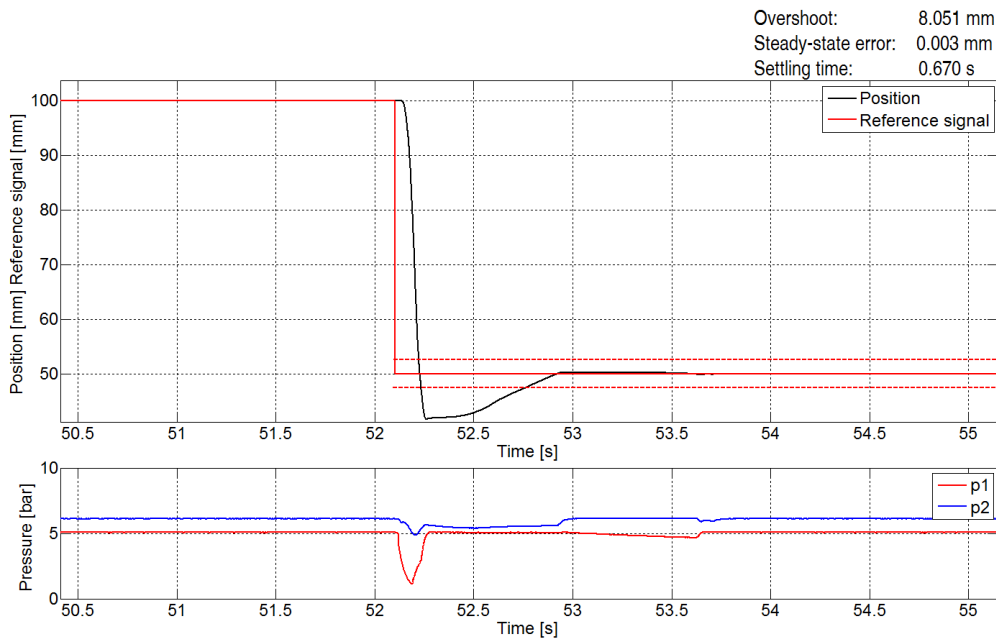


Figure 10. Step response - 100-50 mm

The fifth measurement (Figure 10.) examined a movement in the negative direction the scale of which is 50% of the stroke length of the piston. It is visible that an overshoot similar to that of the second testing appears. The steady-state error is minor, and in this case the settling time is exceptionally good, which is partly due to the fact that the piston moves faster in the negative direction because of the asymmetric construction of the cylinder.

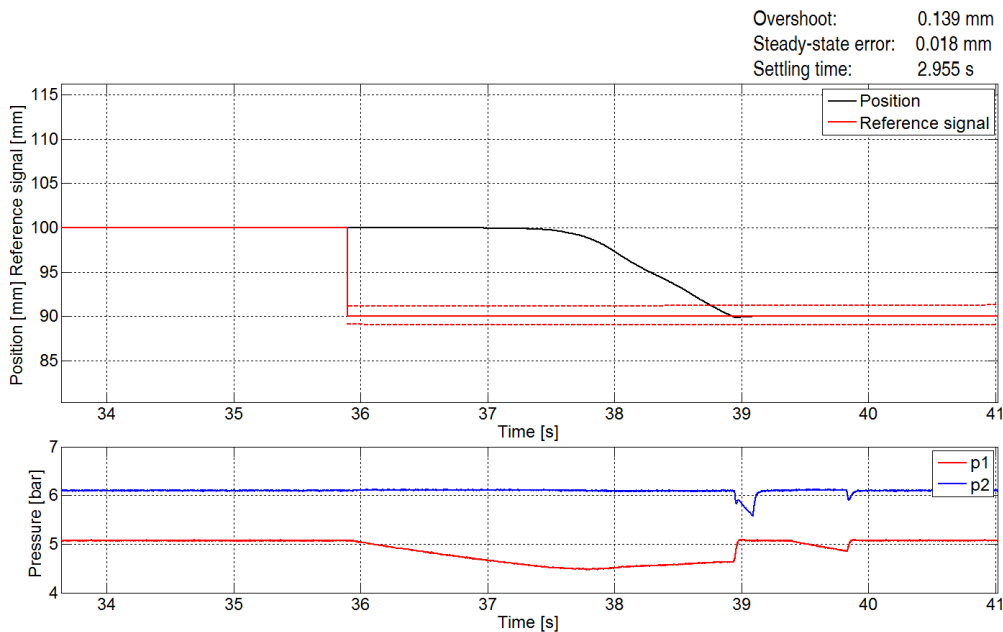


Figure 11. Step response - 100-90 mm

In the last, sixth testing (Figure 11.) we observed the small-scale negative movement with a displacement from 100 mm to 90 mm. The movement of the piston remains in the deceleration band (4) all the way through, thus the speed of displacement is only dependent upon the cylinder loss. As a result, the settling time is significant, but the overshoot is minimal and the steady-state error is almost equivalent to the travel resolution of the displacement encoder.

## 6. SUMMARY

A novel control strategy and the according experimental apparatus to achieve accurate positioning of a pneumatic cylinder using solenoid valves is presented. The most significant features of this pneumatic positioning system are the following:

- *it substitutes the costly proportional valve with the conventional solenoid valve*
- *thanks to a novel control design, the system operates in a chatter free way*
- *the maximal operating velocity and force of the applied pneumatic actuator is not decreased*
- *it contains the least amount of sensors and the least expensive electro-pneumatic elements possible*

Thanks to all these, the system can achieve an adequately high positioning accuracy and reach a favourable price/value ratio at the same time. The paper also sheds light on the fact that the system's steady-state error is highly dependent on the displacement encoder's travel resolution. This holds out the promise that the application of more advanced technology in the area (e.g. using digital sensor with higher travel resolution, or a fast-switching solenoid valve to reduce the overshoot) will further improve the system's positioning accuracy.

## 7. REFERENCES

- [1] Ahn, K., Yokota, S., Intelligent switching control of pneumatic actuator using on/off solenoid valves, *Mechatronics*, 15, 683–702, 2005.
- [2] Akdağ, F.N., Kuzucu, A., Highly accurate pneumatic position control, Istanbul Technical University Mechanical Engineering Department, <http://digital.ni.com/>
- [3] Barth, E.J., Zhang, J., Goldfarb, M., Control Design for Relative Stability in a PWM-Controlled Pneumatic System, *Journal of Dynamic Systems, Measurement, and Control*, 125, 504-508, 2003.
- [4] Isermann, R., *Mechatronic systems : Fundamentals*, Springer, London, 2005.
- [5] Messina, A., Giannoccaro, N.I., Gentile, A., Experimenting and modelling the dynamics of pneumatic actuators controlled by the pulse width modulation (PWM) technique, *Mechatronics*, 15, 859–881, 2005.

- [6] Nguyen, T., Leavitt, J., Jabbari, F., Bobrow, J.E., Accurate Sliding-Mode Control of Pneumatic Systems Using Low-Cost Solenoid Valves, *IEEE/ASME Transactions on mechatronics*, 12(2), 216-219, 2007.
- [7] Parnichkun, M., Ngaecharoenkul, C., Kinematics control of a pneumatic system by hybrid fuzzy PID, *Mechatronics*, 11, 1001-1023, 2001.
- [8] Shih, M.-C., Ma, M.-A., Position control of a pneumatic cylinder using fuzzy PWM control method, *Mechatronics*, 8, 241-253, 1998.
- [9] Thomas, M.B., Maul, G.P., Jayawiyanto, E., A Novel, Low-Cost Pneumatic Positioning System, *Journal of Manufacturing Systems*, 24(4), 377-387, 2005.
- [10] van Varseveld, R.B., Bone, G.M., Accurate position control of a pneumatic actuator using on/off solenoid valves, *IEEE/ASME Transactions on Mechatronics*, 2(3), 195-204, 1997.

# SYMMETRY AND SIMILARITY PROPERTIES OF 2D FIGURES

Z. Szakál<sup>1</sup>, I. Zsoldos<sup>2</sup>

<sup>1</sup> Institute for Mechanical Engineering Technology, Faculty of Mechanical Engineering,  
Szent István University, Gödöllő, Hungary

<sup>2</sup> Szechenyi István University, Győr

**Abstract** A new algorithm has been developed to sort two-dimensional figures by their shape. The algorithm can find the figures having equal or approximately equal shape independently from geometrical measures and the complexity of the shapes. It is based on the definition of the symmetry-diagram which was introduced for symmetry recognition originally. The new method can be used for sorting different parts at assembly lines and for reverse engineering, too.

**Keywords:** Symmetry-diagram, symmetry detection, shape detection

## 1 INTRODUCTION

The sorting algorithm takes advantage of the feature of the symmetry-diagram (in other name the shape-diagram) that it shows a unique shape property of the two-dimensional (2D) figures independently from geometrical measures i.e. it is a shape factor.

The symmetry-diagram was introduced for symmetry detection originally [1]. The problem of symmetry detection has been extensively studied in numerous fields including visual perception, computer vision, robotics, computational geometry and reverse engineering. Early methods concentrated on finding perfect symmetries in 2D or 3D point sets [2], [3]. Since the restriction to exact symmetries limits the use of these methods for real-world objects, a method was introduced for computing approximate global symmetries in 3D point sets [4], but the complexity of the algorithm makes it impractical for large data sets. The notion of approximate symmetry was formalized by expressing symmetry as a continuous feature [5]. The examination of the correlation of the Gaussian image was proposed to recover global reflective and rotational symmetries [6]. A shape descriptor was introduced that concisely encodes global reflective and rotational symmetries [7], [8]. Different applications based on generalized complex moments [9], grouping feature points [10], [11], [12], isometric transformations [13], planar reflective symmetry transform [14] and generalized symmetry transformation [15], [16] are used in image processing and mesh processing for detecting exact local and global reflection-symmetry and rotation- symmetry of 2D and 3D images.

The symmetries are often not exactly present, but only approximately present, due to measurement errors in the scanning process, and approximation and numerical errors in model reconstruction during reverse engineering [17]. Beside this, different CAD systems often use different tolerances [18], and what is symmetric in one CAD system may be only approximately symmetric in another. To solve these problems new algorithms based on the B-rep model were developed to find approximate rotational and translational symmetries of 3D forms built from simple geometric units [19] and complex 3D forms [20] in reverse engineering.

However a number of outstanding methods for symmetry recognition can be found in the literature, most of them do not take advantage of the fact that every symmetry axis of a 2D figure has to cross the gravity centre [2-20].

The symmetry-diagram is defined as the followings [1]:

- The contour of the 2D figure is needed to be known for the definition.
- A number between 0 and 1 signed by 'Z' ( $0 < Z \leq 1$ ) is computed for any line crossing the gravity centre. This 'Z' parameter, in other name the symmetry parameter is defined so that it equals to 1 if the line is an exact symmetry axis and it approximates to 1 if the line is an approximate symmetry axis. The less the line can be considered as a symmetry axis the less is the value of 'Z'.
- The symmetry-diagram shows the values of 'Z' for a set of lines revolving around the gravity centre in an angle range of  $180^\circ$ .

Independently from the fact that a given 2D figure is symmetric or not the symmetry-diagram is a shape factor: The symmetry-diagrams are different for the figures having different shape. Beside this: the symmetry-diagrams of coincident figures are the same and the symmetry-diagrams of approximately coincident figures are approximately same. The symmetry-diagrams of geometrically similar figures are the same (independently from geometrical measures) and the symmetry-diagrams of approximately similar figures are approximately same. Because of this important property of the symmetry-diagram it can be applied for recognition of figures having the same or approximately same shape (independently from geometrical measures). There is only one limit of the recognition: figures having more closed concentric curves as boundary (e.g. two concentric circles, the spacer) have the same symmetry-diagram.

## 2 THE SORTING ALGORITHM

Effective sorting and seeking (e. g. faulty seeking) algorithms are applied in the most different fields as for example in the data sorting [21], [22], in the sound technique [23] and in the image technique [24-33]. In the image technique one of the most relevant problems is the shape detection consisting of two different partial problems: the shape detection as boundary detection of the image segmentation and the shape detection (shape recognition) as making differences between figures having different shape. In the case of the boundary detection a lot of effective algorithms are known [24-28]. In the field of the shape recognition the solutions of the most different special problems are worked out as for example a fruit sorting algorithm [29], a face detection algorithm [30], a traffic sign shape classification algorithm [31]. A so called distance measure [32] and the gradient-based shape descriptor [33] were developed to distinguish different classes of the 2D figures.

The new sorting algorithm shown in this work is a general algorithm which can be used without limits in all 2D application fields of the shape recognition.

Knowing the definition of the symmetry-diagram the sorting algorithm consists of several simple steps:

- The input of the algorithm is the set of the boundaries of the 2D figures.
- The symmetry-diagram of every 2D figure is computed.
- The subsets of same or approximately same diagrams are divided.

We show the process in a case-study from the mechanical engineering. In Figure 1 a photo of screws, screw-nuts and spacers having different measures can be seen. The photo shows the result of an image process, as well. The red curves are fitted to the boundaries of the elements and the set of these contours is the input of the sorting algorithm.



Figure 1. The input of the sorting algorithm is the set of the contours of the elements signed by red curves. The numbers are the identifications of the elements.

At using the sorting algorithm it has to be taken down the outer outline of configurations. Part aggregation can be seen in Figure 1. where the red colour marks the outlines of parts. Numbers mark certain parts in the sake for later identification. We handle separately with the algorithm the outline of certain parts. In case of each part We take down the picture points of outlines forming the parts in a co-ordinate system. The symmetry-diagram calculated to each part after the algorithm run can be seen in Figure 2. arranged. It can be seen well on the symmetry-diagrams the parts examined can be simply grouped. The sorting of parts can be carried out by taken to the Z-parameter to difference but characteristic ranges.

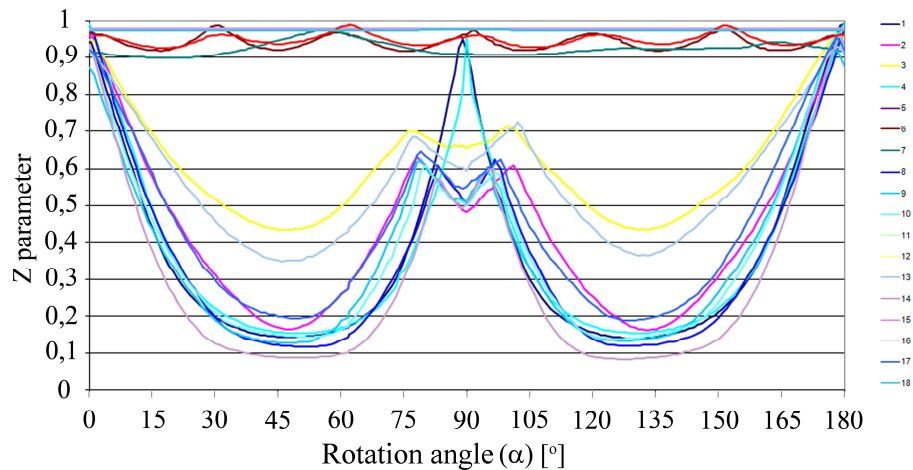


Figure 2. The summed-up results

Those parts are similar to circle which Z parameter is greater than 0,9 in all rotation angle-positions of symmetry-diagrams. For each diagram to be seen in Figure 3. is true  $0,9 < Z < 1$ . The great majority of curves can be found within a strict range in the Figure, these can be seen magnified in Figure 4. The curve marked 7 in Figure 3. though is circular but it differs significantly from the others therefore it has to be examined separately. The curve also shows high Z parameter on the whole however there is also a preferred direction where the value of symmetry-parameter  $Z = 0,976$  at  $\alpha = 61^\circ$ . That means such axis can be taken down surely to the configuration examined which approximate symmetry.

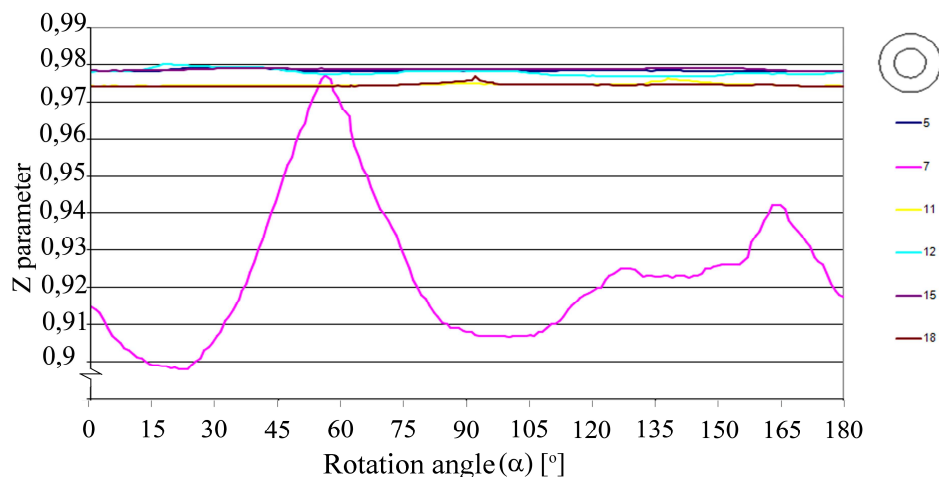


Figure 3. Symmetry-diagrams of circular configurations

The number 7 part is put together by a set of washers and pipe-piece with the marks of Figure 2. The configuration stuck together during taking a photo succeeded to photograph on a optional position this causes deformation on the picture examined. In this case just this deformation makes possible to recognize it as a faulty part. The algorithm would have been surely recognized as a washer if it had been arranged exactly in the vertical position under the camera. Avoiding such cases it is worth to examine pictures made from camera line-up with two different angular positions.

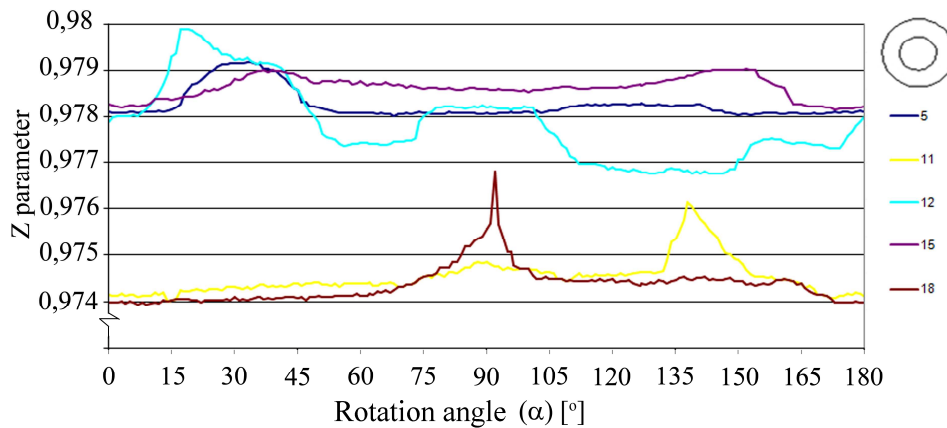


Figure 4. A strict range of circular configuration

Further grouping possibility presents oneself in Figure 4. The value of Z parameter can be found between 0,974-0,98 in 0,006 zone. Examining the shape of curves found in the very strict zone it comes to light that the 11. and 18. configurations differ in some measures from the other similar circular configurations. Beyond on that they resemble to the circle there is surely on then a preferred point (the shot of spring washer). The outstanding parameter values to be found on the various angular positions of the 11. and 18. configuration curves derive from the different orientations of washers.

The number 5. part of the Figure 22. is also a spring washer which can not be distinguished with the present single-camera examination from the other washers. In this case the examination from two separate camera line-ups gives sure solution.

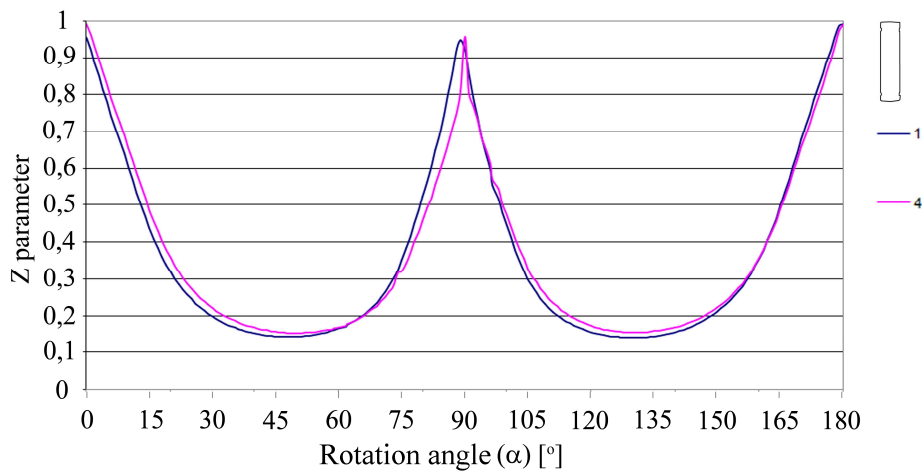


Figure 5. Rectangular like configurations with large side-edge ratio

The characteristic of curves to be seen in Figure 5. is that it can be found parameter near to  $Z=1$  in two angular positions. This type symmetry-diagram is characteristic to rectangles with at least 1/6 side ratio. On the diagrams of number 1. and 4. pin like parts can be seen in present case. In case of both parts the value of visible approximate symmetry in the  $90^\circ$  angular position of the curves is smaller than in  $0^\circ$  angular position of these. The non full symmetry is due to smaller slots on configurations.

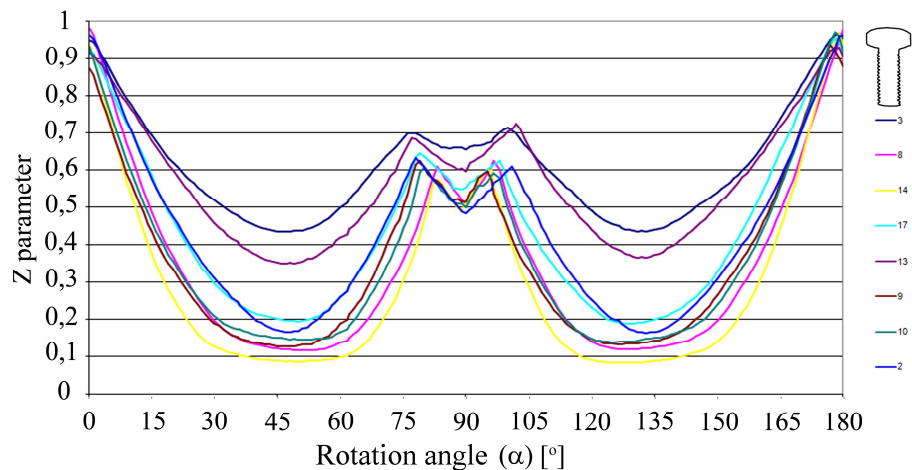


Figure 6. Curves of bolt like configurations

The curves of Figure 6 resemble to curves shown in Figure 5. here it is also true that they mark rectangular like configuration with large side-edge ratio (in 2D rectangular, in 3D it can be just like cylindric). The cause of local parameter reduction of the symmetry-diagram in  $90^\circ$  angular position is the result of irreversible symmetry defect. The symmetry deformation derives from the head formation of bolts and rivets in present case. The aggregation contains also bolts and rivets during examination to which we have carried out the run. The algorithm can not distinguish these parts in this resolution. If there are previous knowledge concerning the configuration examined then increasing the resolution of picture processing these parts already can be distinguished, too.

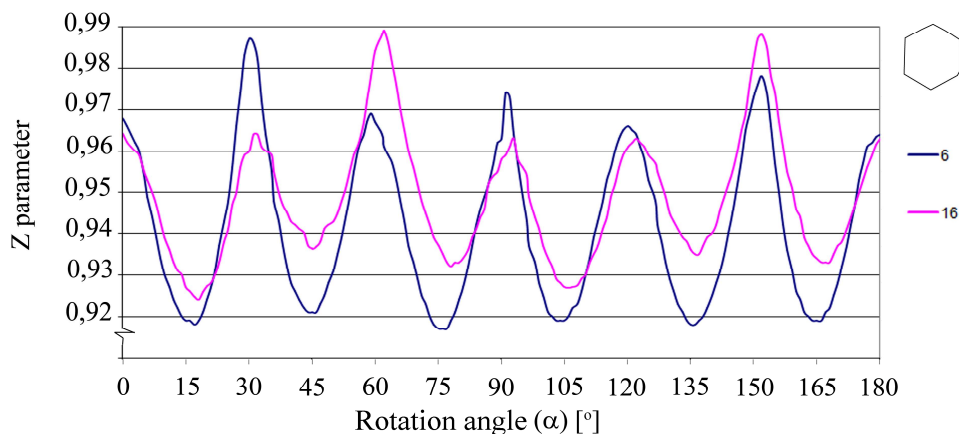


Figure 7. Symmetry-diagram characterizing hexagon parts

The curves having got 6 local maximums can be seen in Figure 7. this means that the configuration 6. and 16. are hexagon among the configurations examined. That comes also to light from the symmetry-diagram that damages, deformations can be found on the hexagon configurations examined. The curves should reach six times the  $Z=1$  value in ideal case.

It can be seen from the results got during the run that the software produced by us recognizes the similarity of optional planar configurations. The algorithm is not suitable determining symmetry characteristic in case of configurations with concentric outline (for example: washer). This during sorting of parts it can not neither distinguish the washer from a disc.

### 3 CONCLUSIONS

The symmetry searching algorithm developed during our research work is suitable to sort for example bulk joint-elements. Presently the algorithm makes possible the classification according to shape. The pre-sorting of bulk parts can be solved by this. It can not be used to sort according to dimension. However the algorithm determines the symmetry characteristics based on digital pictures by setting up proportions from geometric dimensions, because of from the pictures examined the geometric dimensions of configurations can be also decided during processing. By utilizing this the algorithm can be made suitable to classify according to dimension, too.

It has been started the realization in technological circumstances the automatized pre-sorting of bulk joint-elements. We have started with the engineers of the company renewing aeroplane power plants in Veresegyház the practical realization of the method worked out by me. The work is presently in the phase of planning and instrument obtaining.

The cold forming standard (MSZ EN 10142:2000) containing low-carbon content strip steel and plate hot-dip galvanized qualifies the determination the so called zinc-flowers formed during the process by measuring number that can be determined with non exact mode. The standard uses the following ideas for putting in row according to dimension of zinc-flowers formed on the surface galvanized: small-, medium, large zinc-flowers. Putting in row the zinc-flowers according to the standard is important concerning use, as for example cold formability, colorability.

I think so that with the symmetry searching method worked out by us, based on the symmetry characteristics it could be determined unambiguously the dimension steps of zinc-flowers according to various fields of use.

There are in trade straw cutters developed for this aim with various constructions for using as an energetics aim of agricultural crops. The most important viewpoint is the sturdy structure durability and the reliability at designing harvesting machines. The size and the shape of chaff are an important viewpoint during using for energetics aim. The dimension, shape and surface of the chippings have got an emphasized rule concerning the firing technique. The presently wide-spread stem chippings is suitable for firing, but for operating boilers with good efficiency is indispensable to produce homogeneous-and optimum size solid fuel for equipment given.

By using the method drawn up to search the symmetry it can be worked out an appliance provided with an online data collecting system which qualifies the chippings considering morphology during cutting chaff. Based on the results by this way a control can be developed for optimizing the technological parameters of straw cutters.

### 4 ACKNOWLEDGEMENTS

The authors would like to acknowledge the support of supported by OTKA grants K 73776 in Hungary.

### 5 REFERENCES

- [1] Z. Szakal, I. Zsoldos: The Symmetry-Diagram as a Tool of the Pattern Recognition, International Journal of Mathematical Models and Methods in Applied Sciences, Issue 4, Volume 2, 523-532, 2008, ISSN: 1998-0140
- [2] J. WOLTER, T. WOO, R. VOLZ, Optimal algorithms for symmetry detection in two and three dimensions. The Visual Computer, 1985.
- [3] M. ATALLAH, On symmetry detection. IEEE Trans. On Computers 34, 7, 2004, pp. 663–666.
- [4] H. ALT, K. MEHLHORN, H. WAGENER, E. WELZL, Congruence, Similarity and symmetries of geometric objects. Discrete Comput. Geom. 3, 1988, pp. 237–256.
- [5] H. ZABRODSKY, S. PELEG, D. AVNIR, Symmetry as a continuous feature. IEEE PAMI, 17, 1995.
- [6] C.Sun, J. Sherrah, 3D symmetry detection using the extended Gaussian image. IEEE Transactions on Pattern Analysis and Machine Intelligence, 19, 2, 1997, pp. 164–8.
- [7] M.KAZHDAN, B. CHAZELLE, D.P. DOBKIN, A. FINKELSTEIN, T. FUNKHOUSER, A reflective symmetry descriptor. In Proceedings of ECCV, 2002, pp. 642–656.
- [8] M.KAZHDAN, T. FUNKHOUSER, S. RUSINKIEWICZ, Symmetry descriptors and 3d shape matching. In Symposium on Geometry Processing, 2004, pp. 116–125.

- [9] D. Shen, H. Ip, K. Cheung, E. Teoh, Symmetry detection by generalized complex (GC) moments: A close-form solution. *IEEE Transactions on Pattern Analysis and Machine Intelligence*, 21, 5, 1999, pp. 466–76.
- [10] G. Loy, J. Eklundh, Detecting symmetry and symmetric constellations of features. In: *ECCV 2006, Part II*. LNCS, Vol. 3952. Springer-Verlag; 2006, pp. 508–21.
- [11] N. Mitra, L. Guibas, M. Pauly, Partial and approximate symmetry detection for 3D geometry. *ACM Transactions on Graphics*, 25, 3, 2006, pp. 560–8.
- [12] N. Mitra, L. Guibas L, M. Pauly, Symmetrization. *ACM Transactions on Graphics*, 26, 3, 2007, Art. No. 63
- [13] A. Martinet, C. Soler, N. Holzschuch, FX. Sillion, Accurate detection of symmetries in 3D shapes. *ACM Transactions on Graphics*, 25, 2, 2006, pp. 439–64.
- [14] J. Podolak, P. Shilane, A. Golovinskiy, S. Rusinkiewicz, T. Funkhouser, A planar-reflective symmetry transform for 3D shapes. *ACM Transactions on Graphics* 25, 3, 2006, pp. 549–59.
- [15] D. Reissfeld, H. Wolfson, Y. Yeshurun, Context Free Attentional Operators: the Generalized Symmetry Transform, *Int. J. Comput. Vision* 14, 2, 1995, pp. 119–130.
- [16] W.H. Li, A.M. Zhang, L. Kleeman, Global reflectional symmetry detection for robotic grasping and visual tracking, *ACRA 05, Australasian Conference on Robotics and Automation*, 2005. <http://www.visionbib.com/bibliography/journal/acr.html#ACRA05>
- [17] T. Varady, R. Martin, J. Cox, Reverse engineering of geometric models - an introduction, *Computer-Aided Design* 29, 4, 1997, pp. 255–68.
- [18] M. Pratt, B. Anderson, T. Ranger, Towards the standardized exchange of parameterized feature-based CAD models. *Computer-Aided Design* 37, 12, 2005, pp. 1251–65.
- [19] B. Mills, F. Langbein, A. Marshall, R. Martin, Approximate symmetry detection for reverse engineering. In: *Proc. 6<sup>th</sup> ACM symp. solid and physical modeling*, 2001, pp. 241–8.
- [20] M. Li, F. Langbein, R. Martin, Detecting approximate symmetries of discrete point subsets, *Computer-Aided Design* 40, 1, 2008, pp. 76–93.
- [21] Chenn-Jung Huang, Chih-Tai Guan and Yi-Ta Chuang, A Key-Address Mapping Sort Algorithm, *Proceedings of the 5th WSEAS International Conference on Applied Computer Science*, Hangzhou, China, April 16–18, 2006 (pp352–357)
- [22] Changsoo Kim, Sungroh Yoon, Dongseung Kim, Parallel External Sort of Floating-Point Data by Integer Conversion, *APPLIED COMPUTING CONFERENCE (ACC '08)*, Istanbul, Turkey, May 27–30, 2008.
- [23] Ryuichi Ishino, Detection System of Faulty Ground Wires from Aerial Video of Transmission Lines with Consideration of Influence of Devices on Ground Wires, *Proceedings of the 6th WSEAS/IASME Int. Conf. on Electric Power Systems, High Voltages, Electric Machines*, Tenerife, Spain, December 16–18, 2006
- [24] Francesco de Pasquale, Julian Stander, A multi-scale template method for shape detection with bio-medical applications, *Pattern Anal. Applic*, 2009, 12:179–192
- [25] JIAN'AN LUAN, JULIAN STANDER\* and DAVID WRIGHT, On shape detection in noisy images with particular reference to ultrasonography, *Statistics and Computing* (1998) 8:377–389
- [26] Lena Gorelick, Ronen Basri, Shape Based Detection and Top-Down Delineation Using Image Segments, *Int. J. Comput. Vis.* 2009, 83: 211–232
- [27] N. Guil, J.M. Gonzalez-Linares, E.L. Zapata, Bidimensional shape detection using an invariant approach, *Pattern Recognition* 1999, 32:1025–1038
- [28] ROSEMARY IRRGANG, An Intelligent Snake Growing Algorithm for Fuzzy Shape Detection, *Expert Systems With Applications*. 1996 Vol. 11, No. 4, pp. 531–536
- [29] GUI Jiang-sheng, RAO Xiu-qin, YING Yi-bin, Fruit shape detection by level set, *Gui et al. / J. Zhejiang Univ. Sci. A* 2007, 8(8):1232–1236
- [30] Eli Saber, A. Murat Tekalp, Frontal-view face detection and facial feature extraction using color, shape and symmetry based cost functions, *Pattern Recognition Letters* 1998, 19:669–680
- [31] Ryuichi Ishino, Detection System of Faulty Ground Wires from Aerial Video of Transmission Lines with Consideration of Influence of Devices on Ground Wires, *Proceedings of the 6th WSEAS/IASME Int.*

Conf. on Electric Power Systems, High Voltages, Electric Machines, Tenerife, Spain, December 16-18, 2006

- [32] Lena Gorelick · Ronen Basri, Shape Based Detection and Top-Down Delineation Using Image Segments, Int J Comput. Vis. 2009, 83: 211–232
- [33] Abdulkerim Çapar, Binnur Kurt, Muhittin Gökmen, Gradient-based shape descriptors, Machine Vision and Applications 2009, 20:365–378



ISSN : 2032-7471

---

---